

REDUCTION OF CO₂ AND CO MEDIATED BY TRANSITION METAL COMPLEXES

Marsha Denise Massey

A dissertation submitted to the faculty at the University of North Carolina at Chapel Hill in partial fulfillment of the requirements for the degree of Doctor of Philosophy in the Department of Chemistry.

Chapel Hill
2016

Approved by:

Cynthia K. Schauer

Alexander J.M. Miller

Maurice S. Brookhart

Michel R. Gagné

Jillian L. Dempsey

© 2016
Marsha Denise Massey
ALL RIGHTS RESERVED

ABSTRACT

Marsha Denise Massey: Reduction of CO₂ and CO Mediated by Transition Metal Complexes
(Under the direction of Cynthia K. Schauer)

The direct correlation of increasing worldwide energy demand with increasing CO₂ emissions presents a compelling need to devise a method of alternative energy production that will meet demand but limit further CO₂ release into the atmosphere. Catalytic reduction of carbon dioxide to produce a renewable fuel source could be a viable solution, and developing approaches for the conversion of CO₂ to fuel is a current area of intense research activity. The work presented here focuses on evaluation of molecular complexes capable of reducing CO₂.

Chapter 2 considers a ligand-based hydride transfer approach for carbon dioxide reduction to formate using two new manganese cyclohexadienyl complexes of formulation Mn(η^5 -C₆Me₆H)(CO)L₂ with L₂ as a bidentate phosphine ligand. The reductive capabilities of the manganese complexes are demonstrated in reactions with carbon disulfide to form dithioformate at room temperature.

Chapter 3 explores the reactivity of the CO reduction intermediate hydroxymethyl ligand in [Ru(bpy')₂(CO)(CH₂OH)][PF₆] (bpy' = 5,5'-dimethylbipyridine) that has been proposed to be a precursor to MeOH. Reaction with acids and other electrophiles occur at oxygen rather than carbon of the hydroxymethyl ligand, to produce a series Lewis base stabilized carbene complexes (ylide complexes). Of particular interest are the labile nitrile ylide complexes that are

shown to be precursors to the C-C coupled product, ethylene. This system highlights the potential to achieve C₂ products via CO reduction.

Finally, Chapter 4 presents synthetic routes to new ruthenium carbonyl complexes incorporating the bidentate carbene-pyridine ligand, 3-methyl-1-picolylbenzimidazol-2-ylidene (Mebim-pic) to compliment prior studies of 3-methyl-1-pyridylbenzimidazol-2-ylidene (Mebim-py). The methylene spacer between the pyridine and carbene ligands in the Mebim-pic system gives rise to a larger bite angle (87.2°) in comparison to Mebim-py (77.9°), which will change the steric environment at the catalytic site. Synthetic routes to carbonyl complexes [Ru(Mebim-pic)(tpy)(CO)]²⁺ (where tpy is 2,2':3'3''-terpyridine) and [Ru(Mebim-pic)(bpy')(CO)₂]²⁺ are reported. Carbonyl complexes are intermediates in the catalytic cycle for reductive disproportionation of CO₂ as well as the entry point to further reduction of the coordinated CO ligand.

In Honor of My Grandma Louise

Requiescat in Pace

ACKNOWLEDGMENTS

I cannot bear the thought of this document's publication without first offering some words of gratitude to the many people who have guided me to this point in my life. So here I shall make some attempt to put into words the deep sense of appreciation towards many of you.

First and foremost, my family both near and far whom have taught me the power of persistence and patience. My father who's belief in my abilities never wavered. My brother, Brian, for standing by my side and prepared to console me a laugh, chocolate cake, or steak dinner when needed. Thank you Mutti, Vhaeda, for being here in the end for that final push. I won't ever be able to repay your patience with those many low T NMR experiment midnights.

To my best friend in childhood, Jessica Barnard, who provided support in small yet powerful ways. Thank you also to her family, particularly Mr. James Barnard who treated me as one of his own daughters for so many years. I owe you many Fathers' Day cards.

My best friend and better counterpart, Jessica Smart, thank you for your love and compassion for so many years. No matter how many years go by without talking, you have always been present and patient with me.

To my dearest college friends, Wency Zhao, M.D. and Fahad Malik, M.D. for their support largely via Facebook. No matter how far and how busy you both managed to provide a safe place to talk and have fun. I aspire to follow in your footsteps of excellence and compassion for mankind.

Thank you to Nishii, Courtney Talley, for her consistent “jia you!”s no matter how large or small the task. Most of all, I will count myself as accomplished and fortunate should I manage to convey even half of your passion, dedication, and empathy for my future students. You are an exceptional educator and it would be my honour to continue learning from your example.

I would be remiss if I did not express my unwavering, everlasting love to my Sora, Hong Tran, Ph.D. You have always been the light ahead in the darkness that surrounds me. Without your brilliance guiding me I know not where I would be. Plus, your late night video game Skype sessions were helpful. May we karaoke again together soon!

Thank you to Elle L. my friend across the pond who entertained me with unique, personalized fiction as a treat for hard work. I look forward to your future creations!

To so many dear friends and colleagues I had the fortune and pleasure of meeting here in Chapel Hill, thank you for your comradery and company. My worries of graduate school becoming a lonely time were rapidly washed away because of you all. I hope that I have made your worlds better as you have mine.

To my brothers in the chemical bond, members of Alpha Chi Sigma, may the ties of friendship which bind us remain true and everlasting. I appreciate you all for finding me when I became lost. Without your encouragement, I would not have found my calling. Particularly, Prof. Joseph Roberts who heard my every concern, large and small, with saintly patience. Furthermore, Sir Emperor Joe provided engaging and creative bouts of D&D. Thank you to Dr. Njamkou Noucti who stuck beside me through good and not so great times. Particularly, thank you Njamkou for putting your life in my hands on the trip back from Detroit in a Nissan Versa, despite me as being a novice driver. Your belief in my capabilities then and now mean the world to me. Special thanks to my bigs of Alpha Chi Sigma, Kate McGuiness and Sophie Liu. You

introduced me to a great world of future chemist in the making, a debt I will never be able to repay.

I have no idea how to begin properly thanking my former lab neighbours. I have missed you dearly in the last two years at UNC, it was a pleasure visiting many of you in Chicago and Tennessee. Please know, Dr. Joseph Falkowski, Dr. Rachel Huxford-Phillips, Dr. Kathryn Dekraft, Dr. Marcella Wanderley, and Chris Poon, that I appreciated our late nights and weekends in company in lab. Special thanks to Seth Barrett for being there throughout this entire journey, up until the very end. Furthermore, thank you all for the few dinner parties and vacations. But most of all, I could not have reached this point without your feedback on practice talks and paper drafts. All of you contributed to giving me confidence in my abilities as a chemist, for which I will be eternally grateful. May we keep in touch and prosper together in the years to come!

Thank you to the many dedicated undergraduate researchers I had the pleasure of mentoring and collaborating with: Rachel Croome, Jimmy Pan, Bennett Vass, Ian Mercer, Teddy Wong, Ian Moseley, and Kyle Williamson. I know you will all do great things in the future. Furthermore, I owe a great deal of gratitude to other members of the Schauer lab: Kyle Duffe, Dr. Abhigna Polovarapu, and Austin Toman. Thank you for many great presentations, conversations, lunches, and coffee runs. Most of all, I appreciate your willingness and sacrifice in consuming the many cupcakes and desserts I baked.

Sincerest gratitude to the many students, staff and faculty of UNC Chapel Hill's Energy Frontier Research Center. In particular, Dr. Seth Marquard for bouncing ideas for new synthetic approaches around with me. Thank you to the EFRC Catalysis team for many productive and engaging meetings and discussions. In particular, Prof. Thomas J. Meyer, it has been an honour

to work with you and I thank you for inspiring my interest in the field of alternative energy electrocatalysis.

Thank you to my dissertation and candidacy committees for their guidance through the doctorate. It has been an honour to have all of you present for those defining moments and throughout.

My deepest appreciation for Dr. Kathleen Nevins and Prof. Carribeth Bliem for their support and motivation in the toughest times of my journey. I have learned so much working with you. I aspire to follow in your footsteps and can only hope you will feel pride from my future endeavors.

Prof. Alexander J. M. Miller, I appreciate your mentoring and enthusiasm in teaching as well as research. It was my honour to work with you as a Graduate Research Coordinator for CHEM 251. I learned a great deal about classroom management, active learning in the large classroom environment, and problem-based learning through working with you. Furthermore, in collaborating with you I gained confidence not only in my teaching but my skills as a researcher. Thank you for giving me so many opportunities to further myself as a chemist and educator. Most of all, thank you for believing in me.

To Cindy, thank you for inviting me into your lab and your willingness to work with me these past six years. To this day I struggle to understand what you saw in me, but I am fortunate for your patience and persistence in pushing me to better myself as a researcher. Above all, thank you for reinforcing my passions for teaching by allowing me the room to explore undergraduate mentoring and assistant teaching opportunities.

Finally, thank you to the former Alliance for the Graduate and Professoriate (AGEP – NSF) program directors and coordinators (now Initiative for Minority Excellence – IME at UNC

Chapel Hill). Kacey thank you for your encouragement and support, and a kind ear to talk about baking. Noelle Romero, you're such a sweetheart and I adore your kindness in listening but also your saucy personality keeping life interesting. I hope to find myself just as dedicated to students as you have been for IME and the summer undergraduate research program.

Dean Valerie Ashby, I appreciate the many moments of advice you have offered to me on furthering my career goals. Also, thank you Dean Ashby for encouraging me to believe the sky is the limit, that I can achieve what I set my mind to. I learned from you that I have much to offer the scientific community and will endeavor to do so.

I cannot even begin to affectively express my gratitude and adoration for Kathy Wood (IME co-director). Kathy, you have been my biggest fan, cheerleader, and support. I do not know how you do it, but I hope to one day be able to repay the debt to students in need like I have been. I know that without you this undoubtedly would not have been possible. Hopefully, I have made you proud.

I owe a great deal of thanks to so many more for reaching this point on the path of my life aspirations. I wish I could submit an additional dissertation in honour of you all. To those not mentioned by name but most certainly have been in my thoughts and heart, who have guided and supported me in ways both grand and small through this journey, know I will always feel grateful for your presence and none of this work would have been possible without each and every one of you.

TABLE OF CONTENTS

LIST OF TABLES	xiv
LIST OF FIGURES	xv
LIST OF SCHEMES.....	xix
LIST OF EQUATIONS	xx
LIST OF ABBREVIATIONS AND SYMBOLS	xxii
1. INTRODUCTION TO CARBON DIOXIDE REDUCTION USING TRANSITION METAL CATALYSTS	1
1.1. Alternative Fuel Strategy	1
1.2. Dye-Sensitized Photoelectrochemical Cell (DSPEC) Approach	3
1.3. Reduction of Carbon Dioxide	4
1.3.1 General Considerations.....	4
1.3.2 CO ₂ Reduction Strategies.	6
1.3.3 Carbon Monoxide Formation.....	8
1.3.4 Formate Production.....	10
1.3.5 Products Beyond Formate.....	12
1.4. Introduction to Work Herein.....	13
2. MANGANESE CYLCOHEXADIENYL COMPLEXES FOR CARBON DIOXIDE REDUCTION TO FORMATE	14
2.1. Introduction and Background	14
2.2. Results and Discussion	20
2.2.1 Synthesis of Complexes.....	20

2.2.2 Reactivity of Manganese Cyclohexadienyl Complexes.....	27
2.3. Summary	31
2.4. Experimental.....	32
2.5. Acknowledgements.....	37
3. REACTION OF ELECTROPHILES WITH A CO-REDUCTION INTERMEDIATE RUTHENIUM HYDROXYMETHYL COMPLEX.....	38
3.1. Introduction and Background	38
3.2. Results and Discussion	41
3.2.1 Generation of ylides $[\text{Ru}(\text{bpy}')_2(\text{CO})(\text{CH}_2\text{L})]^{2+}$	41
3.2.2 Reactions of $[\text{Ru}(\text{bpy}')_2(\text{CO})(\text{CH}_2\text{OH})]^+$ in the absence of Lewis bases	49
3.2.3 Decomposition of $[\text{Ru}(\text{bpy}')_2(\text{CO})(\text{CH}_2\text{L})]^{2+}$; ethylene forming reactions	56
3.3. Summary	58
3.4. Experimental.....	60
3.5. Acknowledgements.....	72
4. SYNTHESIS OF CARBON DIOXIDE REDUCTION INTERMEDIATE RUTHENIUM BENZIMIDAZOL-2-YLIDENE CARBONYL COMPLEXES.....	74
4.1. Introduction and Background	74
4.2. Results and Discussion	79
4.2.1 Mebim-pic ligand precursor synthesis.	80
4.2.2 Synthesis of $\text{Ru}(\text{Mebim-pic})(\text{CO})_2\text{Cl}_2$ (1a).	81
4.2.3 Synthesis of $\text{Ru}(\text{Mebim-pic})(\text{CO})_2(\text{OTf})_2$ (2a).	82
4.2.4 Synthesis of $[\text{Ru}(\text{Mebim-pic})(\text{bpy}')(\text{CO})_2]^{2+}$ (3a).	83
4.2.5 Synthesis of $[\text{Ru}(\text{Mebim-pic})(\text{tpy})(\text{CO})]^{2+}$ (4a).	84
4.2.6 Attempted synthesis of $[\text{Ru}(\text{Mebim-py})(\text{tpy})(\text{CO})]^{2+}$ (4b).	88
4.2.7 Electrochemical analysis of complex 4a	91

4.3. Summary and Future Directions	92
4.4. Experimental	93
4.5. Acknowledgements.....	100
APPENDIX 1.1: CHAPTER 2 ADDITIONAL SPECTROSCOPIC DATA.....	101
APPENDIX 1.2: COMPLETE X-RAY CRYSTALLOGRAPHIC DATA FOR 1B	104
APPENDIX 2.1: CHAPTER 3 ADDITIONAL SPECTROSCOPIC DATA.....	115
APPENDIX 2.2: COMPLETE X-RAY CRYSTALLOGRAPHIC DATA FOR 5⁺	123
APPENDIX 3.1: CHAPTER 4 ADDITIONAL SPECTROSCOPIC DATA.....	135
REFERENCES	141

LIST OF TABLES

Table 2.1: Summary of Spectroscopic Data for Mn Complexes.	25
Table 2.2: Selected Atom Distances (Å) for Mn(C ₆ Me ₆ H)(CO)(DMPE) (1b).	27
Table 2.3: Crystallographic Parameters for Mn(C ₆ Me ₆ H)(CO)(DMPE) (1b).....	37
Table 3.1: Summary of Spectroscopic Data for Ru Ylide Complexes, [Ru(CH ₂ L)] ²⁺	44
Table 3.2: Crystallographic Parameters for [Ru(5,5'- Me ₂ bpy) ₂ (CO)(CH ₂ OCPh ₃)] [PF ₆] ⁺ •CH ₂ Cl ₂ , 5 ⁺	72
Table 4.1: Spectroscopic Characterization of Ruthenium Complexes	90

LIST OF FIGURES

Figure 1.1: Global energy consumption and CO ₂ emissions vs time.	1
Figure 1.2: Outlined approach for a “solar fuels” energy economy.	2
Figure 1.3: Dye-Sensitized Photoelectrochemical Cell (DSPEC) for artificial photosynthesis.	3
Figure 1.4: Charge distribution in CO ₂ molecule.	4
Figure 1.5: Two approaches to CO ₂ reduction. ⁵	8
Figure 1.6: Selection of catalyst used for CO ₂ reduction.	9
Figure 1.7: Electrocatalytic CO ₂ reduction to formate using Ir(POCOP) catalysts.	11
Figure 2.1: Metal d _{xy} and C ₆ Me ₆ H ligand saturated carbon interaction promoting hydride reactivity.	17
Figure 2.2: Cyclic voltammogram of [(η ⁶ -C ₆ Me ₆)Mn(CO) ₃]BF ₄	18
Figure 2.3: Manganese complexes studied in this work.	20
Figure 2.4: Arene loss complex.	22
Figure 2.5: ¹ H NMR of Manganese DPPE cyclohexadienyl complex 1a	24
Figure 2.6: X-ray crystal structure of Mn(DMPE) cyclohexadienyl complex 1b	26
Figure 2.7: Structure of HTBD ⁺ formate.	29
Figure 2.8: Operando IR analysis of reaction of 1a with CO ₂ in presence of [HTBD]PF ₆	30
Figure 2.9: Solid state IR spectra for salts [HTBD]PF ₆ and [HTBD]O ₂ CH.	31
Figure 3.1: ¹ H NMR of 2a ²⁺ , [Ru(bpy') ₂ (CO)(CH ₂ NCMe)] ²⁺ formed under acidic conditions in CD ₂ Cl ₂	43
Figure 3.2: ¹ H NMR of 4a ²⁺ , [Ru(bpy') ₂ (CO)(CH ₂ py)] ²⁺	46
Figure 3.3: X-ray crystal structure of 5 ⁺ , [Ru(bpy') ₂ (CO)(CH ₂ OCPh ₃)] [PF ₆] ⁻ •CH ₂ Cl ₂	49
Figure 3.4: ¹ H NMR of 6 ²⁺ [Ru(bpy') ₂ (CO)(H ₂ C=CH ₂)] ²⁺ formed under acidic conditions.	51
Figure 3.5: ¹ H NMR of 8 ²⁺ [Ru(CH ₂ OCH ₂)Ru] ²⁺ dimer formed using excess HNTf ₂ acid.	53
Figure 3.6: ¹ H NMR of 8 ²⁺ generated from HNTf ₂ then added HOTf to form 6 ²⁺	54
Figure 3.7: Variable temperature ¹ H NMR of 8 ²⁺ formed using excess HNTf ₂ acid.	55

Figure 3.8: ^1H NMR of $\mathbf{6}^{2+}$ generated from decomposition of $\mathbf{2d}^{2+}$.	57
Figure 4.1: Proposed CO_2 reduction mechanism using Ru polypyridyl complexes.	75
Figure 4.2: Two views of the HOMO of $[\text{Ru}(\text{tpy})(\text{Mebim-py})]^0$.	75
Figure 4.3: Free energy change of isomerization for $[\text{Ru}(\text{tpy})(\text{Mebim-L})\text{X}]^{n+}$ complexes.	76
Figure 4.4: Ligands of interest to this work, 3-methyl-1-picolybenzimidazol-2-ylidene (left) and 3-methyl-1-pyridylbenzimidazol-2-ylidene (right).	77
Figure 4.5: Both carbene- and pyridine- <i>trans</i> to $\text{X} = \text{MeCN}$ isomers for $[\text{Ru}(\text{tpy})(\text{Mebim-L})(\text{MeCN})]^{2+}$ complexes.	78
Figure 4.6: Ruthenium polypyridyl complexes studied to facilitate electrochemical CO_2 reduction by steric hindrance.	79
Figure 4.7: NOESY NMR of pyridine <i>trans</i> to CO isomer of $\mathbf{4a}$ and calculated structure using dotted-lines to indicate correlations to tpy observed in NOESY, where distances.	86
Figure 4.8: DFT calculated C- <i>trans</i> to CO isomer of $\mathbf{4a}$.	87
Figure 4.9: Electrochemical reduction of $\mathbf{4a}$ (3 mM) under nitrogen in acetonitrile with 10% water added.	91
Figure 4.10: Electrochemical reduction of $\mathbf{4a}$ (3 mM) under CO_2 in acetonitrile with 1%, 5%, and 10% water added.	92
Figure A2.1: ^1H NMR of $\mathbf{2a}^+$ $[\text{Mn}(\text{CO})(\text{DPPE})(\text{C}_6\text{Me}_6)][\text{BF}_4]$.	101
Figure A2.2: $^{13}\text{C}\{^1\text{H}\}$ NMR of $\mathbf{1a}$ $\text{Mn}(\text{CO})(\text{DPPE})(\text{C}_6\text{Me}_6\text{H})$.	101
Figure A2.3: ^1H NMR of $\mathbf{1b}$ $\text{Mn}(\text{CO})(\text{DMPE})(\text{C}_6\text{Me}_6\text{H})$.	102
Figure A2.4: $^{13}\text{C}\{^1\text{H}\}$ NMR of $\mathbf{1b}$ $\text{Mn}(\text{CO})(\text{DMPE})(\text{C}_6\text{Me}_6\text{H})$.	102
Figure A2.5: ^1H NMR of reaction of $\mathbf{1a}$ with CS_2 forming $\mathbf{2a}[\text{S}_2\text{CH}]$.	103
Figure A3.1: ^1H NMR of $\mathbf{3}^+$ amide ylide, $[\text{Ru}(\text{bpy}')_2(\text{CO})(\text{CH}_2\text{NHCOMe})]^+$.	115
Figure A3.2: ^1H NMR of $\mathbf{2b}^{2+}$ propionitrile ylide $[\text{Ru}(\text{bpy}')_2(\text{CO})(\text{CH}_2\text{NCEt})]^{2+}$.	115
Figure A3.3: ^1H NMR of $\mathbf{2c}^{2+}$ benzonitrile ylide $[\text{Ru}(\text{bpy}')_2(\text{CO})(\text{CH}_2\text{NCPh})]^{2+}$.	116
Figure A3.4: ^1H NMR of $\mathbf{2d}^{2+}$ fluorinated benzonitrile ylide $[\text{Ru}(\text{bpy}')_2(\text{CO})(\text{CH}_2\text{NCAr}^{\text{F}})]^{2+}$.	116
Figure A3.5: Mass spectroscopic data of $\mathbf{4a}^{2+}$ pyridine ylide $[\text{Ru}(\text{bpy}')_2(\text{CO})(\text{CH}_2\text{py})]^{2+}$.	117
Figure A3.6: ^1H NMR of $\mathbf{4b}^{2+}$ 4-methylpyridine ylide $[\text{Ru}(\text{bpy}')_2(\text{CO})(\text{CH}_2(4\text{-Mepy}))]^{2+}$.	117

Figure A3.7: ^1H NMR of $\mathbf{4c}^{2+}$ 3,5-dimethylpyridine ylide $[\text{Ru}(\text{bpy}')_2(\text{CO})(\text{CH}_2(3,5\text{-Me}_2\text{py}))]^{2+}$	118
Figure A3.8: ^1H NMR of $\mathbf{4d}^{2+}$ 4-cyanopyridine ylide $[\text{Ru}(\text{bpy}')_2(\text{CO})(\text{CH}_2(4\text{-CNpy}))]^{2+}$	118
Figure A3.9: ^1H NMR of $\mathbf{5}^+$ orange crystal triphenylmethoxymethyl $[\text{Ru}(\text{bpy}')_2(\text{CO})(\text{CH}_2\text{OCPh}_3)][\text{PF}_6]\cdot\text{CH}_2\text{Cl}_2$	119
Figure A3.10: Mass spectroscopy data of $\mathbf{5}^+$ orange crystal triphenylmethoxymethyl $[\text{Ru}(\text{bpy}')_2(\text{CO})(\text{CH}_2\text{OCPh}_3)][\text{PF}_6]\cdot\text{CH}_2\text{Cl}_2$	119
Figure A3.11: ^1H NMR of methylene region for hydroxide abstraction from $\mathbf{1}^+$ in presence of pyridines.....	120
Figure A3.12: ^1H NMR of $\mathbf{7}^+$	120
Figure A3.13: $^{13}\text{C}\{^1\text{H}\}$ NMR of $\mathbf{7}^+$	121
Figure A3.14: ^1H NMR reaction forming cyclopropane (at 0.24 ppm) via via hydroxide abstraction using trityl cation from $\mathbf{1}^+$ under ethylene atmosphere.	121
Figure A3.15: Mass spectroscopic data for ether-bridged dimer $\mathbf{8}^{2+}$ complex.	122
Figure A4.1: ^1H NMR of ligand precursor $[\text{Mebim-pic}]\text{I}$	135
Figure A4.2: ^1H NMR of ligand precursor $[\text{Mebim-pic}]\text{I}$	135
Figure A4.3: ^1H NMR of <i>cis</i> - and <i>trans</i> - $\text{Ru}(\text{Mebim-pic})(\text{CO})_2\text{Cl}_2$ (1a).....	136
Figure A4.4: ^1H NMR of <i>cis</i> - $\text{Ru}(\text{Mebim-pic})(\text{CO})_2\text{Cl}_2$ (1a).....	136
Figure A4.5: ^1H NMR of <i>cis</i> - $\text{Ru}(\text{Mebim-pic})(\text{CO})_2\text{Cl}_2$ (1a).....	137
Figure A4.6: ^1H NMR of <i>cis</i> - $\text{Ru}(\text{Mebim-pic})(\text{CO})_2(\text{OTf})_2$ (2a).....	137
Figure A4.7: ^{19}F NMR of <i>cis</i> - $\text{Ru}(\text{Mebim-pic})(\text{CO})_2(\text{OTf})_2$ (2a).....	137
Figure A4.8: ^1H NMR of $[\text{Ru}(\text{Mebim-pic})(5,5'\text{-Me}_2\text{bpy})(\text{CO})_2][\text{PF}_6]_2$ (3a).....	138
Figure A4.9: $^{13}\text{C}\{^1\text{H}\}$ NMR of $[\text{Ru}(\text{Mebim-pic})(5,5'\text{-Me}_2\text{bpy})(\text{CO})_2][\text{PF}_6]_2$ (3a).	138
Figure A4.10: ^1H NMR of pyridine <i>trans</i> to CO isomer of 4a $[\text{Ru}(\text{Mebim-pic})(\text{tpy})(\text{CO})][\text{PF}_6]_2$ (3a).....	138
Figure A4.11: $^{13}\text{C}\{^1\text{H}\}$ NMR of pyridine <i>trans</i> to CO isomer of 4a $[\text{Ru}(\text{Mebim-pic})(\text{tpy})(\text{CO})][\text{PF}_6]_2$ (3a).....	139
Figure A4.12: ^1H NMR of <i>cis</i> - $\text{Ru}(\text{Mebim-py})(\text{CO})_2\text{Cl}_2$ (1a).	139

Figure A4.13: ^1H NMR of <i>cis</i> -Ru(Mebim-py)(CO) ₂ (OTf) ₂ (2a).....	139
Figure A4.14: $^{13}\text{C}\{^1\text{H}\}$ NMR of <i>cis</i> -Ru(Mebim-py)(CO) ₂ (OTf) ₂ (2a).	140
Figure A4.15: ^{19}F NMR of <i>cis</i> -Ru(Mebim-py)(CO) ₂ (OTf) ₂ (2a).....	140

LIST OF SCHEMES

Scheme 1.1: Direct reduction of CO ₂ to its radical anion.....	5
Scheme 1.2: Reduction potentials for CO ₂ to CO, formic acid, and methanol.....	5
Scheme 2.1: Proposed catalytic cycle for CO ₂ reduction using Mn cyclohexadienyl complexes.	14
Scheme 2.2: Synthetic method for making precursor complexes for Mn(C ₆ Me ₆ H) system.	15
Scheme 2.3: Sweigart electrochemical results for reduction of [Mn(η ⁶ -C ₆ Me ₆)(CO) ₃] ⁺	18
Scheme 2.4: Reactivity of η ⁴ complex to give η ⁵ after adding H ⁺ and arene exchange to produce crystallized η ⁴ -naphthalene complex.	19
Scheme 2.5: Synthesis of DPPE manganese hexamethylbenzene piano stool complexes.	21
Scheme 2.6: Synthesis of monodentate DPPE manganese hexamethylbenzene complex.	21
Scheme 3.1: Example scheme for activation of CO ₂ using transition metal catalysts.	38
Scheme 3.2: Synthetic reduction of ruthenium polypyridyl complexes in Tanaka's system.	40
Scheme 3.3: Hypothesis for base-mediated carbene coupling to form ethylene.	58
Scheme 3.4: Summary of reactions of 1 ⁺ (hydroxymethyl, center) with electrophiles forming 2 ²⁺ (nitrile-ylide), 4 ²⁺ (pyridine-ylide), 5 ⁺ (triphenylmethoxymethyl), 8 ²⁺ (ether-bridged dimer) and 6 ²⁺ (ethylene) complexes.....	59
Scheme 4.1: Synthesis method for Mebim-pic ligand precursor compound.	80
Scheme 4.2: Approaches to synthesis of Ru(Mebim-pic)(CO) ₂ Cl ₂ (1a) complex.	81

LIST OF EQUATIONS

Equation 2.1: Eyman's various Mn cyclohexadienyl complexes which transfer hydride to CO ₂ (reactive hydride is shown in blue).	16
Equation 2.2: Hydride addition for synthesizing Mn(DPPE) cyclohexadienyl complex.	22
Equation 2.3: Photolytic method for synthesizing Mn bidentate phosphine cyclohexadienyl complexes.	23
Equation 2.4: Reaction of Mn cyclohexadienyl bidentate phosphine complexes with CS ₂	27
Equation 3.1: Protonation of 1 ⁺ by strong acids to form 2 ²⁺ ruthenium nitrile ylide.....	42
Equation 3.2: Water addition to 2a ²⁺ to form 3 ⁺ ruthenium amido ylide. ⁷⁸	45
Equation 3.3: Hydroxide abstraction using trityl cation to form 2 ²⁺ ruthenium nitrile ylide.	45
Equation 3.4: Hydroxide abstraction using trityl cation to form 4 ²⁺ pyridine ylide.	46
Equation 3.5: Exchange reaction of acetonitrile in 2a ²⁺ for pyridine forming 4a ²⁺	48
Equation 3.6: Hydroxide abstraction from 1 ⁺ using trityl cation in the presence of pyridine N-oxide to form 5 ⁺	48
Equation 3.7: Production of C ₂ product, ethylene (coordinated to Ru in 6 ²⁺), by HOTf protonation of 1 ⁺	50
Equation 3.8: Protonation of [Ru(bpy') ₂ (CO)H] ⁺ using HOTf to form 7 ⁺ , [Ru(bpy') ₂ (CO)(OTf)] ⁺	52
Equation 3.9: HOTf protonation of 1 ⁺ under ethylene to form C ₃ product, cyclopropane, and 7 ⁺	52
Equation 3.10: Protonation reactions with partially soluble acid (HNTf ₂ on top) and weak acid (HNEt ₃ ⁺ on bottom) to form ether-bridged dimer species, 8 ²⁺	54
Equation 3.11: Hydroxide abstraction using trityl cation to form fluorinated-nitrile ylide, 2d ²⁺ , and its subsequent decomposition to ethylene complex, 6 ²⁺ , at higher temperatures.	56
Equation 4.1: Synthesis of triflate intermediate complex <i>cis</i> - 2a , Ru(Mebim-pic)(CO) ₂ (OTf) ₂	83
Equation 4.2: Synthesis of complex 3a , [Ru(Mebim-pic)(bpy')(CO) ₂][PF ₆] ₂	84
Equation 4.3: Synthesis of catalyst 4a , [Ru(Mebim-pic)(tpy)(CO)][PF ₆] ₂	85
Equation 4.4: Synthesis of Ru(Mebim-py)(CO) ₂ Cl ₂ , complex <i>cis</i> - 1b	88
Equation 4.5: Synthesis of Ru(Mebim-py)(CO) ₂ (OTf) ₂ , complex <i>cis</i> - 2b	88

Equation 4.6: Synthetic approach in attempt to make **4b**, $[\text{Ru}(\text{Mebim-py})(\text{tpy})(\text{CO})]^{2+}$ 89

LIST OF ABBREVIATIONS AND SYMBOLS

Å	Angstrom
°C	degrees Celsius
1,2-DCE	1,2-dichlorethane
Ar	aromatic
Ar ^F	3,5-bis(trifluoromethyl)phenyl
Ar ^F CN	3,5-bis(trifluoromethyl)benzonitrile
BAr ^F ₄	tetrakis[3,5-bis(trifluoromethyl)phenyl]borate
bpy or b	2,2'-bipyridine
bpy' or b'	5,5'-dimethyl-2,2'-bipyridine
br	broad
C ₂ H ₄ or CH ₂ CH ₂	ethylene
C ₃ H ₆	cyclopropane
Ch*	hexamethylcyclohexadienyl, C ₆ Me ₆ H
cm	centimeter
CN	nitrile or cyano group
C(O)	double bond carbonyl or C=O group
Cp	cyclopentadienyl
Cp*	hexamethylcyclopentadienyl
CV	cyclic voltammogram
d	doublet
DCM	dichloromethane

dd	doublet of doublets
dt	doublet of triplets
dq	doublet of quartets
E^+	electrophile
e^-	electron(s)
E°	standard reduction potential
eq	equation
equiv	equivalent
ESI	electrospray ionization
est.	estimate(d)
et al.	<i>et alii</i> meaning “and others”
Et	ethyl
EtOH	ethanol
EtCN	propionitrile
Fig.	figure
g	grams
h	hour
HOMO	highest occupied molecular orbital
HTBD ⁺	protonated 1,5,7-triazabicyclo[4.4.0]dec-5-ene
Hz	hertz
H^+	protic acid
IR	infrared
IR-SEC	infrared-spectroelectrochemistry

nJ	n-bond J -coupling constant
K	degrees Kelvin
kJ	kilojoules
LT	low temperature
LUMO	lowest unoccupied molecular orbital
m	multiplet
Me	methyl
Mebim-pic	3-methyl-1-picolybenzimidazol-2-ylidene
Mebim-py	3-methyl-1-pyridylbenzimidazol-2-ylidene
MeCN	acetonitrile
med	medium relative intensity
MeOH	methanol
min	minute
mL	milliliter
mol	moles
m/z	mass to charge ratio
nm	nanometers
NMR	nuclear magnetic resonance
NTf ₂	trifluoromethanesulfonimide anion
Opy	pyridine N-oxide
OTf	trifluoromethanesulfonate or triflate
Ph	phenyl
PhCN	benzonitrile

pic	picoline
ppm	parts per million
py	pyridine
q	quartet
RT	room temperature
s	singlet
(Solv)	solvent ligand
st	strong relative intensity
t	triplet
TBD	1,5,7-triazabicyclo[4.4.0]dec-5-ene
td	triplet of doublets
tpy or (t)	2,2':6',2''-terpyridine
V	volt
VT	variable temperature
w	weak relative intensity
xs	excess
z	charge
δ	relative NMR chemical shift in ppm
δ^- or δ^+	partial negative or positive charge
ΔG°	standard change in Gibb's Free Energy
ν	wavenumber, in cm^{-1}
ν_{CO}	wavenumber for CO stretch by IR, in cm^{-1}
μ	micro-

CHAPTER 1

INTRODUCTION TO CARBON DIOXIDE REDUCTION USING TRANSITION METAL CATALYSTS

1.1. Alternative Fuel Strategy

Globally energy demands continue to increase. In 2013, the United States alone consumed 2.2 billion tons of oil and equivalent substances (representing fossil fuels), which accounted for 17% of the entire world supply.¹ Currently, the majority of worldwide energy demands are met using fossil fuels. There are two deleterious consequences for having fossil fuels as the primary global energy source. First, it is a non-renewable source, so once consumed it is gone forever. Second, the consumption of fossil fuels produces carbon dioxide (CO₂), a greenhouse gas that is implicated in global warming (Figure 1.1). Recent estimates by the European Commission Joint

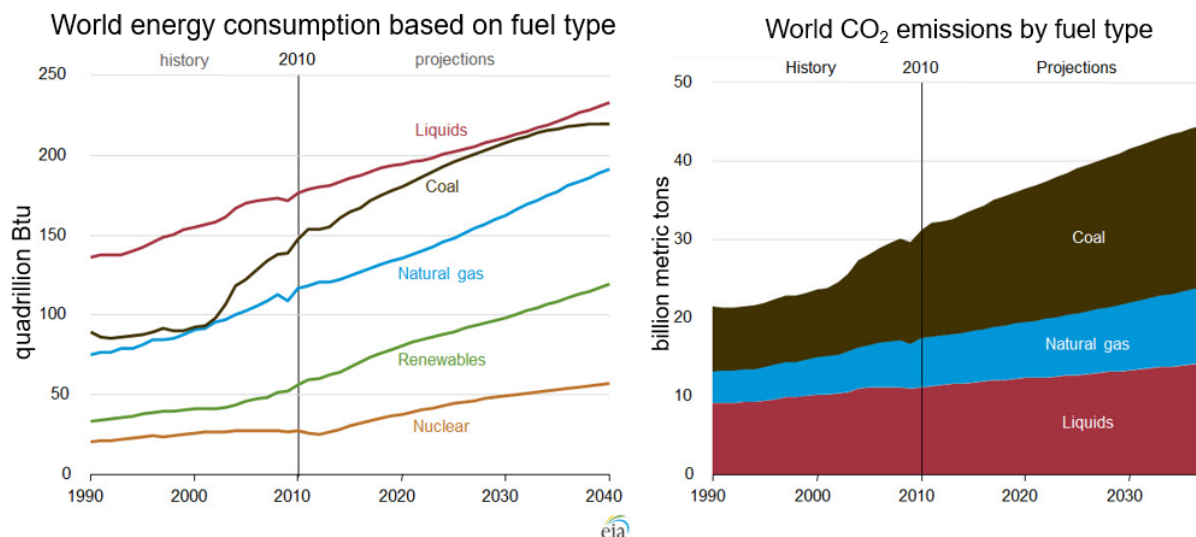


Figure 1.1: Figure demonstrating global energy consumption and CO₂ emissions vs time (over past two decades and future projections).⁴

Research Centre in 2014 indicate that around 30 billion tons per year of carbon dioxide is

produced from burning fossil fuels for energy, an 18% increase over the past decade.²⁻⁴ A shift to providing a greater proportion of our energy from renewable approaches, including solar cells, wind turbines, water turbines, and/or biofuels, would limit CO₂ emissions.

In 2014 the International Energy Agency estimated that only 3.5% of total energy consumption is from renewable resources.¹ Several of these renewable energy approaches require sunlight to generate power, which in isolation would limit the ability to provide energy based on location, weather conditions, or time of day. To overcome this limitation, solar approaches need to be coupled with a method for storing energy to meet energy needs throughout the day, or to transport the energy where needed. A sound approach would be to store the energy formed from renewable methods in the chemical bonds of a fuel, such as methanol. If methods can be developed to use CO₂ as the carbon source for a fuel, the accumulation of carbon dioxide in the earth's atmosphere would also be addressed. The storage of energy in a liquid fuel generated from a recycled greenhouse gas, a so-called “solar fuel” (Figure 1.2), is the core of what makes CO₂ reduction an attractive strategy to meet future energy demands.

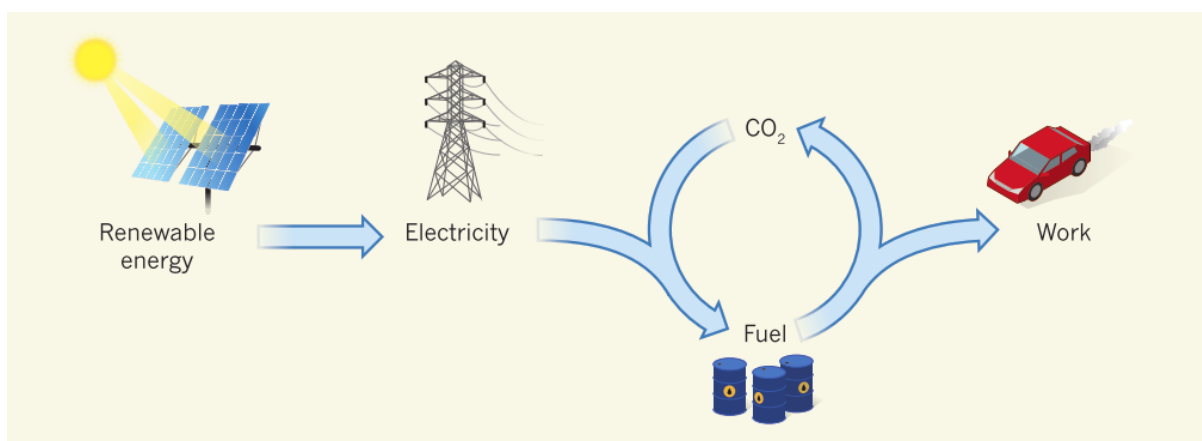


Figure 1.2: Outlined approach for a “solar fuels” energy economy.¹¹¹

1.2. Dye-Sensitized Photoelectrochemical Cell (DSPEC) Approach

One approach to generating “solar fuels” involves the use of a DSPEC device developed in the University of North Carolina at Chapel Hill Energy Frontier Research Center (EFRC). A schematic of a DSPEC device is shown in Figure 1.3.⁵ This type of device is designed to harness

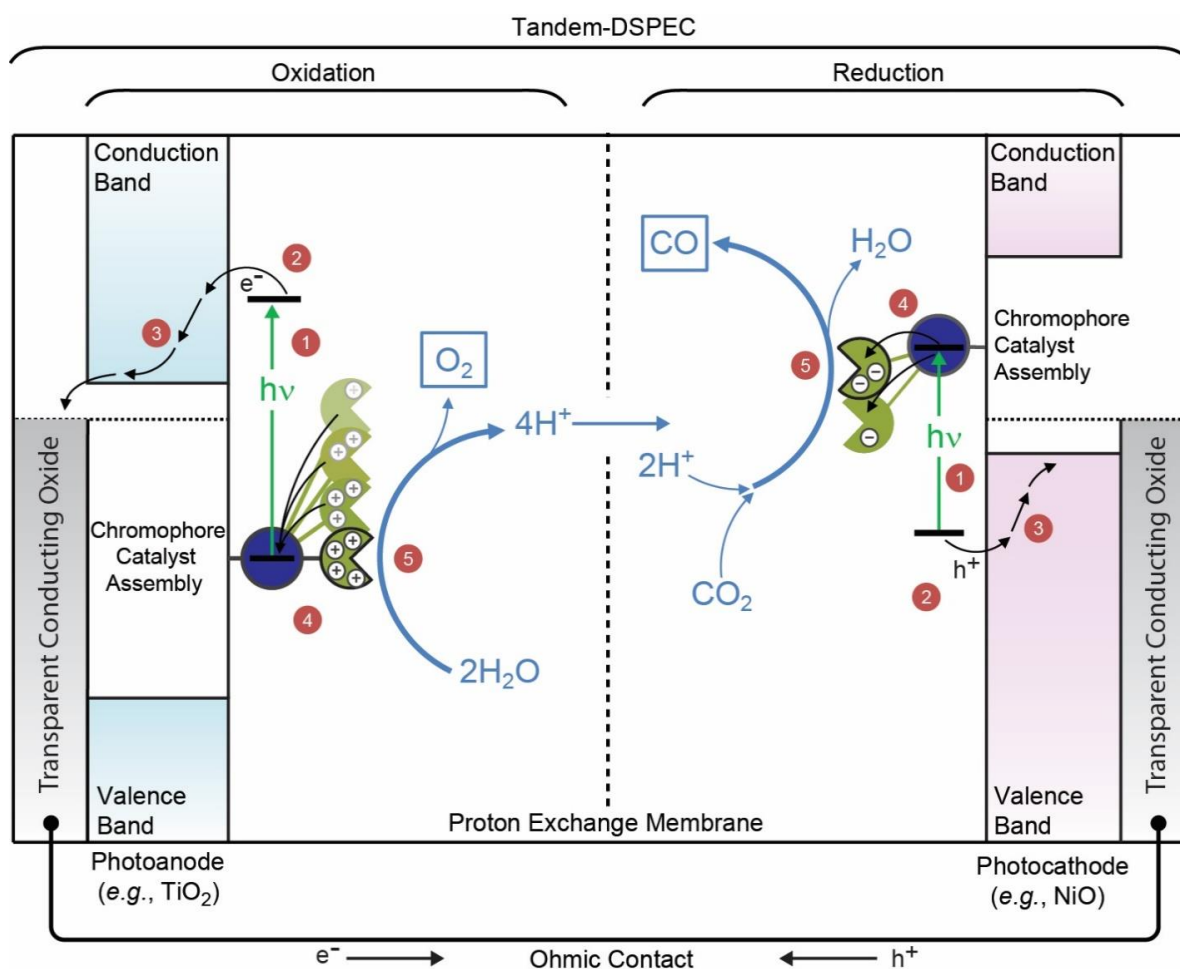


Figure 1.3: Dye-Sensitized Photoelectrochemical Cell (DSPEC) for artificial photosynthesis to directly produce alternative fuels from sunlight (figure by James F. Cahoon).

the sun’s energy to drive catalysis for water oxidation and CO_2 reduction. DSPECs are tandem devices with the electrodes, photoanode (typically TiO_2) and photocathode (NiO), connected. Light (i.e., sunlight) excites the molecular chromophore catalyst assembly attached to either electrode surface. Once excited the chromophore-catalyst complex on the photoanode has an energy match with the conduction band of TiO_2 to which it can transfer electrons. These

electrons are then shuttled to the photocathode for CO₂ reduction by the excited chromophore-catalyst assembly. Analogously, at the photocathode the excitation of the chromophore-catalyst assembly allows for hole transfer into the valence band of the photocathode. These holes are shuttled in the opposite direction from the electrons to the photoanode for water oxidation as shown at the bottom via the ohmic contact connecting the two electrodes. Details of each component in the DSPEC design remain a focus of research to develop a functional and efficient device to generate solar fuels. The reaction of interest in this work, the reduction of CO₂, takes place on the right side of the DSPEC device, at the photocathode.

1.3. Reduction of Carbon Dioxide

1.3.1 General Considerations.

CO₂ is a nonpolar molecule and very stable. The high stability is evidenced by very short C–O bond distances of 1.16 Å.⁸ Carbon dioxide is susceptible to reactions with nucleophiles at carbon. This reactivity can be better visualized by considering the polarity of the C–O bond creating an overall charge distribution more consistent with partial negative charge at each oxygen atom (δ⁻) and a partial positive charge at the central carbon atom (δ⁺) (Figure 1.4).

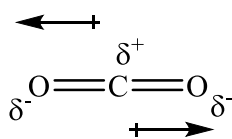


Figure 1.4: Charge distribution in CO₂ molecule, where partial charges at each atom are indicated by the symbol δ. The dipoles are denoted by arrows, where areas of less electron density have a plus symbol end and the arrowhead points towards areas of greater electron density.

Fuel generation from CO₂ has been of interest for decades, where reduction of the molecule could produce fuel precursors like carbon monoxide or directly form fuels such as formic acid or methanol. CO₂ has been an attractive target for energy storage considering reduction to methanol

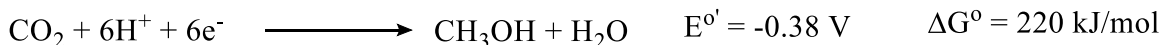
directly results in a liquid fuel.^{6,7} The main challenge to reduction of CO₂ is inherent in its properties as a highly stable, linear molecule. Direct reduction to form the radical anion of CO₂ (CO₂^{•-}, Scheme 1.1) requires high energy input, largely due to the required molecular rearrangement to a bent conformation. More energetically feasible pathways than direct



$E^{\circ'}$ vs NHE in pH 7 aqueous soln

Scheme 1.1: Direct reduction of CO₂ to its radical anion.

reduction are obtained by coupling protons to the electron transfer events (Scheme 1.2).^{6,9,10} The most readily accessible two-electron / two- proton reduction products, CO and formic acid, are



$E^{\circ'}$ vs NHE in pH 7 aqueous soln

Scheme 1.2: Reduction potentials for CO₂ to CO, formic acid, and methanol.

produced at comparatively mild potentials. A six-electron / six-proton process is required for reduction of CO₂ to methanol, an ideal liquid fuel with substantial energy density. This potential for formation of a variety of products electrochemically makes catalysis for these transformations a focal point of research efforts. To place in context the importance of reduction beyond CO and HCOO⁻ we can compare the energy density of HCOOH, MeOH, and petroleum. Formic acid has an energy density approximately half that of methanol, and methanol's energy density is about half that of petroleum.²

1.3.2 CO₂ Reduction Strategies.

Discovery of an efficient catalyst for CO₂ reduction would not only provide a more viable method of producing fuels from CO₂, but also have the potential to increase the yield of desired products, limit the formation of undesired by-products, and decrease the need for harsh reaction conditions such as high temperatures and pressures. Both heterogeneous and homogeneous catalytic methods for CO₂ reduction have been proposed over the course of the past four decades, including approaches using small molecules, enzymes, metal electrodes, nanoparticles, and combinations or variations inspired by each of these.^{7,11–13}

Electrochemical methods are considered one of the best approaches to address the energy input required for these reduction and protonation steps.^{12,14} Further, other alternative, clean-energy sources – such as wind or solar power – can be used to provide the potential to deliver the required electrons for the fuel forming reactions. Electrocatalysis can be executed via both homogeneous (strictly solution phase) and heterogeneous (reactivity occurs on an electrode surface, i.e., as shown at either electrode in the DSPEC device) methods. To frame the work in this dissertation, a brief review of small molecule transition metal electrocatalysts for CO₂ reduction will be presented.

An electrocatalyst for carbon dioxide reduction must accept electrons from the electrode where a potential is applied, and react with the substrate, carbon dioxide, in the reduced state to facilitate transformation to a desired product. An ideal electrocatalyst would operate at the thermodynamic potential for the desired reaction (Scheme 1.2). For example, formation of CO from CO₂ occurs at the thermodynamic potential of -0.52 V vs. NHE in water at pH 7. An electrocatalyst with a reduction potential more positive than -0.52 V will not catalyze the desired reaction. The excess energy input beyond the thermodynamic potential to achieve a desirable

catalytic rate is termed the overpotential. It is a goal to design a catalytic system which minimizes the required overpotential. Tuning the reduction potential for a transition metal electrocatalyst for the appropriate potential can be achieved by systematic modifications in the ligands.

An appropriate ligand scaffold on the metal center of a catalyst can tune CO₂ reduction reactivity by distributing charge, introducing steric constraints, stabilizing reactive intermediates, or reducing the reduction potential. With regard to charge distribution in CO₂ reduction catalysis, pyridyl ligands have demonstrated compelling utility. For most pyridyl containing systems, particularly polypyridyl complexes, low-lying ligand-based LUMOs will accept electrons creating a reduced active catalyst. This active catalyst species will transfer its ligand electrons to the metal center to facilitate CO₂ coordination.^{15–18} A number of studies have shown that steric constraints strategically placed in catalyst structures lower activation energy for intramolecular transformations.^{19,20} Transition metal catalysis design principles historically focus on evaluating ligands with maximum potential for stabilizing intermediates or transition states in the catalytic cycle.^{21,22} In addition to the aforementioned properties, catalyst design should also aim to utilize abundant materials (i.e., first row transition metals) and perform at ambient conditions (i.e., near room temperature and 1 atm pressure) to maximize potential for future industrial application.

There are two main approaches to CO₂ reduction in homogenous systems: hydride transfer to CO₂ from an electroactive metal hydride complex (Figure 1.5, right) or directly coordinating CO₂ at a reduced metal center and activating it for further reduction (Figure 1.5, left).⁵ For many of the complexes discussed in the following sections 1.3.3 to 1.3.5, the proposed mechanism of catalysis has been to bind CO₂ to the metal center to prepare CO₂ for protonation or reduction.²³

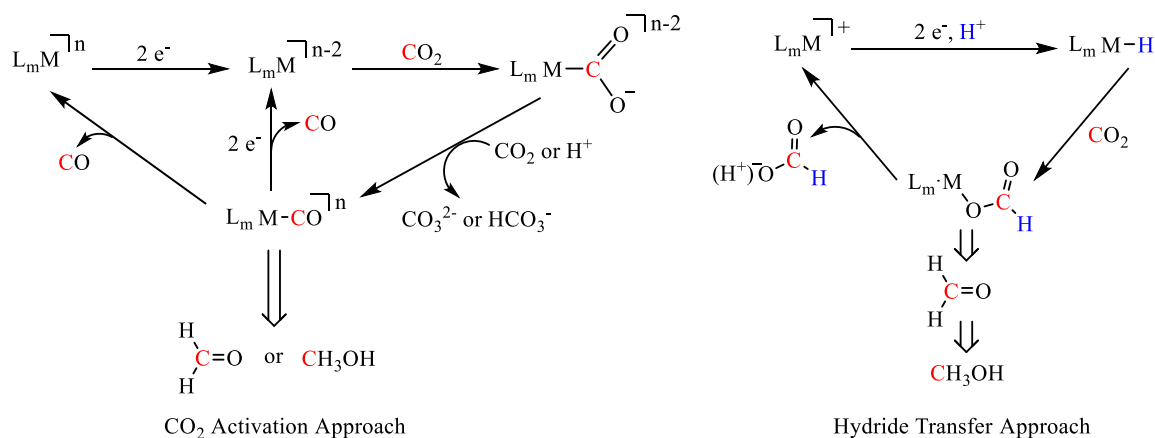


Figure 1.5: Two approaches to CO₂ reduction.⁵

Depending on the identity of the catalysts, a variety of products can be produced electrocatalytically, ranging from carbon monoxide, methanol, and ethylene. In addition to the type of product formed, the particular catalyst used can greatly impact the selectivity of the system. To illustrate the variation of results thus far, a selection of nine systems that electrocatalytically reduce CO₂ to formate, carbon monoxide, and ethylene will be briefly discussed. Figure 1.6 outlines a selection of these catalysts below.

1.3.3 Carbon Monoxide Formation.

Many homogenous systems directly activate CO₂ by coordination to a reduced metal center typically forming CO as the reduction product. Carbon monoxide is a low energy density fuel source and, as a gas, is difficult to directly utilize as a fuel. However, its formation in the CO₂ reduction process is essential to understand as it is typically the first step in the process of many catalyst systems. Furthermore, CO is already an industrially essential fuel precursor compound, where the well-developed and understood Fischer-Tropsch method and water-gas shift reaction use CO with water or hydrogen to form liquid fuels (e.g., gasoline).

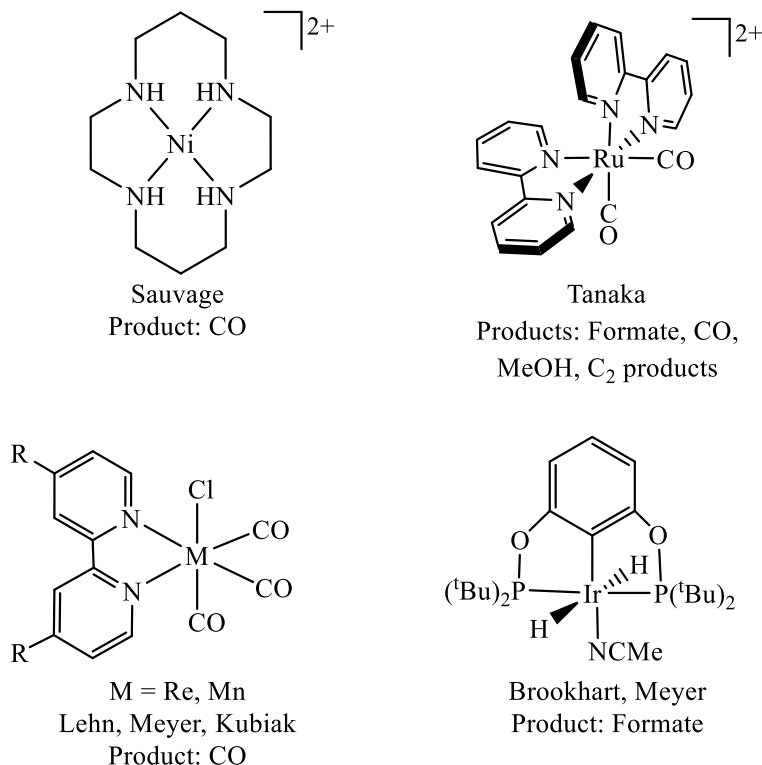


Figure 1.6: Selection of catalysts used for CO₂ reduction which include Sauvage's [Ni(cyclam)]²⁺ system^{24,112–114}, Lehn's Re(bpy)(CO)₃Cl system¹¹⁵, Deronzier's/Kubiak's analogous Mn(bpy)(CO)₃Cl system^{29–32}, Brookhart's Ir pincer complexes^{5,42,43}, and Tanaka's/Meyer's ruthenium polypyridyl complexes^{5,17,42,82}.

One of the first systems reported to reduce CO₂ to CO used Ni complexes with tetraazomacrocyclic ligands like cyclam (Fig. 1.6, top left).^{24,25} Strongly donating phosphine ligands were also found to work very well for CO₂ reduction to CO in Dubois's Pd system. Complexes of the form [Pd(triphos)(NCMe)]²⁺ could be activated after a 1 e[−] reduction for coordination of CO₂ after loss of solvent acting as a ligand at the metal center.^{26,27}

Later Lehn reported photocatalytic reduction of CO₂ using Re bipyridine carbonyl complexes (Fig. 1.6, bottom left). With an applied potential these compounds could also react to give CO as the main reduction product in acetonitrile solvent.²⁸ Later Deronzier and Kubiak found that this reactivity could be carried out with first-row transition metal analogs Mn(bpy)(CO)₃X and Mn(Mebim-py)(CO)₃X complexes (where X = Br or Cl) (Fig. 1.6, bottom left).^{29–32} The

distinction in these polypyridyl systems was that reduction first at the pyridyl ligands facilitated activation at the metal center. Meyer, Turner, and Kubiak were able to characterize the intermediates via infrared spectroelectrochemistry (IR-SEC) for the reduced $[\text{Re}(\text{bpy})(\text{CO})_3]^-$ complex which will coordinate CO_2 readily following reduction.^{15,33,34}

1.3.4 Formate Production.

In the hydride transfer approach, the product most often produced is formate (HCOO^-), or formic acid (HCOOH). Formate is a product of interest given its potential for direct use in fuel cells, in industrial processes (e.g., in textile or rubber manufacturing), and in practical commercial applications (e.g., airport runway de-icing).^{11,35}

A few systems have reported sufficient hydricity to reduce carbon dioxide directly, where the ideal hydride transfer free energy ($\Delta G_{\text{H}}^{\circ}$) would need to be in the range of 24 to 44 kcal/mol dependent on solvent conditions.^{36–41} A recent report from Berben et al. examines the selectivity for CO_2 reduction using Fe cluster systems. Selective CO_2 reduction to formate in lieu of reaction with protons to give hydrogen was observed under aqueous conditions for the iron nitride cluster, $[\text{HFe}_4(\text{N})(\text{CO})_{12}]^-$. They report IR-SEC data as evidence for an intermediate 3-charged catalyst precursor which can be protonated *in situ* to form the μ -bridging hydride species for each system. Overall, the proposed μ -bridged hydride iron clusters are presumed to react via a direct hydride transfer mechanism.^{39–41}

In some cases an intermediate formato complex can be observed after hydride transfer to CO_2 . Brookhart's group found that an iridium POCOP system had high selectivity for production of formate from CO_2 electrocatalytically via this intermediate. The dihydride complex $\text{Ir}(\text{POCOP})(\text{NCMe})(\text{H})_2$ inserts CO_2 into one of the Ir-H bonds, producing coordinated formate (Figure 1.7).^{42,43} Formate leaves the coordination sphere to be replaced with solvent acetonitrile,

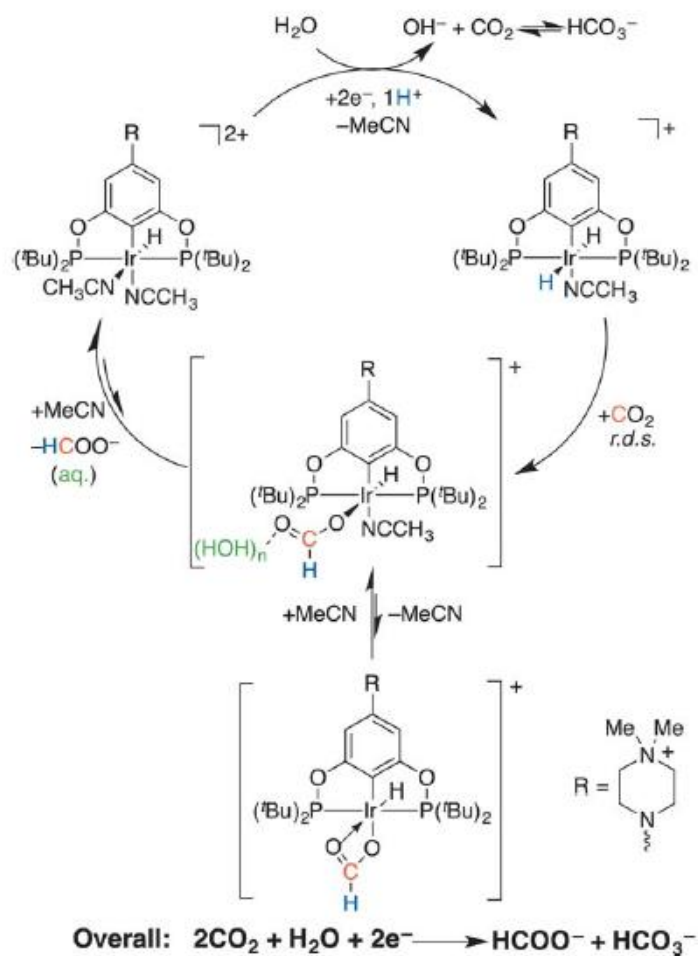


Figure 1.7: Electrocatalytic CO₂ reduction to formate using Ir(POCOP) catalysts.⁴³

and subsequent two-electron reduction and protonation reproduces the reactive catalyst complex.^{5,42} Water soluble analogs have been synthesized which can do the chemistry with minimal organic solvent present.⁴³ Most notably this system displays unique selectivity to produce formate over hydrogen.

An early report of hydride transfer CO₂ reduction producing formate can be found in literature from 1984 where Wagenknecht proposed a Rh-CO₂ intermediate from [Rh(DPPE)₂]⁺ after a 1 e⁻ reduction forming a reactive neutral intermediate. Analogously CO₂ insertion to into the Rh-H bond to form a Rh-OOCH complex was also proposed as a potential mechanism.⁴⁴

1.3.5 Products Beyond Formate.

Routes for reducing carbon dioxide beyond formic acid (or formate) and carbon monoxide are far more challenging as more than one proton-coupled electron transfer step would be necessary. As such, only a few electrocatalytic homogenous systems report formation of reduction products beyond CO and HCOOH.⁸

In the CO₂ activation approach, a reduced transition metal complex typically loses a ligand to create an open vacant site which can coordinate carbon dioxide. Coordination of CO₂ to the metal center to activate it for reduction offers a viable approach to subsequent reactivity if the CO product remains in the coordination sphere of the transition metal. The coordinated CO ligand has the potential to undergo subsequent reduction and protonation to form new products. On the other hand, formate, the product from the hydride transfer approach, is a much weaker ligand than CO, and will likely be displaced from the metal center upon reduction, reducing the possibility for further reactivity.

To date, one of the most intriguing homogenous catalysts for CO₂ reduction beyond CO and HCOO⁻ has been produced by Tanaka using polypyridyl ligands on ruthenium. Initially [Ru(bpy)₂(CO)₂]²⁺ complexes were found to produce not only CO but also formic acid via electrocatalysis in water-DMF depending on pH.^{45,46} Later synthesis of [Ru(tpy)(bpy)(CO)]²⁺ complexes were developed which had improved rates of reactivity.^{45,47} Furthermore, Tanaka reported observation of some methanol and C₂ products using the tpy analog by gas chromatography analysis.⁴⁷

Although not a homogeneous system, a well-known system for production of higher reduced products includes copper electrodes or nanoparticle systems.^{48–50} Fascinatingly, with an applied potential, copper electrodes have been found to catalyze formation of ethylene, another ideal C₂

product. Unfortunately, as for many heterogeneous processes, the mechanism for carbon-carbon bond formation is not yet well understood.^{51,52}

1.4. Introduction to Work Herein

This dissertation focuses on synthetic and evaluating the reaction chemistry of molecular complexes capable of reducing CO₂. Attaining a better understanding of the fundamental reactions in CO₂ reduction scenarios is essential for future progress in the field of alternative energy catalysis.

Chapter 2 reports synthesis, characterization, and reactivity of electron-rich manganese cyclohexadienyl complexes. In contrast to most examples in literature, the hydride ligand transferred to CO₂ originates from the cyclohexadienyl ligand rather than from a metal hydride.

In Chapter 3, the reactivity of the hydroxymethyl ligand, a product of CO reduction in the coordination sphere of a transition metal, with electrophiles is monitored using variable temperature NMR spectroscopy. Insight into the origin of C₂ products from a CO₂ reduction scheme is obtained from these studies.

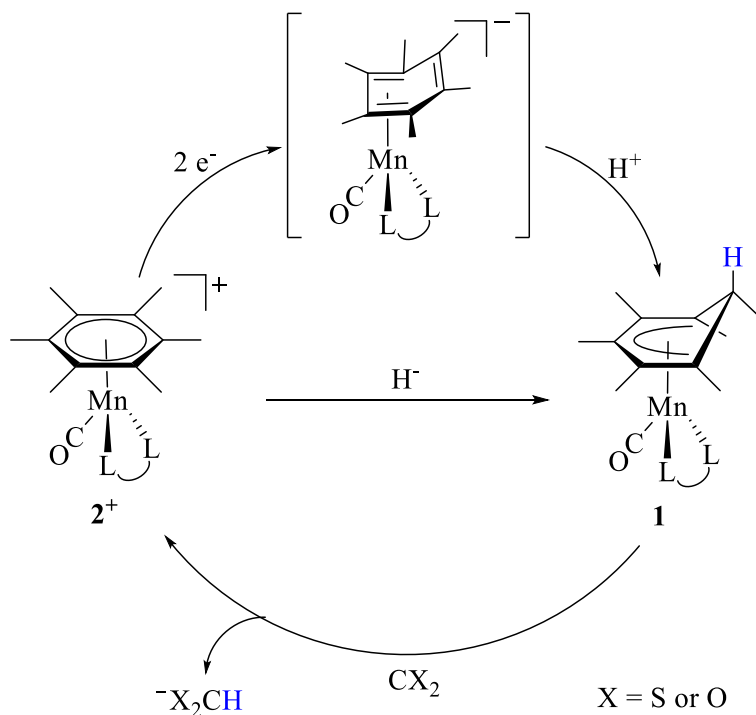
Chapter 4 presents synthesis of a new member of the class of ruthenium terpyridine carbonyl complexes that are efficient electrocatalysts for reductive disproportionation of CO₂. The carbonyl complexes enable the important CO loss step to be studied, and comparison to analogous ruthenium polypyridyl electrocatalysts with a future goal of understanding the CO₂ activation mechanism in more detail. Systematic ligand design for improving efficiency of catalysis and product selectivity will be explored in this chapter as well.

CHAPTER 2

MANGANESE CYCLOHEXADIENYL COMPLEXES FOR CARBON DIOXIDE REDUCTION TO FORMATE

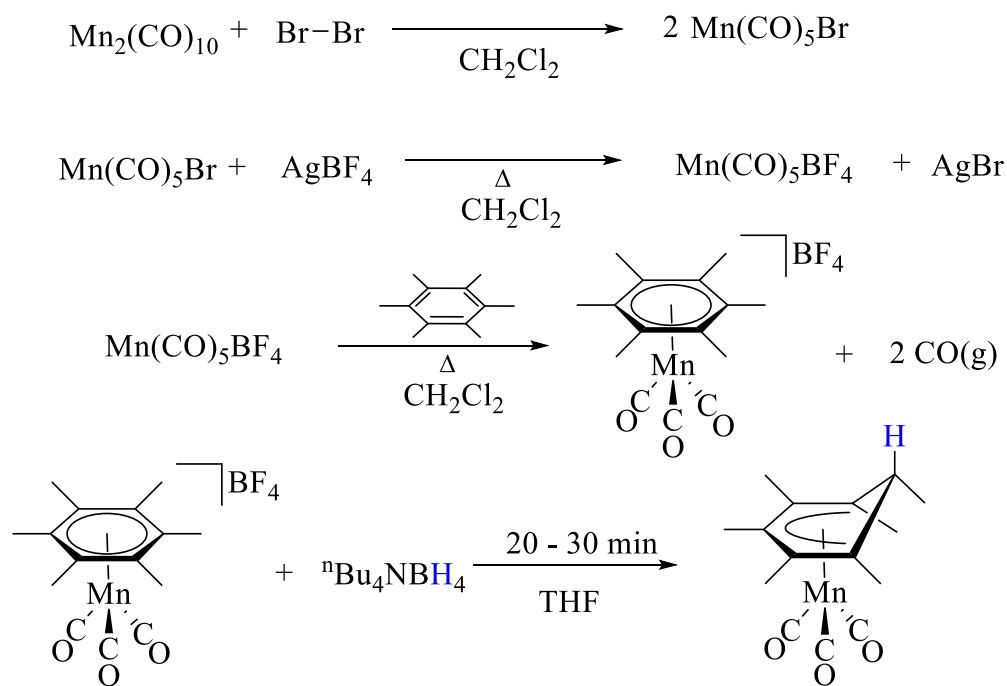
2.1. Introduction and Background

This chapter focuses on evaluating the potential of manganese cyclohexadienyl complexes to act as electrocatalysts for CO₂ reduction. The objective is to explore an electrochemically driven catalytic cycle in which the manganese cyclohexadienyl complex **1** reduces CO₂ to formate with concomitant formation of the η^6 cationic product, **2**⁺ (Scheme 2.1). Following a two-electron reduction/protonation sequence, ligand **1** is regenerated.



Scheme 2.1: Proposed catalytic cycle for CX₂ reduction using Mn cyclohexadienyl complexes.

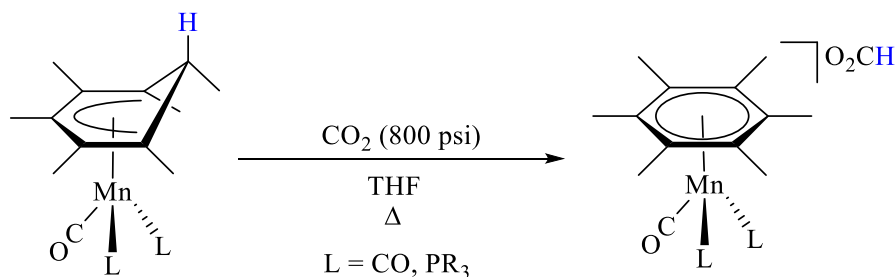
The availability of manganese, the third most abundant transition metal in the Earth's crust, makes it an enticing choice for large scale CO₂ reduction catalysis.⁵³ Synthesis of manganese cyclohexadienyl complexes and their precursors are straightforward and well-studied (Scheme 2.2).⁵⁵⁻⁵⁷



Scheme 2.2: Synthetic method for making precursor complexes for Mn(C₆Me₆H) system.⁵⁴⁻⁵⁷

Prior work by Eyman provides precedence for the hydride transfer step in Scheme 2.1.⁵⁴ Hydride transfer to CO₂ was observed at high temperatures and pressures using manganese cyclohexadienyl complexes of the general formula Mn(η⁵-C₆Me_nH_{7-n})(CO)LL', where L, L' = CO, PR₃ and n = 0, 3, or 6 (eq 2.1).⁵⁴

In these compounds, the hydride is positioned on the cyclohexadienyl ligand *anti* to the metal center (eq 2.1). Prospective reactivity towards CO₂ for the various complexes prepared by Eyman was gauged by the relative rates of reaction with CS₂. Hydride transfer reactions with



Equation 2.1: Eyman's various Mn cyclohexadienyl complexes which transfer hydride to CO_2 (reactive hydride is shown in blue).⁵⁴

CS_2 typically occur more rapidly than with CO_2 due to its lower lying LUMO. Manganese complexes in which CO was replaced by more electron-donating phosphite ligands gave rise to higher reaction rates. The methyl substituents on the cyclohexadienyl ligand were also shown to be critical to the hydride reactivity in these complexes. Complexes without methyl substituents on the cyclohexadienyl ligand were unreactive towards CS_2 . However, the methylated cyclohexadienyl complex with only carbonyl ligands did display CS_2 reactivity, albeit slow.⁵⁴ The most reactive species were those with the greatest number of methyl substituents on the cyclohexadienyl ligand and had phosphite ligands for L and L'.

The key considerations in achieving hydride transfer reactivity from the cyclohexadienyl ligand have been elucidated by an extended Hückel molecular orbital theory analysis of complex *exo*-($\eta^5\text{-C}_6\text{H}_6\text{Ph}$)Mn(CO)(DPPE) by Sweigart and Connelly.⁵⁸ As demonstrated in Figure 2.1 below, only when the hydrogen on the tertiary carbon is *anti* to the metal center will orbital overlap be possible with the Mn d_{xy} orbital. This interaction stabilizes the transition state for hydride transfer. Furthermore, this favorable orbital overlap is increased with more electron-donating ligands at the metal center lowering the activation energy. It is also noteworthy that a methyl substituent on the saturated carbon that is *syn* to the metal center increases the repulsive interaction with the d_{xy} orbital, also lowering the activation energy for hydride transfer.

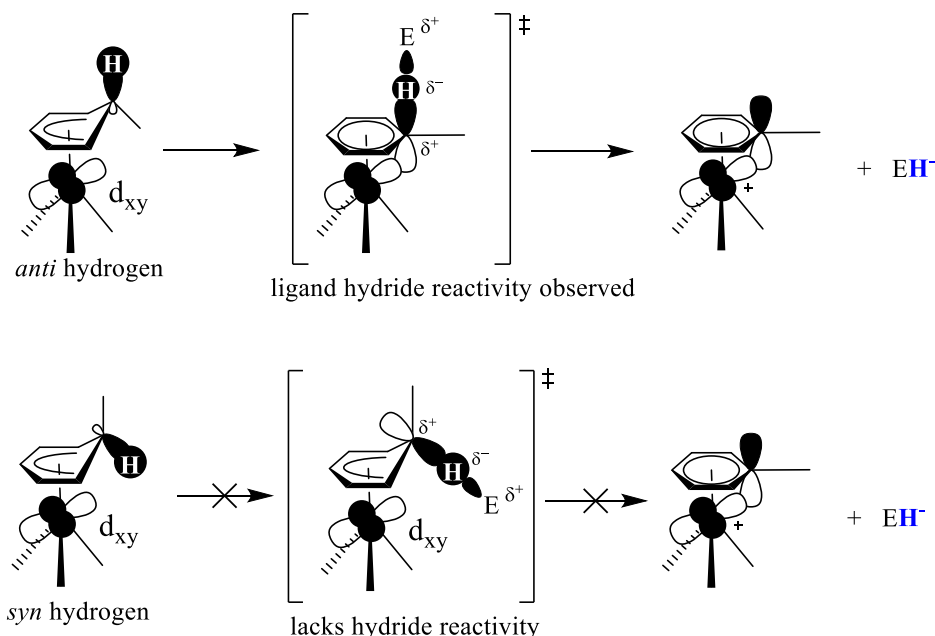


Figure 2.1: Metal d_{xy} and $\text{C}_6\text{Me}_6\text{H}$ ligand saturated carbon interaction promoting hydride reactivity. Partial charges are denoted by symbol δ . The resulting hydride which is transferred is denoted in blue for the products.⁵⁸

In addition to synthetic studies, Sweigart studied the electrochemical activity of the precursor cation complexes, $[\text{Mn}(\eta^6\text{-C}_6\text{Me}_n\text{H}_{6-n})(\text{CO})\text{LL}']^+$. In these experiments, tricarbonyl $[\text{Mn}(\eta^6\text{-C}_6\text{Me}_6)(\text{CO})_3]^+$, formed a Mn – Mn bridged dimer as a result of CO loss upon $1e^-$ reduction. Cyclic voltammetry showed an irreversible oxidative wave at -250 mV vs Fc/Fc^+ for the dimer (Fig. 2.2).⁵⁶ Results were confirmed by addition of phosphine to the electrochemical cell, which readily replaced the CO lost from the reduced cation complex. At low temperatures or under a CO atmosphere, the CO-loss pathway was suppressed and reduction to an η^4 -arene species resulted (Scheme 2.3).⁵⁹ The two-electron reduced η^4 -arene species was the same as the intermediate depicted in electrocatalytic CX_2 reduction in Scheme 2.1.

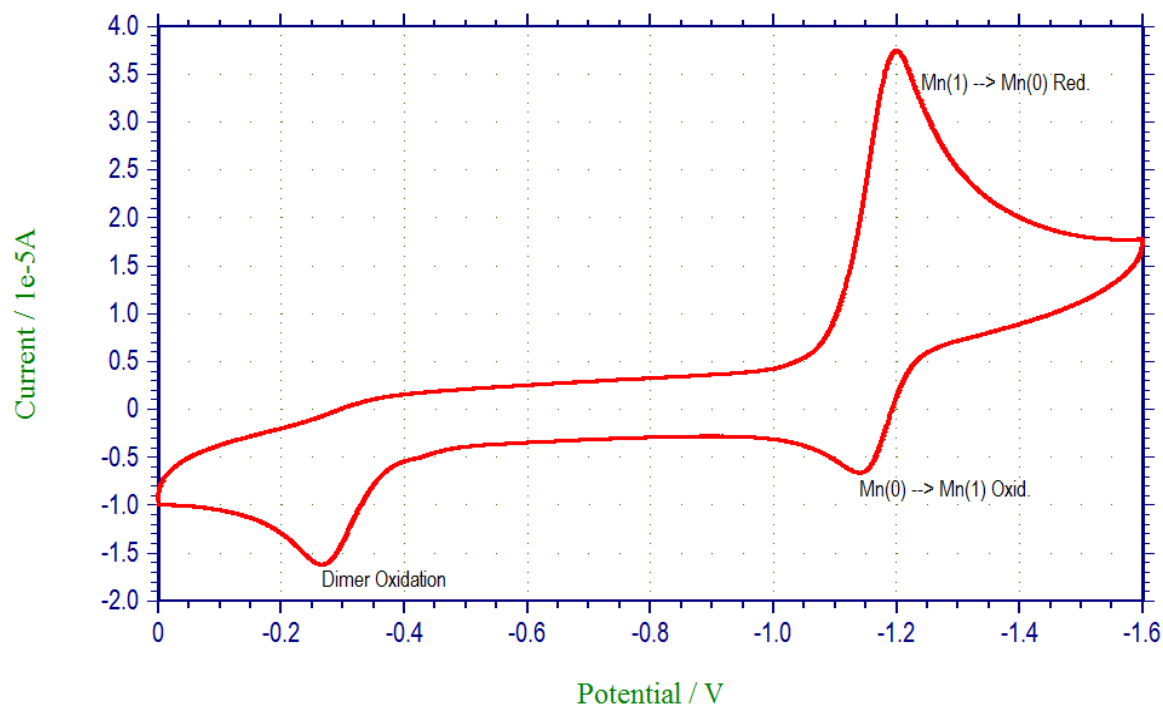
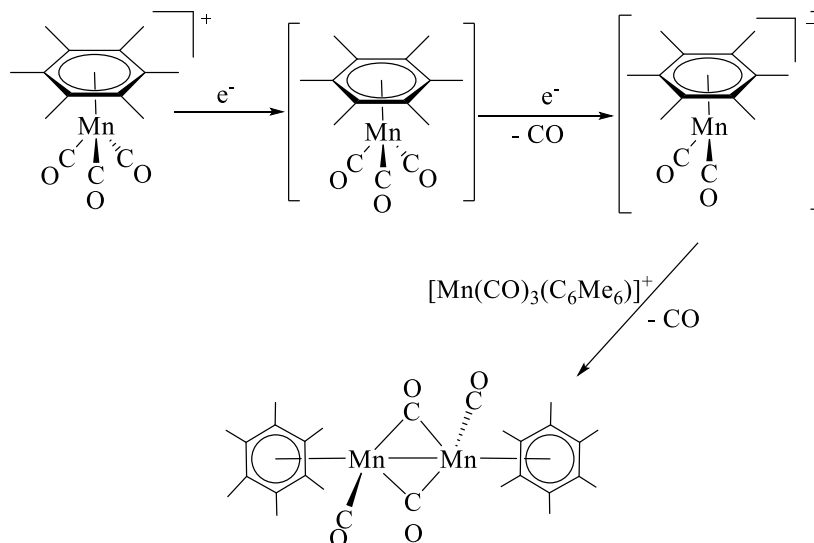
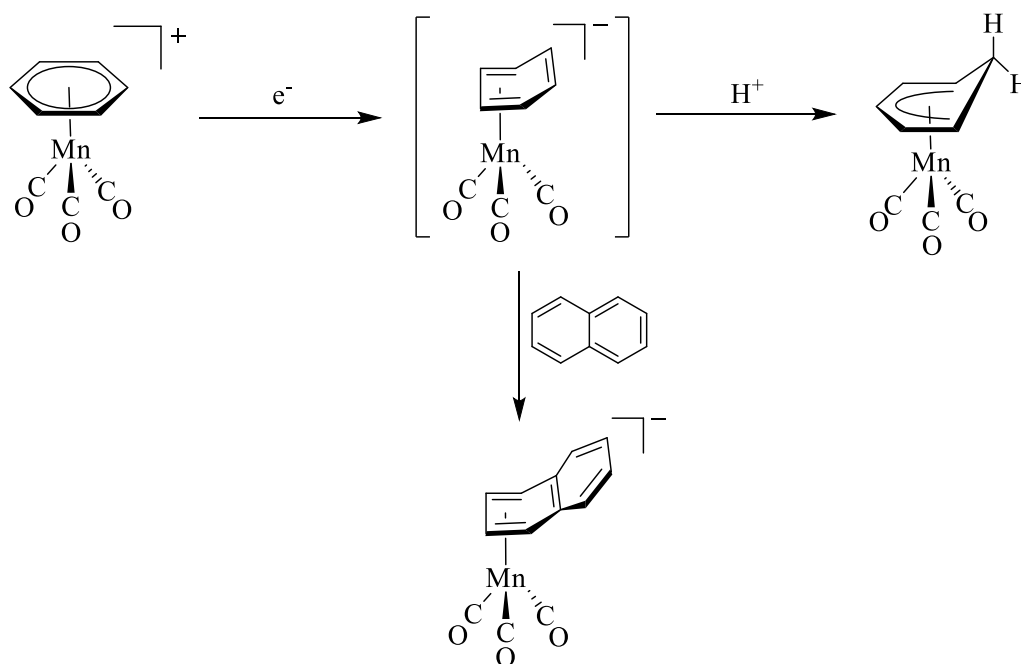


Figure 2.2: Cyclic voltammogram of 1.0 mM $[(\eta^6\text{-C}_6\text{Me}_6)\text{Mn}(\text{CO})_3]\text{BF}_4$ ($E_{1/2}$ vs Fc/Fc^+ ; Ag/AgNO_3 reference, Pt electrode, 100 mM $n\text{Bu}_4\text{NBF}_4$, 100 mV/s, under $\text{N}_2(\text{g})$ in MeCN).⁵⁶



Scheme 2.3: Sweigart electrochemical results for reduction of $[\text{Mn}(\eta^6\text{-C}_6\text{Me}_6)(\text{CO})_3]^+$.⁵⁹

Formation of this rare η^4 -coordinated arene species has been confirmed in work by Cooper et. al., where reduction of cationic benzene complexes, $[\text{Mn}(\eta^6\text{-C}_6\text{H}_6)(\text{CO})_3]^+$, using two equiv of naphthalenide anion ($\text{KC}_{10}\text{H}_{18}$) gave the anionic η^4 species. The identity of this complex was confirmed by NMR, IR, and reactivity studies.⁶⁰ This anionic species was found to react with trifluoroacetic acid to form the neutral η^5 -cyclohexadienyl complex, $\text{Mn}(\eta^5\text{-C}_6\text{H}_7)(\text{CO})_3$. Interestingly, arene exchange with naphthalene occurred with anionic $[\text{Mn}(\eta^4\text{-C}_6\text{H}_6)(\text{CO})_3]^-$, giving an η^4 -naphthalene complex, which was structurally characterized (Scheme 2.4).⁶⁰



Scheme 2.4: Reactivity of η^4 complex to give η^5 after adding H^+ and arene exchange to produce crystallized η^4 -naphthalene complex.⁶⁰

Here we explore the use of manganese cyclohexadienyl complexes as electrocatalysts for the reduction of CO_2 to formate. Towards this aim, this chapter outlines the design of new manganese cyclohexadienyl complexes with bidentate phosphine ligands. Reactivity of these complexes with CS_2 as a model for CO_2 reaction, will also be discussed.

2.2. Results and Discussion

2.2.1 Synthesis of Complexes.

With consideration of the prior studies by Eyman and Sweigart, a design for new complexes was proposed for catalytic CX_2 reduction (Fig. 2.3). The bidentate phosphine ligands (L_2), 1,2-diphenylphosphinoethane (DPPE) and 1,2-dimethylphosphinoethane (DMPE) were employed to promote high rates of reaction for the cyclohexadienyl complexes, $Mn(\eta^5-C_6Me_6H)(CO)L_2$ (**1**). Additionally, a bidentate ligand has the potential to impede the aforementioned dimerization that follows reduction of the cation precursor.

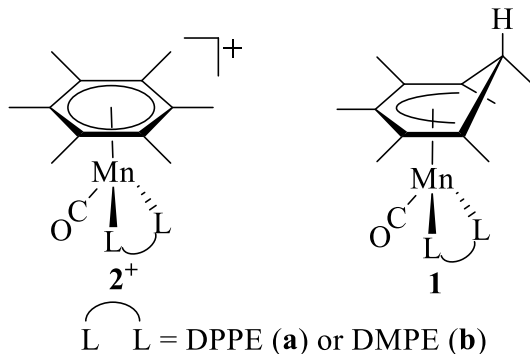
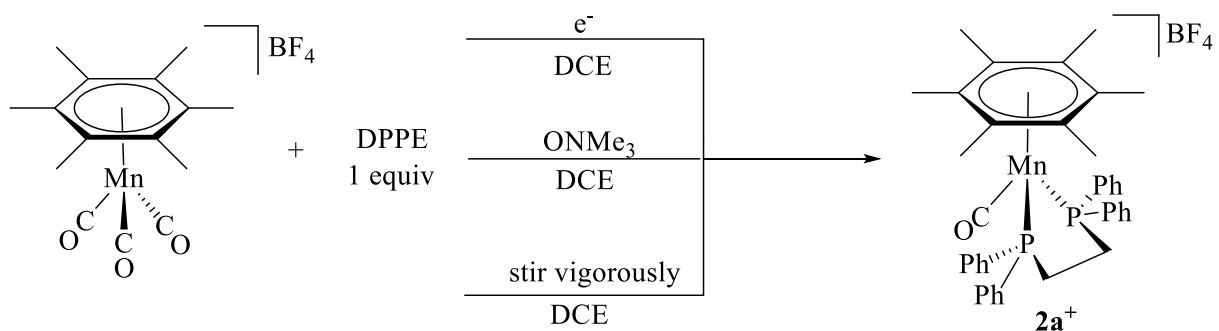


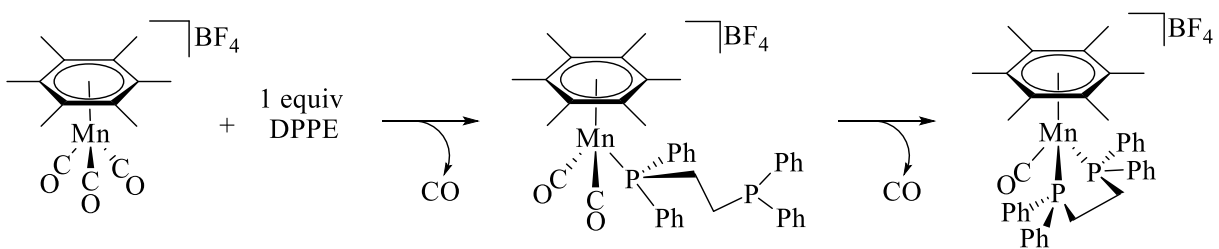
Figure 2.3: Manganese complexes studied in this work.

The cationic arene complex $[Mn(\eta^6-C_6Me_6)(CO)(DPPE)]BF_4$ (**2a⁺**) was the initial synthetic target, which could potentially serve as a precursor to $Mn(\eta^5-C_6Me_6H)(CO)(DPPE)$ (**1a**) by reaction with a hydride source. **2a⁺** was successfully produced from three different routes as outlined in Scheme 2.5. Reaction of $[Mn(C_6Me_6)(CO)_3]BF_4$ with DPPE using a catalytic amount of pentamethylcobaltocene to promote the ligand substitution reaction yielded the desired arene product, along with several undesired by-products. Trimethylamine N-oxide (ONMe₃) was also employed to facilitate the removal of CO ligands, but the reaction to prepare the di-chelate complex was slow. The highest yield route to pure **2a⁺** was reaction of $[Mn(C_6Me_6)(CO)_3]BF_4$ at room temperature with one equiv of DPPE. After stirring for two days, the monodentate product



Scheme 2.5: Synthesis of DPPE manganese hexamethylbenzene piano stool complexes.

was formed, as indicated by disappearance of starting material IR ν_{CO} bands at 2063 and 2003 cm^{-1} and growth of new bands at 1978 and 1930 cm^{-1} . The observed shift to lower energy is also consistent with substitution of a π -backbonding carbonyl ligand with an electron rich σ -donor phosphine ligand. ^{31}P NMR resonances at δ -13 (uncoordinated P) and δ 70 (coordinated P) also agreed with monodentate coordination.^{58,61} Coordination of the second phosphorus required up



Scheme 2.6: Synthesis of monodentate DPPE manganese hexamethylbenzene complex.

to two weeks to go to completion. The chelate has a ^{31}P resonance at δ 96 and a single ν_{CO} at 1895 cm^{-1} . Use of elevated temperatures to drive the reaction resulted in formation of the undesired *trans*-[Mn(CO)₂(DPPE)₂]BF₄ product (Fig. 2.4). The arene-loss product has ν_{CO} at 1986 cm^{-1} , a similar frequency to **2a**⁺, but is readily distinguished by ^{31}P NMR with a resonance at δ 78. The arene-loss product could be separated readily via column chromatography from **2a**⁺.⁶²

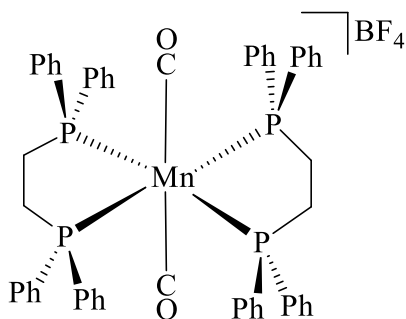
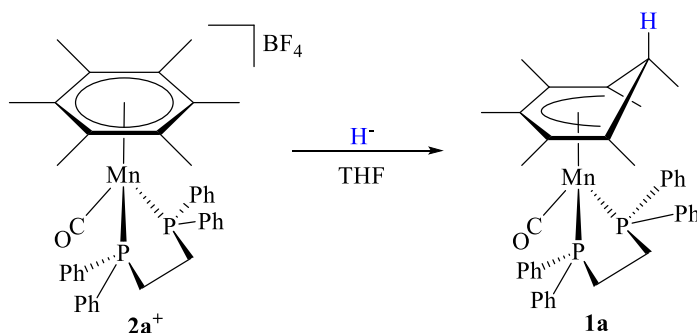


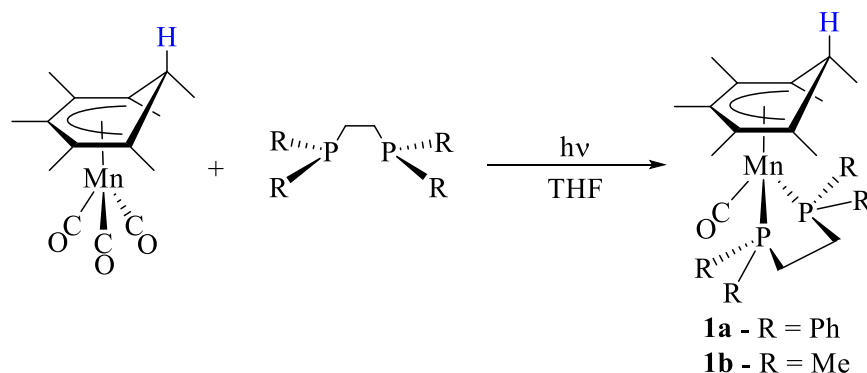
Figure 2.4: Arene loss complex.

With $2a^+$ isolated, synthesis of the cyclohexadienyl complex **1a** from $2a^+$ was explored (eq 2.2).⁵⁴ Hydride additions with $\text{Na}(\text{OMe})_3\text{BH}$ and $^n\text{Bu}_4\text{NBH}_4$ to $2a^+$ in THF solution at room temperature and at elevated temperature were attempted to form neutral hydride **1a**, but only a weak band at 1828 cm^{-1} was observed. These results suggested neither hydride was sufficiently reducing to add to the arene ring quantitatively.



Equation 2.2: Hydride addition for synthesizing Mn(DPPE) cyclohexadienyl complex.

An alternate approach to **1a** was designed, which involved photolytic reaction of DPPE with the cyclohexadienyl complex, $\text{Mn}(\text{C}_6\text{Me}_6\text{H})(\text{CO})_3$. Using this method, conversion of the tricarbonyl to **1a** was complete in 30 min by IR (eq 2.3). The ν_{CO} for the product at 1828 cm^{-1} was the same as that observed previously in attempts to synthesize **1a** in reactions of hydride reagents with cation $2a^+$. The proton ^1H NMR for **1a** showed a pattern consistent with the spectrum of the tricarbonyl cyclohexadienyl starting complex. Five signals for the cyclohexadienyl ligand were



Equation 2.3: Photolytic method for synthesizing Mn bidentate phosphine cyclohexadienyl complexes.

observed with integrations 1:3:6:6:3, as predicted by the vertical mirror plane which bisects the η^5 ligand through the saturated carbon (Fig. 2.5). These resonances corresponded to: (i) the *anti* proton (δ 2.03), (ii) the methyl signal at the saturated carbon (δ 1.20), (iii) the two sets of methyls on either side of the vertical mirror plane (δ 1.72), and (iv) the methyl group opposite the saturated carbon (δ 3.09). The ^{31}P NMR also shifted upfield to δ 93 compared to **2a**⁺. Complex **1a** was purified by column chromatography and isolated from hexanes at -20°C as a deep red powder.

Given the successful photolytic preparation of **1a**, the same method was used to prepare **1b**. A single ν_{co} for **1b** was observed at 1821 cm^{-1} , which is slightly lower in frequency than for **1a**. Similar to **1a**, the ^{31}P NMR shift for **1b** was observed at δ 70 as a singlet, upfield of its cation precursor. For **1b**, purification by silica gel chromatography failed to elute the product. Instead, the product was isolated directly by crystallization from hexanes at -20°C to give bright orange platelet crystals. Spectroscopic data for the synthesized complexes are summarized below in Table 2.1.

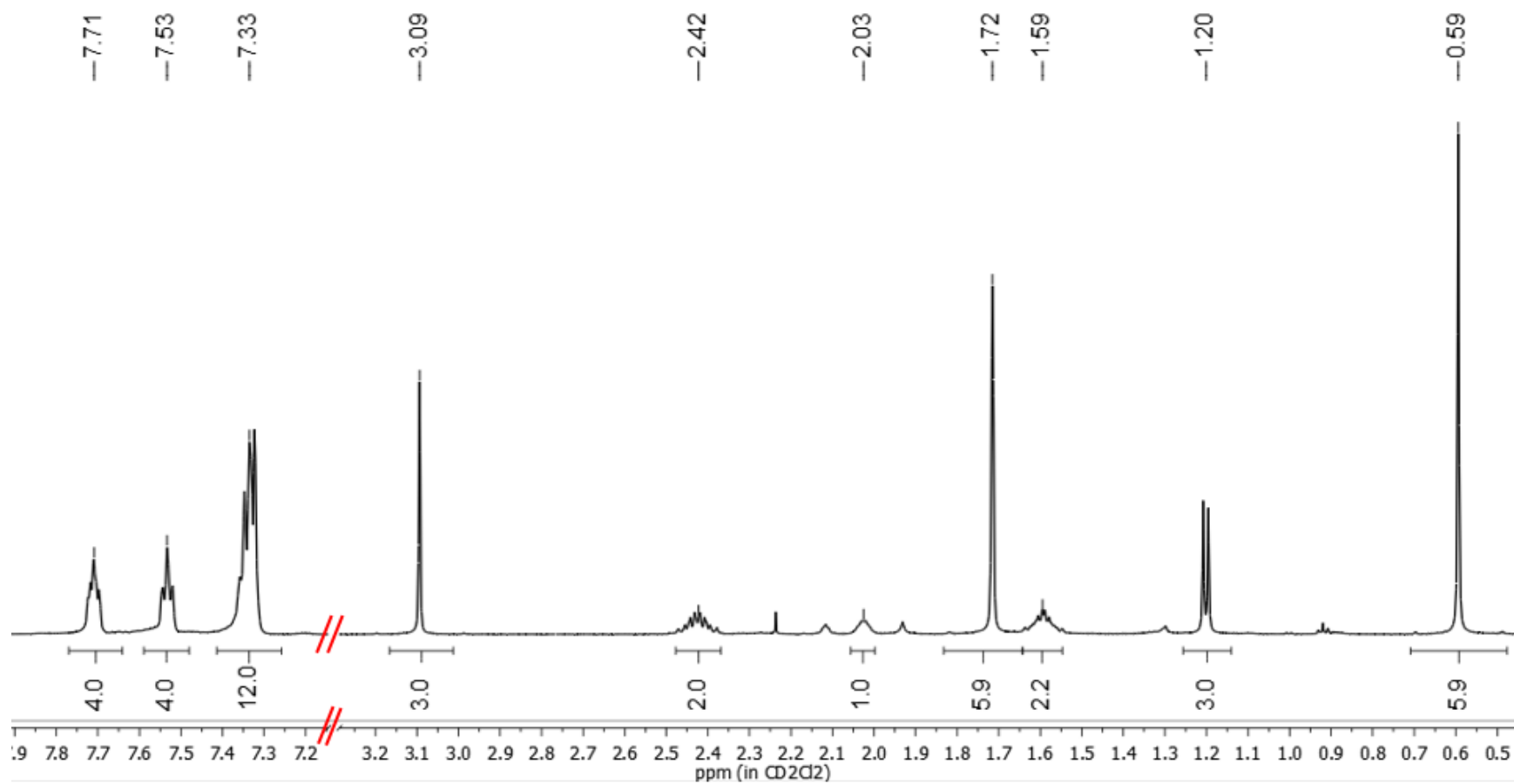


Figure 2.5: ^1H NMR of Manganese DPPE cyclohexadienyl complex **1a** in CD_2Cl_2 .

Table 2.1: Summary of Spectroscopic Data for Mn Complexes

Complex	P-CH ₂ (δ , ppm)	C ₆ Me ₆ (δ , ppm)	H _{exo} on C ₆ Me ₆ H (δ , ppm)	³¹ P NMR (δ , ppm)	IR ν_{CO} (cm ⁻¹)
[Mn(η^6 -C ₆ Me ₆)(CO) ₃]BF ₄	-	2.45 (s)	-	-	2059 2001
[Mn(η^6 -C ₆ Me ₆)(DPPE)(CO)]BF ₄ 2a⁺	2.19 (m)	2.20 (s)	-	96	1895
[Mn(η^6 -C ₆ Me ₆)(DMPE)(CO)]BF ₄ 2b⁺ ^a	1.39 (s)	2.31 (s)	-	74	1888
Mn(η^5 -C ₆ Me ₆ H)(CO) ₃	-	-	2.00 (q)	-	1995 1915
Mn(η^5 -C ₆ Me ₆ H)(DPPE)(CO) 1a	2.42 (m)	-	2.42 (m)	93	1828
Mn(η^5 -C ₆ Me ₆ H)(DMPE)(CO) 1b	0.88 (d) 1.14 (d)	-	2.66 (m)	70	1801
[Mn(η^6 -C ₆ Me ₆)(DPPE)(CO) ₂]BF ₄	-- ^b	-- ^b	-	-13 70	1978 1930
<i>trans</i> -[Mn(CO) ₂ (DPPE) ₂]BF ₄	2.77 (m)	-	-	78	1896

All chemical shifts reported relative to residual solvent CD₂Cl₂ at 20°C unless otherwise noted. ¹H NMR patterns: s (singlet), d (doublet), q (quartet), m (multiplet). IR bands reported in CH₂Cl₂ at 20°C unless otherwise noted. Full spectroscopic details reported in Experimental Section. Spectra for selected compounds in Appendix 1.1. ^a only observed in CS₂ reaction; ^b product not isolated for NMR analysis.

The structure of **1b** was confirmed by single crystal X-ray diffraction (Fig. 2.6). Selected bond distances and angles are listed in Table 2.2 and details of the structure determination are given in Table 2.3 in the experimental section and Appendix 1.1, Figure A2.6.^{63,64} The *anti* position of the hydride relative to the metal center as well as the expected bidentate coordination mode of the phosphine ligand are confirmed by the structure. Of particular interest are the metric parameters for the cyclohexadienyl ring. The bond lengths of the uncoordinated C11 to adjacent

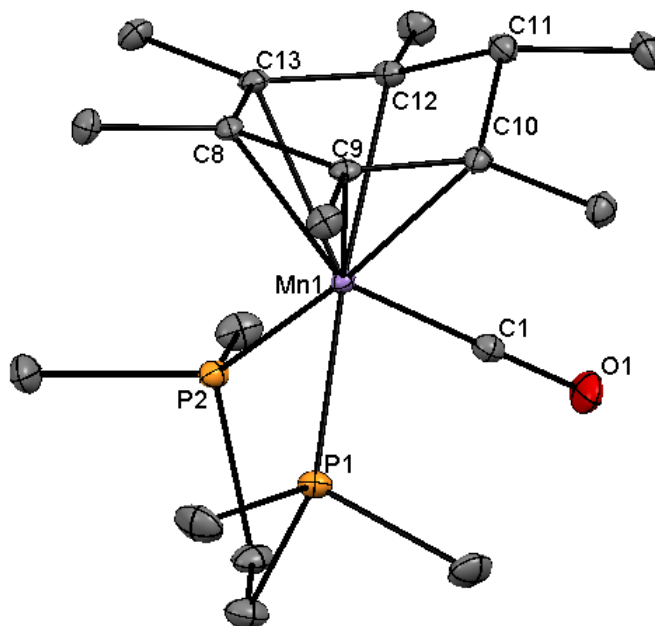


Figure 2.6: X-ray crystal structure of Mn(DMPE) cyclohexadienyl complex **1b** (thermal ellipsoid plot 30% probability), hydrogens not shown for clarity.

carbons in the cyclohexadienyl ring of **1b** ($C-C_{\text{avg}} = 1.521 \text{ \AA}$) were consistent with an sp^3 hybridized carbon.^{63,64} Furthermore, these bond lengths are distinctly different from the other C–C bonds in the cyclohexadienyl ring ($C-C_{\text{avg}} = 1.423 \text{ \AA}$), which have more sp^2 -character. The η^5 coordination of the cyclohexadienyl ligand was apparent in comparison of the through-space distances between Mn and the carbons of the cyclohexadienyl ring. As expected, C11 is the furthest away from the Mn center at a distance of 2.78 \AA relative to the average distance between the other carbons and the metal center of 2.18 \AA (Table 2.2).

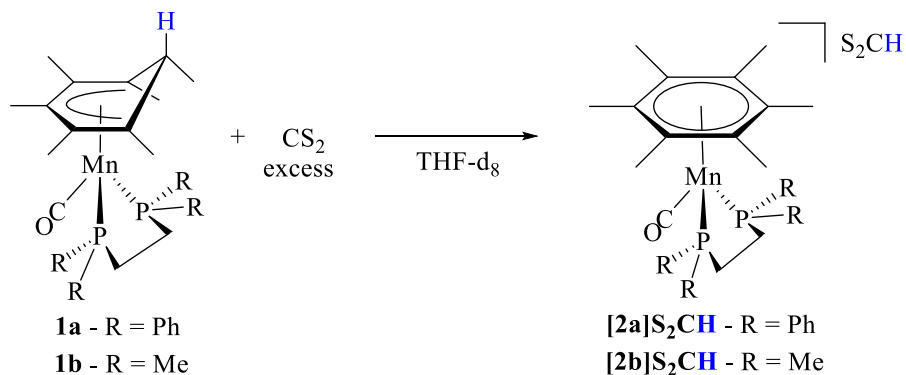
**Table 2.2: Selected Atom Distances (Å)
for Mn(C₆Me₆H)(CO)(DMPE) (**1b**)**

Mn1-C8	2.1552(15)
Mn1-C9	2.1540(15)
Mn1-C10	2.2086(15)
Mn1-C12	2.2041(15)
Mn1-C13	2.1555(15)
Mn1-C11 ^a	2.78
C8-C9	1.438(2)
C8-C13	1.432(2)
C9-C10	1.410(2)
C10-C11	1.523(2)
C11-C12	1.519(2)
C12-C13	1.411(2)

^anot a bond, but through-space distance

2.2.2 Reactivity of Manganese Cyclohexadienyl Complexes.

Complexes **1a** and **1b** were probed for CO₂ reactivity using CS₂, similar to previous studies conducted by Eyman and co-workers on their Mn cyclohexadienyl complexes (eq 2.4).⁵⁴ Both complexes reacted rapidly with CS₂ in NMR experiments as indicated by an immediate color change of the solution. This color change was more apparent in the case of complex **1a**, where the change was from deep red to bright orange. In the case of complex **1a**, a large excess of CS₂



Equation 2.4: Reaction of Mn cyclohexadienyl bidentate phosphine complexes with CS₂.

(~61 equiv) lead to precipitation of red needle-shaped crystals in the NMR tube in less than 20 minutes. Given the lack of solubility for cationic $[\text{Mn}(\text{CO})_3(\eta^6\text{-C}_6\text{Me}_6)]\text{BF}_4$ in THF, precipitation of the dithioformate salt of $\mathbf{2a}^+$ was not surprising. ^1H NMR analysis of the reaction mixture before crystals formed showed the predicted HCS_2^- was present, with a resonance at δ 12.27 ppm. The upfield shift at δ 1.95 ppm for coordinated hexamethylbenzene indicated formation of $\mathbf{2a}^+$. ^1H NMR of the crystals in CD_3CN showed a chemical shift at δ 1.92 ppm for coordinated hexamethylbenzene, comparable to the observed shift at δ 2.20 ppm in CD_2Cl_2 for $\mathbf{2a}^+$. In the region where dithioformate was expected, only a signal at δ 10.32 ppm was observed, which integrated as 0.2 protons relative to the hexamethylbenzene resonance. The fate of the dithioformate is unclear at this time.

Preliminary studies with CO_2 were carried out by bubbling CO_2 through a solution of $\mathbf{1a}$ in THF. Formation of the cationic complex $\mathbf{2a}^+$ occurred as a bright orange solid, which crashed out of solution after stirring overnight. ^1H NMR of the solid in CD_3CN did not show a signal for formate. However the resonances for $\mathbf{2a}^+$ were evident by the shift at δ 1.9 (coordinated hexamethylbenzene) and multiplets at δ 7.6, which are nearly identical to analysis of the red needle crystals in reaction with CS_2 .

Operando IR studies were conducted to better understand the reaction with CO_2 . To circumvent the insolubility of the formate salt formed, $[\text{HTBD}]\text{PF}_6$ (3 equiv) was added to the reaction solution. $[\text{HTBD}]^+$ has a bidentate hydrogen bond donor functionality that has been shown to interact with a carboxylate (Fig. 2.7).⁶⁵ A crystal structure of $[\text{HTBD}]\text{O}_2\text{CH}$ has been reported, confirming a bidentate hydrogen bonding interaction of $[\text{HTBD}]^+$ with formate.⁶⁵ A sample of the salt, $[\text{HTBD}]\text{O}_2\text{CH}$, was prepared according to the literature report. This salt was readily soluble in THF.⁶⁵ The ^1H NMR in $d_8\text{-THF}$ showed a resonance for formate at δ 8.32. The

IR spectrum of [HTBD]O₂CH in THF showed bands at 1668 and 1571 cm⁻¹, providing useful spectroscopic data for comparison with the CO₂ reaction IR data.

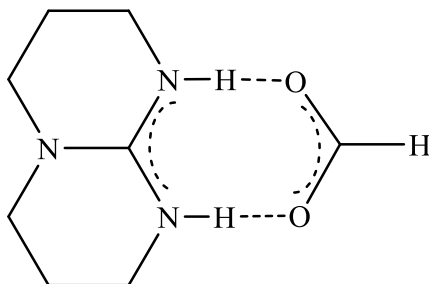


Figure 2.7: Structure of HTBD⁺ formate.

In the Operando IR experiment, 3 equiv of [HTBD]PF₆ was added to the THF reaction solution of **1a**. As shown in Figure 2.8, the peaks for starting materials, **1a** and excess HTBD⁺, can be observed at 1830 and 1638 cm⁻¹, respectively. The most apparent features are the growth of a broad band at approximately 1550 cm⁻¹, which is indicative of formate. Both of these bands increased over time as the CO₂ band around 2350 cm⁻¹ decreased (see Fig. 2.8). It is noteworthy that the increase in intensity and broadening of the HTBD⁺ band around 1638 cm⁻¹ is consistent with formation of the formate complex, which has a signal that overlaps with the hexafluorophosphate complex. Comparison of the solid state IR spectra for both HTBD⁺ salts showed that exchanging the ⁻PF₆ counterion for formate gives rise to a shift in the HTBD⁺ band to higher energy (Fig. 2.9), which is consistent with what is observed in the solution spectra.

The changes in the spectrum in the region for the manganese complex were surprisingly small in comparison. Over the two-day reaction time, the band for **1a** at 1830 cm⁻¹ changed very little in intensity, and only a small feature in the region for **2a**⁺ was observed. The reaction between **1a** and CO₂ is expected to be slow at room temperature based on similar complexes reported in the literature. One possible explanation for the relatively intense spectroscopic features for [HTBD]O₂CH is precipitation of that salt on the surface of the ReactIR probe. In

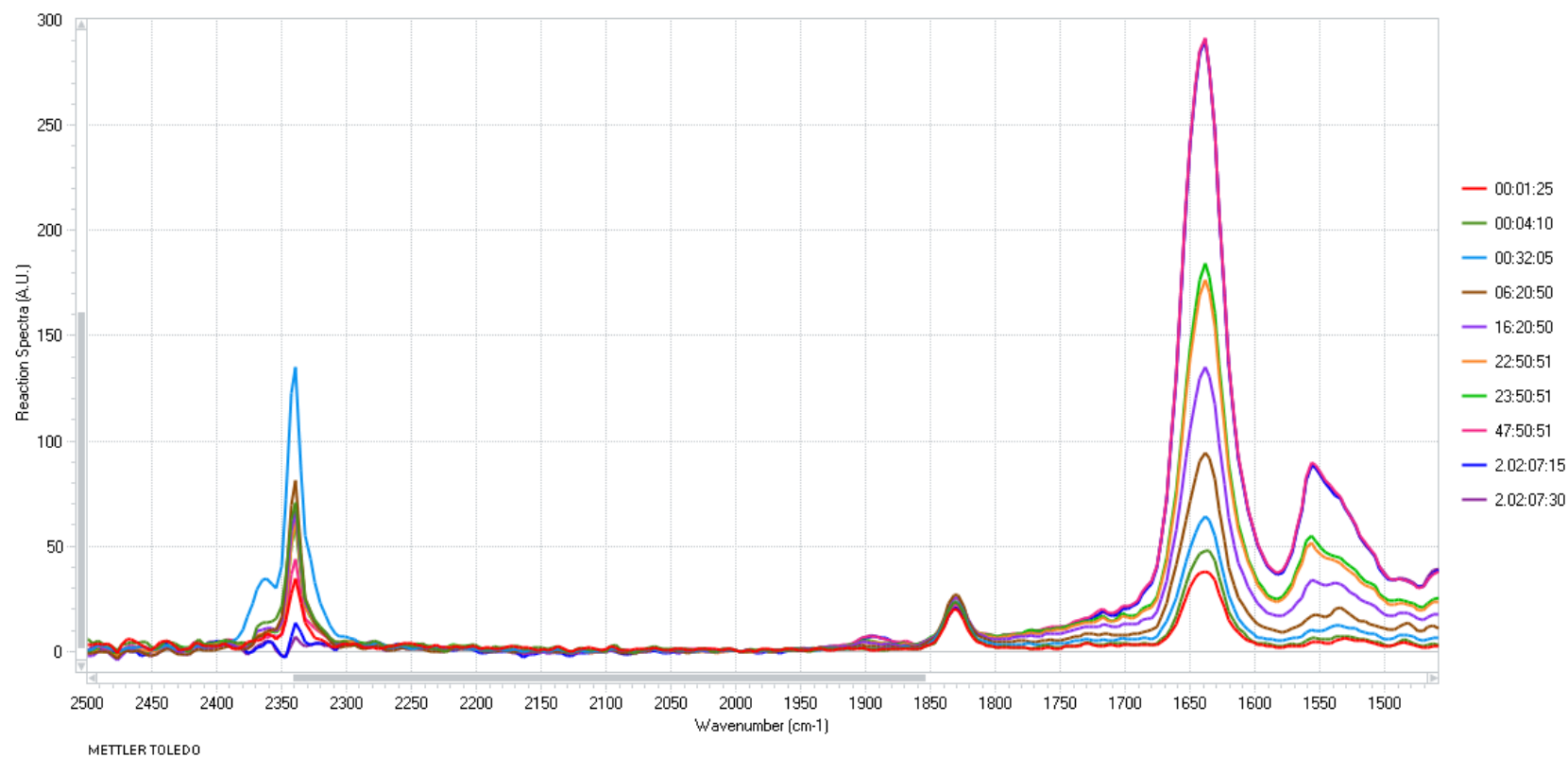


Figure 2.8: Operando IR analysis of reaction of **1a** with CO₂ in presence of [HTBD]PF₆ in THF monitored two days.

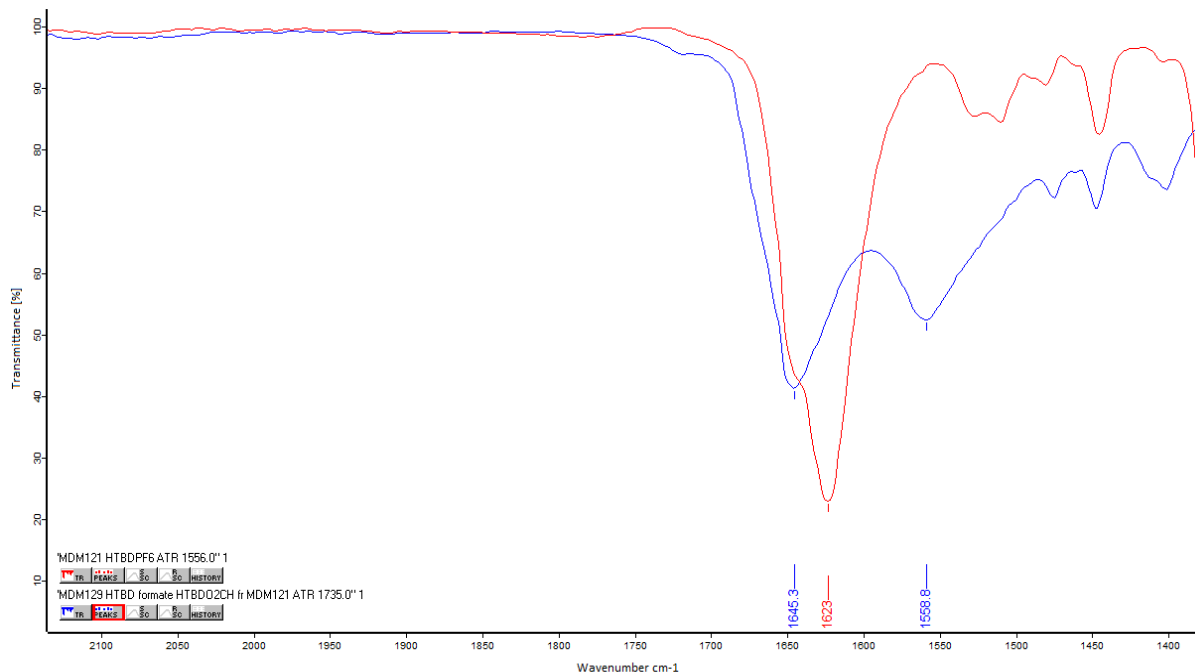


Figure 2.9: Solid state IR spectra for salts [HTBD]PF₆ (red trace) and [HTBD]O₂CH (blue trace).

other reactions we have monitored using the ReactIR instrument, the selective precipitation of one solution component over the other has been shown to skew the relative intensities of different components in comparison to a spectrum of the bulk solution.

2.3. Summary

Two new cyclohexadienyl complexes, Mn(C₆Me₆H)(CO)(DPPE) (**1a**) and Mn(C₆Me₆H)(CO)(DMPE) (**1b**) with bidentate phosphine ligands were prepared via a photolytic route from Mn(C₆Me₆H)(CO)₃. This photolytic route was found to be more productive than the alternate route, which involved the reaction of cationic arene complexes with hydride donors. Several approaches were investigated for synthesis of **2a**⁺, of which the most effective required several days of reaction time to form clean product in moderate yield. Use of heat in the synthesis of the cationic complexes to shorten reaction times typically resulted in loss of the arene ring from manganese to form di-substituted *trans*-carbonyl complexes.

Hydride transfer reactivity of the cyclohexadienyl complexes **1a** and **1b** was demonstrated in reaction with CS₂ to form the cationic complexes **2a**⁺ and **2b**⁺. Preliminary IR data suggests that **1a** has the reductive power to reduce CO₂ to HCO₂⁻. Reaction of CO₂ in the presence of HBTD⁺ indicated formation of formate by IR.

2.4. Experimental

All manipulations except otherwise stated were performed under a nitrogen atmosphere using standard Schlenk and vacuum line techniques. Photolysis experiments were performed in a custom-made jacketed vessel under constant purge of nitrogen gas at -10°C using a 450 W mercury vapor lamp supplied from ACE Glass. For further instrumental specifications see Chapter 3, section 3.4 experimental, general methods.

The reagents Mn₂(CO)₁₀, Br₂, AgBF₄, C₆Me₆, ⁿBu₄NBH₄, DPPE, DMPE, metallic sodium, CoCp^{*}₂ were all purchased and used without further purification. The complexes Mn(CO)₅Br, [Mn(η⁶-C₆Me₆)(CO)₃]BF₄ and [HTBD]O₂CH were prepared as described in the literature.^{55–57,65} In the case of Mn(η⁵-C₆Me₆H)(CO)₃, purification was performed by extraction into toluene in lieu of column chromatography, followed by crystallization from hexanes to yield a bright yellow solid.⁵⁴

[Mn(η⁶-C₆Me₆)(CO)(DPPE)]BF₄ (2a**⁺).** This complex was prepared through 3 different approaches.

(1) *Reductive catalysis method*: To a flask containing [Mn(η⁶-C₆Me₆)(CO)₃]BF₄ (51.0 mg, 0.132 mmol), DPPE (50.5 mg, 0.132 mmol, 1.0 equiv) and CoCp^{*}₂ (3.4 mg, 0.010 mmol, est. 8% by mol) was added 3 mL of 1,2-dichloroethane (1,2-DCE). Immediate formation of the monodentate product was observed by IR at 1978 and 1930 cm⁻¹. After stirring the

resulting green solution for four days, only a weak band at 1985 cm^{-1} assigned to $2\mathbf{a}^+$ was observed.

(2) *ONMe₃ Method*: A sample of $[\text{Mn}(\eta^6\text{-C}_6\text{Me}_6)(\text{CO})_3]\text{BF}_4$ (50.2 mg, 0.129 mmol), DPPE (55.0 mg, 0.138 mmol, 1.1 equiv) and ONMe₃ (9.7 mg, 0.129 mmol, 1.0 equiv) were combined and dissolved in 3 mL of 1,2-DCE. The bright orange solution was allowed to vent for 30 min. After stirring for five days at room temperature, a second equiv of ONMe₃ was added. In 1 – 2 h the reaction was judged to be complete by observation of a single CO stretching frequency at 1895 cm^{-1} in the IR spectrum.

(3) *Unassisted method*: A sample of $[\text{Mn}(\eta^6\text{-C}_6\text{Me}_6)(\text{CO})_3]\text{BF}_4$ (38.5 mg, 0.099 mmol) and DPPE (41.2 mg, 0.103 mmol, 1.0 equiv) were dissolved in 3 mL of 1,2-DCE. The bright yellow solution gradually turned orange. The reaction was stirred at room temperature for two weeks, until only the product CO stretch was observed in the IR spectrum at 1895 cm^{-1} .

For all methods, product $2\mathbf{a}^+$ was purified by column chromatography on silica gel as outlined below. $[\text{Mn}(\eta^6\text{-C}_6\text{Me}_6)(\text{CO})(\text{DPPE})]\text{BF}_4$ was eluted as an orange band from a silica gel column using 10% acetone/ CHCl_3 solution.⁵⁴ When separating products by chromatography for the reductive catalysis method, a dark band remained at the top of the column, indicating the presence of several by-products. $2\mathbf{a}^+$ was concentrated in CH_2Cl_2 and crystallized by slow diffusion of ether into the CH_2Cl_2 solution. Approximately twice as much material was obtained from uncatalyzed method (est. 10 mg) compared to the ONMe₃ method (est. 4 mg). ^1H NMR (CD_2Cl_2 , δ , ppm, 400 MHz): 2.19 (obscured, 4 H, CH_2), 2.20 (s, 6 H, C_6Me_6), 7.05 – 7.71 (multiplet, 20 H, Ph). $^{31}\text{P}\{^1\text{H}\}$ NMR (CD_2Cl_2 , δ , ppm, 162 MHz): 96 (s). IR (1,2-DCE, ν_{CO}): 1895 cm^{-1} .

Mn(η^5 -C₆Me₆H)(CO)(DPPE) (1a). A solution of Mn (η^5 -C₆Me₆H)(CO)₃ (100 mg, 0.331 mmol) and DPPE (133 mg, 0.334 mmol, 1.0 equiv) in 40 mL THF was photolyzed for 30 min. The reaction was monitored by IR spectroscopy and the photolysis was terminated upon observation of a single CO stretch at 1828 cm⁻¹. The resulting product was chromatographed on column of silica gel and eluted as a deep red band using 3:2 toluene:hexanes.⁵⁸ The product was crystallized from cold hexanes. Isolated yield: 18%. ¹H NMR (CD₂Cl₂, δ , ppm, 600 MHz): 0.59 (s, 2 H, CH₃ on Ch*), 1.20 (d, ²J_{HH} = 7.2 Hz, 1 H, *syn*-CH₃ on Ch*), 1.59 (m, 2 H, P-CH₂ on DPPE), 1.72 (s, 3 H, CH₃ on Ch*), 2.03 (br. q, 1 H, H_{anti} on Ch*), 2.42 (m, 2 H, P-CH₂ on DPPE), 3.09 (s, 1 H, CH₃ on Ch*), 7.33 (m, 12 H, Ph on DPPE), 7.53 (m, 4 H, Ph on DPPE), 7.71 (m, 4 H, Ph on DPPE). ¹³C{¹H} NMR (CD₂Cl₂, δ , ppm, 151 MHz): 14.3, 15.5, 17.2, 17.8 (Me on Ch*), 33.5 (CH₂ on DPPE, J_{CP} = 20.9 Hz), 39.9, 52.0 (Ch*), 87.7 (Ch*, ligand-hydride carbon), 99.8 (Ch*), 127.0, 127.4, 127.8, 128.9 (Ph on DPPE), 131.9 (Ph on DPPE), 132.7 (P-Ph on DPPE, J_{CP} = 17.6 Hz), 134.0 (Ph on DPPE), 143.5 (P-Ph on DPPE, J_{CP} = 17.2 Hz), 242.8 (CO). ³¹P{¹H} NMR (CD₂Cl₂, δ , ppm, 243 MHz): 93 (s). IR (THF, ν_{co}): 1828 cm⁻¹. IR (CH₂Cl₂, ν_{co}): 1821 cm⁻¹.

Mn(η^5 -C₆Me₆H)(CO)(DMPE) (1b). A sample of Mn (η^5 -C₆Me₆H)(CO)₃ (100 mg, 0.331 mmol) and DMPE (55 μ L, 0.331 mmol, 1.0 equiv) were combined in 40 mL THF and photolyzed for 30 - 35 min. The progress of the reaction was monitored by IR spectroscopy, and the reaction was terminated upon observation of a CO stretch at 1821 cm⁻¹. The resulting yellow solution was purified by crystallization from cold (-20 °C) hexanes, to yield red-orange crystals. Isolated yield: est. 2 – 3 mg. ¹H NMR (C₆D₆, δ , ppm, 400 MHz): 1.02 (m, 2 H, P-CH₂ bridge of DMPE), 1.14 (“d”, 6 H, P-CH₃ on DMPE), 1.36 (s, 6 H, P-CH₃ on DMPE), 1.47 (s, 9 H, overlapped CH₃ on Ch*), 1.89 (s, 6 H, CH₃ on Ch*), 2.42 (s, 3 H, CH₃ on Ch*), 2.66 (m, 1 H,

H_{anti}). ^1H NMR (CD_2Cl_2 , δ , ppm, 600 MHz): multiplicities not reported given very broad spectrum, 1.21 (15 H), 1.32 (6 H), 1.50 (2 H, CH_2 on DMPE), 1.92 (6 H), 2.27 (1 H, H_{anti} on Ch^*), 2.44 (3 H). $^{13}\text{C}\{^1\text{H}\}$ NMR (CD_2Cl_2 , δ , ppm, 151 MHz): 16.38, 16.62, 17.36 (Me on Ch^*), 19.58 (Me on DMPE), 20.02 (Me on Ch^*), 32.07 (P- CH_2 bridge of DMPE), 38.92, 49.39, 85.87, 101.53 (Ch^*), 235.08 (CO). $^{31}\text{P}\{^1\text{H}\}$ NMR (CD_2Cl_2 , δ , ppm, 242 MHz): 71 (s). IR (THF, ν_{co}): 1821 cm^{-1} .

NMR study of the reaction of CS_2 with **1a, $\text{Mn}(\eta^5\text{-C}_6\text{Me}_6\text{H})(\text{CO})(\text{DPPE})$.** A sample of **1a** (5.3 mg, 0.00822 mmol) was dissolved in d_8 -THF to give a dark red solution. The NMR tube was covered in foil during transport to the instrument. The $^{31}\text{P}\{^1\text{H}\}$ spectrum showed a single resonance at δ 93, characteristic of the cyclohexadienyl starting material. To this NMR sample, a large excess of CS_2 (30 μL , est. 61 equiv) was added and the tube was gently shaken to mix. The color of the solution changed to bright orange and after ~ 10 min formed red needle-like crystals. The $^{31}\text{P}\{^1\text{H}\}$ NMR spectrum of this solution gave a single resonance at δ 97, characteristic of the arene product, **2a**⁺.

NMR reaction of CS_2 with **1b, $\text{Mn}(\eta^5\text{-C}_6\text{Me}_6\text{H})(\text{CO})(\text{DMPE})$.** A single orange-red crystal of **1b** (est. 2.3 mg, 0.00656 mmol), was dissolved in d_8 -THF (400 μL) resulting in an orange-yellow solution. No solids were observed in the reaction even after sitting overnight at low temperature. $^{31}\text{P}\{^1\text{H}\}$ NMR spectrum of the sample showed only cyclohexadienyl **1b** at δ 70. After addition of excess CS_2 (2.5 μL , 0.041 mmol, est. 6.3 equiv), the $^{31}\text{P}\{^1\text{H}\}$ spectrum changed to δ 73 indicative of **2b**⁺ formation.

Operando IR study of CO_2 reaction with **1a, $\text{Mn}(\eta^5\text{-C}_6\text{Me}_6\text{H})(\text{CO})(\text{DPPE})$, in presence of $[\text{HTBD}]\text{PF}_6$.** A Schlenk tube sealed with a custom adaptor designed to fit an IR probe was equipped with a stir bar and a dark red solution of **1a** (36.5 mg, 0.057 mmol) and $[\text{HTBD}]\text{PF}_6$

(47.6 mg, 0.17 mmol, 3 equiv) in 3 mL of dry THF was added. The reaction was monitored by operando IR technique at room temperature for one week. After stirring overnight, a cloudy sample solution was observed due to the presence of a white precipitate. After nearly one week orange and white solids had collected above an orange sample solution.

X-ray Structure Determination of $\text{Mn}(\eta^5\text{-C}_6\text{Me}_6\text{H})(\text{CO})(\text{DMPE})$, 1b. Crystallographic data^{63,64,66} and experimental parameters are summarized in Tables 2.2 and 2.3. Crystals suitable for X-ray diffraction were obtained from a concentrated solution of cold hexanes (-20 °C). The red crystal was mounted in oil and kept at 100 K in a stream of N₂ during data collection using a Bruker SMART Apex II CCD based X-ray diffractometer system equipped with a Cu –target X-ray tube ($\mu(\text{CuK}\alpha) = 6.899$) operated at 1600 watts. The structure was solved using Olex2 software⁶⁴ with olex2.solve structure solution program⁶⁶ using Charge Flipping and refined with XL refinement package using Least Squares minimization.⁶³ 17867 reflections were measured and 3724 unique reflections ($R_{\text{int}} = 0.0243$) were used in all calculations. The final wR_2 was 0.0744 (all data) and R_1 was 0.0278 ($>2\sigma(I)$). Complete crystallographic data can be found in Appendix 1.2.

Table 2.3: Crystallographic Parameters for Mn(C₆Me₆H)(CO)(DMPE) (1b)

fw	369.35
temp, K	100
space group	P2 ₁ /n
a, Å	8.6431(2)
b, Å	15.4462(4)
c, Å	14.9509(3)
α , °	90.00
β , °	92.4250(10)
γ , °	90.00
V, Å ³	1994.20(8)
Z	4
ρ_{calc} , mg/mm ³	1.320

Electrochemistry. Cyclic voltammetry experiments were conducted using a glassy carbon working electrode (polished with 0.05 μm alumina powder between scans), a Ag quasi-reference electrode (pre-treated with 1 M HCl solution), and a Pt wire auxiliary electrode. Measurements were made with 100 mM TBABF₄ as electrolyte in a custom-made, single-compartment Schlenk cell. All potentials are reported versus Fc/Fc⁺, as determined by subtracting 0.075 V from experimentally determined potentials.

2.5. Acknowledgements

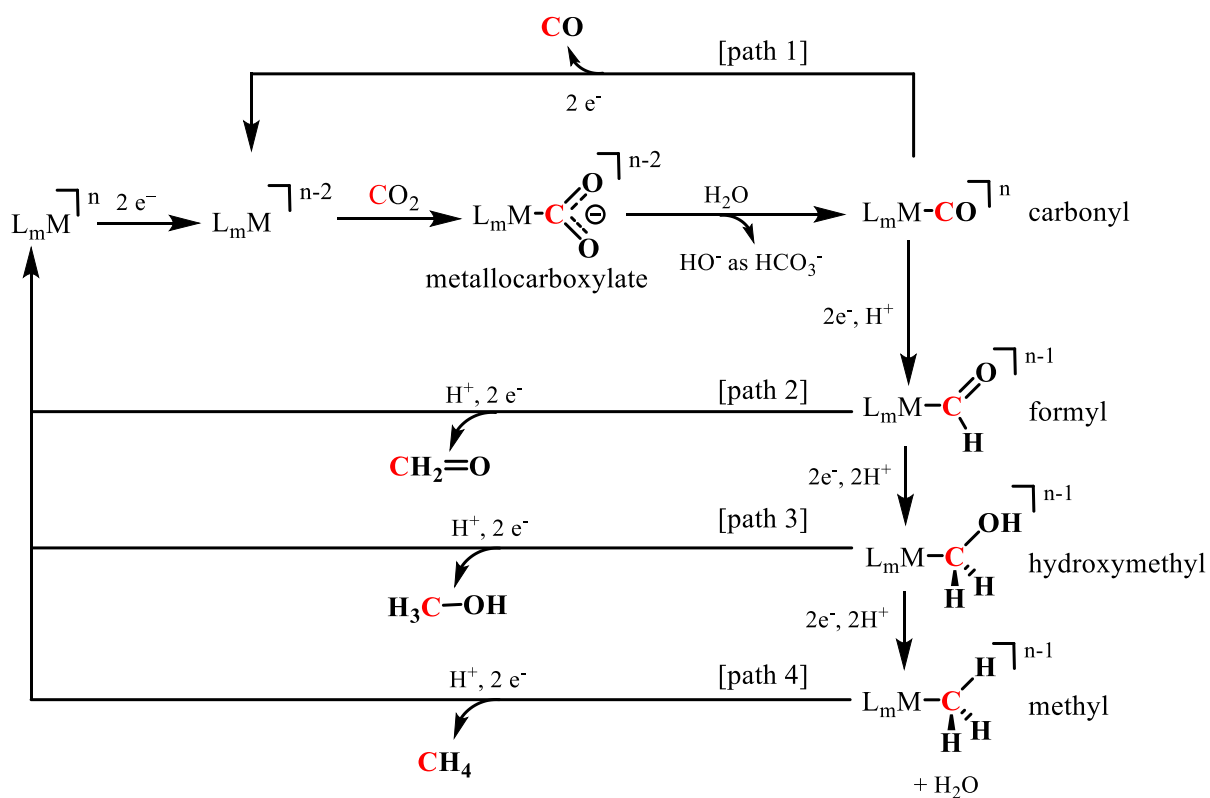
We acknowledge Dr. Peter White for x-ray crystallography and Dr. Marc ter Horst for NMR consultation. Undergraduate researchers, Jimmy Pan and Bennett Vass provided assistance in synthesis of starting Mn(CO)₅Br and tricarbonyl Mn complexes. Prof. Michel R. Gagné provided for the use of his lab's ReactIR system for operando IR studies in this chapter.

CHAPTER 3

REACTION OF ELECTROPHILES WITH A CO-REDUCTION INTERMEDIATE RUTHENIUM HYDROXYMETHYL COMPLEX

3.1. Introduction and Background

In the catalytic cycle for the reductive disproportionation of CO₂ to CO (Scheme 3.1, path 1), a reduced metal complex reacts with CO₂. Protonation of the resulting metallocarboxylate



Scheme 3.1: Example scheme for activation of CO₂ using transition metal catalysts.

ultimately produces a metal carbonyl complex. If the product carbonyl ligand is retained in the coordination sphere of the transition metal complex rather than released from the metal, the possibility is opened for further reduction of the coordinated CO ligand.

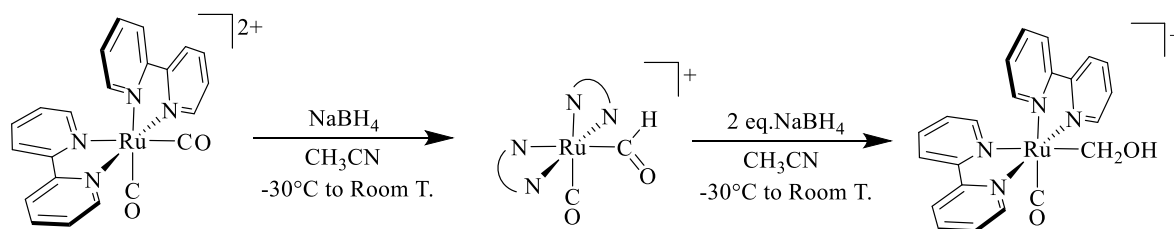
Intermediate carbonyl, formyl, hydroxymethyl, and methyl complexes can be accessed from sequential reduction/protonation sequences (Scheme 3.1, right). Subsequent protonation of these species can theoretically produce formaldehyde, methanol, and methane as C₁ products (Scheme 3.1, paths 2 – 4). These proposed transformations are unprecedented in an electrochemical reduction scenario.

Using NaBH₄ as a reagent, Graham and co-workers demonstrated the stepwise reduction of one of the carbonyl groups of [CpRe(NO)(CO)₂]⁺ to Re-CHO, Re-CH₂OH, and Re-CH₃ under different solvent conditions.^{67,68} Use of borohydride in these synthetic reductions mimics the electrochemical process of a two-electron reduction/protonation step. Transition metal hydroxymethyl complexes have also been proposed as intermediates in the Fischer-Tropsch process. Casey reported the first isolated transition metal hydroxymethyl complex, CpRe(CO)(NO)(CH₂OH).^{69–71} Protonation of the hydroxymethyl ligand of this rhenium complex lead to the formation of several products: a carbonyl, a methyl, a methoxymethyl complex of rhenium, and an ether-bridged bimetallic complex.⁷¹ Casey proposed the formation of an intermediate carbene complex to explain the observed products from the protonation reaction. Further attempts to independently synthesize the proposed carbene complex from a rhenium methyl complex generated only a rhenium ethylene complex. Although the putative carbene complex intermediate was not observed directly, the formation of a coordinated ethylene ligand could be explained by the formation of a transient carbene complex.⁷¹

Further research to identify carbene or methylidene intermediate complexes led to the first spectroscopic observation of a CpRe(PPh₃)(NO) methylidene complex.⁷⁶ Later the isolation of a stable biscyclopentadienyl rhenium methylidene cation was reported.⁷² In both reports, Gladysz

and Heinekey observed the stabilization of the carbene ligand with nucleophilic reagents such as phosphine, amines, and pyridines to form ylide structures.^{73–76,72}

Two ruthenium systems that have received considerable attention in the CO₂ reduction area are Tanaka's [Ru(bpy)₂(CO)₂]²⁺ and [Ru(tpy)(bpy)(CO)]²⁺.^{77,79–81} The dicarbonyl ruthenium bis-bipyridine complex, like the [CpRe(NO)(CO)₂]⁺, undergoes reduction of a coordinated carbonyl ligand to form isolable ruthenium formyl and hydroxymethyl complexes using NaBH₄ as a reducing agent (Scheme 3.2). In this system, further reduction to a ruthenium methyl complex is



Scheme 3.2: Synthetic reduction of ruthenium polypyridyl complexes in Tanaka's system.^{77–81}

not observed. The observed chemical reduction for the dicarbonyl has fueled speculation on the mechanism for product formation under electrocatalytic conditions. Products such as carbon monoxide, formic acid, methanol and C₂ products are observed depending on the electrocatalyst and reaction conditions.^{77–81,82–85} The bis-bipyridine complex, for example, produces formic acid as the major product in controlled-potential electrolysis experiments.⁴⁷ Alternatively, electrocatalytic carbon dioxide reduction using [Ru(tpy)(bpy)(CO)]²⁺ as an entry point in EtOH/H₂O shows hydroxyacetic acid (HOCH₂COOH) to be the primary product, but formic acid, formaldehyde, methanol, and formylformic acid (H(C=O)COOH) were also observed.^{45,47} The transformation of carbon dioxide to methanol is particularly intriguing, which Tanaka proposes to result from protonation of an intermediate hydroxymethyl complex, [Ru-CH₂OH]⁺ during electrocatalysis.^{45,77}

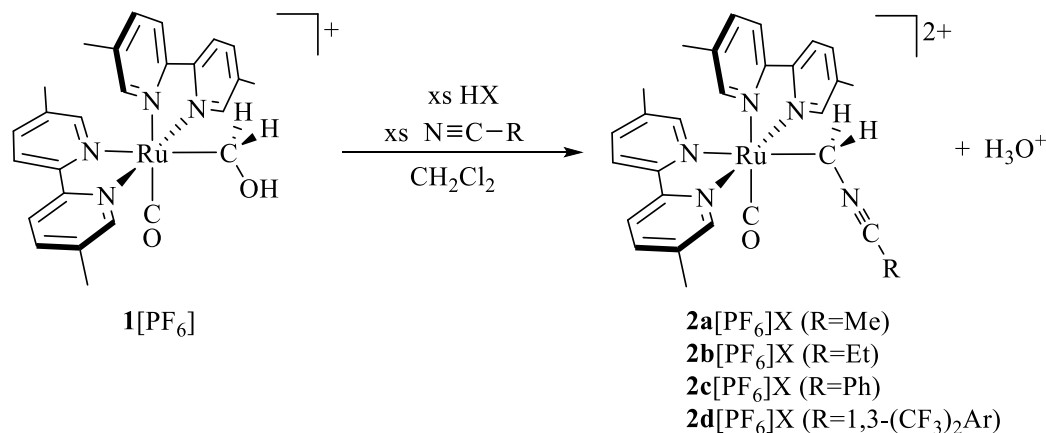
This chapter focuses on evaluating the reactivity of the hydroxymethyl ligand in the isolable complex, $[\text{Ru}(\text{bpy}')_2(\text{CO})(\text{CH}_2\text{OH})]^+$ (where bpy' represents 5,5'-dimethyl-2,2'-bipyridine), with Brønsted-Lowry and Lewis acids. Reactions carried out in the presence of Lewis bases (L = nitriles or pyridines) afford ruthenium ylide complexes of the form $[\text{Ru}(\text{bpy}')_2(\text{CO})(\text{CH}_2\text{L})]^{2+}$. The observed reactivity of these ylide complexes provide insight into potential pathways for formation of C_2 products from CO_2 .

3.2. Results and Discussion

The hydroxymethyl ligand in the complex $[\text{Ru}(\text{bpy}')_2(\text{CO})(\text{CH}_2\text{OH})]^+$ (**1**⁺) presents two potential sites for reaction with electrophiles, at the ruthenium-carbon bond or at the hydroxyl group. In the discussion below, reactions between **1**⁺ and electrophiles conducted in the presence of Lewis base additives (L) are presented first, followed by a discussion of reactions in the absence of Lewis bases.

3.2.1 Generation of ylides $[\text{Ru}(\text{bpy}')_2(\text{CO})(\text{CH}_2\text{L})]^{2+}$

Protonation experiments of hydroxymethyl **1**⁺ were conducted with 2 – 20 equiv of triflic acid at -78 °C in an NMR tube in the presence of 5 – 10 equiv of added acetonitrile and monitored by ¹H NMR spectroscopy. Addition of acid is accompanied by a color change from bright red for **1**⁺ to bright yellow. The diastereotopic protons of the methylene group for the hydroxymethyl complex at δ 4.40 and δ 4.52 ($^2J_{\text{HH}} = 7.0$ Hz) disappeared completely, and complete conversion to a new species is observed. This new complex is formulated as an acetonitrile ylide complex, $[\text{Ru}(\text{bpy}')_2(\text{CO})(\text{CH}_2\text{NCMe})]^{2+}$ (**2a**²⁺), indicating that oxygen is the site of protonation (eq 3.1).



Equation 3.1: Protonation of $\mathbf{1}^+$ by strong acids to form $\mathbf{2}^{2+}$ ruthenium nitrile ylide.

The diastereotopic methylene protons of $\mathbf{2a}^{2+}$ at δ 3.90 and δ 3.30, appear as doublets of quartets ($^2J_{\text{HH}} = 13.5$ Hz, $^5J_{\text{HH}} = 3.0$ Hz) (Fig. 3.1). The related methyl signal is observed as a triplet at δ 2.33. The $^5J_{\text{HH}}$ of 3.0 Hz is comparable to the methylnitrilium cation (MeNCMe^+) and substituted alkynes (e.g., functionalized butynes).^{86,87} As further support for the formation of $\mathbf{2a}^{2+}$, a reaction between $\mathbf{1}^+$ with acetonitrile present and 20 equiv of triflic acid, resulted in protonation at the carbon of the nitrile ylide ligand for $\mathbf{2a}^{2+}$ affording methylnitrilium cation.⁸⁶ The acetonitrile ylide $\mathbf{2a}^{2+}$ was also formed using $[\text{H}(\text{OEt}_2)_2]\text{BAr}^{\text{F}}_4$ and $[\text{H}(\text{OEt}_2)]\text{BF}_4$, as the proton source, indicating the counterion does not influence the observed site of reaction. The 6 and 6' hydrogens and the methyl substituents on the 5,5'-dimethyl-2,2'-bipyridine ligand provided diagnostic singlet resonances which allowed for facile reaction monitoring (Table 3.1).⁸⁸

The formation of the nitrile ylide $\mathbf{2a}^{2+}$ was also monitored by operando IR of a reaction of $\mathbf{1}^+$ with 3 equiv of triflic acid at -78 °C. The carbonyl band for $\mathbf{1}^+$ at 1930 cm^{-1} shifts to 1965 cm^{-1} with addition of acid, indicating the formation $\mathbf{2a}^{2+}$. If the acetonitrile reagent is not rigorously anhydrous, the observed product has a band instead at 1949 cm^{-1} , which is identified by ^1H NMR spectroscopy as the amide ylide, $\mathbf{3}^+$ (eq 3.2). This species has been independently synthesized by

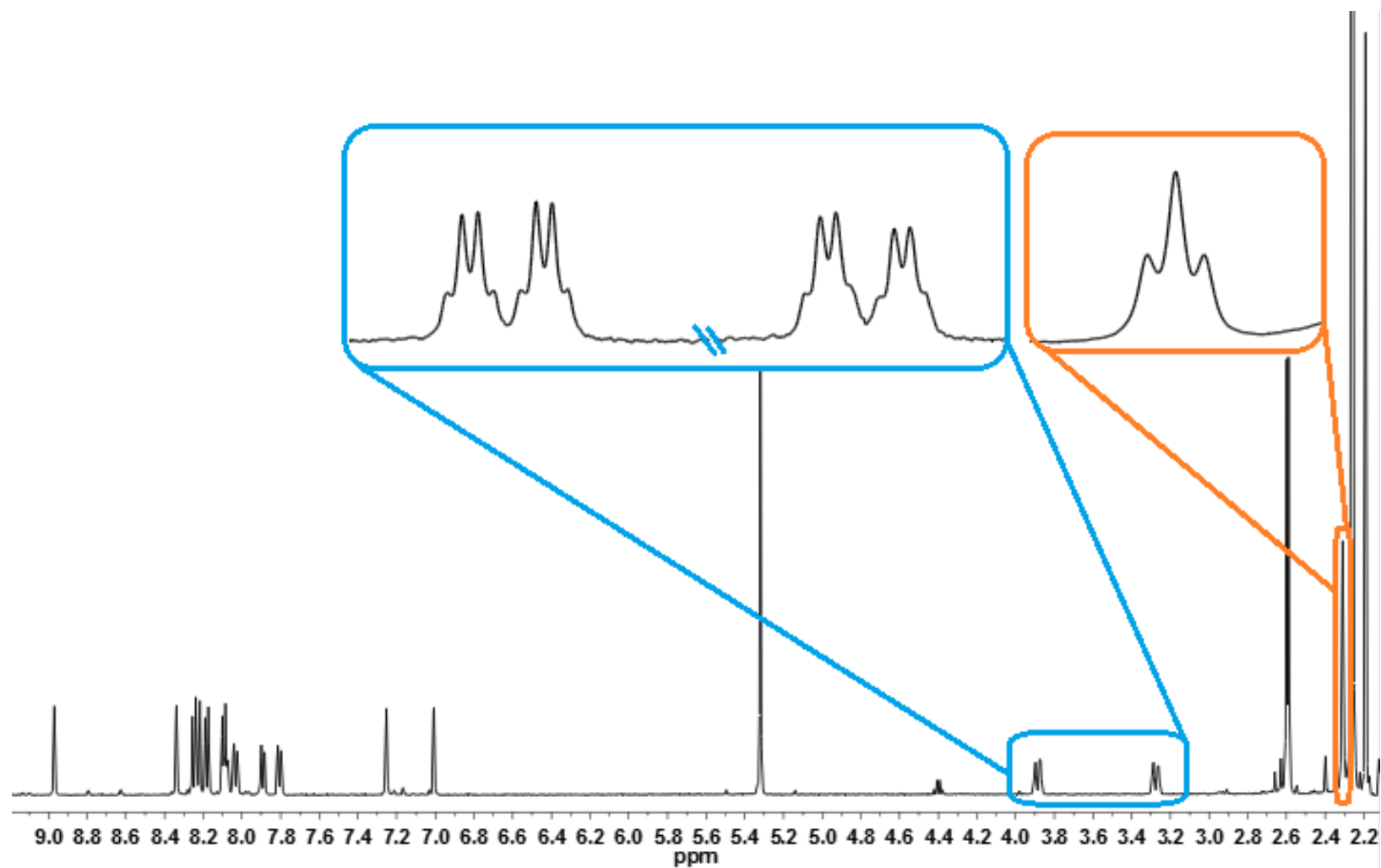


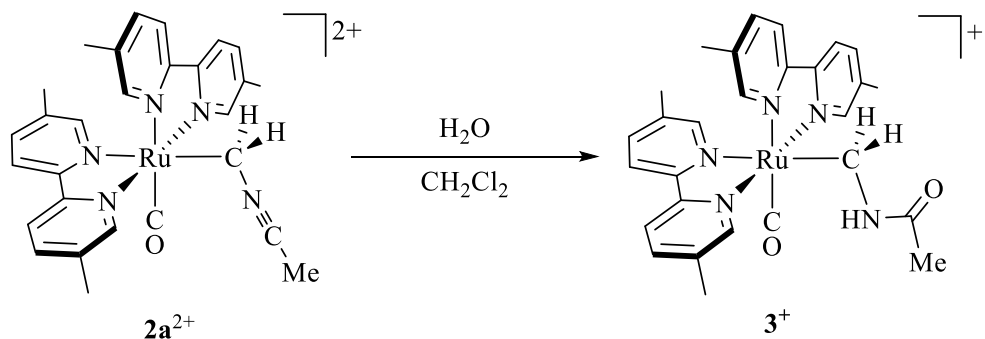
Figure 3.1: ^1H NMR of $2\mathbf{a}^{2+}$, $[\text{Ru}(\text{bpy}')_2(\text{CO})(\text{CH}_2\text{NCMe})]^{2+}$ formed under acidic conditions in CD_2Cl_2 with zoomed-in views of diagnostic methylene protons (blue) and coordinated MeCN methyl of ylide showing $^5J_{\text{HH}}$ coupling (orange).

Table 3.1: Summary of Spectroscopic Data for Ru Ylide Complexes, [Ru(CH₂L)]²⁺

Complex	Ru(CH ₂) (δ , ppm) J_{HH} (Hz)	Me on bpy' (δ , ppm)	Upfield bpy' (δ , ppm)	Downfield bpy' (δ , ppm)	IR ν_{CO} (cm ⁻¹)
1⁺ - [Ru(CH ₂ OH)] ⁺	4.40 dd 4.52 dd ² J = 7.5 ³ J = 5.0	2.16, 2.19 2.53, 2.57	7.03 7.43	9.02 9.30	1934
2a²⁺ - [Ru(CH ₂ NCMe)] ²⁺	3.48 dq 3.89 dq ² J = 13.5 ⁵ J = 3.0	2.19, 2.20 2.60, 2.61	7.08 7.27	8.49 8.98	1965
2b²⁺ - [Ru(CH ₂ NCEt)] ²⁺	3.47 dt 3.92 dt ² J = 13.5 ⁵ J = 2.5	2.20, 2.21 2.60, 2.63	7.11 7.26	8.57 8.97	1964
2c²⁺ - [Ru(CH ₂ NCPPh)] ²⁺ (at 10 °C)	4.26 d 3.82 d ² J = 13.5	2.18, 2.20 2.43, 2.64	obscured	8.64 8.96	—*
2d²⁺ - [Ru(CH ₂ NCAr ^F)] ²⁺ (at 0 °C)	4.27 d 3.80 d ² J = 13.5	2.18, 2.20 2.50, 2.63	obscured	8.66 9.01	—*
4a²⁺ - [Ru(CH ₂ py)] ²⁺	4.80 d 5.52 d ² J = 10.0	2.15, 2.28 2.37, 2.66	7.16 7.21	8.41 8.51	1955
4b²⁺ - [Ru(CH ₂ (4-Mepy))] ²⁺	4.71 d 5.47 d ² J = 10.0	2.19, 2.30 2.42, 2.69	7.19 7.20	8.47 8.52	1953
4c²⁺ - [Ru(CH ₂ (3,5-Me ₂ py))] ²⁺	4.78 d 5.40 d ² J = 10.0	2.15, 2.29 2.45, 2.66	7.19 7.46	8.56 8.64	1952
4d²⁺ - [Ru(CH ₂ (4-CNpy))] ²⁺	4.89 d 5.66 d ² J = 9.0	2.15, 2.27 2.46, 2.66	7.14 7.21	8.52 8.59	1965
5⁺ - [Ru(CH ₂ OCPh ₃)] ⁺	3.63 d 3.67 d ² J = 6.0	2.11, 2.20 2.35, 2.54	6.92 7.46	8.72 9.06	1936

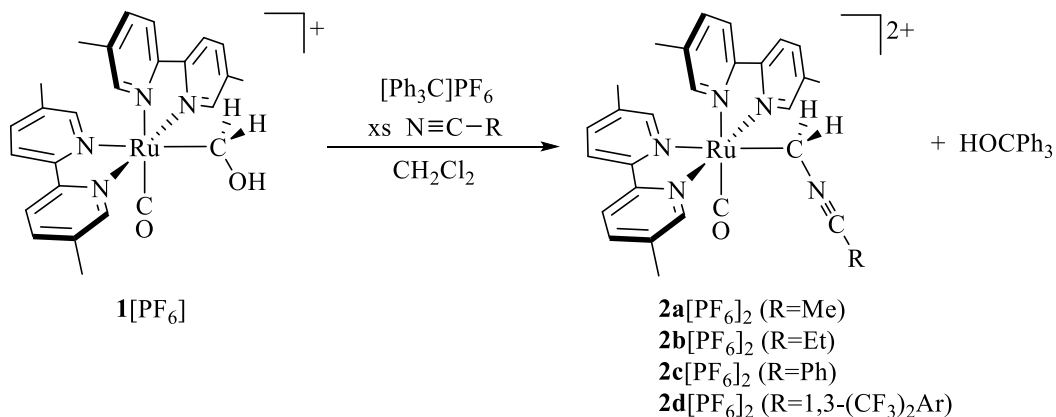
All chemical shifts reported relative to residual solvent CD₂Cl₂ at 20°C unless otherwise noted. ¹H NMR pattern indicated by the following: s (singlet), d (doublet), dd (doublet of doublets), dt (doublet of triplets), dq (doublets of quartets). Obscured indicates unable to report due to overlap with other aromatic resonances. IR bands reported in CH₂Cl₂ at 20°C unless otherwise noted. *Unobserved by IR due to temperature sensitivity. Full spectroscopic details reported in Experimental Section 3.4 and selected spectra shown in Appendix 2.1.

the protonation of the parent bpy analogue of **1⁺** with acetic acid .⁷⁸



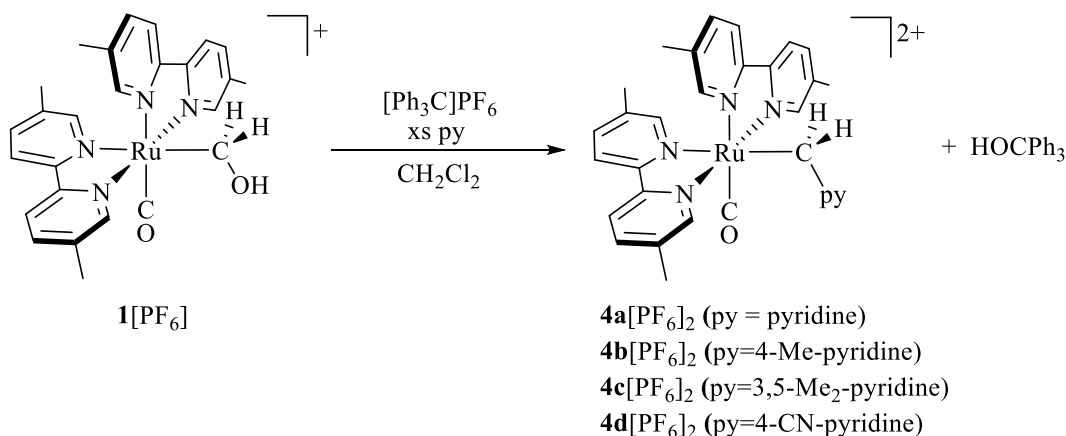
Equation 3.2: Water addition to **2a**²⁺ to form **3**⁺ ruthenium amido ylide.⁷⁸

A variety of nitrile ylides can be prepared by this protonation route. For the propionitrile ylide, **2b**²⁺, each of the diastereotopic methylene proton resonances appear as a doublet of triplets at δ 3.47 and δ 3.90 from coupling to the methylene protons of the coordinated propionitrile ligand at δ 2.62. When the less electron-donating benzonitrile and 3,5-bis(trifluoromethyl)benzonitrile (Ar^FCN) were used as Lewis base trapping agents, the resulting nitrile ylide products, **2c**²⁺ and **2d**²⁺ respectively, were only observed at low temperatures (< 10 °C). The thermal sensitivity of all **2**²⁺ complexes hindered our attempts to grow crystals suitable for single crystal X-ray diffraction. The nitrile-ylide complexes **2**²⁺ can also be prepared using a stoichiometric amount of trityl cation to abstract hydroxide from **1**⁺ with concomitant formation of triphenylmethanol (eq 3.3). In contrast to the protonation reactions, these trityl reactions proceeded rapidly and cleanly at 0 °C.



Equation 3.3: Hydroxide abstraction using trityl cation to form **2**²⁺ ruthenium nitrile ylides.

Given the sensitivity of the nitrile ylides 2^{2+} towards H_2O , we sought to explore reactions with pyridine, which would not be expected to undergo the same hydrolysis reaction. Using the hydroxide abstraction route, a variety of pyridine ylide complexes could readily be prepared (eq 3.4).



Equation 3.4: Hydroxide abstraction using trityl cation to form 4^{2+} pyridine ylides.

Furthermore, the use of trityl hexafluorophosphate eliminated the need for a subsequent anion metathesis to isolate the ylide product. Addition of a solution of $1[PF_6]$ and two equiv of pyridine to slightly less than one equiv of solid $Ph_3C[PF_6]$ in an NMR tube at 0 °C resulted in a rapid color change from red-orange to bright orange-yellow. In the 1H NMR spectrum, doublets at δ 4.76 and δ 5.53 ($^2J_{HH} = 10$ Hz) are assigned to the methylene group of the product $4a^{2+}$ (Fig

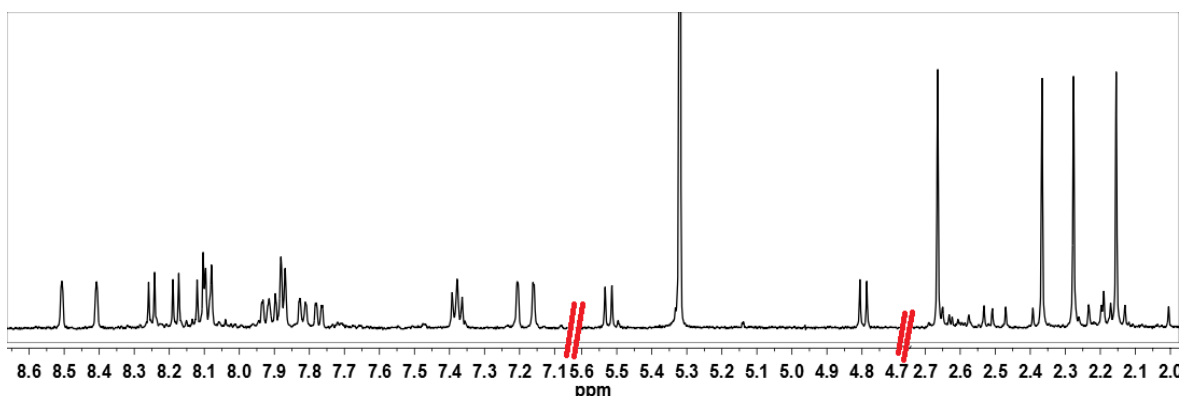
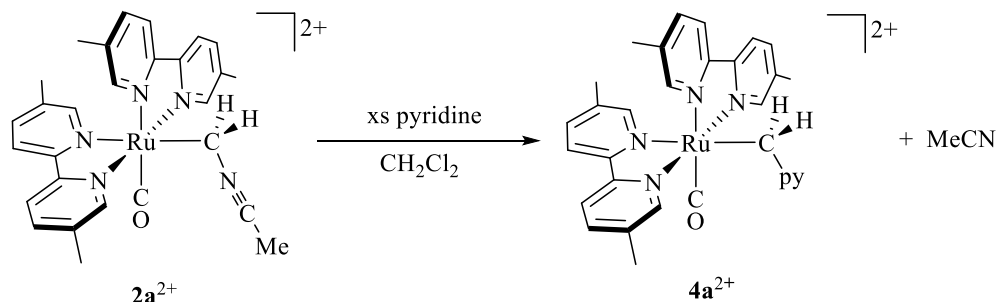


Figure 3.2: 1H NMR of $4a^{2+}$, $[Ru(bpy')_2(CO)(CH_2py)]^{2+}$ in CD_2Cl_2 .

3.2). For all pyridine ylide experiments, NMR spectroscopy indicated free rotation about the ylide C – N(pyridine) bond as indicated by the equivalency of the *ortho*- and *meta*- hydrogens of the pyridine ring. The crude pyridine ylide complexes could be isolated from aqueous solutions, demonstrating the stability of the product toward water. The pyridine ylide complexes could also be prepared by the addition of acid to **1**[PF₆]. However, the reaction rate for these experiments was strongly dependent on the basicity of the substituted pyridine. Slower reaction rates were observed for more basic pyridines which would be protonated by the strong acid before **1**⁺.

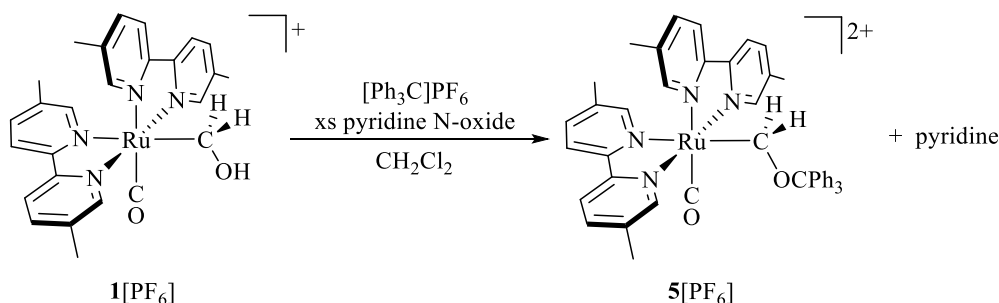
The CO stretching frequency for pyridine ylide **4a**²⁺ is observed at 1955 cm⁻¹ in CH₂Cl₂, at lower frequency than the acetonitrile ylide **2a**²⁺ (at 1965 cm⁻¹). The difference in CO stretching frequencies indicates that the electronic characteristics of the pyridine are effectively transmitted to the metal center. The observed stretching frequency for 4-cyanopyridine ylide **4d**²⁺ (ν_{co} = 1965 cm⁻¹) is similar in energy to the parent nitrile **2a**²⁺, while **4a**²⁺ and 4-methylpyridine ylide **4b**²⁺ (ν_{co} = 1953 cm⁻¹) appear at a lower frequency.

An exchange reaction was attempted by heating a solution of 4-cyanopyridine complex **4d**²⁺ with 2 – 20 equiv of 3,5-Me₂pyridine in 1,2-dichloroethane at 80 °C for several hours. No exchange of the pyridine ligand was observed after heating for 8 h at 80 °C. In contrast, the addition of an excess of pyridine to a solution of the acetonitrile ylide, **2a**²⁺, showed rapid conversion to the pyridine ylide, **4a**²⁺ and free acetonitrile by ¹H NMR spectroscopy at 0 °C (eq 3.5).



Equation 3.5: Exchange reaction of acetonitrile in $2a^{2+}$ for pyridine to form $4a^{2+}$.

When pyridine N-oxide is employed as the Lewis base additive in reactions of 1^+ with $[\text{Ph}_3\text{C}]\text{PF}_6$, the triphenylmethoxymethyl complex, 5^+ , is formed (eq 3.6). The methylene resonances for 5^+ are considerably upfield from starting material 1^+ at δ 3.67 and δ 3.63 ($^2J_{\text{HH}}$ of 6.0 Hz). Electrospray ionization mass spectral analysis (m/z of 771.23, $z = 1$) and single crystal X-ray diffraction confirmed the identity of the product (Fig. 3.3). Crystallographic data for $5[\text{PF}_6]$ are outlined in Appendix 2.2.



Equation 3.6: Hydroxide abstraction from 1^+ using trityl cation in the presence of pyridine N-oxide to form 5^+ .

Trace amounts of 5^+ are also observed by ^1H NMR spectroscopy in reactions to prepare pyridine ylides (4^{2+}) using trityl cation. In contrast, no 5^+ is observed in any experiments with added nitrile. In exchange experiments adding pyridine to the nitrile ylide ruthenium complex, 5^+ is also not observed. Thus, we hypothesize that a portion of the excess pyridine deprotonates the triphenylmethanol formed *in situ* after hydroxide abstraction from 1^+ by trityl cation. The deprotonated triphenylmethoxide anion then attacks the intermediate carbene complex to give 5^+ .

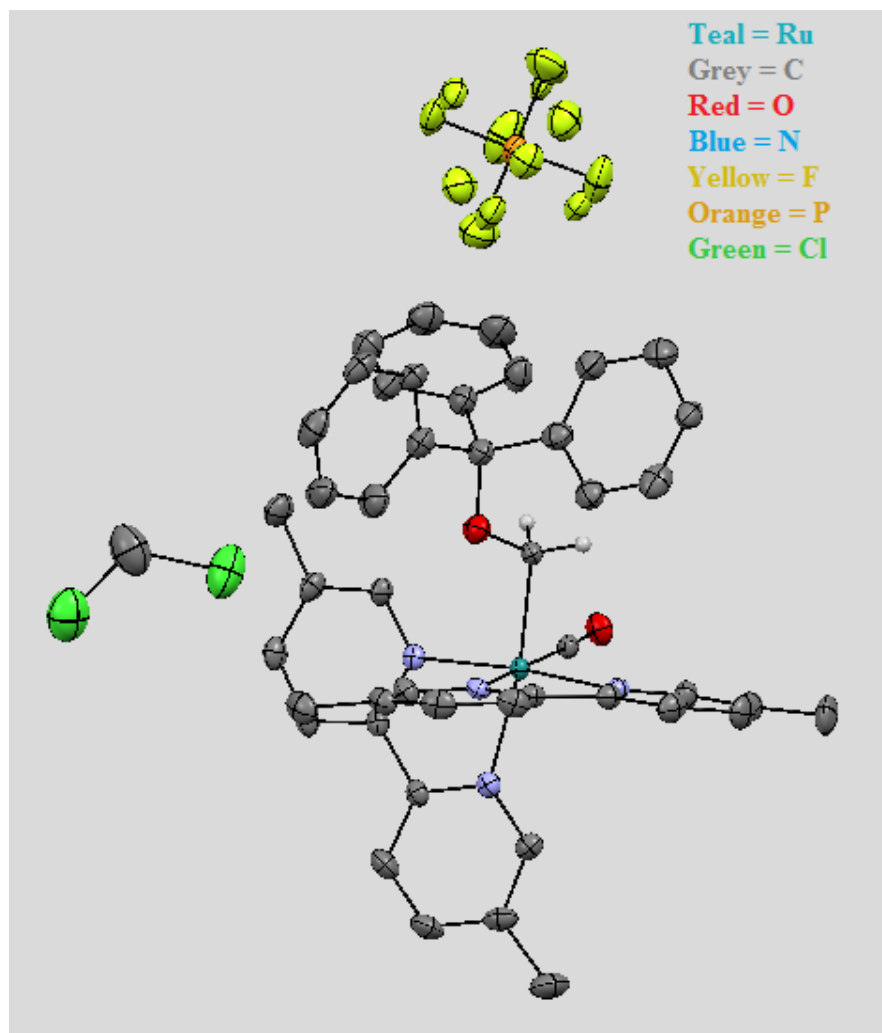


Figure 3.3: X-ray crystal structure of **5**⁺, [Ru(bpy')₂(CO)(CH₂OCPh₃)]⁺[PF₆]⁻•CH₂Cl₂.

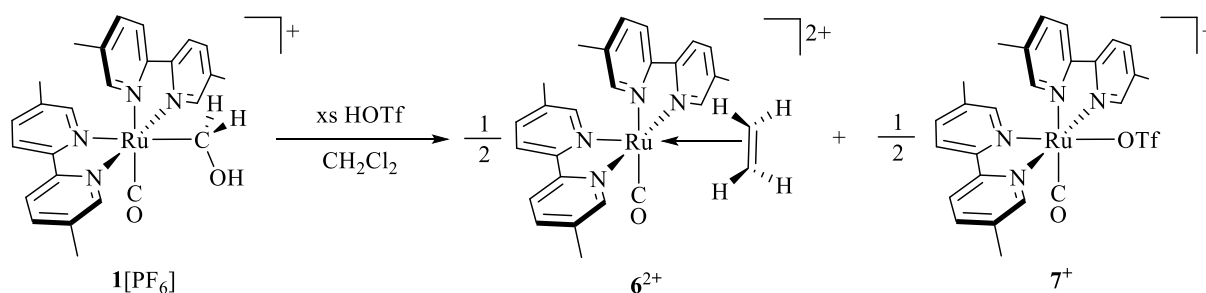
To summarize the spectroscopic data for pyridine and nitrile ylides reported in this work are given in Table 3.1.

3.2.2 Reactions of [Ru(bpy')₂(CO)(CH₂OH)]⁺ in the absence of Lewis bases

3.2.2.1 Generation of ethylene

Formation of the ylide complexes **2**²⁺ and **4**²⁺ implicate the intermediacy of a carbene complex. In an attempt to directly observe the carbene species, a protonation reaction of **1**⁺ with acid was conducted in the absence of a Lewis base stabilizing reagent while cooled in a dry ice/acetone bath. The solution of **1**⁺ and excess triflic acid was mixed at low temperature and

then inserted into an NMR spectrometer pre-cooled to $-70\text{ }^{\circ}\text{C}$. In the initial ^1H NMR spectrum taken at $-70\text{ }^{\circ}\text{C}$, no resonances were observed in the carbene complex region of the spectrum (i.e., downfield of $\delta\text{ }12\text{ ppm}$)^{119,123}, but two characteristic AA'XX' multiplets were observed in the ^1H NMR at $\delta\text{ }4.19$ and $\delta\text{ }4.52$ (Fig. 3.4). These new resonances are assigned to a coordinated ethylene ligand in complex $\mathbf{6}^{2+}$ (eq 3.7). Upon warming to room temperature, the resonances for the ethylene ligand disappear over time and a new resonance appears at $\delta\text{ }5.40$ corresponding to free ethylene.⁸⁹ Conducting the experiment at $-90\text{ }^{\circ}\text{C}$ in methylene chloride did not allow for direct observation of the intermediate carbene complex, unlike other reported ethylene-forming systems.^{74,76,91,92,119-123}



Equation 3.7: Production of C_2 product, ethylene (coordinated to Ru in $\mathbf{6}^{2+}$), by HOTf protonation of $\mathbf{1}^+$.

The multiplet pattern for $\mathbf{6}^{2+}$ could be simulated using coupling constants for the coordinated ethylene ligand of $^2J_{\text{geminal}} = 0\text{ Hz}$, $^2J_{\text{cis}} = 10.0\text{ Hz}$, and $^2J_{\text{trans}} = 20.0\text{ Hz}$; chemical shift equivalence of the *trans* pairs of protons indicates rapid rotation of the ethylene ligand, even at low temperature. These calculated coupling constants are very similar to those reported for free ethylene measured in a liquid crystal matrix ($^2J_{\text{geminal}} = 2.35\text{ Hz}$, $^2J_{\text{cis}} = 11.65\text{ Hz}$, and $^2J_{\text{trans}} = 19.01\text{ Hz}$), suggesting ethylene is a very weakly coordinated ligand.⁹⁰

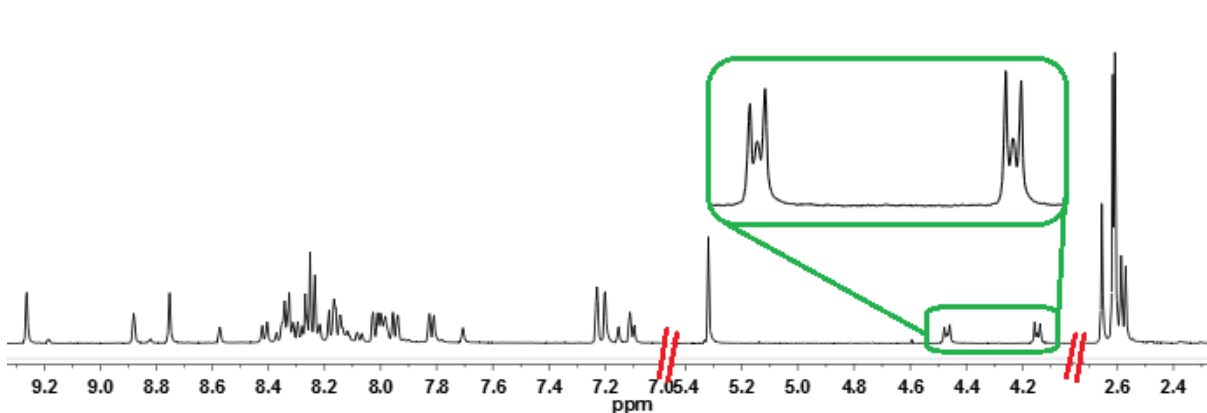
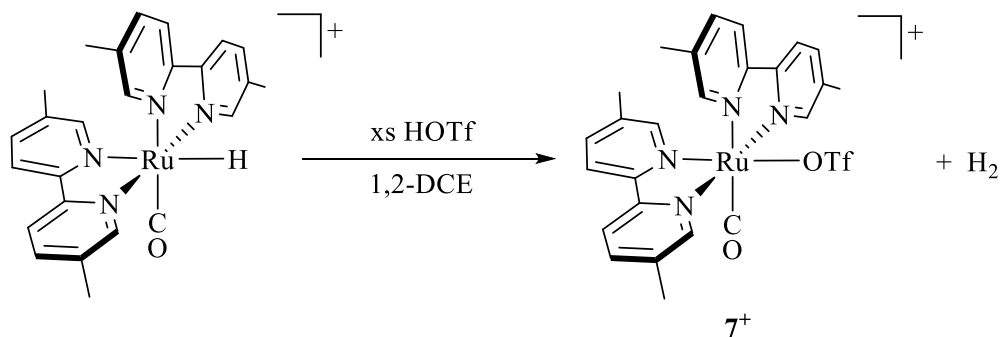


Figure 3.4: ^1H NMR of 6^{2+} $[\text{Ru}(\text{bpy}')_2(\text{CO})(\text{H}_2\text{C}=\text{CH}_2)]^{2+}$ formed under acidic conditions (zoomed in region highlights distinct coordinated ethylene resonances).

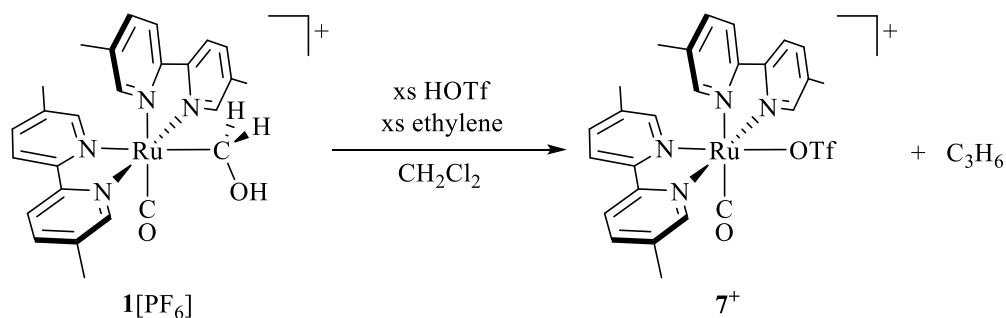
The formation of one ethylene molecule requires two methylene units, and the mass balance requires $[\text{Ru}(\text{bpy}')_2(\text{CO})(\text{OTf})]^+$ (7^+) as a co-product. In an independent experiment, 7^+ was prepared by protonation of $[\text{Ru}(\text{bpy}')_2(\text{CO})(\text{H})]^+$ in 1,2-dichloroethane by the addition of HOTf (eq 3.8). The observed ^1H NMR resonances in protonation of the ruthenium hydride with HOTf matches the proposed 7^+ resonances in HOTf protonation experiments forming 6^{2+} . Surprisingly, the triflate ligand of 7^+ is not very labile, requiring temperatures up to 70 °C in the presence of excess MeCN before partial substitution of the triflate was observed. The same ruthenium ethylene complex is observed using $[\text{H}(\text{OEt}_2)_2]\text{BAr}^{\text{F}}_4$ acid, however given the weakly coordinating counterion additional unidentified by-products are formed. Alternatively, using trityl cation formed half an equivalent of an unidentified ruthenium complex by-product (Appendix 2.1, Fig. A3.14).

To further probe the formation of an intermediate carbene complex, protonation of 1^+ with HOTf was conducted under an atmosphere of ethylene gas at -78 °C. This reaction cleanly generates 7^+ as well as cyclopropane, as identified by ^1H NMR spectroscopy with a resonance at δ 0.2 and ^{13}C NMR spectroscopy with a resonance at δ -3.0 (eq 3.9). Brookhart and others



Equation 3.8: Protonation of $[\text{Ru}(\text{bpy}')_2(\text{CO})\text{H}]^+$ using HOTf to form 7^+ , $[\text{Ru}(\text{bpy}')_2(\text{CO})(\text{OTf})]^+$.

observed similar reactivity using CpFe and other transition metal carbonyl methyldene complexes, where coupling to a variety of alkenes produces cyclopropanes.¹¹⁹⁻¹²³ The only ruthenium containing product observed was 7^+ , even at low temperatures. The integration of the cyclopropane singlet with respect to the signals for 7^+ indicates quantitative transfer of the ruthenium carbene to ethylene. The fact that no 6^{2+} is observed in this experiment also suggests that ethylene is a poor ligand for the ruthenium complex.



Equation 3.9: HOTf protonation of 1^+ under ethylene to form C₃ product, cyclopropane, and 7^+ .

3.2.2.2 Generation of ether-bridged ruthenium dimer complex

Reactions between hydroxymethyl 1^+ and the weak acid, triethylammonium hexafluorophosphate, take a different course than the reactions with strong acids.⁹³ The addition of a weak acid is not accompanied by a dramatic color change as for HOTf, and no ethylene

complex is observed in the ^1H NMR spectrum. Protonation proceeds slowly using $[\text{HNEt}_3]\text{PF}_6$ and required heating for several days to reach partial conversion. The same product is obtained instantaneously in the reaction of $\mathbf{1}[\text{PF}_6]$ with HNTf_2 acid. The lower solubility of HNTf_2 in methylene chloride reduces the concentration of acid in solution, which results in a course similar to reactions using weak acids. The resulting ^1H NMR spectrum from protonation with HNTf_2 is shown in Figure 3.5. Two resonances are observed between δ 3.7 and δ 4.0, which integrate in a 2:1 ratio with respect to each other. One is an apparent singlet and the second appears as an AB pattern. These resonances are in a similar region of the spectrum as the CH_2 signals for hydroxymethyl $\mathbf{1}^+$ and triphenylmethoxymethyl $\mathbf{5}^+$. In the bipyridine region of the spectrum, related sets of resonances are observed that integrate in a 2:1 ratio as shown in blue and green in Figure 3.5. This product was identified as an ether-bridged ruthenium dimer, $\mathbf{8}^{2+}$

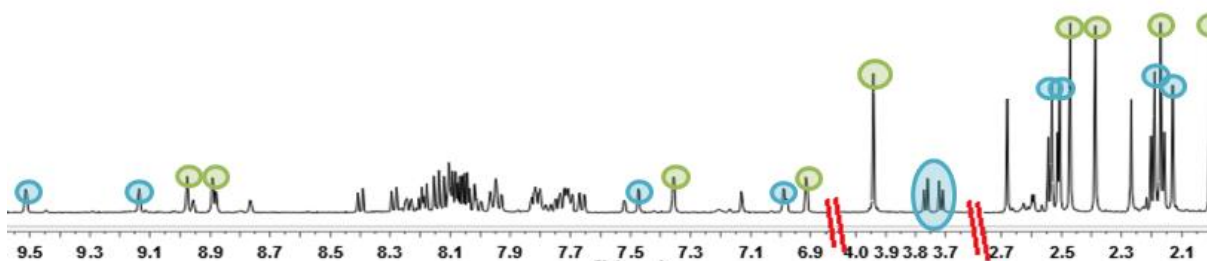
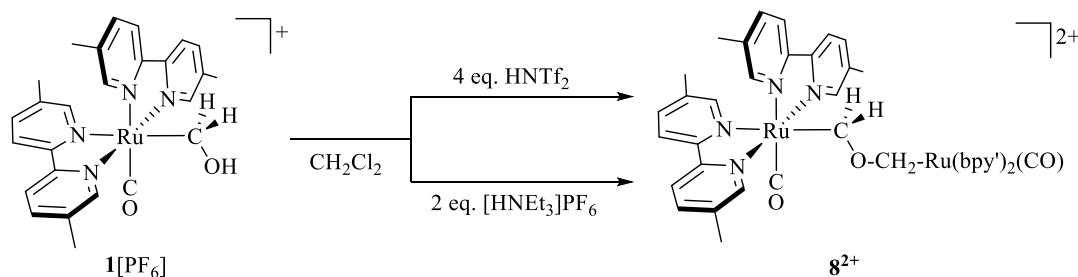


Figure 3.5: ^1H NMR of $\mathbf{8}^{2+}$ $[\text{Ru}(\text{CH}_2\text{OCH}_2)\text{Ru}]^{2+}$ dimer formed using excess HNTf_2 acid.

(eq 3.10), based on electrospray mass spectral analysis, which showed signals with a two-ruthenium isotope distribution pattern at mass-to-charge ratios of 520.07 $[\text{M}]^{2+}$, 1185.11 $[\text{M}+\text{PF}_6]^+$, and 1320.05 $[\text{M}+\text{NTf}_2]^+$. Casey previously observed an analogous ether-bridged dimer structure in the CpRe systems.⁷¹



Equation 3.10: Protonation reactions with partially soluble acid (HNTf₂ on top) and weak acid (HNET₃⁺ on bottom) to form ether-bridged dimer species, **8**²⁺.

In these reactions with weak or low-solubility acids, partial protonation of **1**⁺ produces the reactive intermediate carbene complex in a solution of predominantly **1**⁺. Formation of the bimetallic ether-bridged product **8**²⁺ presumably arises by reaction of the carbene complex with unreacted **1**⁺, followed by deprotonation. The formation of the ether-bridged dimer is not irreversible. The addition of HOTf to a solution of **8**²⁺ leads to the formation of ethylene complex **6**²⁺, indicated by the characteristic AA'XX' resonances observed downfield (Fig. 3.6).

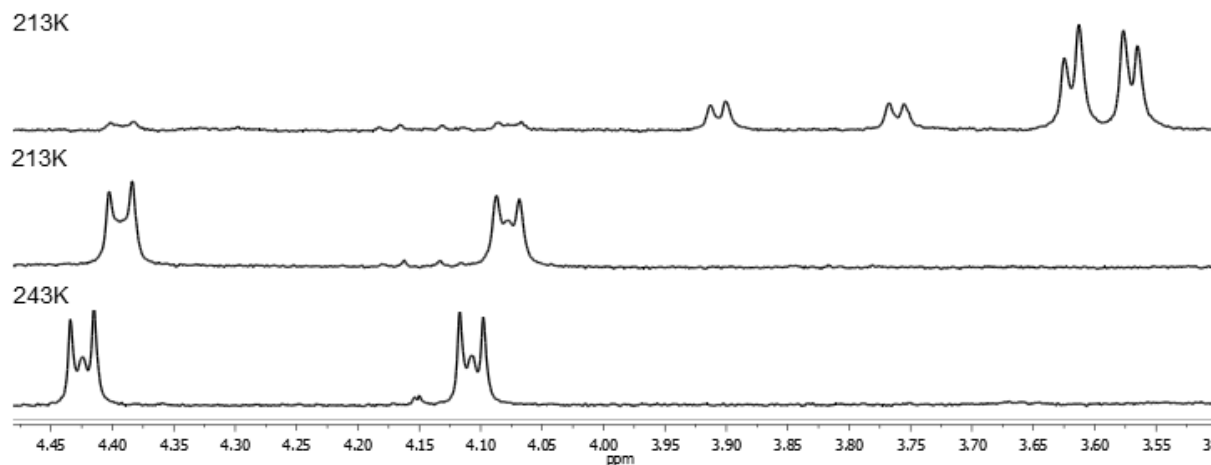


Figure 3.6: ¹H NMR of **8**²⁺ generated from HNTf₂ then added 1 eq. HOTf to form **6**²⁺ (from top to bottom: 213 K after addition of HNTf₂, then 213 K and 243 K after HOTf added).

The presence of two sets of resonances for the ether-bridged dimer is a result of the chirality of the ruthenium bis-bipyridine complexes. Coupling of these two chiral ruthenium complexes to form the ether-bridged complex results in four potential stereoisomers that fall into two

spectroscopically distinct sets: an enantiomer pair of C_2 symmetry (Δ,Δ and Λ,Λ isomers), and a *meso* pair of C_s symmetry (Δ,Λ and Λ,Δ). Insight into the pattern of resonances observed for the diastereotopic methylene groups is obtained from variable temperature ^1H NMR spectra of a protonation reaction using HNTf_2 (Fig. 3.7). As the temperature is decreased, the apparent

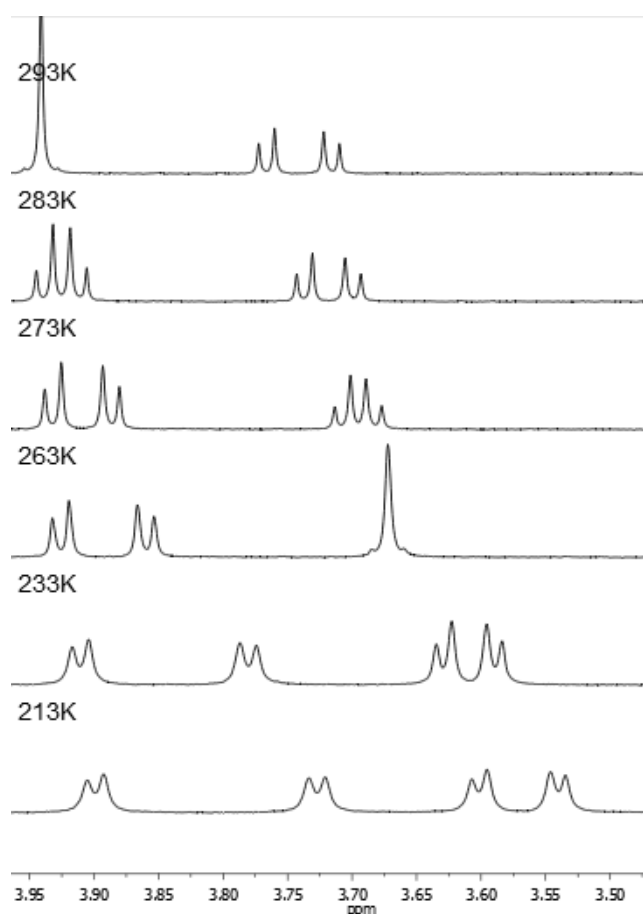


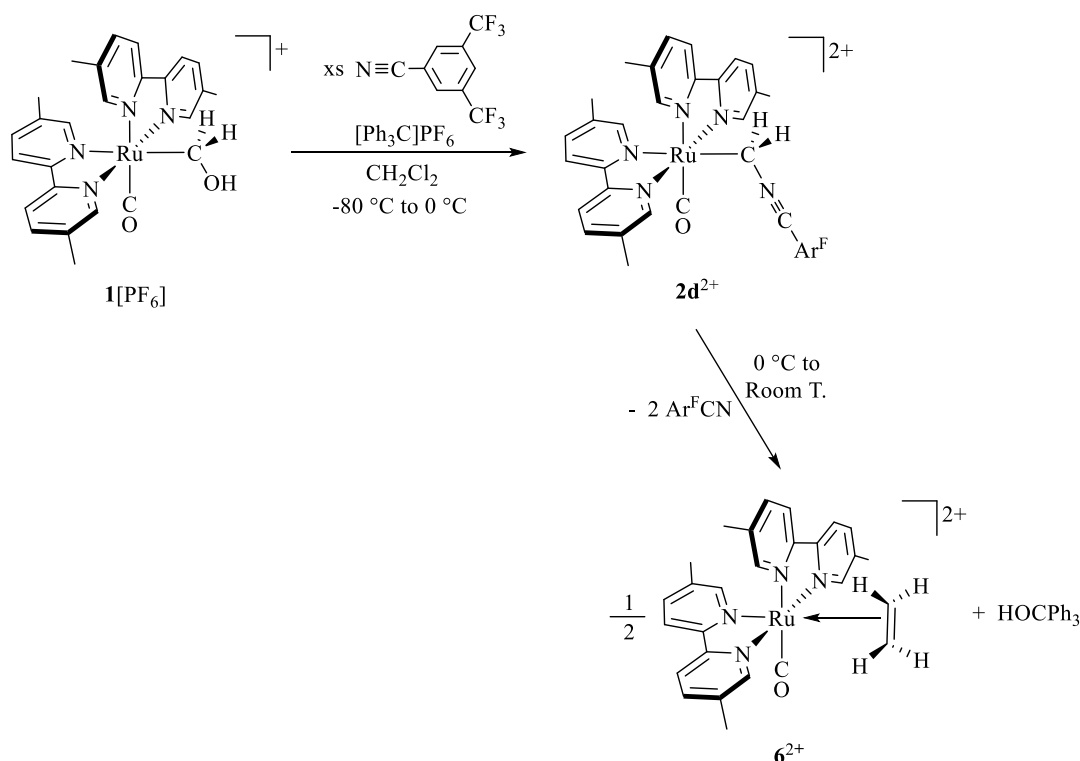
Figure 3.7: Variable temperature ^1H NMR of 8^{2+} formed using excess HNTf_2 acid.

singlet at δ 3.94 in the 293 K spectrum shows the expected AB pattern. The room temperature AB pattern for the second isomer centered at δ 3.74 is an apparent singlet in the 263 K spectrum. The chemical shift difference between the individual A and B resonances for each diastereotopic pair changes considerably with temperature, likely a result of changes in rotamer populations with temperature.

3.2.3 Decomposition of $[Ru(bpy')_2(CO)(CH_2L)]^{2+}$; ethylene forming reactions

Previously we noted the high lability of the nitrile ylide complexes 2^{2+} which hindered solid-state isolation of the complex. All nitrile ylide complexes decomposed under 24 h at room temperature. Depending on the nitrile stabilizing ligand for 2^{2+} complexes, different decomposition pathways were observed by 1H NMR spectroscopy.

The most informative decomposition reaction of a nitrile ylide was observed for $2d^{2+}$, with the electron deficient nitrile ligand, 1,3-(CF_3) $_2$ PhCN (Ar^F CN), prepared via the trityl cation route (eq 3.11). A series of spectra recorded at increasing temperatures are shown in Figure 3.8. In the



Equation 3.11: Hydroxide abstraction using trityl cation to form fluorinated-nitrile ylide, $2d^{2+}$, and its subsequent decomposition to ethylene complex, 6^{2+} , at higher temperatures.

203 K spectrum, the doublets corresponding to the ylide are observed at δ 4.19 and δ 3.58. As the temperature is raised above 253 K, resonances for the ethylene complex 6^{2+} first appear, and by 293 K, complete transformation to 6^{2+} has occurred and no ylide remains. The benzonitrile

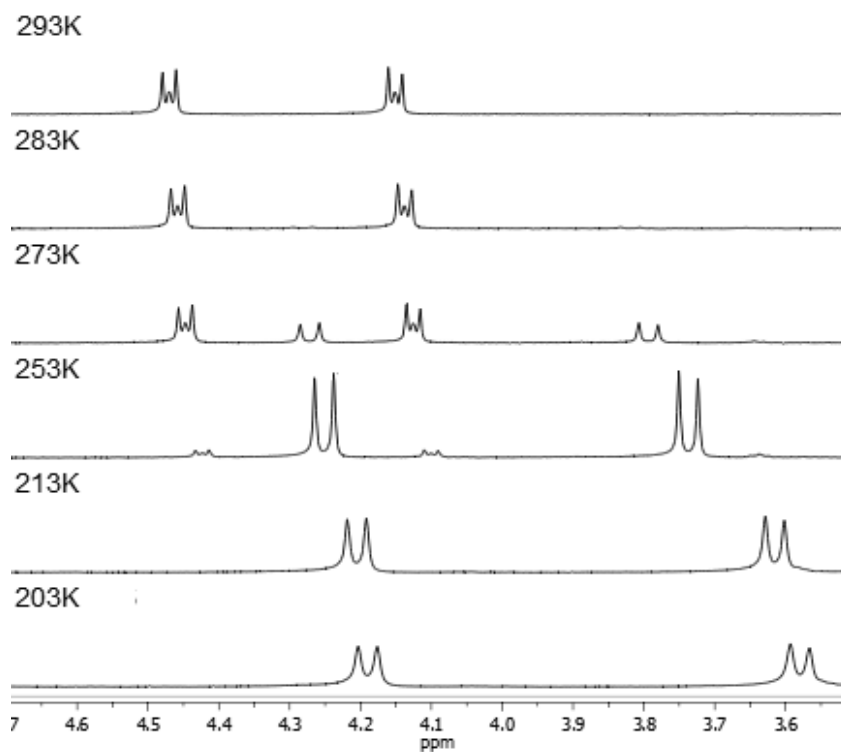


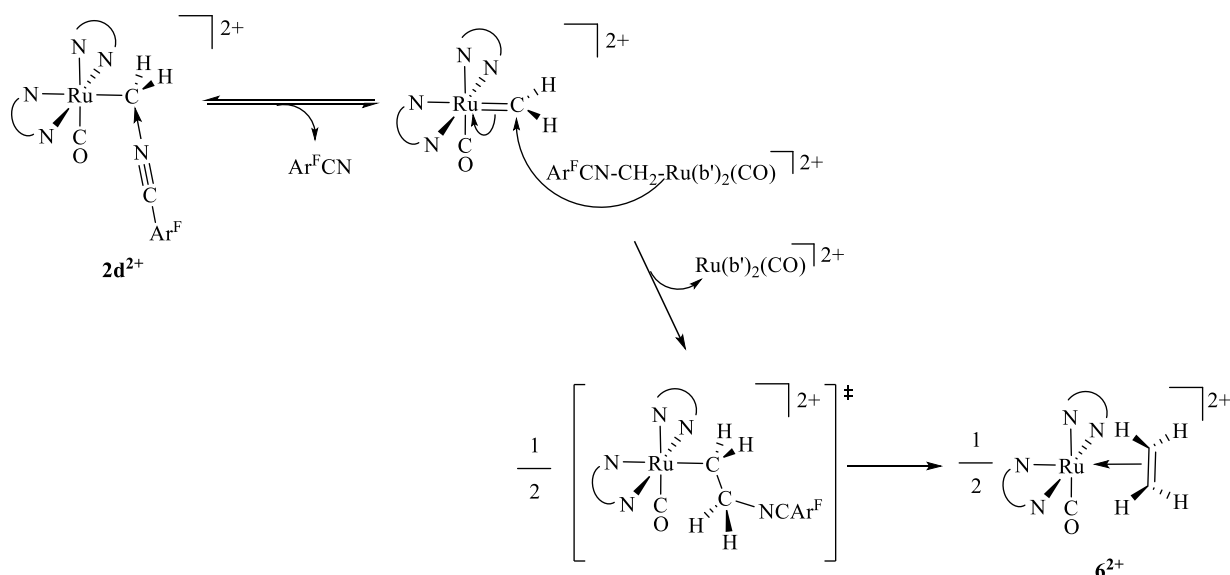
Figure 3.8: ^1H NMR of $\mathbf{6}^{2+}$ generated from decomposition of $\mathbf{2d}^{2+}$ (from bottom to top: 203 K, 213 K, 253 K where first see small resonances for downfield $\mathbf{6}^{2+}$, 273K, 283 K where $\mathbf{2d}^{2+}$ no longer observed, and 293K).

ylide, $\mathbf{2c}^{2+}$, displays analogous behavior. In contrast, the acetonitrile and propionitrile ylide complexes, $\mathbf{2a}^{2+}$ and $\mathbf{2b}^{2+}$, prepared by HOTf route, were found to be stable at room temperature over several hours in the presence of more than two equiv of acid. The ultimate fate of $\mathbf{2a}^{2+}$ and $\mathbf{2b}^{2+}$ is still under investigation, but the ethylene complex $\mathbf{6}^{2+}$ is not observed as a product for the cases of propionitrile and acetonitrile using either method. The metal product of the decomposition reaction in these cases was identified to be $[\text{Ru}(\text{bpy}')_2(\text{CO})(\text{NCR})]^{2+}$ by IR and ^1H NMR analysis.

The mechanism of ethylene formation in this system remains an area of active investigation. Formation of ethylene in previously reported systems has been proposed to take place by bimolecular coupling of two carbene ligands.^{71,72,75,119-123} The production of ethylene from the labile nitrile ylide, $\mathbf{2d}^{2+}$, suggests that in this case, the most likely pathway to ethylene is via

reaction of a free carbene complex, generated by nitrile loss, with the nitrile ylide **2d**²⁺ (Scheme 3.3.). This reaction can be described as an S_E² reaction, in which the coordinatively unsaturated ruthenium complex is the electrophile that leaves.

This same type of reaction mechanism may also be operative in the low temperature reaction of hydroxymethyl **1**⁺ with acids, in which the conjugate base of the acid may play a similar role. Such a Lewis-base assisted coupling pathway avoids the direct coupling of two electrophilic carbene ligands that display substantial positive charge at carbon.

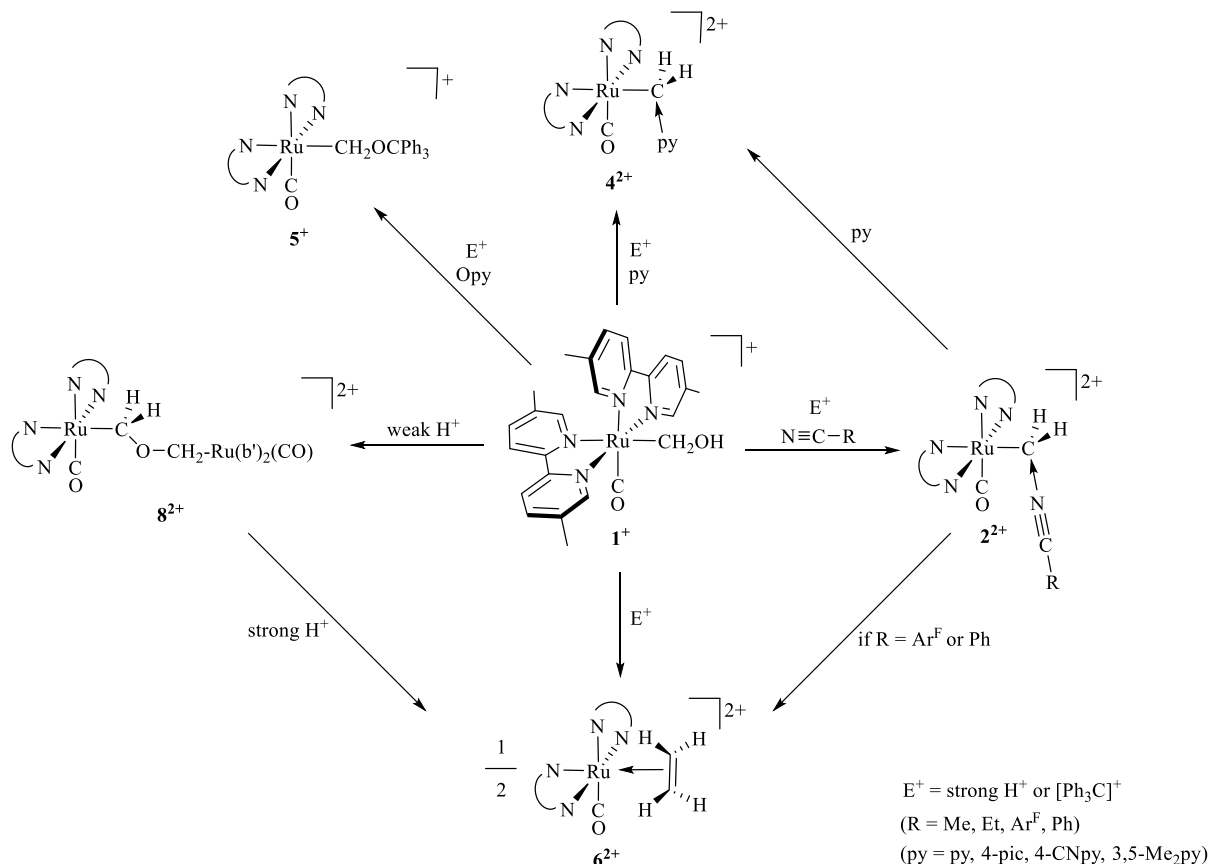


Scheme 3.3: Hypothesis for base-mediated carbene coupling to form ethylene.

3.3. Summary

All observed reactivity of **1**⁺ with electrophiles presented in this work is summarized in Scheme 3.4 below. We have shown the ruthenium hydroxymethyl, **1**⁺, reacts with electrophiles at the oxygen of the hydroxymethyl ligand. Although not directly observed, the resulting carbene complex can be stabilized and trapped using Lewis bases. The high electrophilicity of the carbene complex is demonstrated by formation of an adduct with acetonitrile, reactivity that has not been observed in other carbene or methyldene complex systems.^{72–76,119–123} The formation of

cyclopropane in reactions of 1^+ with electrophiles carried out under an ethylene atmosphere is also consistent with the intermediacy of an electrophilic carbene complex. The C_2 product,



Scheme 3.4: Summary of reactions of 1^+ (hydroxymethyl, center) with electrophiles forming 2^{2+} (nitrile-ylide), 4^{2+} (pyridine-ylide), 5^+ (triphenylmethoxymethyl), 8^{2+} (ether-bridged dimer) and 6^{2+} (ethylene) complexes.

ethylene, is formed via reactions of 1^+ with electrophiles in the absence of an added Lewis base, or by thermal decomposition of the labile nitrile ylides complexes, $2c^{2+}$ and $2d^{2+}$. The production of ethylene from these nitrile ylides complexes suggests that the C-C bond forming step takes place by reaction between the electrophilic carbene complex and the nitrile ylide complex, an S_E^2 reaction. While this chemistry is not directly linked to reactions of ruthenium polypyridyl complexes under electrocatalytic conditions for CO_2 reduction, the observed reaction chemistry provides insight into potential reaction pathways to C_2 products in these systems.

3.4. Experimental

General Methods

All methods were performed under an atmosphere of dry nitrogen using either standard Schlenk-line or glove box techniques, except where noted. Optima grade dichloromethane and acetonitrile solvents were dried through two columns of alumina and dispensed into Teflon-sealed schlenk flasks for storage. Solvents acetone, diethyl ether, ethanol (200 proof), and hexanes were purged with nitrogen gas and dried over 4Å molecular sieves. Solvents methanol and 1,2-dichloroethane were purchased dry from Sigma-Aldrich (Sure-Sealed under nitrogen gas) and used without further purification or drying. Deuterated dichloromethane and acetonitrile were stored over P₂O₅ to dry, “freeze-pump-thawed” to remove oxygen, and distilled prior to use. Acetonitrile, methylene chloride, and propionitrile were prepared as described for deuterated solvents when used in NMR and IR experiments. Reagents 1,3-bis(trifluoromethyl)benzonitrile, benzonitrile, and [H(OEt)]BF₄ (tetrafluoroboric acid) were stored in a Teflon-sealed Schlenk tube and “freeze-pump-thawed” to remove oxygen.

The reagents NaBH₄, 5,5'-dimethyl-2,2'-bipyridine, RuCl₃•xH₂O, paraformaldehyde, formic acid (88% or 99%), NH₄PF₆, and trityl hexafluorophosphate were all purchased and used without further purification. Starting material reagents polymer [RuCl₂(CO)₂]_n + dimer [RuCl₂(CO)₃]₂ mixture, Ru(5,5'-Me₂bpy)Cl₂(CO)₂, Ru(5,5'-Me₂bpy)(OTf)₂(CO)₂, and [H(OEt)₂]BAr^F₄ (tetrakis[3,5-bis(trifluoromethyl)phenyl]boronic acid) were prepared based on modified literature procedures.^{88,94,96} The reagents [Ru(5,5'-Me₂bpy)₂(CO)(H)][PF₆], [Ru(5,5'-Me₂bpy)₂(CO)(MeCN)][PF₆]₂, [Ru(5,5'-Me₂bpy)₂(CO)₂][PF₆]₂, and [Ru(5,5'-Me₂bpy)₂(CO)(CH₂OH)][PF₆] were prepared using modified literature methods outlined

below.^{47,88,94,97,98} Triethylammonium and pyridinium salts were prepared based on reported literature procedures.^{93,99}

¹H, ¹³C, and ¹⁹F NMR spectra were obtained on either a Bruker 400 MHz Nanobay or Bruker AVANCE III 600 MHz spectrometer with either QCI (four nucleus, inverse) or QNP (four nucleus, 2 channel) cryoprobe at standard parameter settings and calibrated pulse widths using Topspin 3 software. Variable temperature spectra were obtained on a Bruker AVANCE III 500 MHz spectrometer with BBI (inverse broadband, for ¹H experiments) or BBO (broad band observe, for ¹³C experiments) at standard parameter settings and calibrated pulse widths using Topspin 3 software. Probe temperature was monitored using a thermocouple just below the sample in the probe and readings were calibrated using a standard methanol sample. Spectra data are reported with ¹H and ¹³C chemical shifts in parts per million (ppm) and are referenced to residual solvent signals for the deuterated solvents.⁸⁹ Spectroscopic data are reported in the following manner: chemical shift (multiplicity [singlet (s), doublet (d), triplet (t), quartet (q), doublet of doublet (dd), doublet of triplet (dt), doublet of quartet (dq), multiplet (m), and broad resonance (br)], integration, assignment, *J*-coupling constants [in Hz]). NMR samples were prepared in 500 MHz NMR tubes fitted with rubber septa and sealed with parafilm in drybox under a nitrogen atmosphere. Samples were prepared by cannula transfer of solvent to the NMR tube. NMR samples for low temperature experiments were treated with the following basic procedure: The sample was cooled to -78 °C using a dry ice/acetone cold bath in a tall dewar fitted with foam lid used to keep NMR tube in place. The sample was monitored by NMR where the temperature was gradually increased by 10 °C intervals starting at -70 °C until reaching room temperature.

Infrared spectra were recorded on a Bruker ALPHA Fourier Transform IR spectrometer with universal sampling module QuickSnap Sampling attachment, using liquid sample cells with CaF₂ windows. Infrared band intensity is described in the following manner: strong (st), medium (m), weak (w), broad resonance (br). Operando IR experiments were conducted using a Mettler Toledo ReactIR 15 system with a silicon crystal fiber optic probe.

Direct infusion electrospray ionization mass spectroscopy analysis was conducted on Triple Q spectrometer using TriVersa Nanomate with Advion ESI chip. Samples were prepared using dried solvents. Data analysis was conducted using MassLynx software. Reported m/z measurements agree with calculated m/z values within ± 0.15 .

[Ru(5,5'-Me₂bpy)₂(CO)₂][PF₆]₂. To a mixture of [Ru(5,5'-Me₂bpy)(CO)₂(OTf)₂] (0.6837 g, 1.17 mmol) and 5,5'-Me₂bpy (0.4522 g, 2.45 mmol, 2.2 equiv), 60 mL of 200 proof ethanol was added. The pink-tinted cloudy mixture in ethanol gradually became a bright golden yellow solution upon heating. The reaction was refluxed for 90 min. The solution gradually darkened to golden orange. Removal of solvent gave a dark blue residue. The product was extracted from the residue with hot water, and the golden-yellow supernatant was separated from the residue by filtration. After concentration of the solution, addition of 6 equiv of NH₄PF₆ (1.005 g, 6.17 mmol) was added, and an immediate precipitate formed. The metathesis reaction was allowed to stir for 10 min before filtering to collect solids. The crude tan solid was purified by recrystallization from acetone/diethyl ether to give a white powder. Isolated yield: 0.6632 g (76.3%), Average isolated yield 71%. ¹H NMR (CD₂Cl₂, δ , ppm, 600 MHz): 2.28 (s, 6H, Me on Me₂bpy), 2.69 (s, 6H, Me on Me₂bpy), 7.14 (s, 2H, bpy on Me₂bpy), 8.00 (d, 2H, bpy on Me₂bpy, ³J_{HH} = 8.4 Hz), 8.24 (d, 2H, bpy on Me₂bpy, ³J_{HH} = 8.4 Hz), 8.27 (d, 2H, bpy on

Me₂bpy, $^3J_{\text{HH}} = 8.4$ Hz), 8.38 (d, 2H, bpy on Me₂bpy, $^3J_{\text{HH}} = 8.4$ Hz), 8.88 (s, 2H, bpy on Me₂bpy). IR (ATR solid, ν_{CO}): 2098 cm⁻¹ (st), 2046 cm⁻¹ (st).

[Ru(5,5'-Me₂bpy)₂(CO)(CH₂OH)][PF₆] (**1[PF₆]**). A sample of [Ru(5,5'-Me₂bpy)₂(CO)₂][PF₆]₂ (206.8 mg, 0.307 mmol) was dissolved in MeCN in a Schlenk flask. An 11 mL aqueous solution of NaBH₄ (208.0 mg, 5.50 mmol) was prepared in a separate Schlenk flask. Excess NaBH₄ (1.8 equiv = 1.1 mL of stock soln) was added to the MeCN solution of the ruthenium complex cooled to approximately -30 °C using a salt water/ice bath. The slightly yellow-tinted solution became bright yellow, then orange and finally a deep red color. The crude sample mixture was allowed to gradually warm to room temperature overnight. The reaction was shown to be complete by a single IR band at 1928 cm⁻¹. The solution was concentrated to an estimated quarter volume upon which a fine deep red solid crashed out of solution. The product was isolated by filtration and then washed with water and then Et₂O. Recrystallization from dichloromethane/diethyl ether yielded a bright orange-red powder that was stored in the glovebox. Isolated yield: 122.8 mg (71.9%), Average isolated yield 70%. ¹H NMR (CD₂Cl₂, δ , ppm, 500 MHz): 0.85 (t, 1H, OH in CH₂OH, $^3J_{\text{HH}} = 5.0$ Hz), 2.16, 2.19, 2.53, 2.57 (s, 3H, Me on Me₂bpy), 4.40, 4.52 (dd, 1H, CH₂ in CH₂OH, $^2J_{\text{HH}} = 7.0$ Hz, $^3J_{\text{HH}} = 5.0$ Hz), 7.03 (s, 1H, bpy on Me₂bpy), 7.43 (s, 1H, bpy on Me₂bpy), 7.74, 7.77, 7.83, 7.97 (d, 1H, bpy on Me₂bpy, $^3J_{\text{HH}} = 8.5$ Hz), 8.10 (m, 3H, bpy on Me₂bpy), 8.19, (d, 1H, bpy on Me₂bpy, $^3J_{\text{HH}} = 8.5$ Hz), 9.02 (s, 1H, bpy on Me₂bpy), 9.30 (s, 1H, bpy on Me₂bpy). IR (CH₂Cl₂, ν_{CO}): 1934 cm⁻¹. ESI-MS m/z (CH₃CN): 529.16.

[Ru(5,5'-Me₂bpy)₂(CO)(NCMe)][PF₆]₂. A solution of dry ONMe₃ (36.5 mg, 0.486 mmol, 1.2 equiv) in acetonitrile was added dropwise to a solution of [Ru(5,5'-Me₂bpy)₂(CO)₂][PF₆]₂ (0.330 g, 0.405 mmol) in 30 mL acetonitrile. The color changed from pale yellow to bright

yellow after the ONMe₃ addition. After stirring overnight, diethyl ether was added to precipitate a bright yellow solid, which was isolated by filtration, washed with diethyl ether, and dried under vacuum. Isolated yield: 268.5 mg (80%). ¹H NMR (CD₂Cl₂, δ, ppm, 400 MHz): 2.21, 2.26 (s, 3H, Me of Me₂bpy), 2.40 (s, 3H, Me of coordinated MeCN), 2.65, 2.69 (s, 3H, Me of Me₂bpy), 7.18, 7.24 (s, 1H, bpy on Me₂bpy), 7.85, 7.95 (d, 1H, bpy on Me₂bpy, ³J_{HH} = 10.5 Hz), 8.14 (“q”, 3H, bpy on Me₂bpy), 8.26 (“t”, 2H, bpy on Me₂bpy), 8.34 (d, 1H, bpy on Me₂bpy), 8.86, 9.03 (s, 1H, bpy on Me₂bpy). IR (CH₃CN, ν_{CO}): 2011 cm⁻¹.

[Ru(5,5'-Me₂bpy)₂(CO)(H)][PF₆]. An aqueous solution of NaBH₄ (24.1 mg, 0.637 mol, 2.3 equiv) was added dropwise to [Ru(bpy')₂(CO)(NCCH₃)](PF₆)₂ (0.278 g, 0.335 mmol) dissolved in 2:1 ethanol (200 proof): degassed H₂O, and stirred for 5 h. Over the course of the reaction, the yellow solution became a deep red color. The solution was concentrated to one-quarter of the original volume, resulting in precipitation of a fine red-brown solid, which was collected by filtration, washed with water, and dried under vacuum. Average isolated crude yield: 70 %. The product was further purified on an alumina column using 2:1 toluene:acetonitrile as eluent. The red and yellow product bands eluted first. The product was recrystallized from acetonitrile/water. Isolated yield for purified complex: 43.1 mg (20 %). ¹H NMR (d₄-1,2-DCE, δ, ppm, 500 MHz): -11.52 (s, 1H, H⁻ on Ru), 2.15, 2.20, 2.49, 2.50 (s, 3H, Me on Me₂bpy), 7.07 (s, 1H, bpy on Me₂bpy), 7.45 (s, 1H, bpy on Me₂bpy), 7.77 (t, 3H, bpy on Me₂bpy, ³J_{HH} = 6.4 Hz), 7.92 (d, 1H, bpy on Me₂bpy, ³J_{HH} = 8.4 Hz), 8.08 (t, 3H, bpy on Me₂bpy, ³J_{HH} = 8.0 Hz), 8.16 (d, 1H, bpy on Me₂bpy, ³J_{HH} = 8.4 Hz), 9.01 (s, 2H, bpy on Me₂bpy). FTIR (CH₃CN, ν_{CO}): 1933 cm⁻¹. ESI-MS *m/z* (CH₃CN): 499.00.

General procedure for low temperature NMR protonation of 1⁺ with strong acids in presence of Lewis bases. To a sample of 1[PF₆] (2.0 – 10.0 mg) around 5 – 10 equiv of dry

MeCN was added and the sample dissolved in CD₂Cl₂ (500 – 800 μ L). A stock solution of strong acid was prepared (between 150 and 300 mM). Approximately 2 – 20 equiv of the strong acid stock solution was slowly added via syringe to the sample cooled at -78 °C. Solution color changed from red to bright yellow/orange. This procedure was followed for a variety of aforementioned nitrile, pyridine, and/or acid reagents. Spectroscopic data for experiments forming **2**²⁺ are presented below. See later section on pyridinium and ammonium salt reactions for pyridine ylide, **4**²⁺, data.

¹H NMR for **2a**²⁺ (20 °C, CD₂Cl₂, δ , ppm, 500 MHz): 2.20 (s, 6H, Me on Me₂bpy), 2.33 (br t, 3H, Me on MeCN-ylide, ⁵*J*_{HH} = 3.0 Hz), 2.62, 2.63 (s, 3H, Me on Me₂bpy), 3.30 (dq, 1H, CH₂ on MeCN-ylide, ²*J*_{HH} = 13.5 Hz, ⁵*J*_{HH} = 3.0 Hz), 3.90 (dq, 1H, CH₂ on MeCN-ylide, ²*J*_{HH} = 13.5 Hz, ⁵*J*_{HH} = 3.0 Hz), 7.03 (s, 1H, bpy on Me₂bpy), 7.27 (s, 1H, bpy on Me₂bpy), 7.82, 7.91, 8.05 (d, 1H, bpy on Me₂bpy, ³*J*_{HH} = 8.5 Hz), 8.10 (d, 2H, bpy on Me₂bpy, ³*J*_{HH} = 8.0 Hz), 8.20, 8.23, 8.26 (d, 1H, bpy on Me₂bpy, ³*J*_{HH} = 8.0 Hz), 8.37 (s, 1H, bpy on Me₂bpy), 8.99 (s, 1H, bpy on Me₂bpy). IR (CH₂Cl₂, ν_{CO}): 1965 cm⁻¹.

¹H NMR for **2b**²⁺ (20 °C, CD₂Cl₂, δ , ppm): 1.19 (t, 3H, Me on EtCN-ylide, ³*J*_{HH} = 8.4 Hz), 2.20, 2.21 (s, 3H, Me on Me₂bpy), 2.60, 2.63 (s, 3H, Me on Me₂bpy), 3.47, 3.90 (dt, 1H, CH₂ on EtCN-ylide, ²*J*_{HH} = 13.5 Hz, ⁵*J*_{HH} = 2.5 Hz), 7.11, 7.26 (s, 1H, aromatic bpy'), 7.80, 7.90, 8.04, 8.07, 8.14, 8.26, 8.29, 8.36 (d, 1H, aromatic bpy'), 8.59, 8.97 (s, 1H, bpy on Me₂bpy), The CH₂ on coordinated EtCN is hypothesized to overlap with two of the bpy' Me groups around δ 2.62. See Figure A3.2 in Appendix 2.1 for full spectrum. IR (CH₂Cl₂, ν_{CO}): 1964 cm⁻¹.

¹H NMR for **2c**²⁺ (10 °C, CD₂Cl₂, δ , ppm): 2.18, 2.20, 2.41, 2.63 (s, 3H, Me on Me₂bpy), 3.80, 4.25 (d, 1H, CH₂ on PhCN-ylide, ²*J*_{HH} = 13.5 Hz), 8.62, 8.95 (s, 1H, bpy on Me₂bpy), 15H

bpy' resonances were observed between δ 7.2 and δ 8.4. The coordinated PhCN resonances were obscured by other products. See Figure A3.3 in Appendix 2.1 for full spectrum.

^1H NMR for 2d^{2+} ($-30\text{ }^\circ\text{C}$, CD_2Cl_2 , δ , ppm): 2.16, 2.18, 2.46, 2.60 (s, 3H, Me on Me_2bpy), 3.71, 4.24 (d, 1H, CH_2 on $\text{Ar}^{\text{F}}\text{CN}$ -ylide, $^2J_{\text{HH}} = 13.5\text{ Hz}$), 8.59 (s, 1H, bpy on Me_2bpy), 8.98 (s, 1H, bpy on Me_2bpy), 13H bpy' and coordinated $\text{Ar}^{\text{F}}\text{CN}$ resonances were overlapped in the region of δ 7.0 – δ 8.4. See Figure A3.4 in Appendix 2.1 for full spectrum.

^1H NMR for $[\text{CH}_3\text{NCCH}_3]^+$ ($20\text{ }^\circ\text{C}$, CD_2Cl_2 , δ , ppm, 500 MHz): 2.95 (m, 1H, Me on C end of nitrile, $^2J_{\text{NH}} = ^5J_{\text{HH}} = 2.5\text{ Hz}$), 3.87 (m, 3H, Me on N of nitrile, $^2J_{\text{NH}} = ^5J_{\text{HH}} = 2.5\text{ Hz}$).

Low temperature operando IR protonation of $1[\text{PF}_6]$ with MeCN under acidic conditions. A sample of $1[\text{PF}_6]$ (25.0 mg, 0.037 mmol) was added to a Schlenk tube sealed with a custom adaptor designed to fit an IR probe. A second schlenk tube of 2.0 mL dichloromethane with added 10 μL of acetonitrile was prepared. The solvent solution was transferred into the schlenk tube of ruthenium solids via cannula transfer to dissolve the starting material. Sample solution was then cooled in a dry ice/acetone cold bath to $-78\text{ }^\circ\text{C}$. A 371 mM stock solution of HOTf in CH_2Cl_2 was prepared by addition of 30 μL of neat HOTf to 870 μL of CH_2Cl_2 . Slowly, an estimated 3.0 equiv of HOTf stock solution (300 μL , 0.11 mmol) was added via syringe to sample. Sample was monitored by IR at low temperature for 13 min before removing cold bath and warming to room temperature. A bright yellow solution was formed upon reaction with HOTf.

General procedure for ^1H NMR protonation experiments of $1[\text{PF}_6]$ with pyridinium or ammonium salts. A sample of $1[\text{PF}_6]$ (2.0 – 5.0 mg) was dissolved in CD_2Cl_2 (400 – 800 μL). In a separate NMR tube the salt was added (2.0 – 3.0 equiv). The ruthenium solution was then cannula transferred into the tube of solid salt and sonicated to mix, then centrifuged. A bright

orange or yellow solution with fine white precipitate was observed. For weaker acids refluxing between 5 – 10 min in water bath at up to 70 °C was required to observe further conversion to product by ^1H NMR. Final solution color appeared light yellow. Spectroscopic data for experiments forming $\mathbf{4}^{2+}$ are presented below. See below section on protonation with HNTf₂ for spectroscopic results on formed $\mathbf{8}^{2+}$ from using salt [HNEt₃]PF₆ via this method.

^1H NMR of $\mathbf{4a}^{2+}$ (20 °C, CD₂Cl₂, δ , ppm, 500 MHz): 2.15, 2.28, 2.37, 2.66 (s, 3H, Me on Me₂bpy), 4.80 (d, 1H, CH₂ on py-ylide, $^2J_{\text{HH}} = 10.0$ Hz), 5.52 (d, 1H, CH₂ on py-ylide, $^2J_{\text{HH}} = 10.0$ Hz), 7.16 (s, 1H, bpy on Me₂bpy), 7.21 (s, 1H, bpy on Me₂bpy), 7.38 (t, 2H, coordinated py), 7.77, 7.82 (d, 1H, bpy on Me₂bpy, $^3J_{\text{HH}} = 8.5$ Hz) 7.88 (m, 3H, bpy on Me₂bpy overlapped with coordinated py resonance), 7.91 (d, 1H, bpy on Me₂bpy, $^3J_{\text{HH}} = 8.5$ Hz), 8.10 (dd, 3H, bpy on Me₂bpy overlapped with coordinated py resonance, $^3J_{\text{HH}} = 8.0$ Hz), 8.18, 8.25 (d, 1H, bpy on Me₂bpy, $^3J_{\text{HH}} = 8.0$ Hz), 8.41 (s, 1H, bpy on Me₂bpy), 8.51 (s, 1H, bpy on Me₂bpy). IR (CH₂Cl₂, ν_{CO}): 1955 cm⁻¹. IR (ATR, ν_{CO}): 1949 cm⁻¹ (br). ESI-MS m/z (CH₂Cl₂): 736.12 ($z = 1$, $^-\text{PF}_6$) and 295.58 ($z = 2$).

^1H NMR for $\mathbf{4b}^{2+}$ (20 °C, CD₂Cl₂, δ , ppm, 500 MHz): 2.19, 2.30 (s, 3H, Me on Me₂bpy), 2.40 (s, 3H, Me on coordinated 4-Mepy), 2.42, 2.69 (s, 3H, Me on Me₂bpy), 4.71, 5.47 (d, 1H, CH₂ on 4-Mepy-ylide, $^2J_{\text{HH}} = 10$ Hz), 7.19, 7.20 (s, 1H, bpy on Me₂bpy, partially overlapping with coordinated 4-Mepy aromatic resonance), 7.21 (m, 2H, aromatic on coordinated 4-Mepy), 7.70 (d, 2H, aromatic on coordinated 4-Mepy), 7.81, 7.87, 7.95 (d, 1H, bpy on Me₂bpy), 8.14 (m, 4H, bpy on Me₂bpy), 8.22, 8.29 (d, 1H, bpy on Me₂bpy, $^3J_{\text{HH}} = 8.0$ Hz), 8.47, 8.52 (s, 1H, bpy on Me₂bpy). See Figure A3.6 in Appendix 2.1 for full spectrum. IR (CH₂Cl₂, ν_{CO}): 1953 cm⁻¹.

^1H NMR for **4c**²⁺ (20 °C, CD₂Cl₂, δ , ppm, 500 MHz): 2.09 (s, 6H, 2Me on coordinated 3,5-Me₂py), 2.15, 2.29, 2.45, 2.66 (s, 3H, Me on Me₂bpy), 4.76, 5.39 (d, 1H, CH₂ on 3,5-Me₂py-ylide, $^2J_{\text{HH}} = 10$ Hz), 7.19, 7.32 (s, 1H, bpy on Me₂bpy), 7.38 (s, 2H, aromatic on coordinated 3,5-Me₂py), 7.46 (s, 1H, bpy on Me₂bpy), 7.76, 7.86, 7.89 (d, 1H, bpy on Me₂bpy, $^3J_{\text{HH}} = 8.0$ Hz), 8.07 – 8.16 (m, 5H, bpy on Me₂bpy) 8.56, 8.64 (s, 1H, bpy on Me₂bpy). See Figure A3.7 in Appendix 2.1 for full spectrum. IR (CH₂Cl₂, ν_{CO}): 1952 cm⁻¹.

^1H NMR for **4d**²⁺ (20 °C, CD₂Cl₂, δ , ppm, 500 MHz): 2.15, 2.27, 2.46, 2.66 (s, 3H, Me on Me₂bpy), 4.89, 5.66 (d, 1H, CH₂ on 4CNpy-ylide, $^2J_{\text{HH}} = 9.0$ Hz), 7.14, 7.21 (s, 1H, bpy on Me₂bpy), 7.60 (m, 1H, py on coordinated 4CNpy), 7.77, 7.86, 7.92 (d, 1H, bpy on Me₂bpy, $^3J_{\text{HH}} = 8.0$ Hz), 8.10 (m, 5H, bpy on Me₂bpy and coordinated 4CNpy), 8.20, 8.16, 8.25 (d, 1H, bpy on Me₂bpy, $^3J_{\text{HH}} = 8.5$ Hz), 8.52, 8.59 (s, 1H, bpy on Me₂bpy). IR (CH₂Cl₂, ν_{CO}): 1965 cm⁻¹. See Figure A3.8 in Appendix 2.1 for full spectrum (note that free 4-cyanopyridine observed in the spectrum at δ 7.55 and δ 8.80). IR (CH₂Cl₂, ν_{CO}): 1965 cm⁻¹.

Low temperature NMR Protonation of 1[PF₆] using HOTf: formation of 6²⁺. An analogous procedure for formation of **2a**²⁺ via HOTf as outlined above was followed using **1**[PF₆] (3.2 mg, 0.0048 mmol) and 2.3 equiv of HOTf (0.0112 mmol) in 600 μL CD₂Cl₂. The sample was stirred slowly with a 2 mm glass rod at low temperature. A bright yellow solution was formed upon reaction with HOTf. ^1H NMR for **6**²⁺ (20 °C, CD₂Cl₂, δ , ppm, 500 MHz): 2.24, 2.27, 2.61, 2.62 (s, 3H, Me on Me₂bpy), coordinated C₂H₄ (AA'XX' due to rotation): 4.19, 4.52 (m, 2H, calculated $^2J_{\text{HH cis}} = 0$ Hz, $^3J_{\text{HH cis}} = 10.0$ Hz, $^3J_{\text{HH trans}} = 20.0$ Hz), 7.79 (s, 1H, bpy on Me₂bpy), 8.10, 8.33, 8.42, 8.48 (d, 1H, bpy on Me₂bpy, $^3J_{\text{HH}} = 8.0$ Hz), 8.61 (s, 1H, bpy on Me₂bpy), 8.93 (s, 1H, bpy on Me₂bpy) unreported 5H bpy resonances overlapped with other

products between 8.2 – 8.4. ^1H NMR for by-product 7^+ reported in following procedure. Analogous procedures were followed using acids $[\text{H}(\text{OEt}_2)_2]\text{BAr}^{\text{F}}_4$ and $[\text{H}(\text{OEt}_2)]\text{BF}_4$.

Room Temperature NMR Protonation of $[\text{Ru}(5,5'\text{-Me}_2\text{bpy})_2(\text{CO})(\text{H})][\text{PF}_6]$ using strong acid, HOTf: formation of 7^+ . A sample of $[\text{Ru}(5,5'\text{-Me}_2\text{bpy})_2(\text{CO})(\text{H})][\text{PF}_6]$ (1.5 mg, 0.0023 mmol) was added to NMR tube and dissolved using 500 μL d_4 -1,2-dichloroethane (d_4 -1,2-DCE). A 226 mM stock solution of HOTf in d_4 -1,2-DCE was prepared by addition of 2 μL of neat HOTf to 100 μL of d_4 -DCE. Slowly, an estimated 2.5 equiv of HOTf stock solution (25 μL , 0.0023 mmol) was slowly added via syringe to the sample. The sample was gently agitated to mix and an immediate color change from golden yellow-orange to a brighter yellow was observed. ^1H NMR for 7^+ (20 $^\circ\text{C}$, CD_2Cl_2 , δ , ppm, 500 MHz): 2.18, 2.25, 2.61, 2.62 (s, 3H, Me on Me_2bpy), 7.21, 7.25 (s, 1H, bpy on Me_2bpy), 7.81, 7.95, 8.02, 8.14 (d, 1H, bpy on Me_2bpy , $^3J_{\text{HH}} = 8.5$ Hz), 8.24 (t, 3H, bpy on Me_2bpy), 8.30 (d, 1H, bpy on Me_2bpy , $^3J_{\text{HH}} = 8.5$ Hz), 8.76, 9.26 (s, 1H, bpy on Me_2bpy). $^{13}\text{C}\{^1\text{H}\}$ (25 $^\circ\text{C}$, CD_2Cl_2 , δ , ppm, 151 MHz): 18.74, 18.99, 19.01, 19.23 (Me on Me_2bpy), 123.22, 123.51, 123.68, 123.99, 124.15, 139.19, 139.22, 139.62, 140.69, 140.89, 141.46, 141.78, 148.35, 152.12, 152.71, 153.27, 154.09, 154.55, 155.39, 156.93, 198.15 (CO). IR (CH_2Cl_2 , ν_{CO}): 2001 cm^{-1} . IR (CH_3CN , ν_{CO}): 1997 cm^{-1} .

General procedure for NMR reaction of trityl cation with 1^+ in the presence of Lewis bases. A sample of $1[\text{PF}_6]$ (2.0 – 10.0 mg) and Lewis base reagent (5.0 – 10.0 equiv) were dissolved in CD_2Cl_2 (500 – 800 μL). A second NMR tube of $[\text{Ph}_3\text{C}]\text{PF}_6$ (0.9 – 1.5 equiv) was prepared and both tubes were cooled in ice water cold bath. While cold, the ruthenium sample solution was cannula transferred into the tube of trityl solids and shaken. The reaction solution became a bright yellow or orange color. The reaction was analyzed at room temperature by ^1H NMR. This procedure was followed for a variety of aforementioned nitrile and pyridine reagents.

Spectroscopic data for experiments forming 2^{2+} and 4^{2+} are presented above following procedures using strong acid and salt reagents, respectively. Spectroscopic data for using pyridine N-oxide under these conditions to form 5^{+} are presented below.

^1H NMR for 5^{+} (CD_2Cl_2 , δ , ppm, 500 MHz): 2.11, 2.20, 2.35, 2.54 (s, 3H, Me on Me_2bpy), 3.63, 3.67 (d, 1H, CH_2 on CH_2OCPh_3 , $^2J_{\text{HH}} = 5.0$ Hz), 6.92, 7.46 (s, 1H, bpy on Me_2bpy), 7.73 (m, 3H, Ph on CH_2OCPh_3), 7.82, 7.91, 8.05 (d, 2H, bpy on Me_2bpy , $^3J_{\text{HH}} = 7.0$ Hz), 8.04 (d, 2H, bpy on Me_2bpy , $^3J_{\text{HH}} = 7.0$ Hz), 8.09 (m, 3H, Ph on CH_2OCPh_3), 8.16 (d, 2H, bpy on Me_2bpy , $^3J_{\text{HH}} = 8.0$ Hz), 8.72, 9.06 (s, 1H, bpy on Me_2bpy). IR (CH_2Cl_2 , ν_{CO}): 1936 cm^{-1} . ESI-MS m/z (CH_2Cl_2): 771.23 ($z = 1$).

Lewis base exchange reaction of 2a^{2+} with pyridine to form 4a^{2+} . Complex 2a^{2+} was prepared as described previously using $[\text{Ph}_3\text{C}]\text{PF}_6$ in CD_2Cl_2 . A bright yellow solution formed in the NMR tube was confirmed to be 2a^{2+} . Then pyridine (2.0 μL , 5.0 equiv) was added at $0\text{ }^\circ\text{C}$ and shaken to mix. An immediate color change from bright yellow to bright orange occurred. NMR analysis confirmed displacement of MeCN for pyridine giving 4a^{2+} .

Reaction of trityl cation with 1^{+} under an ethylene atmosphere. The same general procedure was followed as with Lewis base reactions outlined previously, except the solution was purged with ethylene gas for 60 seconds at room temperature before addition to the sample of $[\text{Ph}_3\text{C}]\text{PF}_6$. The NMR reaction was mixed by purging the sample with ethylene gas while submerged in the ice bath. The solution color changed from orange-red to bright orange while cold, then to bright yellow at room temperature. ^1H NMR for unidentified product **9** ($20\text{ }^\circ\text{C}$, CD_2Cl_2 , δ , ppm, 500 MHz): 2.18, 2.24, 2.62, 2.63 (s, 3H, Me on Me_2bpy), 8.78, 9.19 (s, 1H, bpy on Me_2bpy), unreported 10H bpy resonances obscured by other products between 7.1 – 7.4 and 7.7 – 8.4 for bpy resonances. Cyclopropane (C_3H_6) observed as singlet at 0.24 ppm (6H).

Reaction of trityl cation with 1^+ without Lewis base trapping ligand. An analogous procedure for formation of $2a^{2+}$ (outlined above) was followed using 2.2 mg of $1[PF_6]$ (0.0033 mmol) and 1.6 mg of $[Ph_3C]PF_6$ (1.3 equiv) in 500 μ L of CD_2Cl_2 at $-78\text{ }^\circ\text{C}$ (acetone/dry ice bath). At room temperature the NMR tube contained a bright yellow solution. 1H NMR of 6^{2+} ($20\text{ }^\circ\text{C}$, CD_2Cl_2 , δ , ppm, 500 MHz): 2.23, 2.26, 2.59, 2.61 (s, 3H, Me on Me_2bpy), coordinated C_2H_4 (AA'XX' pattern related by rotation): 4.15, 4.47 (m, 2H, calculated $^2J_{HH\text{ cis}} = 0\text{ Hz}$, $^3J_{HH\text{ cis}} = 10.0\text{ Hz}$, $^3J_{HH\text{ trans}} = 20.0\text{ Hz}$), 7.70, 8.79, 9.17 (s, 1H, bpy on Me_2bpy) unreported 9H bpy resonances overlapped with other products between 7.1 – 7.4 and 7.8 – 8.4. 1H NMR for unidentified product 9 given in above procedure for reaction of 1^+ with trityl cation under ethylene gas.

Low temperature NMR Protonation of $1[PF_6]$ using HNTf₂: formation of 8^{2+} . An analogous procedure for formation of $2a^{2+}$ via HOTf as outlined above was followed using $1[PF_6]$ (3.6 mg, 0.0053 mmol) and 4.4 equiv of HNTf₂ (0.0231 mmol) in 600 μ L CD_2Cl_2 . The sample was stirred slowly with a thin gauge Cu(s) wire at low temperature. The solution appeared more brightly colored upon addition of acid. Key resonances in 1H NMR for 8^{2+} isomer 1: (CD_2Cl_2 , δ , ppm, 500 MHz): 2.01, 2.17, 2.39, 2.47 (s, 3H, Me on Me_2bpy), 3.95 (s, 4H, CH_2 of ether bridge), 6.92, 7.36, 8.90, 8.98 (s, 1H, bpy on Me_2bpy), unreported 8H bpy resonances overlapped with other products between 7.6 – 8.5. Key resonances in 1H NMR for 8^{2+} isomer 2: 2.13, 2.19, 2.50, 2.53 (s, 3H, Me on Me_2bpy), 3.72, 3.78 (d, 2H, CH_2 of ether bridge, $^2J_{HH} = 5.5\text{ Hz}$), 7.00, 7.47, 9.13, 9.51 (s, 1H, bpy on Me_2bpy), unreported 8H bpy resonances overlapped with other products between 7.6 – 8.5. ESI-MS m/z (CH_3CN): 520.07 ($z = 2$), 1185.11 ($z = 1$, PF_6), 1320.05 ($z = 1$, NTf_2).

X-ray structure determination of 5[PF₆]. Crystallographic data and experimental parameters are summarized in Table 3.2 below. Crystals suitable for X-ray diffraction were obtained from layering NMR sample reaction with approximately 1 mL of Et₂O. A single bright orange crystal was mounted in oil and kept at 100 K using a stream of N₂ during data collection. An X-ray structure was obtained using a Bruker Apex II CCD based X-ray diffractometer system equipped with a Cu-target X-ray tube ($\mu(\text{CuK}\alpha) = 5.066 \text{ mm}^{-1}$). Structure was solved using olex2 software with olex2.solve structure solution program using Charge Flipping and refined with XL refinement package using Least Squares minimization.^{63,64,66} Complete crystallographic data can be found in Appendix 2.2.

Table 3.2: Crystallographic Parameters for
[Ru(5,5'-Me₂bpy)₂(CO)(CH₂OCPPh₃)] [PF₆] \cdot CH₂Cl₂, 5⁺

Formula weight	1000.78
temp, K	100
space group	P2 ₁ /c
a, Å	16.2910(10)
b, Å	14.9484(10)
c, Å	18.5327(12)
α , °	90
β , °	108.149(3)
γ , °	90
V, Å ³	4288.6(5)
Z	4
ρ_{calc} , mg/mm ³	1.550

3.5. Acknowledgements

We acknowledge Dr. Peter White for x-ray crystallography and Dr. Marc ter Horst for NMR consultation. Prof. Maurice S. Brookhart, Prof. Joeseeph Templeton, and Dr. Christopher Turlington are acknowledged for assistance with low temperature NMR experimental set up. We

also acknowledge undergraduate researcher, Bennett Vass, for synthesis of $[\text{Ru}(\text{bpy})_2(\text{CO})_2]^{2+}$ and its associated starting materials. We further acknowledge undergraduate researcher, Ian Mercer, for synthesis of $[\text{Ru}(\text{bpy}')_2(\text{CO})\text{H}]^+$. Prof. Cynthia K. Schauer is also acknowledged for computational analysis of $[\text{Ru}(\text{bpy})(\text{CO})(\text{CH}_2\text{OH})]^+$.

CHAPTER 4

SYNTHESIS OF CARBON DIOXIDE REDUCTION INTERMEDIATE RUTHENIUM BENZIMIDAZOL-2-YLIDENE CARBONYL COMPLEXES

4.1. Introduction and Background

The reduction of CO₂ to CO is one of the most accessible transformations of CO₂ to a useful product. Tanaka's [Ru(bpy)(tpy)(Solv)]²⁺ complex, where Solv represents the solvent ligands (water or acetonitrile) is an effective catalyst for this reductive disproportionation of CO₂.^{45,47} Previous reports by the Meyer group have demonstrated an improvement in the rate of carbon dioxide reduction to carbon monoxide by the use of ruthenium polypyridyl complexes incorporating a carbene-pyridine bidentate ligand, 3-methyl-1-pyridylbenzimidazol-2-ylidene (Mebim-py).^{17,82} The carbene complex [Ru(Mebim-py)(tpy)(Solv)]²⁺ exhibited a rate of electrocatalytic carbon monoxide formation three-fold higher than [Ru(bpy)(tpy)(Solv)]²⁺.¹⁷ Figure 4.1 outlines the proposed catalytic mechanism for CO₂ reduction for ruthenium terpyridine (tpy) complexes where LL' represents either bidentate ligand NHC pyridyl (Mebim-py) or bipyridine (bpy).

Entry into the catalytic cycle is preceded by two-electron reduction of [(tpy)(LL')Ru(Solv)]²⁺. Computational analysis using Density Functional Theory shows the LUMO to be centered primarily on the tpy ligand, thus the Ru center remains formally at the 2+ oxidation state. Upon loss of solvent, the electrons in the tpy-based orbital are shared with the metal that is the site of reaction with CO₂. The HOMO of five-coordinate [Ru(tpy)(LL')]⁰, which

The proposed mechanism relies on electrochemical studies, and few synthetic studies have been conducted to prepare proposed intermediates in the catalytic cycle and independently examine their voltammetric behavior. Computational studies have highlighted one particular feature in the $[\text{Ru}(\text{Mebim-py})(\text{tpy})(\text{Solv})]^{2+}$ system that may play a role in catalytic performance. As shown in the top of Figure 4.3, there are two isomers that differ in the ligand *trans* to the

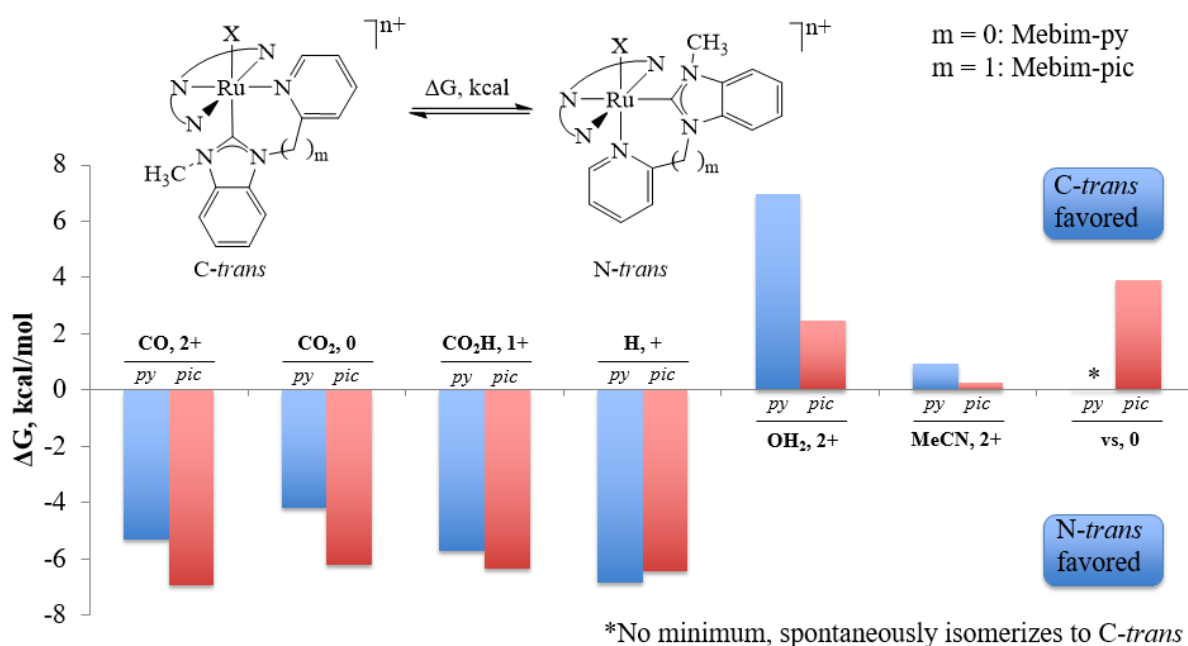


Figure 4.3: Free energy change of isomerization for $[\text{Ru}(\text{tpy})(\text{Mebim-L})\text{X}]^{n+}$ complexes (where L = py for pyridine or pic for picoline; X = CO, CO₂, CO₂H, H, H₂O, MeCN or vacant site (vs); and n = 0, 1, 2) (Duffee, Schauer, Muckerman, 2016).

catalytic site, *C-trans* and *N-trans*. The second ligand system, with a methylene spacer between the carbene and the pyridine ligand is discussed in more detail below. The chart in Figure 4.3 shows the free energy for the *C-trans* to *N-trans* isomerization as a function of ligand X. For H₂O, the *C-trans* isomer is preferred, the acetonitrile complex shows no preference for the *trans* ligand, while CO, CO₂, CO₂H, and H favor the *N-trans* isomer (Fig. 4.3). With regard to the catalytic cycle, of particular interest is that independent of the starting point, the carbene is the preferred *trans* ligand to the vacant site in the five-coordinate $[\text{Ru}(\text{Mebim-py})(\text{tpy})]^{0}$

intermediate, which is the active catalytic species that will coordinate CO₂ (Fig. 4.3). In this work we seek to probe the catalytic cycle by independent synthesis of the carbonyl complex, [Ru(Mebim-py)(tpy)(CO)]²⁺ (**4a**), and the analogous carbene-pyridine ligand with a methylene spacer (3-methyl-1-picolybenzimidazol-2-ylidene or Mebim-pic), to gain insight into the role isomer preferences play in the catalytic reaction (Figure 4.4).

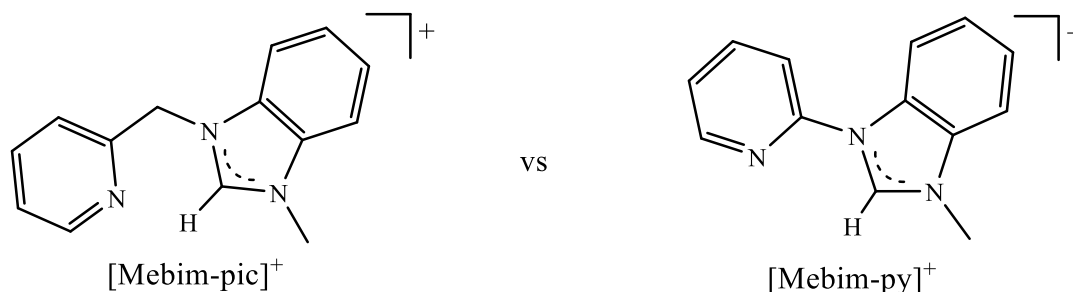


Figure 4.4: Ligands of interest to this work, 3-methyl-1-picolybenzimidazol-2-ylidene (left) and 3-methyl-1-pyridylbenzimidazol-2-ylidene (right).

The Ru(Mebim-pic)(tpy) complex is expected to have comparable reactivity to Mebim-py based on computational studies (Duffee and Schauer, 2016). The introduction of a methylene spacer between the carbene and the pyridine ligands will have both steric and electronic consequences. The carbene ligand in Mebim-pic is anticipated to be a stronger donor due to the interruption of conjugation to the pyridine ring. The bite angle for Mebim-pic is expected to be larger than Me-bim-py (87° in comparison to 78° in the calculated structures for the *C-trans* acetonitrile complex) (Figure 4.5), which will change the steric environment around the catalytic site.

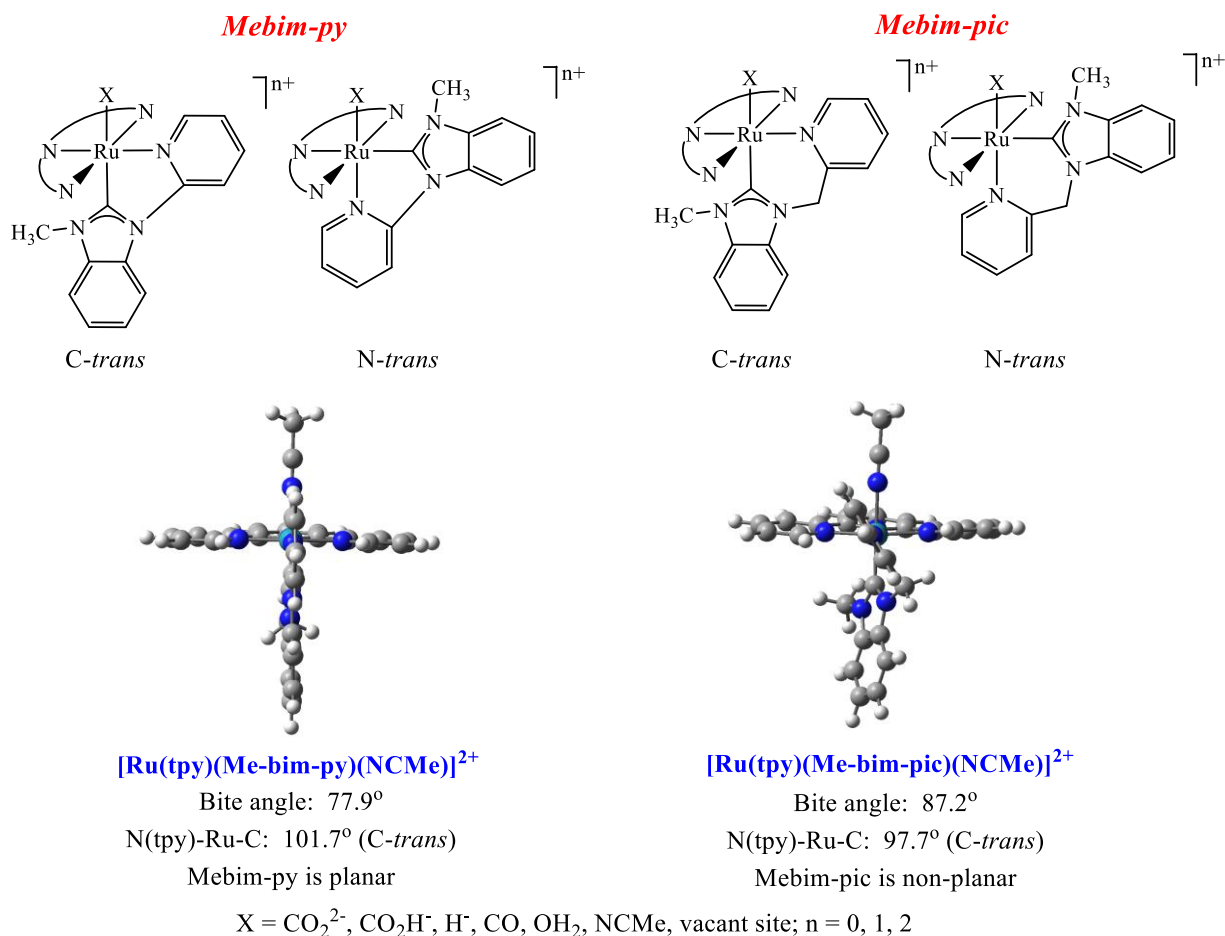


Figure 4.5: Top: Different potential isomers for complexes $[\text{Ru}(\text{Mebim-L})(\text{tpy})\text{X}]^{n+}$ complexes. Bottom: Both carbene- and pyridine-*trans* to X = MeCN isomers for $[\text{Ru}(\text{tpy})(\text{Mebim-L})(\text{MeCN})]^{2+}$ complexes (where L = py for pyridine or pic for picoline) (Duffee, Schauer, Muckerman 2016).

A recent report by Ott et al. suggests that the steric environment around the catalytic site is important.²⁰ Control complex $[\text{Ru}(4,4',4''\text{-tBu}_3\text{-tpy})(4,4'\text{-Me}_2\text{bpy})(\text{MeCN})]^{2+}$ (Figure 4.6, right) required a $2e^-$ reduction at most scan rates to initiate catalysis. Interestingly, for a derivative with a single Me-group at the 6-position on one pyridyl ring of bpy and directed towards the $\text{tBu}_3\text{-tpy}$ ligand (Figure 4.6, left), catalysis began at a lower potential at all scan rates after only $1e^-$ reduction. Given work by Ott et al. strategically methylating the bpy ligands, it is conceivable that Mebim-pic's increased bite angle could favor electrocatalysis at a lower overpotential.^{19,20}

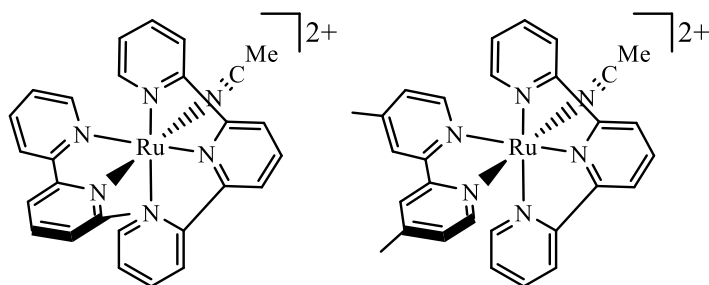


Figure 4.6: Ott et al. ruthenium polypyridyl complexes studied to facilitate electrochemical CO₂ reduction by steric hindrance: (right) control complex [Ru(4,4',4''-tBu₃-tpy)(4,4'-Me₂bpy)(MeCN)]²⁺ and (left) [Ru(4,4',4''-tBu₃-tpy)(6-Mebpy)(MeCN)]²⁺ with strategically placed Me-group at a single 6-position on bpy pointed towards tBu₃-tpy in complex.²⁰

In addition to the monocarbonyl complexes, [Ru(tpy)(Mebim-L)(CO)]²⁺, the corresponding dicarbonyl complexes, [Ru(bpy)(Mebim-L)(CO)₂]²⁺, are also synthetic targets. While the corresponding [Ru(bpy)₂(CO)₂]²⁺ complexes are not effective molecular catalysts for CO₂ reduction due to a detrimental polymerization/precipitation reaction involving loss of bipyridine following two-electron reduction, the dicarbonyl system has proven to be a useful starting material for the preparation of a wide range of intermediates in CO₂ and CO reduction, including metallocarboxylate, metallocarboxylic acid, formyl, and hydroxymethyl complexes (Scheme 3.1 in Chapter 3).

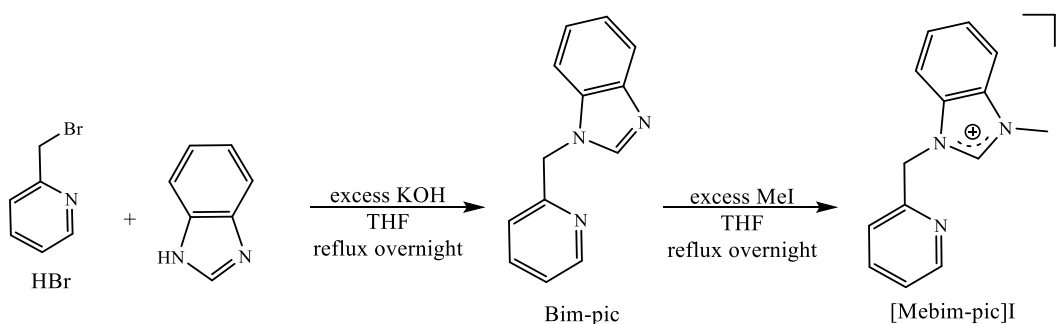
4.2. Results and Discussion

Approaches to synthesizing [Ru(Mebim-L)(tpy)(CO)]²⁺ and [Ru(Mebim-L)(5,5'-Me₂bpy)(CO)₂]²⁺ are outlined starting from the ligand precursor salts [Mebim-L]⁺ (where L = py for pyridine, or pic for picoline). Intermediates Ru(Mebim-L)(CO)₂X₂ (where X = Cl or OTf) were synthesized using [Mebim-L]⁺. Terpyridine and bipyridine complexes where L = pic complexes have been isolated successfully and preliminary electrocatalytic CO₂ reduction experiments are presented.

4.2.1 Mebim-pic ligand precursor synthesis.

The initial synthetic approach to 3-*N*-methyl-1-*N'*-(2-picolyl)benzimidazolium iodide (abbreviated [Mebim-pic]I) involved a reaction between 1-methylbenzimidazole and 2-picolyl bromide complex directly in acetonitrile solvent.¹⁰⁰ The yield from this reaction is low and the desired compound could not be readily isolated from the crude reaction mixture. An alternative procedure, which involved the addition of a catalytic amount of *n*-butylammonium iodide to facilitate the nucleophilic substitution by a classic Finkelstein mechanism, also resulted in a low yield of the desired product, even with extension of the reaction times to several days in refluxing acetonitrile.

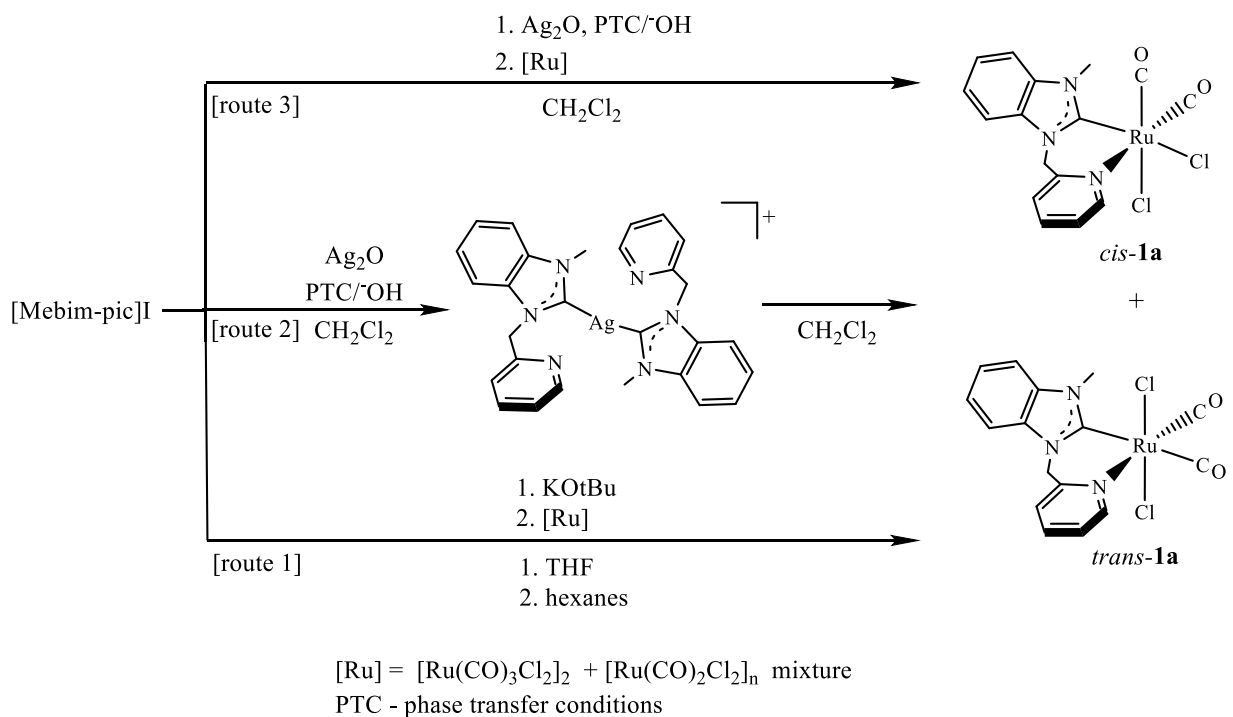
The successful route to [Mebim-pic]I was via 1-picolylbenzimidazol-2-ylidene, prepared by direct reaction of benzimidazole and 2-picolyl bromide with excess KOH in refluxing tetrahydrofuran solvent, to form the desired product in 85% yield.^{101,102} Alkylation with excess methyl iodide produces the desired NHC precursor compound, [Mebim-pic]I, in greater than 60% yield (Scheme 4.1).¹⁰¹



Scheme 4.1: Synthesis method for Mebim-pic ligand precursor compound.¹⁰¹

4.2.2 Synthesis of $\text{Ru}(\text{Mebim-pic})(\text{CO})_2\text{Cl}_2$ (**1a**).

To synthesize the desired carbonyl complexes, the ruthenium starting material employed is a mixture of the ruthenium carbonyl chloride dimer $[\text{Ru}(\text{CO})_3\text{Cl}_2]_2$ and the related polymer, $[\text{Ru}(\text{CO})_2\text{Cl}_2]_n$, hereafter referred to as the ruthenium dimer/polymer mixture. Coordination of the pyridyl-NHC ligand to the mixture of Ru carbonyl complexes was investigated by three different methods: direct coordination of the free carbene following deprotonation (route 1), transmetalation by reaction with an isolated silver carbene complex (route 2), and an *in situ* silver transmetalation (route 3) (Scheme 4.2). Deprotonation of $[\text{Mebim-pic}]\text{I}$ using sodium *tert*-



Scheme 4.2: Approaches to synthesis of $\text{Ru}(\text{Mebim-pic})(\text{CO})_2\text{Cl}_2$ (**1a**) complex.^{103,107,116}

butoxide base to form the free carbene followed by transfer to the ruthenium complex mixture did not afford desired **1a** (Scheme 4.2, route 1). The silver carbene complex $[\text{Ag}(\text{Mebim-pic})_2]^+$ for route 2 was prepared by stirring a methylene chloride solution of $[\text{Mebim-pic}]\text{I}$ over solid Ag_2O for 12 hours.^{103,104} To more effectively deprotonate the carbene in the presence of Ag_2O , it

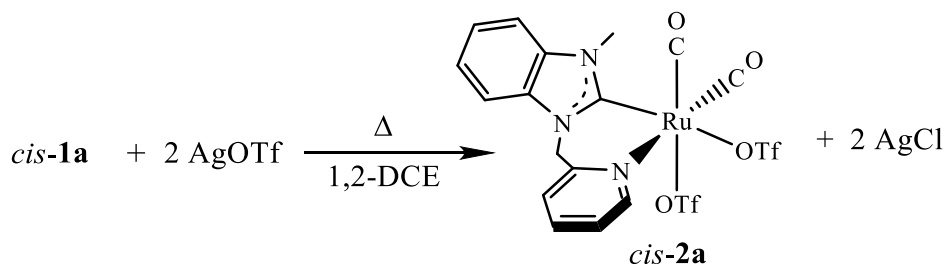
was found to be necessary to add potassium hydroxide in the presence of a phase transfer catalyst $n\text{Bu}_4\text{NI}$. Transmetalation from the isolated silver carbene, $[\text{Ag}(\text{Mebim-pic})_2]^+$, as either the I^- or PF_6^- salt showed only partial coordination of the carbene ligand and some free $[\text{Mebim-pic}]^+$ by ^1H NMR (Scheme 4.2, route 2).

The most successful route to **1a** was by reaction of an *in situ* generated silver carbene with the ruthenium dimer/polymer mixture to form *cis* and *trans* isomers of **1a** (Scheme 4.2, route 3). Only reactions using the iodide salt of $[\text{Mebim-pic}]^+$ instead of the hexafluorophosphate salt successfully formed **1a**. An insoluble yellow powder formed from a methylene chloride solution of crude $\text{Ru}(\text{Mebim-pic})(\text{CO})_2\text{X}_2$. ^1H NMR analysis in $\text{d}_6\text{-DMSO}$ revealed pure *cis*-**1a**. Solid state IR of the precipitate exhibited two carbonyl stretches at 2053 and 1995 cm^{-1} , which were in agreement with *cis*-**1a** ν_{CO} reported by Li *et al.*¹⁰⁵ Analysis of the remaining supernatant showed a mixture of isomers by ^1H NMR as evidenced by the presence of many doublets (*cis* isomers) and singlets (*trans* isomers) in the methylene region. The suspected mixture of geometrical isomers of the Cl complex and halide substitution isomers (Cl for I) were separable via column chromatography, however isolating *cis*-**1a** from methylene chloride was the most reproducible.

4.2.3 Synthesis of $\text{Ru}(\text{Mebim-pic})(\text{CO})_2(\text{OTf})_2$ (**2a**).

Complex **2a** was targeted as a precursor to the desired bpy and tpy complexes. Both triflic acid and silver triflate were considered as triflate sources to displace chlorides in **1a** based on previous literature methods.^{88,106} Reaction of a mixture of *cis* and *trans* **1a** with excess triflic acid in 1,2-dichloroethane resulted in decomposition of the starting material as determined by ^1H NMR spectroscopy. Reaction of *cis*-**1a** with two equiv of AgOTf in refluxing 1,2-dichloroethane for 2 h successfully produced *cis*- $\text{Ru}(\text{Mebim-pic})(\text{CO})_2(\text{OTf})_2$, *cis*-**2a** (eq 4.1). IR analysis showed a distinct shift of ν_{CO} to higher energy (2092 and 2025 cm^{-1}) compared to starting

material bands (2064 and 1995 cm^{-1}). Product was confirmed by ^1H and ^{19}F NMR spectroscopy, where the ^{19}F NMR of **2a** showed two resonances for coordinated triflate at δ -77.9 and δ -77.5, downfield of free AgOTf (δ -79). Only partial substitution is achieved in a room temperature



Equation 4.1: Synthesis of triflate intermediate complex *cis*-**2a**, $\text{Ru}(\text{Mebim-pic})(\text{CO})_2(\text{OTf})_2$.

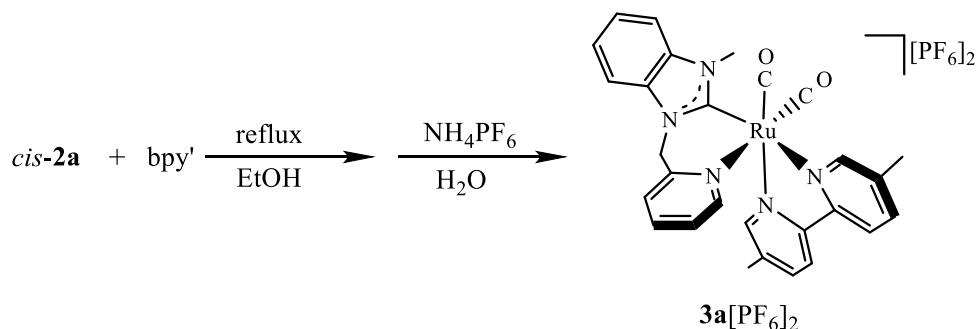
reaction with AgOTf, an intermediate monotriflate complex is observed with ν_{co} at 2073 and 2007 cm^{-1} in 1,2-dichloroethane. ^{19}F NMR also indicated only partial triflate incorporation.

In a separate experiment, pure *trans*-**1a** was isolated via column chromatography and then the crude sample was reacted with excess AgOTf to form *trans*-**2a** in the same manner as for *cis*-**2a**. Each of these samples were used without further purification for synthesis of $[\text{Ru}(\text{Mebim-pic})(\text{bpy}')(\text{CO})_2]^{2+}$ and $[\text{Ru}(\text{Mebim-pic})(\text{tpy})(\text{CO})]^{2+}$ as described below.

4.2.4 Synthesis of $[\text{Ru}(\text{Mebim-pic})(\text{bpy}')(\text{CO})_2]^{2+}$ (**3a**).

Both *cis* and *trans* isomers of **2a** were individually allowed to react with 5,5'-dimethylbipyridine (bpy') in refluxing ethanol for 2 – 3 h. The crude *cis*-**2a** product suspension gradually changed from a pale yellow to a bright yellow suspension. Product formation was confirmed by a shift in the IR to higher energy at 2090 and 2037 cm^{-1} in ethanol. The solution was filtered through celite to remove AgCl remaining from earlier preparation of *cis*-**2a** to give a bright yellow solution in ethanol. Aqueous NH_4PF_6 was added to metathesize the triflate salt, yielding the product as a pale yellow solid of the hexafluorophosphate salt. The identity of the final product as $[\text{Ru}(\text{Mebim-pic})(\text{bpy}')(\text{CO})_2][\text{PF}_6]_2$ (**3a**) was confirmed by ^1H NMR

spectroscopy, IR spectroscopy in methylene chloride, as well as high resolution mass spectrometry in MeCN (eq 4.2). Complex **3a** exhibited carbonyl stretching frequencies in the IR spectrum in methylene chloride at 2090 and 2034 cm^{-1} .



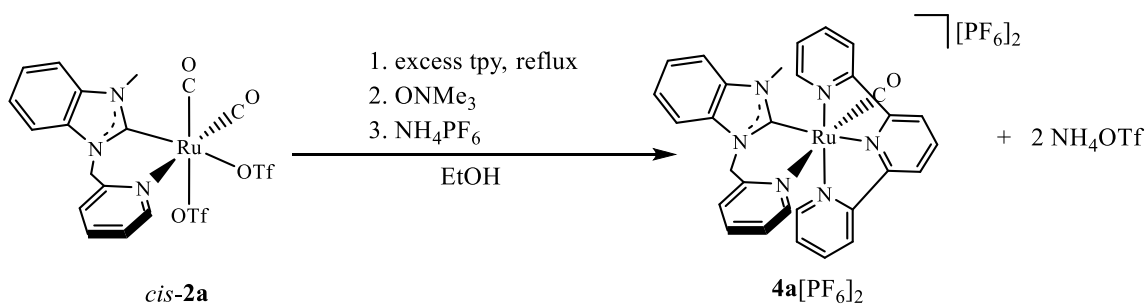
Equation 4.2: Synthesis of complex **3a**, $[\text{Ru}(\text{Mebim-pic})(\text{bpy}')(\text{CO})_2][\text{PF}_6]_2$.

Attempts to form $[\text{Ru}(\text{Mebim-pic})(\text{bpy}')(\text{CO})_2][\text{PF}_6]_2$ (**3a**) from *trans*-**2a** did not proceed under the same reaction conditions as *cis*-**2a**. Unlike the *cis*-**2a** product, the *trans*-**2a** complex was soluble in the ethanol reaction solvent. Addition of NH_4PF_6 to the heated solution of *trans*-**2a** and bpy' afforded a small amount (est. 5 mg) of a light yellow solid which was identified as the desired **3a**. This result indicates that isomerization from *trans*-**2a** to the *cis*-**2a** occurs under the reaction conditions in the presence of bpy' , but the isomerization reaction must be slow due to the low yield of the product **3a**.

4.2.5 Synthesis of $[\text{Ru}(\text{Mebim-pic})(\text{tpy})(\text{CO})]^{2+}$ (**4a**).

Reaction of a tridentate ligand, terpyridine (tpy), with *cis*-**2a** generated an intermediate κ^2 -chelated tpy complex. Monitoring the reaction by IR spectroscopy showed a shift of ν_{co} from 2088 to 2035 cm^{-1} for one of the bands, confirming bidentate chelation of tpy. One equiv of trimethylamine N-oxide (ONMe_3) was added to the ethanolic reaction κ^2 -ligated terpyridine complex. The addition of ONMe_3 resulted in an immediate color change from pale yellow to bright yellow with the formation of a dark precipitate. An IR spectrum of the precipitate in ethanol revealed a single band at 1984 cm^{-1} . Metathesis with aqueous NH_4PF_6 afforded a bright

yellow solid. Recrystallization of the solid from methylene chloride/diethyl ether afforded a light yellow powder. The ^1H NMR and mass spectrum are consistent with formation of the desired product **4a**.



Equation 4.3: Synthesis of catalyst **4a**, $[\text{Ru}(\text{Mebim-pic})(\text{tpy})(\text{CO})][\text{PF}_6]_2$.

The ^1H NMR spectrum of **4a** in CD_2Cl_2 exhibited a large downfield singlet for the three protons on the central ring of the tpy ligand at δ 8.6 ppm and a distinct singlet for the methylene bridge of the Mebim-pic ligand at δ 5.7 ppm, indicating an average plane of symmetry that bisects the tpy ligand. The proton at the 6-position of the pyridyl ring of the Mebim-pic ligand is now pointed towards the tpy, resulting in an upfield shift to around δ 7.6 ppm. The methyl resonance for the Mebim-pic ligand was observed as a singlet at δ 4.4.

A NOESY NMR study (Figure 4.7, top) of complex **4a** confirmed that the product is the isomer in which the pyridine of the Mebim-pic ligand is *trans* to the carbonyl ligand as shown above in Equation 4.3, and also predicted by DFT calculations to be more stable than the *C-trans* isomer by ~ 7 kcal/mol (Fig. 4.3). The Mebim-pic ligand methyl group shows a through-space correlation to tpy ring protons at the 6 and 6'' positions on the outer pyridine rings of tpy at δ 8.2 ppm (closest approach = 2.48 Å based on a DFT structure of *N-trans*- $[\text{Ru}(\text{Mebim-pic})(\text{tpy})(\text{CO})]^{2+}$, Figure 4.7, bottom). The methyl group also correlated with a proton on the adjacent benzimidazole ring at δ 7.8.

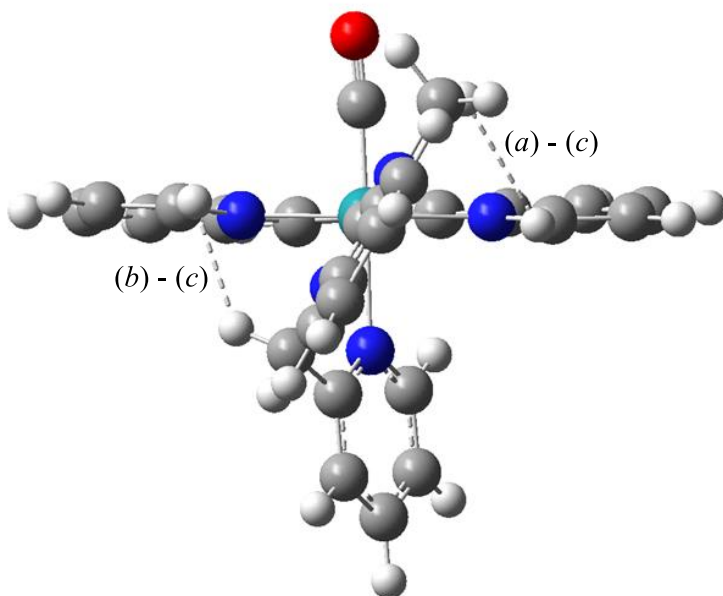
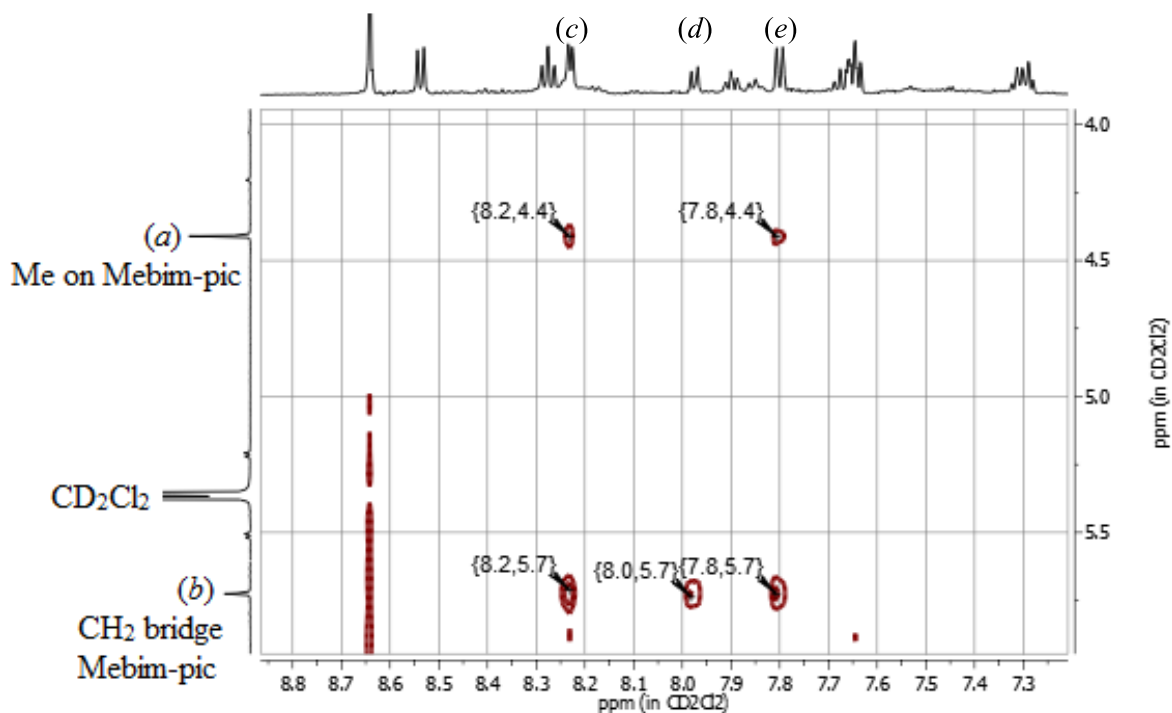


Figure 4.7: On top NOESY NMR of pyridine *trans* to CO isomer of **4a** in CD_2Cl_2 showing correlation of Me group on Mebim-pic (*a*) to tpy 6, 6''- ^1H at δ 8.2 (*c*) and to benzimidazole aromatic resonance at δ 7.8 (*e*) and correlation of methylene bridge (*b*) to tpy 6, 6''- ^1H (*c*), benzimidazole aromatic resonance (*d*), and pyridyl 3- ^1H on Mebim-pic (*e*). On bottom DFT calculated structure using dotted-lines to indicate correlations to tpy observed in NOESY, where distances (*a*) – (*c*) = 2.48 Å and (*b*) – (*c*) = 2.26 Å (Duffee and Schauer, 2016).

A second through-space correlation between the methylene bridge of the Mebim-pic ligand and the 6, 6'' terpyridine protons is also observed due to canting of the pyridine ring (closest approach = 2.26 Å, Figure 4.7, bottom). An analysis of the DFT structure for *C-trans*-[Ru(Mebim-pic)(tpy)(CO)]²⁺ (Figure 4.8) shows no through-space interactions < 3 Å between

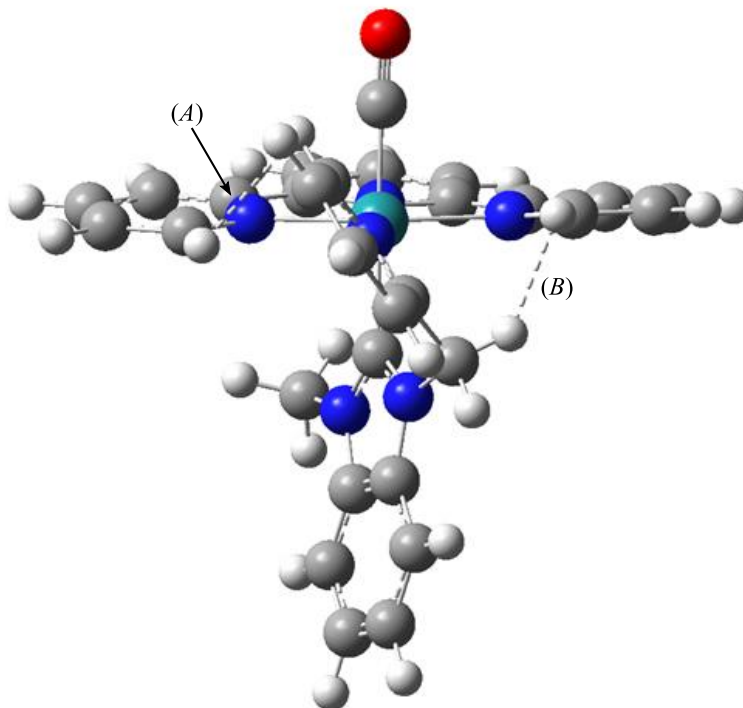
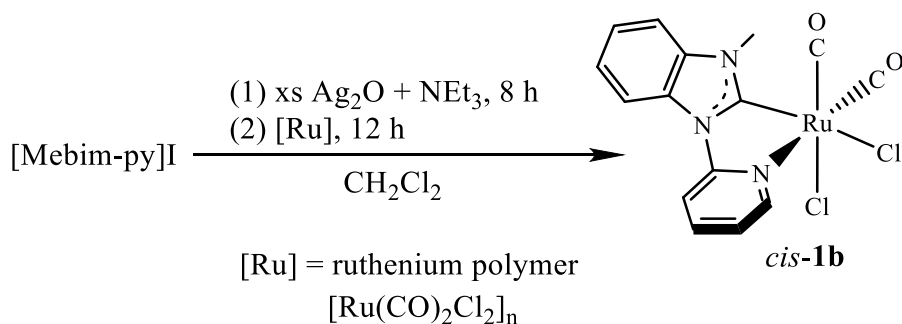


Figure 4.8: DFT calculated carbene *trans* to CO isomer of **4a** demonstrating the > 3 Å distance between the Me group on Mebim-pic to the tpy ligand. Dotted lines indicate the expected observable NOESY correlations where (A, left) 6-pyridyl proton (2.60 Å) and (B, right) methylene bridge (2.11 Å) of Mebim-pic are closest to tpy 6, 6''-¹H (Duffee and Schauer, 2016).

the Mebim-pic methyl group and the tpy ring. The shortest through-space interactions are between the methylene bridge of the Mebim-pic ligand and the 6,6'' terpyridine protons (closest approach = 2.11 Å, Figure 4.8) (Duffee and Schauer, 2016).

4.2.6 Attempted synthesis of $[Ru(\text{Mebim-py})(\text{tpy})(\text{CO})]^{2+}$ (**4b**).

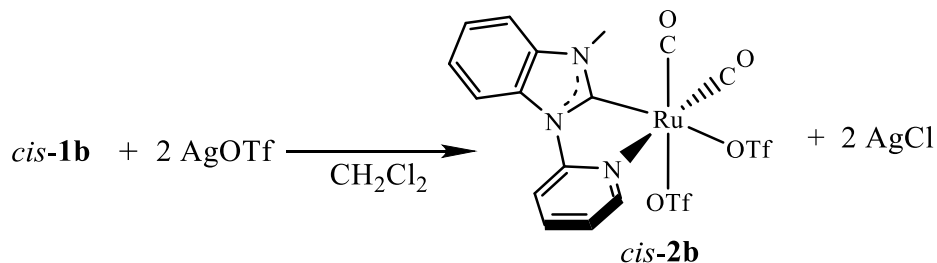
An alternative method was used for synthesis of complex $Ru(\text{Mebim-py})(\text{CO})_2\text{Cl}_2$ (**4b**). This modified procedure relies on the use of an organic base triethylamine rather than the use of NaOH as described previously. First, $[\text{Mebim-py}]\text{I}$ complex was reacted with Ag_2O and triethylamine at ambient temperature in the dark (eq 4.4). The *in situ* formed $[\text{Ag}(\text{Mebim-py})_2]^+$



Equation 4.4: Synthesis of $Ru(\text{Mebim-py})(\text{CO})_2\text{Cl}_2$, complex *cis-1b*.

complex was reacted with the ruthenium dimer/polymer mixture for a day at room temperature in the dark. ^1H NMR and IR spectroscopy confirmed the formation of the product based on the previously reported procedure by Li et al.¹⁰⁷

The triflate complex $Ru(\text{Mebim-py})(\text{CO})_2(\text{OTf})_2$ was prepared in a reaction between *cis-1b* and 2 equiv of AgOTf in 1,2-DCE at room temperature (eq 4.5). A shift

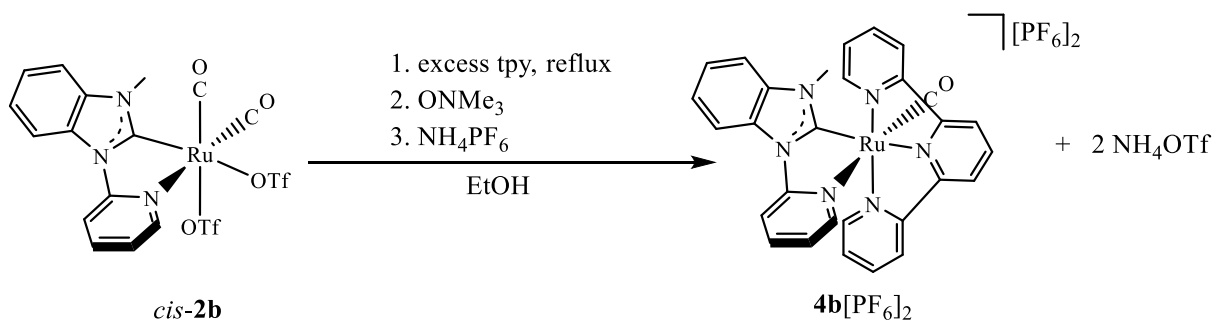


Equation 4.5: Synthesis of $Ru(\text{Mebim-py})(\text{CO})_2(\text{OTf})_2$, complex *cis-2b*.

in the carbonyl stretching frequencies in the IR spectrum to higher energy from 2065 and 2002 cm^{-1} to 2095 and 2036 cm^{-1} was observed. Heating the reaction between **1b** and AgOTf to reflux

in 1,2-DCE did not change the stretching frequencies in the IR spectrum, but rather aided in driving reaction of the partially soluble starting material to completion. The identity of the isolated product was confirmed by ^1H and ^{19}F NMR spectroscopy in CD_2Cl_2 . The distinct 6-pyridyl proton on Mebim-py in *cis*-**2b** at δ 8.99 ppm shifted slightly upfield compared to *cis*-**2a** (9.02 ppm), as predicted for the conjugated and less donating Mebim-py carbene. ^{19}F NMR showed resonances downfield of free AgOTf in methylene chloride at δ -77 and -78 ppm, similar to those observed in synthesis of *cis*-**2a**.

The crude triflate complex **2b** was then reacted with tpy in ethanol to give the κ^2 -tpy complex. The reaction in ethanol was monitored by IR, and a shift from 2089 and 2032 cm^{-1} to 2094 and 2045 cm^{-1} indicated κ^2 -coordination. As observed in synthesis of $[\text{Ru}(\text{bpy}')_2(\text{CO})_2]^{2+}$, **3a**, and **4a**, the lower energy CO vibration shifts most noticeably to higher energy. A difficulty was encountered in the ONMe_3 step, and no solid was isolated that was shown to have tpy or Mebim-py present by ^1H NMR. The synthesis of complex **4b** remains under investigation (eq 4.6).



Equation 4.6: Synthetic approach in attempt to make **4b**, $[\text{Ru}(\text{Mebim-py})(\text{tpy})(\text{CO})]^{2+}$.

All complexes prepared in this work in addition to related compounds previously reported and analyzed in the literature are compared in Table 4.1 below. The resulting Mebim-pic compounds compare closely to those of the Mebim-py system based on the spectroscopic

characterization. As expected, the CO stretch for the carbene compounds are observed at considerably lower energy than the $[\text{Ru}(\text{tpy})(\text{bpy})(\text{CO})]^{2+}$ or $[\text{Ru}(\text{bpy})_2(\text{CO})_2]^{2+}$ analogues due to the presence of the more electron donating carbene ligand.

Table 4.1: Spectroscopic Characterization of Ruthenium Complexes

Complex	CH ₂ bridge (δ , ppm)	py-6 on Mebim (δ , ppm)	Me on Mebim (δ , ppm)	Downfield bpy' or (t) (δ , ppm)	IR ν_{CO} (cm ⁻¹)
1a - Ru(Mebim-pic)(CO) ₂ Cl ₂	5.43 d 5.86 d ² J=16.0 Hz	9.64 d	4.26 s	-	2064 1996
1b - Ru(Mebim-py)(CO) ₂ Cl ₂	-	8.20 d (DMSO)	3.14 s (DMSO)	-	2061 1984
2a - Ru(Mebim-pic)(CO) ₂ (OTf) ₂	5.63 d 6.04 d ² J=16.4 Hz	9.02 d	4.19 s	-	2092 2025
2b - Ru(Mebim-py)(CO) ₂ (OTf) ₂	-	8.99 d	4.30 s	-	2095 2036
3a – [Ru(Mebim-pic)(b')](CO) ₂] ²⁺	5.59 d 5.77 d ² J=17.3 Hz	obscured	4.25 s	9.03 s	2090 2034
4a - [Ru(Mebim-pic)(t)(CO)] ²⁺	5.68 s	7.93 d	4.37 s	8.60 s	1984
[Ru(bpy)(tpy)(CO)] ²⁺ (ref: 117)	-	-	-	9.60 d (DMSO)	1985
[Ru(bpy') ₂ (CO) ₂] ²⁺ (ref: 118)	-	-	-	8.88 s	2085 2040
[Ru(Mebim-py)(tpy)(NCMe)] ²⁺ (ref: 21)	-	9.44 d (CD ₃ CN)	2.90 s (CD ₃ CN)	8.40 d (CD ₃ CN)	-

All chemical shifts reported relative to residual solvent CD₂Cl₂ at 20°C unless otherwise noted. ¹H NMR pattern indicated by the following: s (singlet) or d (doublet). Obscured indicates unable to report due to overlap with other aromatic resonances. IR bands reported in CH₂Cl₂ at 20°C unless otherwise noted with exception of literature values (Nujol mull). Full spectroscopic details reported in Experimental Section 4.4 and selected spectra shown in Appendix 3.1.

4.2.7 Electrochemical analysis of complex **4a**

Reported here with consent of Matthew Kita and Prof. Alexander J.M. Miller.

Having synthesized complex **4a** preliminary electrochemical analysis studies were carried out to gauge electrocatalytic CO₂ reduction capabilities in collaboration with Matthew Kita. In particular, these complexes will be compared to previously reported catalyst [Ru(Mebim-py)(tpy)(NCMe)]²⁺, which reduces both protons and CO₂ to give mixtures of H₂ and CO known as synthesis gas.¹⁷

Complex **4a** shows two reversible reduction waves at -1.46 and -1.72 V vs. Fc/Fc⁺, each assigned as one-electron reductions of the terpyridine ligand (Fig. 4.9). In comparison, the

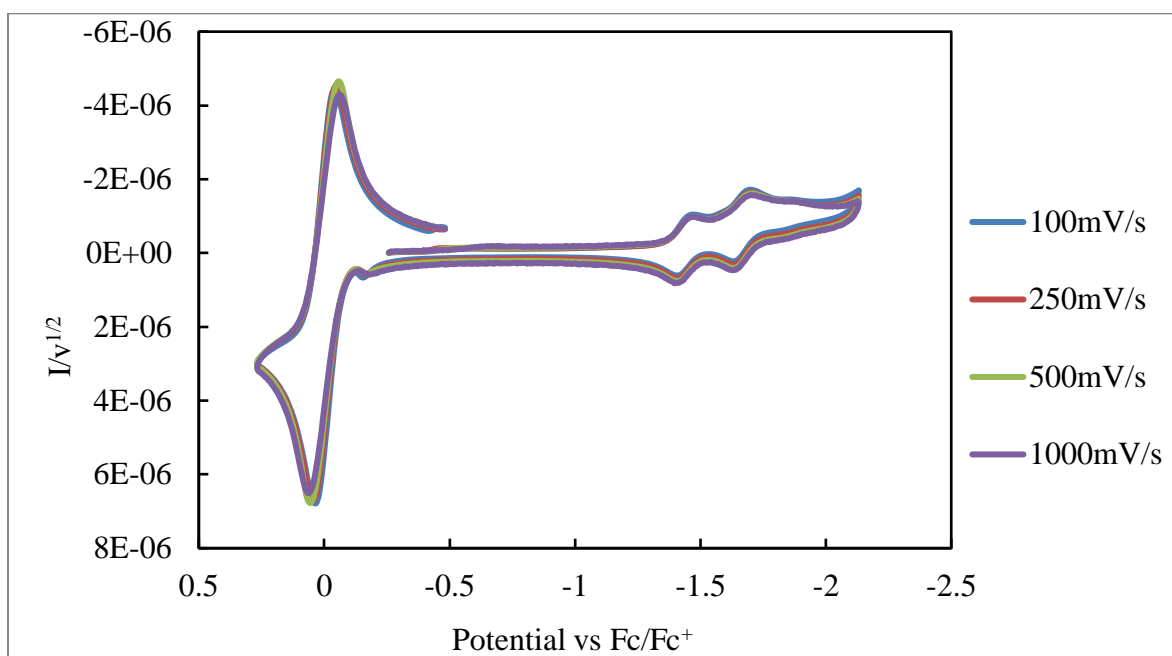


Figure 4.9: Electrochemical reduction of **4a** (3 mM) under nitrogen in acetonitrile with 10% water added using glassy carbon working electrode, Pt counter electrode, and Ag wire reference electrode in a 100 mM TBAPF₆ electrolyte solution at varied scan rates. Internal standard ferrocene (left reversible wave) set to 0 V.

previously analyzed complex, [Ru(Mebim-py)(tpy)(NCMe)]²⁺, gave reductions at -1.70 and -1.96 V (vs. Fc/Fc⁺) under similar conditions.^{82,108} Interestingly, unlike the previously reported syn gas catalyst, [Ru(Mebim-py)(tpy)(NCMe)]²⁺, which produced mixtures of H₂ and CO,

complex **4a** shows no change in current with up to 10% added water). However, current enhancements are observed with water present under CO₂, where the onset of CO₂ reduction catalysis occurs at a more negative potential than the second ligand reduction at around -1.56 V vs. Fc/Fc⁺ (Fig. 4.10).

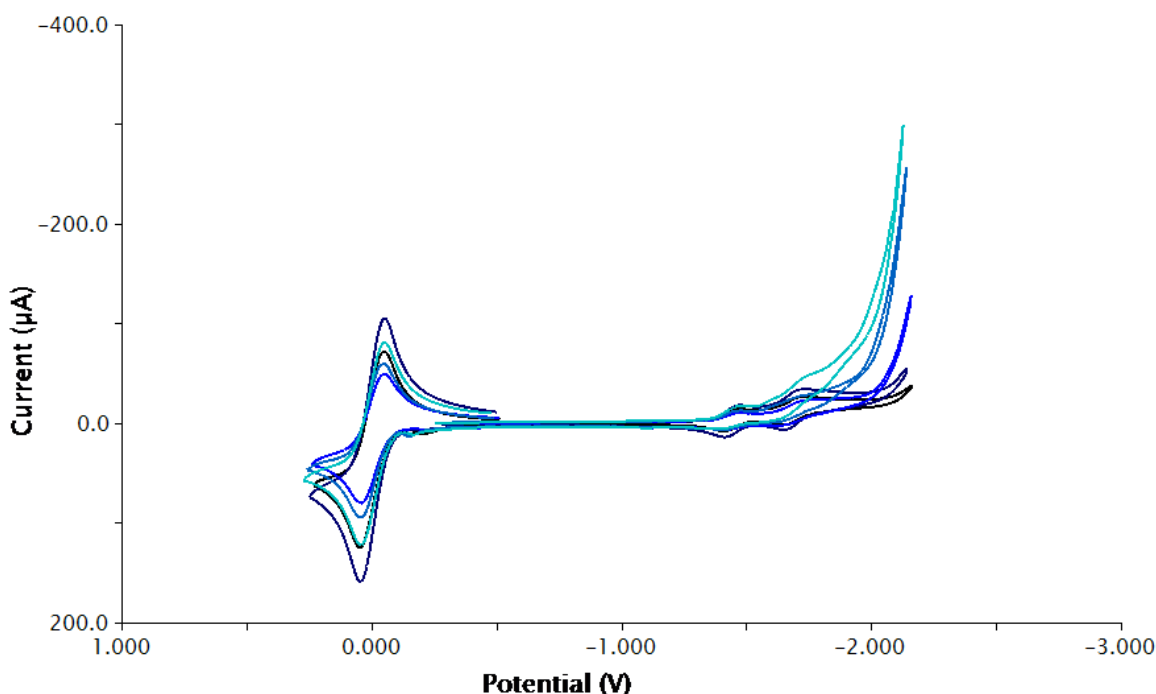


Figure 4.10: Electrochemical reduction of **4a** (3 mM) under CO₂ in acetonitrile with 0%, 1%, 5%, 7.5%, and 10% water added (intensity of blue color means higher water concentration) using glassy carbon working electrode, Pt counter electrode, and Ag wire reference electrode in a 100 mM TBAPF₆ electrolyte solution. Internal standard ferrocene (left reversible wave) set to 0 V.

4.3. Summary and Future Directions

Ru(Mebim-pic) tpy and bpy' carbonyl complexes analogous to previously reported electrocatalyst [Ru(Mebim-py)(tpy)(Solv)]²⁺ have been synthesized. Preliminary electrochemical and computational analyses of **4a**, [Ru(Mebim-pic)(tpy)(CO)]²⁺, indicate it is also an effective catalyst for reductive disproportionation of CO₂ to CO. The precursor bis-triflate, Ru(Mebim-py)(CO)₂(OTf)₂ (**2b**), has been prepared and will be used to access the intermediate tpy and bpy carbonyl complexes, **3b** and **4b**. Given the facile syntheses of **3a** and **4a**, the Mebim-py

analogues should be accessible. Further synthetic and electrochemical analysis of these complexes will inform strategies for optimizing these electrocatalysts for CO₂ reduction to CO, and elucidate the role isomer preference plays in the catalytic cycle.

4.4. Experimental

All manipulations were performed under an atmosphere of dry nitrogen using either standard Schlenk-line or glove box techniques unless noted otherwise. Solvents were purchased from commercial sources and purged under nitrogen atmosphere and dried over 4Å molecular sieves or through packed activated alumina. Deuterated solvent d₆-DMSO was degassed by three “freeze-pump-thaw” cycles then stored in Kontes tube over 4Å molecular sieves. All other deuterated solvents were purified by distillation from P₂O₅.

Reagents 1-methylbenzimidazole, benzimidazole, 2-picoly bromide hydrobromide, silver(I) oxide, NaPF₆, hydroxide salts, and *n*-tetrabutylammonium salts were purchased from commercial sources and used without further purification. Methyl iodide was stored under nitrogen atmosphere in Teflon sealed Schlenk flask over copper turnings. Starting materials 1-picolybenzimidazol-2-ylidene (Bim-pic)^{101,102}, 3-methyl-1-picolybenzimidazol-2-ylidene iodide ([Mebim-pic]I)^{101,109} and ruthenium dimer/polymer mixture⁸⁸ were made following literature procedures. Ru(Mebim-pic)(CO)₂Cl₂ and Ru(Mebim-py)(CO)₂Cl₂ were made via a modified literature procedures.^{107,110}

¹H, ¹³C, and ¹⁹F NMR spectra were recorded on Bruker 400 MHz Nanobay, Bruker AVANCE III 500 MHz, or Bruker AVANCE III 600 MHz spectrometer. Spectral data are referenced to residual solvent signals.⁸⁹ Spectroscopic data are reported in the following manner: chemical shift (multiplicity [singlet (s), doublet (d), triplet (t), doublet of doublet (dd), triplet of doublet (td), multiplet (m), and broad resonance (br)], integration, assignment, *J*-coupling

constants [in Hz]). NMR samples were prepared in NMR tubes fitted with rubber septa and sealed with parafilm under a nitrogen atmosphere.

Infrared spectra were recorded on a Bruker ALPHA Fourier Transform IR spectrometer, using liquid sample cells with CaF₂ windows. Infrared band intensity is described in the following manner: strong (st), medium (m), weak (w), broad resonance (br).

1-picolybenzimidazol-2-ylidene, Bim-pic.¹⁰¹ In a flask open to air, benzimidazole (2.008 g, 17.0 mmol) and 2-bromomethylpyridine hydrobromide (4.286 g, 17.0 mmol, 1 equiv) were dissolved in dry THF (102 mL) giving a bright fuchsia suspension. Next KOH pellets (3.899 g, 70.0 mmol, 4.1 equiv) were added while stirring. The reaction was refluxed overnight to give a dark brown-black suspension with grey-brown solids. The completion of the reaction was confirmed by ¹H NMR analysis of an aliquot of the reaction solution in CDCl₃ or d₆-DMSO. The mixture was filtered to separate off grey-brown salts. After removal of solvent, the dark brown residue was redissolved in chloroform and the solvent was removed under vacuum to yield a brown powder. Isolated yield: 3.546 g (16.9 mmol, 95 %). ¹H NMR (20 °C, d₆-DMSO, δ, ppm, 500 MHz): 5.59 (s, 2H, CH₂ bridge), 7.19 (m, 2H), 7.27 (d, 1H), 7.30 (dd, 1H), 7.48 (m, 1H), 7.77 (td, 1H), 7.66 (m, 1H), 8.37 (s, 1H, NCHN), 8.51 (d, 1H, pyridyl-6). ¹H NMR (20 °C, CDCl₃, δ, ppm, 500 MHz): 5.52 (s, 2H, CH₂ bridge), 6.93 (d, 1H), 7.25 (dd, 1H), 7.30 (m, 3H), 7.62 (td, 1H), 7.86 (d, 1H), 8.08 (s, 1H, NCHN), 8.63 (d, 1H, pyridyl-6).

3-methyl-1-picolybenzimidazol-2-ylidene iodide, [Mebim-pic]I.¹⁰¹ A sample of Bim-pic (1.235 g, 5.9 mmol) was dissolved in dry THF (110 mL). To this solution, MeI (850 μL, 13.6 mmol, 2.3 equiv) was added via syringe. The bright red-brown reaction solution was heated at reflux overnight. After the reaction was cooled to room temperature, the brown solid that precipitated was collected by filtration. The dark brown solid product was triturated with hexanes

overnight to wash away dark impurities resulting in a lighter-brown/tan powder. Isolated yield: 1.682 g (4.4 mmol, 75%). ^1H NMR (20 °C, d_6 -DMSO, δ , ppm, 500 MHz): 4.14 (s, 3H, Me on Mebim), 5.92 (s, 2H, CH_2 bridge), 7.38 (dd, 1H), 7.66 (m, 3H), 7.90 (td, 1H), 7.93 (d, 1H), 8.04 (d, 1H), 8.49 (d, 1H, pyridyl-6), 9.88 (s, 1H, NCHN). ^1H NMR (20 °C, CD_2Cl_2 , δ , ppm, 500 MHz): 4.23 (s, 3H, Me on Mebim), 5.98 (s, 2H, CH_2 bridge), 7.30 (m, 1H), 7.66 (m, 2H), 7.71 (t, 1H), 7.80 (m, 2H), 7.87 (d, 1H), 8.51 (d, 1H, pyridyl-6), 11.12 (s, 1H, NCHN).

3-methyl-1-picolybenzimidazol-2-ylidene hexafluorophosphate, [Mebim-pic]PF₆. A sample of [Mebim-pic]I (98.0 mg, 0.26 mmol) was dissolved in water (30 mL) and to it NaPF₆ (173 mg, 1.0 mmol, 3.8 equiv) was added. The metathesis reaction was stirred for 10 min and then filtered to collect the off-white solids. The solid product collected was dried under vacuum. Isolated yield: 78.5 mg (0.21 mmol, 83%).

***cis*-Ru(Mebim-pic)(CO)₂Cl₂, *cis*-1a.**^{107,110} This compound was made via modified literature procedures as follows. A flask containing [Mebim-pic]I (879.7 mg, 2.5 mmol), $n\text{Bu}_4\text{NI}$ (33.0 mg, 0.1 mmol, 4 mol %), and Ag₂O (279.8 mg, 1.2 mmol, 1 equiv) was prepared then purged under nitrogen. Next, an aqueous NaOH solution was made (853 mM – 170.6 mg in 5.0 mL). The solids were suspended in methylene chloride (97.5 mL) and then 2.5 mL of NaOH (aq) solution (0.85 equiv) was added. The reaction was stirred at room temperature overnight (8 - 24 h) under exclusion of light. A dark brown suspension formed containing the intermediate [Ag(Mebim-pic)₂]⁺. This solution was filtered through glass wool into a flask of ruthenium dimer/polymer mixture ([Ru(CO)₃Cl₂]₂ + [Ru(CO)₂Cl₂]_n). The reaction was stirred for another 24 h under exclusion of light to yield a bright yellow-orange solution with dark brown/black precipitate. The solution was filtered through celite and the solvent was removed in vacuo to yield a dark orange residue. The residue was re-dissolved using minimal dry methylene chloride (5.0 mL) and

allowed to sit in an ice bath for 2 – 4 h. The low-solubility *cis* product, which precipitated as a light yellow powder, was isolated by filtration and collected on a glass frit. Isolated yield: 131.6 mg (0.29 mmol, 13.6% based on Ru). ^1H NMR (20 °C, $\text{d}_6\text{-DMSO}$, δ , ppm, 500 MHz): 4.20 (s, 3H, Me on Mebim), 5.39 (d, $^2J_{\text{HH}} = 16.2$ Hz, 1H, CH_2 bridge), 6.34 (d, $^2J_{\text{HH}} = 16.2$ Hz, 1H, CH_2 bridge), 7.46 (m, 3H), 7.72 (t, 1H), 7.78 (d, 1H), 8.01 (d, 1H), 8.09 (d, 1H), 8.18 (t, 1H), 9.38 (d, 1H, pyridyl-6). ^1H NMR (20 °C, CD_2Cl_2 , δ , ppm, 500 MHz): 4.26 (s, 3H, Me on Mebim), 5.43 (d, $^2J_{\text{HH}} = 16.0$ Hz, 1H, CH_2 bridge), 5.86 (d, $^2J_{\text{HH}} = 16.0$ Hz, 1H, CH_2 bridge), 7.44 (m, 3H), 7.52 (m, 1H), 7.56 (t, 1H), 7.62 (m, 2H), 7.96 (td, 1H), 9.64 (d, 1H, pyridyl-6). IR (CH_2Cl_2 , ν_{co}): 2064 cm^{-1} (st) and 1996 cm^{-1} (st).

***cis*-Ru(Mebim-pic)(CO) $_2$ (OTf) $_2$, *cis*-2a.** To a sample of Ru(Mebim-pic)(CO) $_2$ Cl $_2$ (30.8 mg, 0.068 mmol) was added AgOTf (35.2 g, 0.137 mmol, 2.0 equiv) in air. The solids were purged under inert atmosphere then 1,2-dichloroethane (2.0 mL) was added. The reaction was refluxed at 100 °C for 10 min. A color change from pale yellow to white was observed for the suspension. All solvent was removed in vacuo to give a bright white residue. The crude product residue was used without further purification to make tpy and bpy' complexes **3a** and **4a**. ^1H NMR (20 °C, CD_2Cl_2 , δ , ppm, 400 MHz): 4.19 (s, 3H, Me on Mebim), 5.63 (d, $^2J_{\text{HH}} = 16.4$ Hz, 1H, CH_2 bridge), 6.04 (d, $^2J_{\text{HH}} = 16.4$ Hz, 1H, CH_2 bridge), 7.54 (m, 2H), 7.61 (m, 1H), 7.72 (m, 2H), 7.81 (d, 1H), 8.12 (td, 1H), 9.02 (d, 1H, pyridyl-6). ^{19}F NMR (20 °C, CD_2Cl_2 , δ , ppm, 376 MHz): -77.9 (s), -77.5 (s). IR (1,2-DCE, ν_{co}): 2092 cm^{-1} (st) and 2025 cm^{-1} (st).

[Ru(Mebim-pic)(5,5'-Me $_2$ bpy)(CO) $_2$][PF $_6$] $_2$, **3a.** Crude *cis*-Ru(Mebim-pic)(CO) $_2$ (OTf) $_2$ (est. 90% yield = 60.1 mg, 0.089 mmol) and 5,5'-Me $_2$ bpy (24.5 mg, 0.13 mmol, 1.5 equiv) were added to a Schlenk flask in air, then suspended in 8.0 mL of 190 proof ethanol. The suspension was refluxed for 35 min at 95 °C under nitrogen. The sample was cooled to room temperature

and then filtered through celite. Excess NH_4PF_6 was added to the EtOH sample solution forming a yellow precipitate. The yellow solids were isolated by filtration then recrystallized from methylene chloride/diethyl ether. Isolated yield: 36.4 g (0.043 mmol, 48%). ^1H NMR (20 °C, CD_2Cl_2 , δ , ppm, 500 MHz): 2.36 (s, 3H, Me on bpy'), 2.69 (s, 3H, Me on bpy'), 4.25 (s, 3H, Me on Mebim), 5.59 (d, $^2J_{\text{HH}} = 17.3$ Hz, 1H, CH_2 bridge), 5.77 (d, $^2J_{\text{HH}} = 17.3$ Hz, 1H, CH_2 bridge), 7.40 (t, 1H), 7.66 (m, 2H), 7.70 (d, 1H), 7.76 (d, 1H), 7.96 (m, 3H), 8.01 (d, 1H), 8.12 (d, 1H), 8.21 (d, 1H), 8.36 (t, 2H), 9.03 (s, 1H, bpy on Me_2bpy). $^{13}\text{C}\{^1\text{H}\}$ NMR (20 °C, CD_2Cl_2 , δ , ppm, 151 MHz): 18.85 (Me on bpy'), 18.98 (Me on bpy'), 36.01 (Me on Mebim-pic), 51.32 (CH_2 bridge of Mebim-pic), 111.51, 111.97, 124.92, 125.38, 126.15, 126.16, 127.51, 128.43, 134.65, 135.65, 141.16, 141.91, 142.50, 143.05, 143.69, 151.09, 152.38, 152.59, 153.76, 154.86 (total 19C in aromatic region, 2C unobserved), 176.57 (NCN carbene), 191.43 (CO), 192.02 (CO). IR (CH_2Cl_2 , ν_{co}): 2090 cm^{-1} (st) and 2034 cm^{-1} (st).

[Ru(Mebim-pic)(tpy)(CO)][PF₆]₂, 4a. Crude *cis*-Ru(Mebim-pic)(CO)₂(OTf)₂ (46.3 mg, 0.068 mmol) and tpy (20.8 mg, 0.010 mmol, 1.5 equiv) were added to a Schlenk flask in air then suspended in 5.0 mL of 190 proof ethanol. The suspension was refluxed at 85 °C for 1 h. The reaction changed from a pale pink suspension to a bright pink solution with the formation of a dark-colored precipitate. After cooling to room temperature, the mixture was filtered through celite to remove solids. To the collected supernatant, an ethanol solution of 5.7 mg (0.076 mmol, 1.1 equiv) of trimethylamine *N*-oxide was added. The solution was stirred for 5 min, where it changed from pale yellow to bright yellow. An aqueous solution of NH_4PF_6 14.0 mg (0.086 mmol, 1.3 equiv in 1.0 mL) was added to the reaction mixture and stirred for 5 min. A bright yellow precipitate formed immediately which was collected by filtration. Isolated yield: est. 10 mg (0.014 mmol, 20%). ^1H NMR (20 °C, CD_2Cl_2 , δ , ppm, 500 MHz): 4.37 (Me on Mebim-pic),

5.68 (s, CH₂ bridge of Mebim-pic), 7.26 (m, 2H, tpy), 7.61 (m, 3H, 6-pyridyl of Mebim-pic + tpy overlapped), 7.76 (d, 2H, benzimidazole of Mebim-pic), 7.86 (td, 1H, Mebim-pic), 7.93 (d, 1H, 3-pyridyl of Mebim-pic), 8.19 (br d, 2H, 6,6'' of tpy), 8.24 (td, 2H, tpy), 8.50 (d, 2H, tpy), 8.60 (s, 3H, middle ring of tpy). ¹³C{¹H} NMR (20 °C, CD₂Cl₂, δ, ppm, 151 MHz): 35.85 (Me on Mebim-pic), 50.48 (CH₂ bridge of Mebim-pic), 110.96, 111.30, 125.10, 125.44, 126.58, 127.25, 127.28, 129.74, 135.12, 136.02, 141.39, 141.47, 142.09, 148.59, 154.91, 155.23, 156.55, 158.22 (total 18C in aromatic region, 2C unobserved), 190.52 (NCN carbene), 195.02 (CO). IR (ATR, ν_{co}): 1981 cm⁻¹.

***cis*-Ru(Mebim-py)(CO)₂Cl₂, *cis*-1b.**^{107,110} This compound was made via modification of a literature procedure as follows. A flask containing [Mebim-py]I (374.7 mg, 1.11 mmol), and Ag₂O (132.6 mg, 0.57 mmol, 0.52 equiv) was placed under nitrogen and NEt₃ (300 μL, 2.1 mmol, 1.9 equiv) was added. The reagents were suspended in methylene chloride (47 mL) and stirred at room temperature for 5 h under exclusion of light. A pale yellow/white suspension with fine solids formed containing the intermediate [Ag(Mebim-py)₂]⁺. This solution was filtered through glass wool into a flask of 259.6 mg of ruthenium polymer ([Ru(CO)₂Cl₂]_n) to give a bright orange solution. The reaction was stirred for 24 h under exclusion of light to form a bright yellow solution with dark precipitate. The solution was filtered through celite, and removal of solvent under vacuum yielded an orange crunchy oil. The residue was re-dissolved using dry acetonitrile (5.0 mL) and allowed to sit for 2 – 4 h. The low-solubility *cis* product, which crashed out of solution as a bright yellow solid, was isolated by filtration. Isolated yield: 37.0 mg (0.085 mmol, 7.6 %). ¹H NMR (20 °C, d₆-DMSO, δ, ppm, 500 MHz): 4.21 (s, 3H, Me on Mebim-py), 7.63 (m, 2H), 7.76 (t, 1H), 8.00 (d, 2H), 8.43 (td, 1H), 8.51 (d, 1H), 8.66 (d, 1H), 9.40 (d, 1H,

pyridyl-6). IR (CH₂Cl₂, ν_{co}): 2061 cm⁻¹ (st) and 1984 cm⁻¹ (st). IR (ATR, ν_{co}): 2052 cm⁻¹ (st) and 1986 cm⁻¹ (st).

***cis*-Ru(Mebim-py)(CO)₂(OTf)₂, *cis*-2b.** To a sample of Ru(Mebim-py)(CO)₂Cl₂ (est. 97.0 mg, 0.22 mmol) was added AgOTf (125.0 mg, 0.49 mmol, 2.2 equiv) in air. The solids were placed under a nitrogen atmosphere, and after addition of 1,2-dichloroethane (10.0 mL), the reaction was refluxed for 1 h. A cloudy grey suspension formed which was filtered through celite, and solvent was removed under vacuum from the pale golden yellow solution to give an oily off-white residue. The product residue was used without further purification in attempts to make tpy complex **4b**. ¹H NMR (20 °C, CD₂Cl₂, δ , ppm, 600 MHz): 4.30 (s, 3H, Me on Mebim-py), 7.68 (m, 2H), 7.73 (m, 1H), 8.11 (m, 2H), 8.29 (d, 1H), 8.41 (td, 1H), 8.99 (d, 1H, pyridyl-6). ¹⁹F NMR (20 °C, CD₂Cl₂, δ , ppm, 376 MHz): -77.4 (s), -78.1 (s). ¹³C{¹H} NMR (20 °C, CD₂Cl₂, δ , ppm, 151 MHz): 36.0 (Me on Mebim-py), 112.7 (2 C, aromatic Mebim-py overlapped), 113.5 (1 C, aromatic Mebim-py), 118.3 (d, 1 C, J_{CF} = 90 Hz, OTf), 120.4 (d, 1 C, J_{CF} = 90 Hz, OTf), 124.2, 126.8, 127.0, 130.9, 136.2, 144.2, 149.7, 152.6 (8 aromatic carbons on Mebim-py), 184.9 (NCN carbene), 189.6 (CO), 191.9 (CO). IR (1,2-DCE, ν_{co}): 2095 and 2036 cm⁻¹.

Electrochemistry. Cyclic voltammetry experiments were conducted using a glassy carbon working electrode (polished with 0.05 μm alumina powder between scans), quasi-reference Ag wire, and Pt wire auxiliary. Measurements were made under nitrogen gas atmosphere with 100 mM TBAPF₆ as electrolyte in acetonitrile inside a glass vial sealed with Teflon cap (single-compartment). Sample solutions were purged with nitrogen gas for at least 10 min prior to analysis. An internal reference of ferrocene was added to all samples at final concentration 3 mM. All potentials are reported versus internal Fc/Fc⁺ couple (calibrated to 0 V).

4.5. Acknowledgements

We acknowledge Matthew Kita and Prof. Alexander J.M. Miller for the electrochemical analyses. We also acknowledge undergraduate researcher Teddy Wong for assistance in synthesis of $\text{Ru}(\text{Mebim-pic})(\text{CO})_2\text{Cl}_2$ and $[\text{Ru}(\text{Mebim-pic})(\text{bpy}')(\text{CO})_2]^{2+}$ complexes. We also acknowledge Dr. James Muckerman at Brookhaven National Labs, Kyle Duffee, and Prof. Cynthia K. Schauer are acknowledged for computational studies of the $\text{Ru}(\text{Mebim-L})(\text{tpy})$ complexes.

APPENDIX 1.1

CHAPTER 2 ADDITIONAL SPECTROSCOPIC DATA

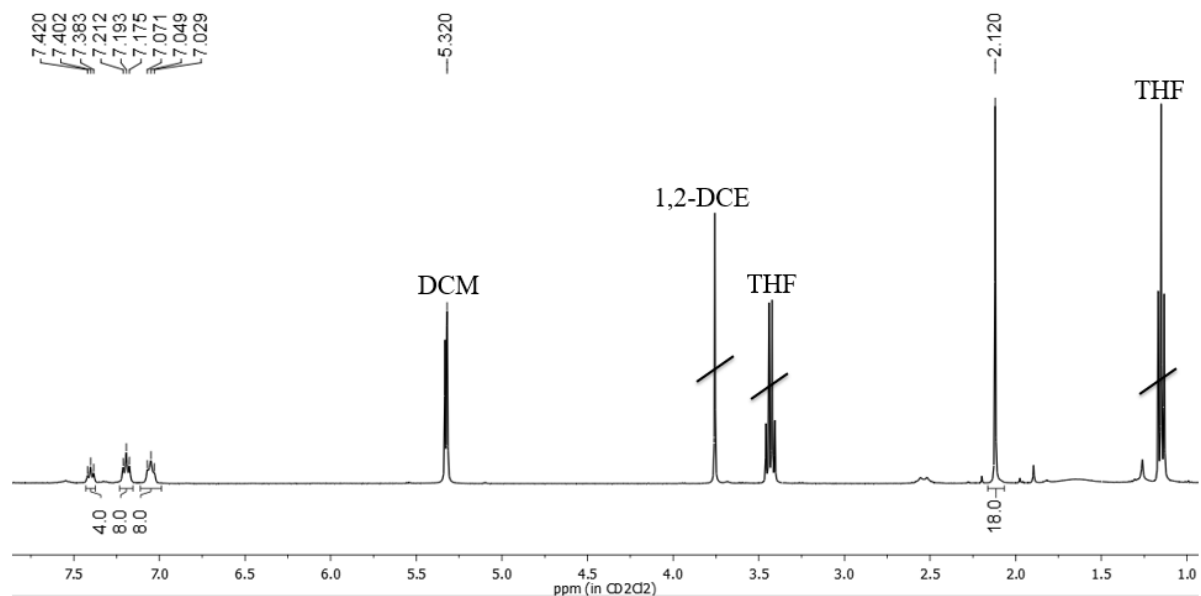


Figure A2.1: ¹H NMR of **2a**⁺ [Mn(CO)(DPPE)(C₆Me₆)] [BF₄] in CD₂Cl₂.

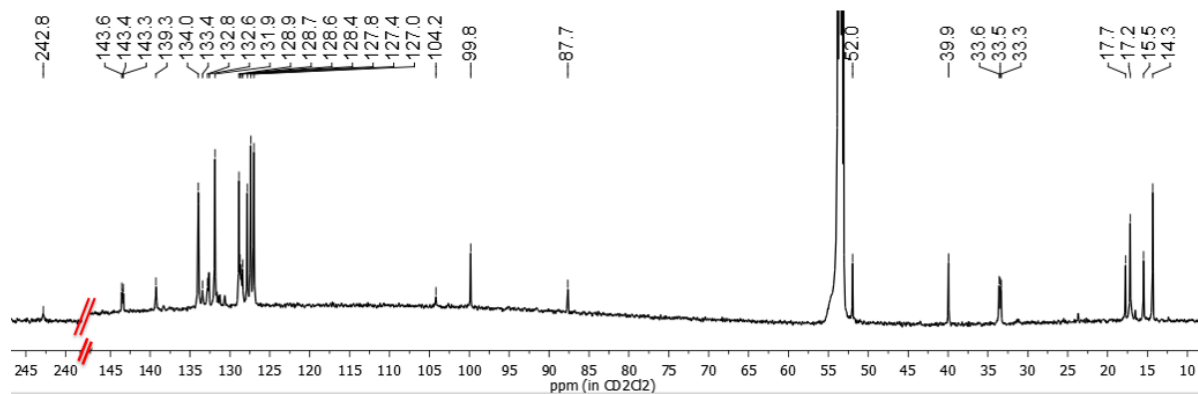


Figure A2.2: ¹³C{¹H} NMR of **1a** Mn(CO)(DPPE)(C₆Me₆H) in CD₂Cl₂.

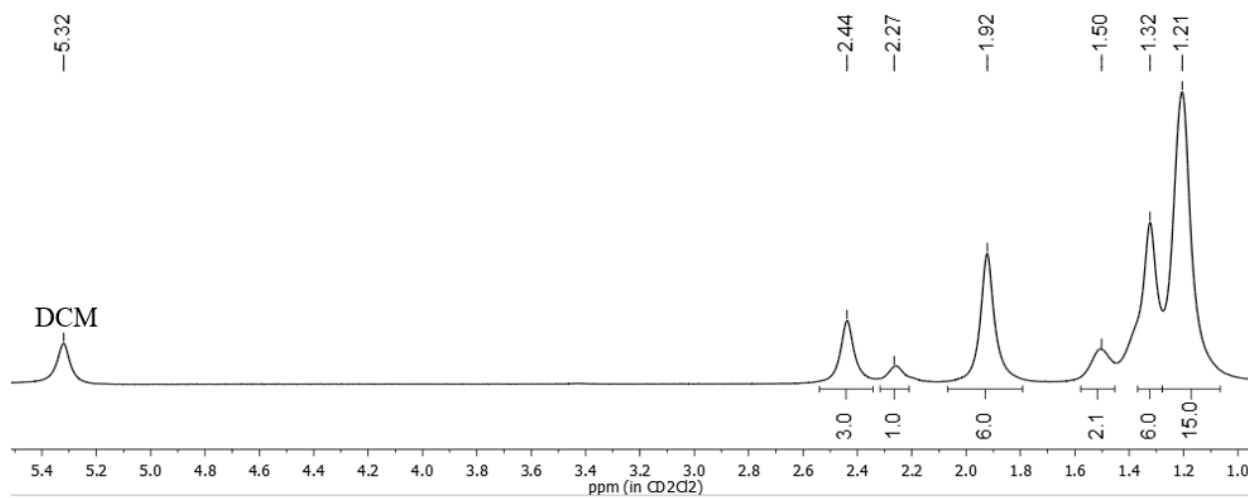


Figure A2.3: ^1H NMR of **1b** $\text{Mn}(\text{CO})(\text{DMPE})(\text{C}_6\text{Me}_6\text{H})$ in CD_2Cl_2 .

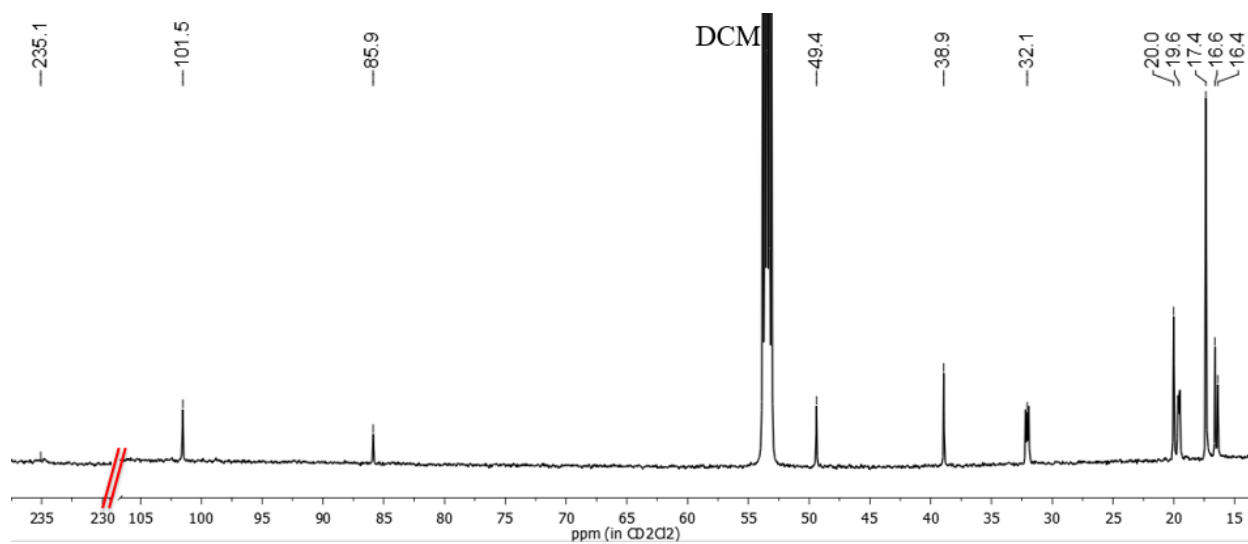


Figure A2.4: $^{13}\text{C}\{^1\text{H}\}$ NMR of **1b** $\text{Mn}(\text{CO})(\text{DMPE})(\text{C}_6\text{Me}_6\text{H})$ in CD_2Cl_2 .

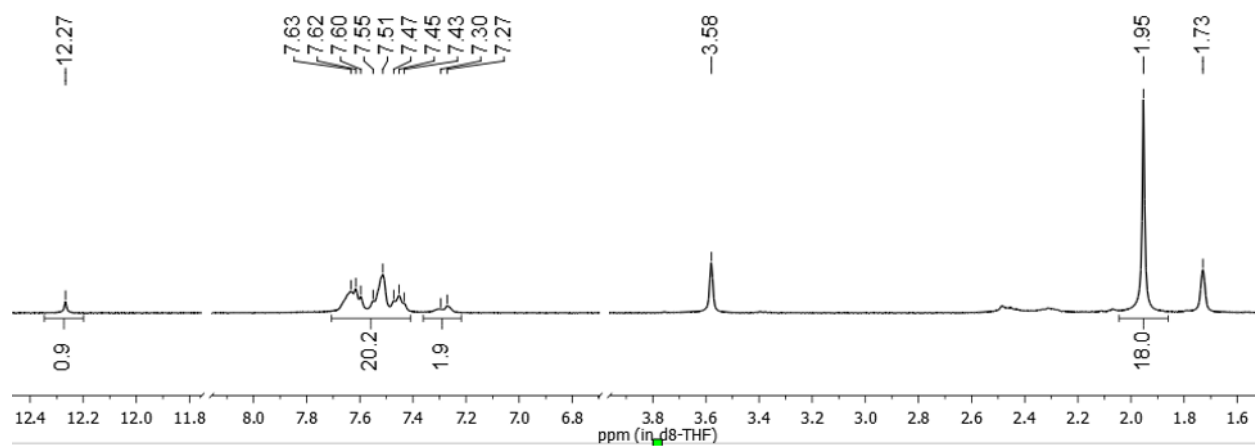


Figure A2.5: ^1H NMR of reaction of **1a** with CS_2 forming **2a**[S_2CH] in $\text{d}_8\text{-THF}$.

APPENDIX 1.2

COMPLETE X-RAY CRYSTALLOGRAPHIC DATA FOR **1B**

x1201021

Table of Crystal data and structure refinement for x1201021

Identification code	x1201021
Empirical formula	C ₁₉ H ₃₅ MnOP ₂
Formula weight	396.35
Temperature/K	100
Crystal system	monoclinic
Space group	P2 ₁ /n
a/Å	8.6431(2)
b/Å	15.4462(4)
c/Å	14.9509(3)
α /°	90.00
β /°	92.4250(10)
γ /°	90.00
Volume/Å ³	1994.20(8)
Z	4
ρ_{calc} /mg/mm ³	1.320
μ /mm ⁻¹	6.899
F(000)	848.0
Crystal size/mm ³	0.402 × 0.391 × 0.115
2 θ range for data collection	8.24 to 140.26°
Index ranges	-10 ≤ h ≤ 10, -18 ≤ k ≤ 18, -18 ≤ l ≤ 17
Reflections collected	17867
Independent reflections	3724[R(int) = 0.0243]
Data/restraints/parameters	3724/0/218
Goodness-of-fit on F ²	1.069
Final R indexes [$I \geq 2\sigma(I)$]	R ₁ = 0.0278, wR ₂ = 0.0737
Final R indexes [all data]	R ₁ = 0.0288, wR ₂ = 0.0744
Largest diff. peak/hole / e Å ⁻³	0.37/-0.38

Table of Fractional Atomic Coordinates ($\times 10^4$) and Equivalent Isotropic Displacement Parameters ($\text{\AA}^2 \times 10^3$) for x1201021. U_{eq} is defined as 1/3 of of the trace of the orthogonalised U_{ij} tensor.

Atom	x	y	z	U_{eq}
Mn1	3815.3 (3)	3046.05 (15)	8184.94 (15)	9.88 (9)
P1	4697.5 (5)	4094.9 (2)	7315.2 (3)	14.73 (11)
P2	2660.1 (4)	4137.6 (2)	8851.6 (3)	14.51 (10)
O1	6542.9 (15)	3307.0 (8)	9390.9 (9)	28.1 (3)
C1	5445.7 (19)	3206.5 (10)	8913.6 (10)	15.8 (3)
C2	6787 (2)	4105.9 (12)	7148.1 (13)	26.9 (4)
C3	3987 (2)	4360.1 (12)	6165.6 (12)	29.7 (4)
C4	4401 (2)	5179.4 (11)	7821.9 (12)	24.1 (4)
C5	3929 (2)	5090.1 (11)	8781.7 (12)	22.4 (4)
C6	2370 (2)	4125.4 (11)	10062.1 (11)	24.3 (4)
C7	778 (2)	4574.9 (11)	8452.5 (13)	26.3 (4)
C8	2137.0 (17)	2280.9 (9)	7427.4 (10)	12.9 (3)
C9	3658.9 (18)	2110.7 (9)	7116.4 (10)	12.8 (3)
C10	4836.3 (18)	1821.3 (10)	7726.7 (11)	14.0 (3)
C11	4354.2 (18)	1306.7 (10)	8538 (1)	16.1 (3)
C12	3141.6 (19)	1887.1 (10)	8935.5 (11)	14.5 (3)
C13	1905.3 (17)	2174.6 (10)	8363.9 (10)	13.4 (3)
C14	802.2 (19)	2517.6 (11)	6782.6 (10)	18.0 (3)
C15	3970.2 (19)	2217.1 (11)	6134.6 (10)	17.8 (3)
C16	6465.7 (18)	1679.9 (11)	7424.7 (11)	18.9 (3)
C17	5696 (2)	1076.4 (11)	9194.8 (11)	22.5 (4)
C18	2924 (2)	1800.2 (11)	9929.9 (11)	20.7 (3)
C19	321.8 (18)	2338.2 (11)	8727.7 (11)	18.3 (3)

Table of Anisotropic Displacement Parameters ($\text{\AA}^2 \times 10^3$) for x1201021. The Anisotropic displacement factor exponent takes the form: $-2\pi^2[h^2a^{*2}U_{11}+...+2hka \times b \times U_{12}]$

Atom	U_{11}	U_{22}	U_{33}	U_{23}	U_{13}	U_{12}
Mn1	9.58 (14)	9.65 (14)	10.39 (13)	-0.76 (8)	0.20 (9)	-0.68 (8)
P1	17.9 (2)	12.5 (2)	13.96 (19)	0.26 (14)	2.14 (15)	-2.30 (14)
P2	13.6 (2)	12.3 (2)	17.8 (2)	-2.85 (14)	3.38 (15)	-0.44 (14)
O1	24.2 (7)	28.6 (7)	30.3 (7)	-1.5 (5)	-14.6 (6)	-0.9 (5)
C1	18.0 (8)	12.4 (7)	17.2 (7)	-0.1 (6)	1.5 (7)	0.7 (6)
C2	22.0 (9)	27.6 (9)	32.0 (9)	2.3 (7)	9.9 (8)	-7.1 (7)
C3	44.2 (11)	23.7 (9)	21.0 (8)	7.0 (7)	-2.7 (8)	-1.9 (8)
C4	30.3 (9)	14.4 (8)	28.2 (9)	-0.9 (7)	6.7 (7)	-3.0 (7)
C5	24.2 (9)	14.1 (8)	29.3 (9)	-6.3 (6)	5.9 (7)	-4.4 (6)

C6	28.3 (9)	25.0 (9)	20.4 (8)	-7.9 (7)	8.9 (7)	-5.2 (7)
C7	19.3 (8)	20.7 (9)	38.9 (10)	-1.2 (7)	0.5 (8)	5.4 (7)
C8	13.0 (7)	10.4 (7)	15.0 (7)	-1.6 (5)	-1.9 (6)	-1.5 (6)
C9	15.5 (7)	9.6 (7)	13.4 (7)	-2.8 (5)	1.0 (6)	-2.3 (6)
C10	12.9 (8)	11.8 (7)	17.1 (7)	-3.1 (6)	0.1 (6)	-0.2 (6)
C11	17.6 (8)	13.4 (7)	17.1 (7)	0.0 (6)	-1.4 (6)	0.9 (6)
C12	16.2 (8)	12.5 (7)	14.7 (7)	0.3 (5)	0.6 (6)	-2.7 (6)
C13	13.3 (7)	10.0 (7)	17.1 (7)	-1.6 (6)	1.2 (6)	-3.6 (6)
C14	14.8 (7)	21.7 (8)	17.3 (7)	0.0 (6)	-2.4 (6)	0.6 (6)
C15	19.4 (8)	19.7 (8)	14.5 (7)	-2.7 (6)	1.9 (6)	-1.5 (6)
C16	14.3 (8)	19.9 (8)	22.5 (8)	-2.4 (6)	1.4 (6)	1.8 (6)
C17	24.2 (9)	19.6 (8)	23.3 (8)	2.2 (7)	-4.3 (7)	6.5 (7)
C18	24.1 (9)	22.8 (8)	15.3 (8)	3.3 (6)	1.8 (7)	-1.6 (7)
C19	14.2 (8)	20.9 (8)	20.1 (8)	-1.2 (6)	2.9 (6)	-3.2 (6)

Table of Bond Lengths for x1201021.

Atom	Atom	Length/Å	Atom	Atom	Length/Å
Mn1	P1	2.2318 (4)	O1	C1	1.173 (2)
Mn1	P2	2.2174 (4)	C4	C5	1.515 (2)
Mn1	C1	1.7619 (17)	C8	C9	1.438 (2)
Mn1	C8	2.1552 (15)	C8	C13	1.432 (2)
Mn1	C9	2.1540 (15)	C8	C14	1.517 (2)
Mn1	C10	2.2086 (15)	C9	C10	1.410 (2)
Mn1	C12	2.2041 (15)	C9	C15	1.512 (2)
Mn1	C13	2.1555 (15)	C10	C11	1.523 (2)
P1	C2	1.8337 (18)	C10	C16	1.513 (2)
P1	C3	1.8465 (18)	C11	C12	1.519 (2)
P1	C4	1.8607 (17)	C11	C17	1.530 (2)
P2	C5	1.8405 (17)	C12	C13	1.411 (2)
P2	C6	1.8377 (17)	C12	C18	1.513 (2)
P2	C7	1.8372 (18)	C13	C19	1.515 (2)

Table of Bond Angles for x1201021.

Atom	Atom	Atom	Angle/°	Atom	Atom	Atom	Angle/°
P2	Mn1	P1	83.188 (17)	C7	P2	C5	102.06 (8)
C1	Mn1	P1	88.52 (5)	C7	P2	C6	99.66 (9)
C1	Mn1	P2	88.78 (5)	O1	C1	Mn1	179.09 (15)
C1	Mn1	C8	154.83 (6)	C5	C4	P1	110.55 (11)
C1	Mn1	C9	125.20 (7)	C4	C5	P2	108.16 (11)
C1	Mn1	C10	89.58 (7)	C9	C8	Mn1	70.46 (8)
C1	Mn1	C12	91.21 (7)	C9	C8	C14	121.35 (13)
C1	Mn1	C13	127.43 (7)	C13	C8	Mn1	70.60 (8)
C8	Mn1	P1	109.32 (4)	C13	C8	C9	117.57 (14)
C8	Mn1	P2	110.33 (4)	C13	C8	C14	121.00 (13)
C8	Mn1	C10	68.66 (6)	C14	C8	Mn1	132.75 (11)
C8	Mn1	C12	68.64 (6)	C8	C9	Mn1	70.55 (8)
C8	Mn1	C13	38.81 (6)	C8	C9	C15	119.78 (14)
C9	Mn1	P1	93.84 (4)	C10	C9	Mn1	73.25 (9)
C9	Mn1	P2	145.90 (4)	C10	C9	C8	119.58 (14)
C9	Mn1	C8	38.98 (6)	C10	C9	C15	120.61 (14)
C9	Mn1	C10	37.70 (6)	C15	C9	Mn1	129.70 (11)
C9	Mn1	C12	79.82 (6)	C9	C10	Mn1	69.05 (9)
C9	Mn1	C13	69.44 (6)	C9	C10	C11	117.80 (14)
C10	Mn1	P1	106.87 (4)	C9	C10	C16	120.53 (14)
C10	Mn1	P2	169.77 (4)	C11	C10	Mn1	94.22 (9)
C12	Mn1	P1	172.03 (4)	C16	C10	Mn1	127.26 (11)
C12	Mn1	P2	104.78 (4)	C16	C10	C11	116.86 (14)
C12	Mn1	C10	65.16 (6)	C10	C11	C17	114.02 (14)
C13	Mn1	P1	143.90 (4)	C12	C11	C10	102.71 (12)
C13	Mn1	P2	93.28 (4)	C12	C11	C17	113.77 (13)
C13	Mn1	C10	79.73 (6)	C11	C12	Mn1	94.51 (9)
C13	Mn1	C12	37.76 (6)	C13	C12	Mn1	69.26 (9)
C2	P1	Mn1	116.67 (6)	C13	C12	C11	117.77 (14)
C2	P1	C3	99.32 (9)	C13	C12	C18	120.03 (14)
C2	P1	C4	101.57 (8)	C18	C12	Mn1	128.25 (11)
C3	P1	Mn1	126.51 (7)	C18	C12	C11	116.67 (14)
C3	P1	C4	97.65 (9)	C8	C13	Mn1	70.58 (8)
C4	P1	Mn1	111.09 (6)	C8	C13	C19	119.84 (14)
C5	P2	Mn1	107.56 (6)	C12	C13	Mn1	72.99 (9)
C6	P2	Mn1	121.18 (6)	C12	C13	C8	119.63 (14)
C6	P2	C5	99.82 (8)	C12	C13	C19	120.49 (14)
C7	P2	Mn1	122.88 (6)	C19	C13	Mn1	130.43 (11)

Table of Torsion Angles for x1201021.

A	B	C	D	Angle/°
Mn1	P1	C4	C5	11.25 (14)
Mn1	P2	C5	C4	48.94 (13)
Mn1	C8	C9	C10	56.51 (13)
Mn1	C8	C9	C15	-125.34 (13)
Mn1	C8	C13	C12	-56.13 (12)
Mn1	C8	C13	C19	126.19 (14)
Mn1	C9	C10	C11	83.53 (12)
Mn1	C9	C10	C16	-121.80 (14)
Mn1	C10	C11	C12	16.18 (12)
Mn1	C10	C11	C17	-107.38 (12)
Mn1	C12	C13	C8	54.97 (12)
Mn1	C12	C13	C19	-127.36 (14)
P1	Mn1	P2	C5	-32.70 (6)
P1	Mn1	P2	C6	-146.31 (7)
P1	Mn1	P2	C7	85.03 (7)
P1	Mn1	C1	O1	-79 (10)
P1	Mn1	C8	C9	71.32 (9)
P1	Mn1	C8	C13	-158.47 (8)
P1	Mn1	C8	C14	-43.76 (15)
P1	Mn1	C9	C8	-116.36 (8)
P1	Mn1	C9	C10	112.87 (8)
P1	Mn1	C9	C15	-3.31 (14)
P1	Mn1	C10	C9	-73.87 (9)
P1	Mn1	C10	C11	167.93 (8)
P1	Mn1	C10	C16	39.22 (14)
P1	Mn1	C12	C11	10.9 (4)
P1	Mn1	C12	C13	-107.1 (3)
P1	Mn1	C12	C18	140.4 (3)
P1	Mn1	C13	C8	36.00 (12)
P1	Mn1	C13	C12	167.00 (7)
P1	Mn1	C13	C19	-77.13 (16)
P1	C4	C5	P2	-36.71 (15)
P2	Mn1	P1	C2	130.15 (7)
P2	Mn1	P1	C3	-103.17 (8)
P2	Mn1	P1	C4	14.41 (7)
P2	Mn1	C1	O1	-162 (10)
P2	Mn1	C8	C9	161.08 (8)
P2	Mn1	C8	C13	-68.71 (9)
P2	Mn1	C8	C14	46.00 (15)
P2	Mn1	C9	C8	-32.84 (12)

P2	Mn1	C9	C10	-163.61 (7)
P2	Mn1	C9	C15	80.21 (16)
P2	Mn1	C10	C9	117.1 (2)
P2	Mn1	C10	C11	-1.1 (3)
P2	Mn1	C10	C16	-129.9 (2)
P2	Mn1	C12	C11	-166.08 (8)
P2	Mn1	C12	C13	75.89 (9)
P2	Mn1	C12	C18	-36.62 (15)
P2	Mn1	C13	C8	118.94 (8)
P2	Mn1	C13	C12	-110.07 (9)
P2	Mn1	C13	C19	5.81 (14)
C1	Mn1	P1	C2	41.21 (9)
C1	Mn1	P1	C3	167.88 (10)
C1	Mn1	P1	C4	-74.53 (8)
C1	Mn1	P2	C5	55.95 (8)
C1	Mn1	P2	C6	-57.66 (9)
C1	Mn1	P2	C7	173.69 (9)
C1	Mn1	C8	C9	-61.64 (18)
C1	Mn1	C8	C13	68.57 (18)
C1	Mn1	C8	C14	-176.72 (15)
C1	Mn1	C9	C8	152.74 (9)
C1	Mn1	C9	C10	21.98 (12)
C1	Mn1	C9	C15	-94.21 (15)
C1	Mn1	C10	C9	-162.19 (10)
C1	Mn1	C10	C11	79.61 (10)
C1	Mn1	C10	C16	-49.11 (14)
C1	Mn1	C12	C11	-77.03 (10)
C1	Mn1	C12	C13	164.94 (10)
C1	Mn1	C12	C18	52.43 (15)
C1	Mn1	C13	C8	-150.09 (9)
C1	Mn1	C13	C12	-19.10 (12)
C1	Mn1	C13	C19	96.78 (15)
C2	P1	C4	C5	-113.50 (13)
C3	P1	C4	C5	145.29 (13)
C6	P2	C5	C4	176.23 (12)
C7	P2	C5	C4	-81.59 (13)
C8	Mn1	P1	C2	-120.65 (8)
C8	Mn1	P1	C3	6.02 (9)
C8	Mn1	P1	C4	123.61 (8)
C8	Mn1	P2	C5	-140.83 (8)
C8	Mn1	P2	C6	105.56 (8)
C8	Mn1	P2	C7	-23.09 (9)

C8	Mn1	C1	O1	57(10)
C8	Mn1	C9	C10	-130.76(13)
C8	Mn1	C9	C15	113.05(18)
C8	Mn1	C10	C9	30.77(9)
C8	Mn1	C10	C11	-87.43(10)
C8	Mn1	C10	C16	143.85(15)
C8	Mn1	C12	C11	87.50(10)
C8	Mn1	C12	C13	-30.53(9)
C8	Mn1	C12	C18	-143.04(16)
C8	Mn1	C13	C12	131.00(13)
C8	Mn1	C13	C19	-113.12(18)
C8	C9	C10	Mn1	-55.21(12)
C8	C9	C10	C11	28.3(2)
C8	C9	C10	C16	-177.01(14)
C9	Mn1	P1	C2	-83.97(8)
C9	Mn1	P1	C3	42.70(9)
C9	Mn1	P1	C4	160.28(8)
C9	Mn1	P2	C5	-119.49(10)
C9	Mn1	P2	C6	126.90(10)
C9	Mn1	P2	C7	-1.75(11)
C9	Mn1	C1	O1	15(10)
C9	Mn1	C8	C13	130.21(13)
C9	Mn1	C8	C14	-115.08(18)
C9	Mn1	C10	C11	-118.20(13)
C9	Mn1	C10	C16	113.09(17)
C9	Mn1	C12	C11	48.56(10)
C9	Mn1	C12	C13	-69.47(9)
C9	Mn1	C12	C18	178.02(16)
C9	Mn1	C13	C8	-30.87(9)
C9	Mn1	C13	C12	100.13(10)
C9	Mn1	C13	C19	-143.99(16)
C9	C8	C13	Mn1	54.28(12)
C9	C8	C13	C12	-1.8(2)
C9	C8	C13	C19	-179.52(13)
C9	C10	C11	C12	-52.33(17)
C9	C10	C11	C17	-175.89(14)
C10	Mn1	P1	C2	-47.90(8)
C10	Mn1	P1	C3	78.77(9)
C10	Mn1	P1	C4	-163.65(8)
C10	Mn1	P2	C5	136.8(2)
C10	Mn1	P2	C6	23.2(3)
C10	Mn1	P2	C7	-105.5(3)

C10	Mn1	C1	O1	28 (10)
C10	Mn1	C8	C9	-29.82 (9)
C10	Mn1	C8	C13	100.39 (10)
C10	Mn1	C8	C14	-144.90 (16)
C10	Mn1	C9	C8	130.76 (13)
C10	Mn1	C9	C15	-116.19 (18)
C10	Mn1	C12	C11	11.95 (9)
C10	Mn1	C12	C13	-106.08 (10)
C10	Mn1	C12	C18	141.41 (16)
C10	Mn1	C13	C8	-68.60 (9)
C10	Mn1	C13	C12	62.39 (9)
C10	Mn1	C13	C19	178.27 (15)
C10	C11	C12	Mn1	-16.22 (12)
C10	C11	C12	C13	52.68 (17)
C10	C11	C12	C18	-153.49 (13)
C11	C12	C13	Mn1	-84.01 (12)
C11	C12	C13	C8	-29.0 (2)
C11	C12	C13	C19	148.63 (14)
C12	Mn1	P1	C2	-46.9 (3)
C12	Mn1	P1	C3	79.8 (3)
C12	Mn1	P1	C4	-162.7 (3)
C12	Mn1	P2	C5	146.88 (8)
C12	Mn1	P2	C6	33.27 (8)
C12	Mn1	P2	C7	-95.39 (9)
C12	Mn1	C1	O1	93 (10)
C12	Mn1	C8	C9	-100.46 (10)
C12	Mn1	C8	C13	29.75 (9)
C12	Mn1	C8	C14	144.46 (16)
C12	Mn1	C9	C8	68.51 (9)
C12	Mn1	C9	C10	-62.25 (9)
C12	Mn1	C9	C15	-178.44 (15)
C12	Mn1	C10	C9	106.28 (10)
C12	Mn1	C10	C11	-11.91 (9)
C12	Mn1	C10	C16	-140.63 (15)
C12	Mn1	C13	C8	-131.00 (13)
C12	Mn1	C13	C19	115.88 (18)
C13	Mn1	P1	C2	-143.63 (10)
C13	Mn1	P1	C3	-16.95 (11)
C13	Mn1	P1	C4	100.63 (10)
C13	Mn1	P2	C5	-176.63 (8)
C13	Mn1	P2	C6	69.76 (8)
C13	Mn1	P2	C7	-58.89 (8)

C13	Mn1	C1	O1	105 (10)
C13	Mn1	C8	C9	-130.21 (13)
C13	Mn1	C8	C14	114.71 (18)
C13	Mn1	C9	C8	30.74 (9)
C13	Mn1	C9	C10	-100.02 (10)
C13	Mn1	C9	C15	143.79 (15)
C13	Mn1	C10	C9	69.56 (9)
C13	Mn1	C10	C11	-48.63 (9)
C13	Mn1	C10	C16	-177.35 (15)
C13	Mn1	C12	C11	118.03 (13)
C13	Mn1	C12	C18	-112.51 (18)
C13	C8	C9	Mn1	-54.35 (12)
C13	C8	C9	C10	2.2 (2)
C13	C8	C9	C15	-179.69 (13)
C14	C8	C9	Mn1	128.84 (14)
C14	C8	C9	C10	-174.65 (14)
C14	C8	C9	C15	3.5 (2)
C14	C8	C13	Mn1	-128.90 (14)
C14	C8	C13	C12	174.97 (14)
C14	C8	C13	C19	-2.7 (2)
C15	C9	C10	Mn1	126.65 (14)
C15	C9	C10	C11	-149.82 (14)
C15	C9	C10	C16	4.9 (2)
C16	C10	C11	C12	152.07 (13)
C16	C10	C11	C17	28.50 (19)
C17	C11	C12	Mn1	107.51 (12)
C17	C11	C12	C13	176.41 (14)
C17	C11	C12	C18	-29.8 (2)
C18	C12	C13	Mn1	123.08 (14)
C18	C12	C13	C8	178.05 (14)
C18	C12	C13	C19	-4.3 (2)

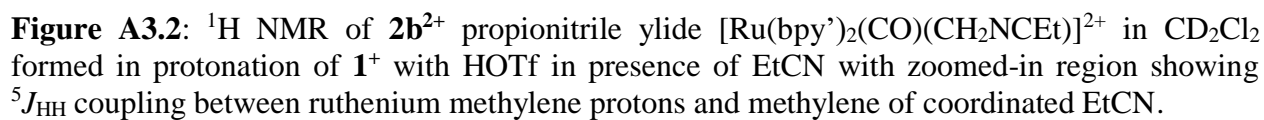
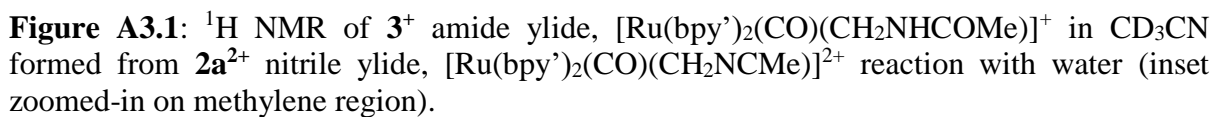
Table of Hydrogen Atom Coordinates ($\text{\AA} \times 10^4$) and Isotropic Displacement Parameters ($\text{\AA}^2 \times 10^3$) for x1201021.

Atom	<i>x</i>	<i>y</i>	<i>z</i>	U(eq)
H2A	7349	4119	7731	40
H2B	7053	4620	6803	40
H2C	7076	3584	6821	40
H3A	4362	3926	5749	45
H3B	4369	4933	6000	45
H3C	2852	4362	6138	45
H4A	5371	5518	7805	29
H4B	3586	5495	7470	29
H5A	3372	5617	8967	27
H5B	4858	5016	9185	27
H6A	1481	3757	10186	37
H6B	2174	4716	10269	37
H6C	3300	3897	10377	37
H7A	782	4664	7804	39
H7B	593	5129	8749	39
H7C	-43	4165	8592	39
H11	3843	759	8325	19
H14A	545	3131	6854	27
H14B	-102	2163	6910	27
H14C	1101	2412	6167	27
H15A	3204	2613	5858	27
H15B	3897	1653	5837	27
H15C	5011	2455	6073	27
H16A	6685	2094	6949	28
H16B	6563	1088	7197	28
H16C	7204	1766	7932	28
H17A	6436	707	8895	34
H17B	5296	767	9708	34
H17C	6216	1608	9402	34
H18A	3926	1866	10255	31
H18B	2492	1228	10056	31
H18C	2212	2250	10124	31
H19A	439	2638	9304	28
H19B	-208	1785	8810	28
H19C	-290	2698	8304	28

Crystal Data. $\text{C}_{19}\text{H}_{35}\text{MnOP}_2$, $M = 396.35$, monoclinic, $a = 8.6431(2) \text{ \AA}$, $b = 15.4462(4) \text{ \AA}$, $c = 14.9509(3) \text{ \AA}$, $\beta = 92.4250(10)^\circ$, $V = 1994.20(8) \text{ \AA}^3$, $T = 100$, space group $\text{P2}_1/\text{n}$ (no. 14), $Z = 4$, $\mu(\text{CuK}\alpha) = 6.899$, 17867 reflections measured, 3724 unique ($R_{\text{int}} = 0.0243$) which were used in all calculations. The final wR_2 was 0.0744 (all data) and R_1 was 0.0278 ($>2\sigma(I)$).

This report has been created with Olex2, compiled on Jan 17 2012 15:45:47.

CHAPTER 3 ADDITIONAL SPECTROSCOPIC DATA



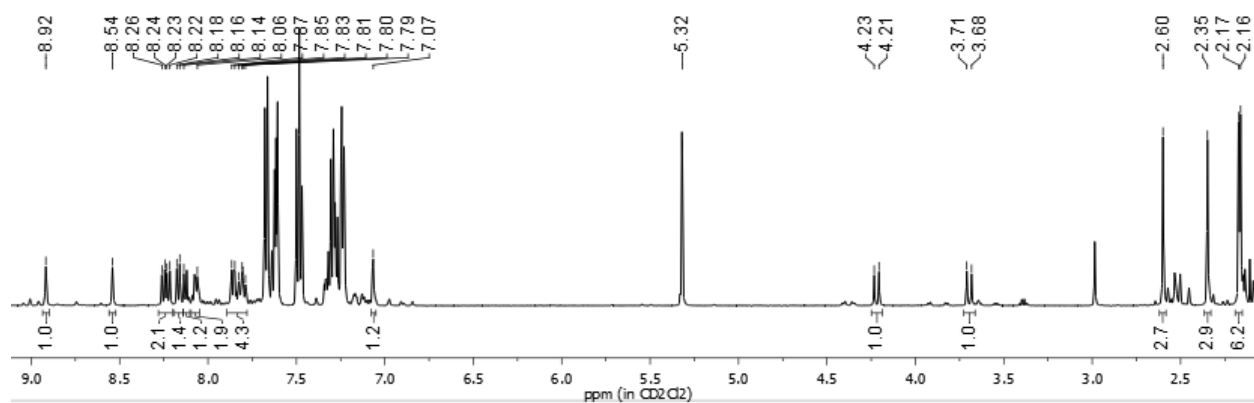


Figure A3.3: ^1H NMR of 2c^{2+} benzonitrile ylide $[\text{Ru}(\text{bpy}')_2(\text{CO})(\text{CH}_2\text{NCPh})]^{2+}$ in CD_2Cl_2 formed in hydroxide abstraction from 1^+ at 243K.

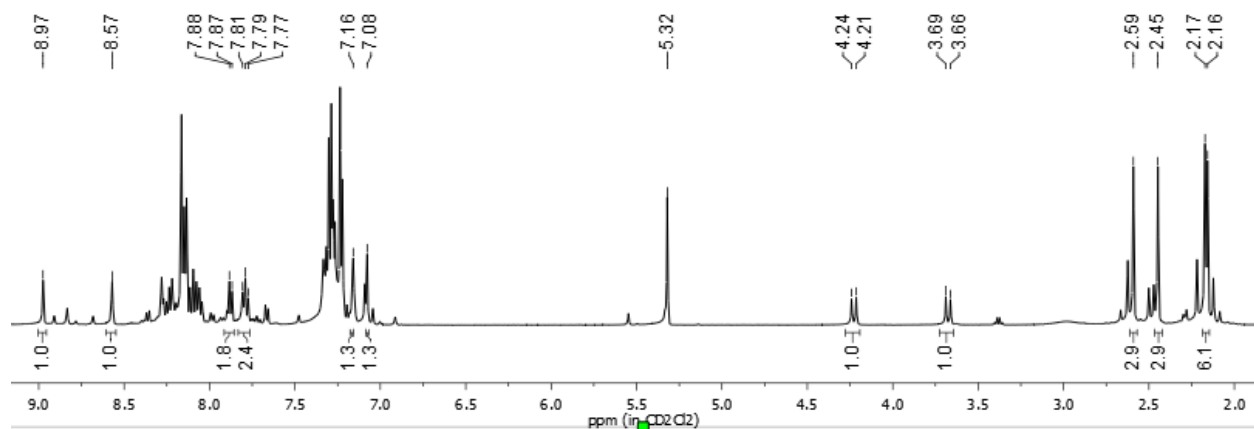


Figure A3.4: ^1H NMR of 2d^{2+} fluorinated benzonitrile ylide $[\text{Ru}(\text{bpy}')_2(\text{CO})(\text{CH}_2\text{NCAr}^{\text{F}})]^{2+}$ in CD_2Cl_2 formed in hydroxide abstraction from 1^+ at 233K.

Schauer_MDM247 #1-250 RT: 0.00-3.74 AV: 250 NL: 2.41E6
T: FTMS + p ESI Full ms [50.00-1000.00]

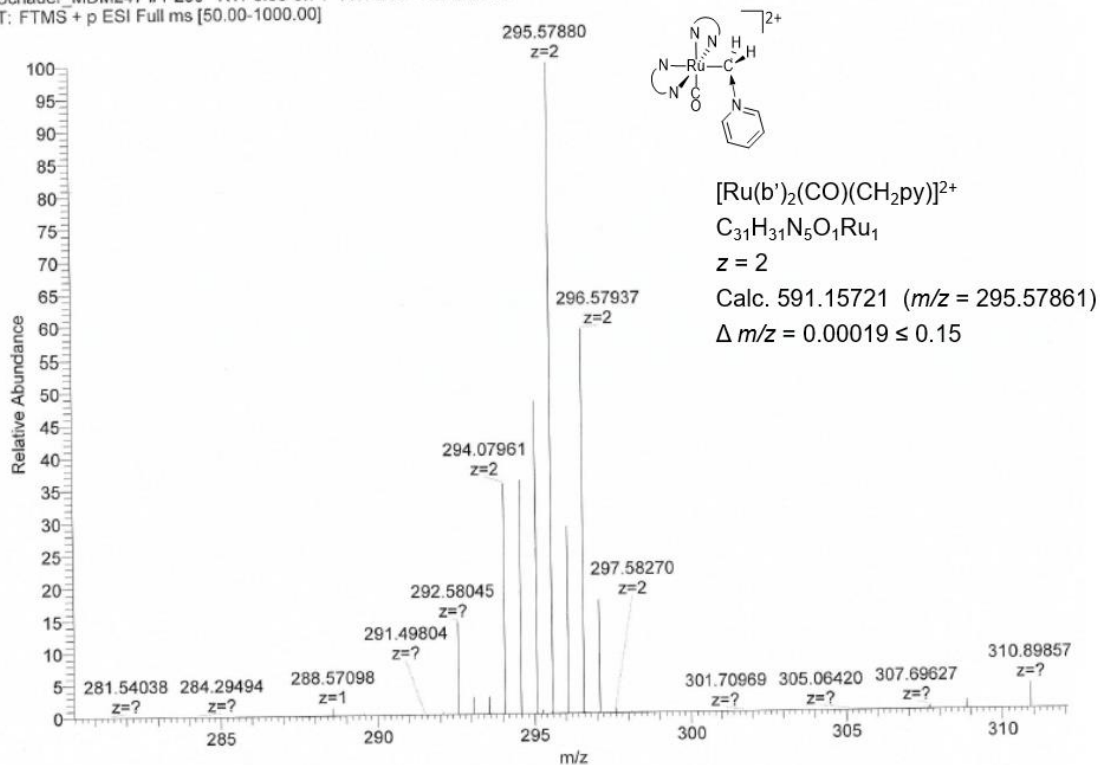


Figure A3.5: Mass spectroscopic data of 4a^{2+} pyridine ylide $[\text{Ru}(\text{bpy}')_2(\text{CO})(\text{CH}_2\text{py})]^{2+}$ in DCM formed in hydroxide abstraction from 1^+ .

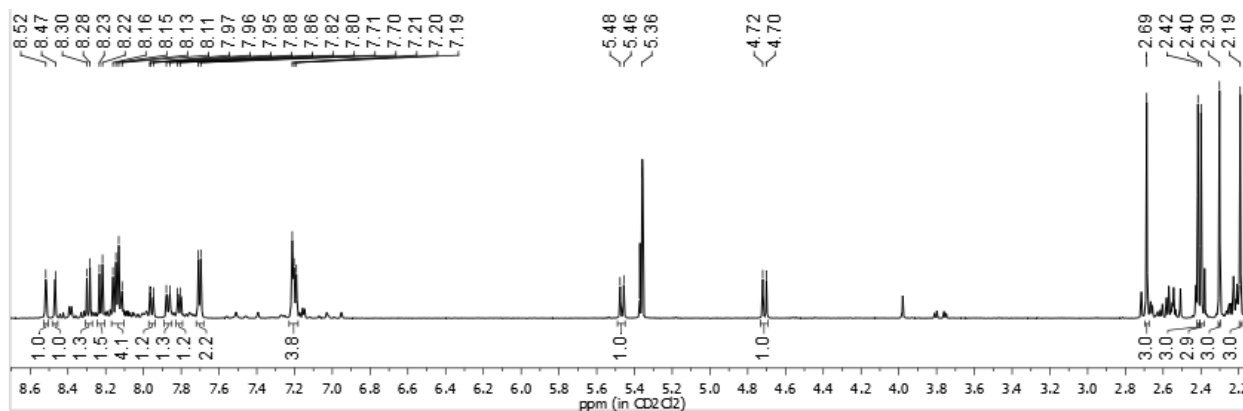
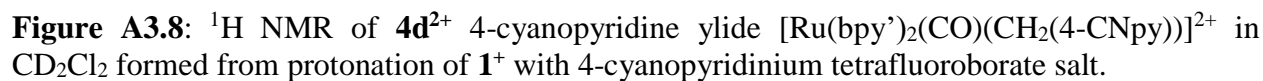
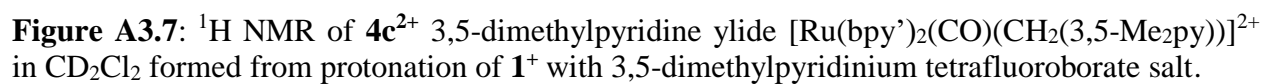


Figure A3.6: ^1H NMR of 4b^{2+} 4-methylpyridine ylide $[\text{Ru}(\text{bpy}')_2(\text{CO})(\text{CH}_2(4\text{-Mepy}))]^{2+}$ in CD_2Cl_2 formed in protonation of 1^+ in the presence of 4-methylpyridine.



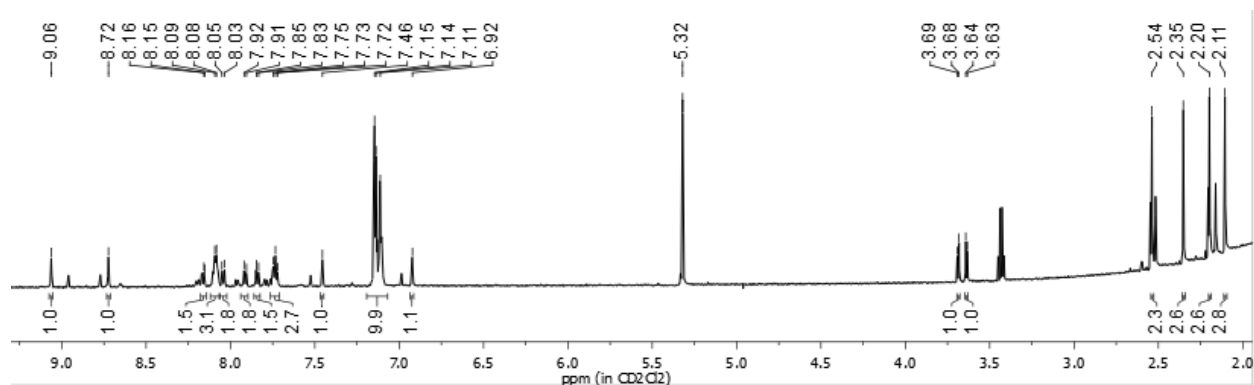


Figure A3.9: ¹H NMR of **5**⁺ orange crystal triphenylmethoxymethyl [Ru(bpy')₂(CO)(CH₂OCPh₃)] [PF₆]•CH₂Cl₂ in CD₂Cl₂.

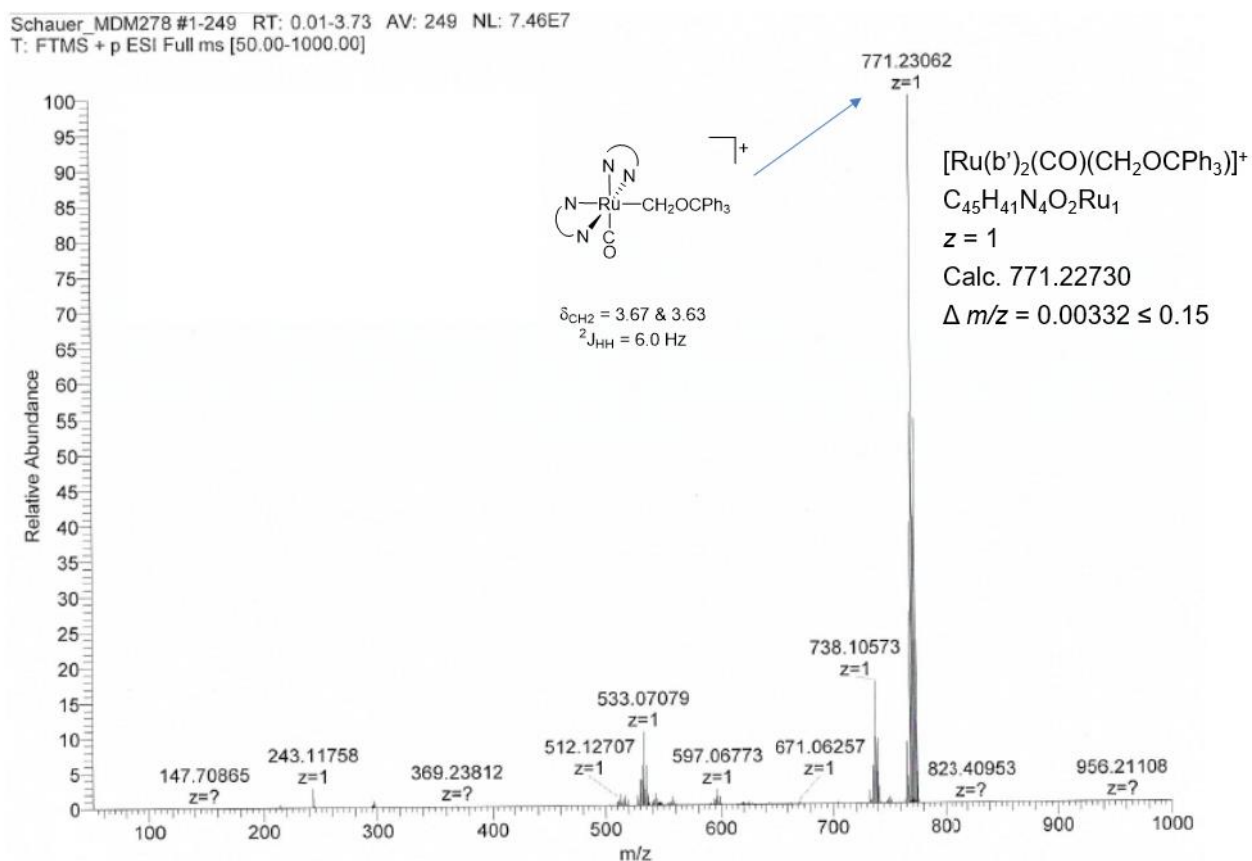


Figure A3.10: Mass spectroscopy data of **5**⁺ orange crystal triphenylmethoxymethyl [Ru(bpy')₂(CO)(CH₂OCPh₃)] [PF₆]•CH₂Cl₂ in DCM.

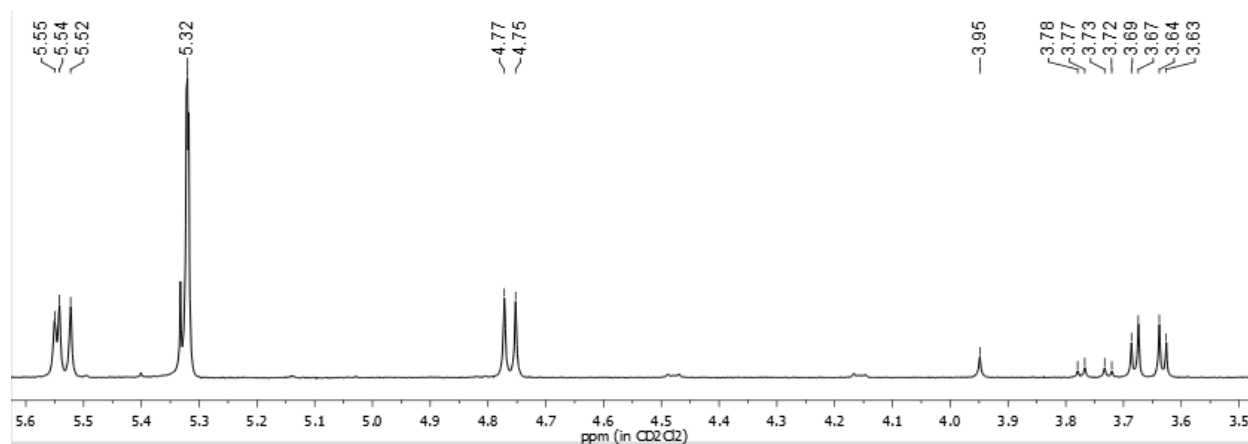


Figure A3.11: ^1H NMR of methylene region for hydroxide abstraction from $\mathbf{1}^+$ in presence of pyridines noting formation of minor products $\mathbf{5}^+$ (at 3.78 – 3.72 ppm) and dimer $\mathbf{8}^{2+}$ (at 3.95 and 3.69 – 3.63 ppm) along with major product $\mathbf{4a}^{2+}$ (at 5.53 and 4.76 ppm) in CD_2Cl_2 .

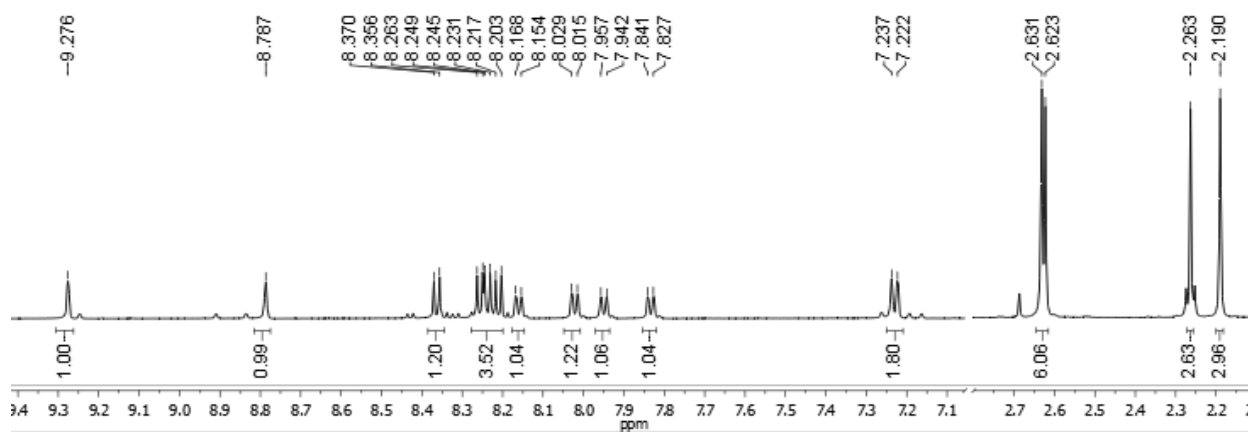


Figure A3.12: ^1H NMR of $\mathbf{7}^+$ formed in protonation of $[\text{Ru}(\text{bpy}')_2(\text{CO})\text{H}]\text{PF}_6$ with HOTf in d_4 -1,2-DCE

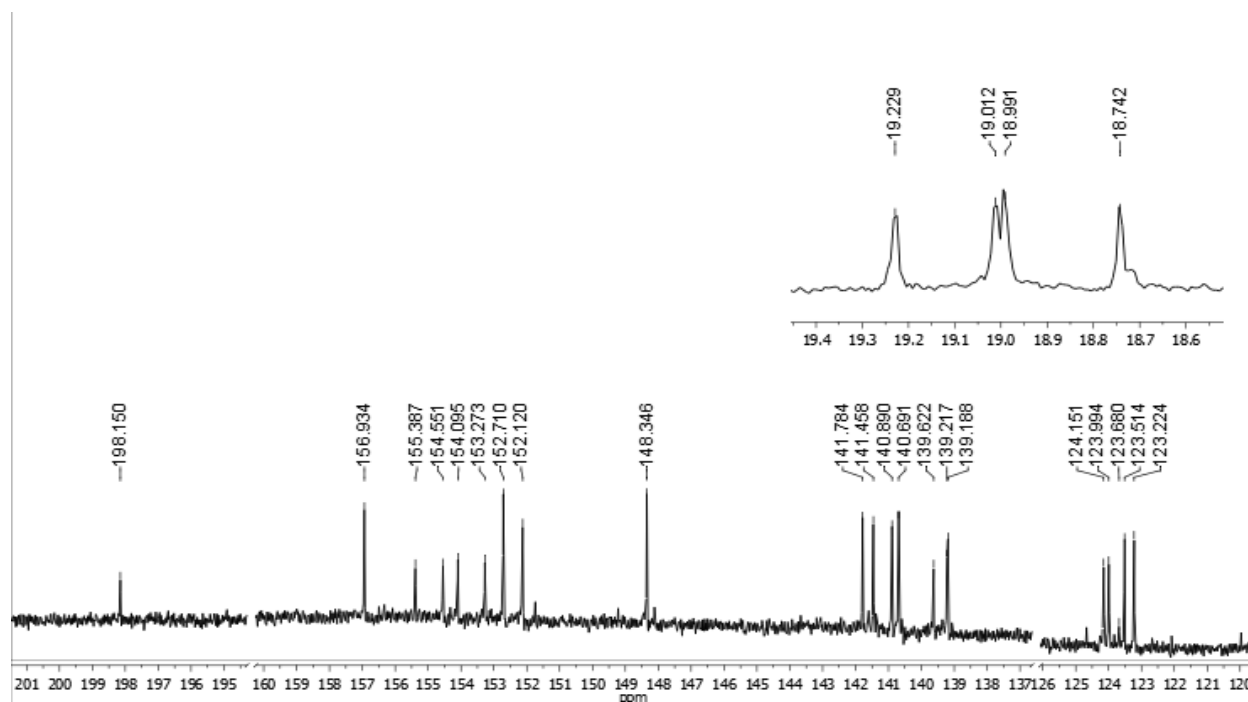


Figure A3.13: $^{13}\text{C}\{^1\text{H}\}$ NMR of 7^+ formed in protonation of 1^+ with HOTf in presence of ethylene in CD_2Cl_2 .

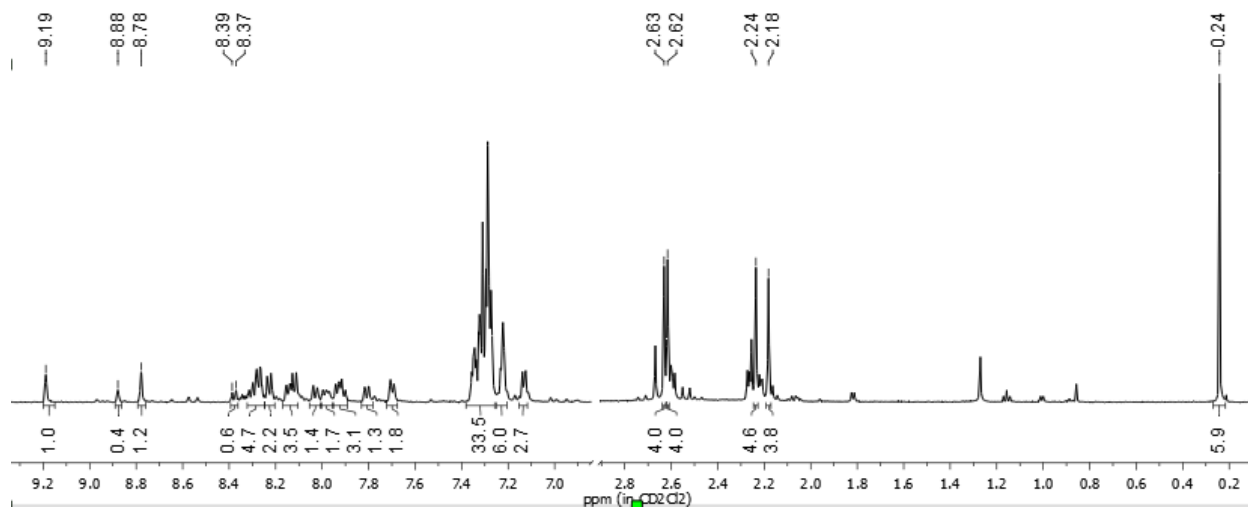


Figure A3.14: ^1H NMR reaction forming cyclopropane (at 0.24 ppm) via hydroxide abstraction using trityl cation from 1^+ under ethylene atmosphere in CD_2Cl_2 with major Ru product as unknown **9** (indicative resonances downfield at 9.19 and 8.78 ppm).

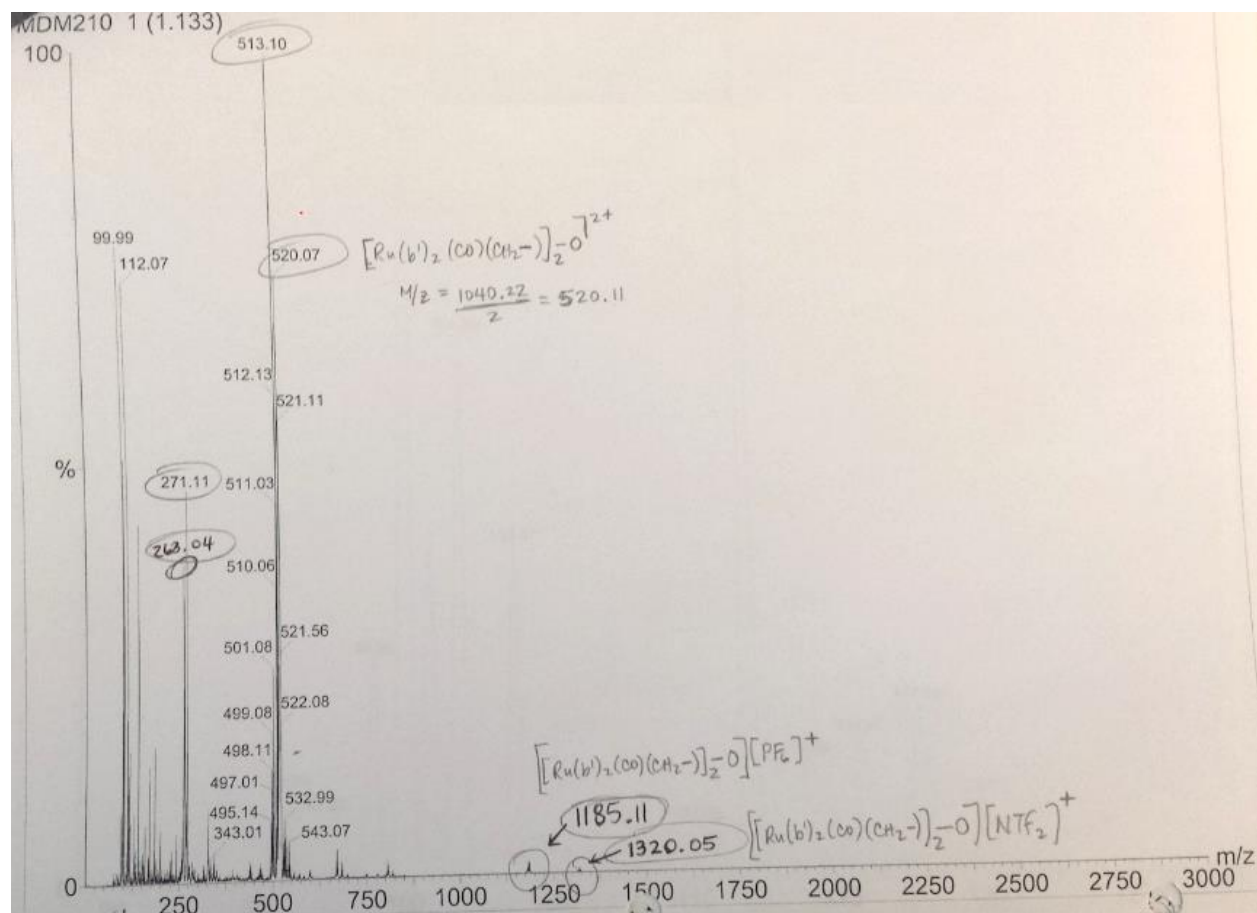


Figure A3.15: Mass spectroscopic data for ether-bridged dimer 8^{2+} complex in CH_2Cl_2 .

APPENDIX 2.2

COMPLETE X-RAY CRYSTALLOGRAPHIC DATA FOR **5⁺**

x1505009

Table of Crystal data and structure refinement for x1505009.

Identification code	x1505009
Empirical formula	C ₄₆ H ₄₃ Cl ₂ F ₆ N ₄ O ₂ PRu
Formula weight	1000.78
Temperature/K	100
Crystal system	monoclinic
Space group	P2 ₁ /c
a/Å	16.2910(10)
b/Å	14.9484(10)
c/Å	18.5327(12)
α/°	90
β/°	108.149(3)
γ/°	90
Volume/Å ³	4288.6(5)
Z	4
ρ _{calc} /g/cm ³	1.550
μ/mm ⁻¹	5.066
F(000)	2040.0
Crystal size/mm ³	0.142 × 0.134 × 0.108
Radiation	CuKα (λ = 1.54178)
2θ range for data collection/°	5.708 to 140.49
Index ranges	-19 ≤ h ≤ 19, -18 ≤ k ≤ 18, -21 ≤ l ≤ 19
Reflections collected	64649
Independent reflections	8013 [R _{int} = 0.0785, R _{sigma} = 0.0444]
Data/restraints/parameters	8013/130/618
Goodness-of-fit on F ²	1.089
Final R indexes [I ≥ 2σ (I)]	R ₁ = 0.0672, wR ₂ = 0.1891
Final R indexes [all data]	R ₁ = 0.0762, wR ₂ = 0.1955
Largest diff. peak/hole / e Å ⁻³	1.16/-1.63

Table of Fractional Atomic Coordinates ($\times 10^4$) and Equivalent Isotropic Displacement Parameters ($\text{\AA}^2 \times 10^3$) for x1505009. U_{eq} is defined as 1/3 of of the trace of the orthogonalised U_{ij} tensor.

Atom	<i>x</i>	<i>y</i>	<i>z</i>	$U(eq)$
Ru1	2663.4 (2)	8966.3 (3)	3739.1 (2)	24.66 (15)
C2	3223 (4)	9439 (4)	3102 (3)	30.4 (12)
O3	3570 (3)	9695 (3)	2686 (2)	44.8 (11)
N4	2615 (3)	10146 (3)	4403 (3)	30.8 (10)
C5	1978 (4)	10757 (4)	4252 (4)	36.4 (13)
C6	1926 (5)	11415 (5)	4764 (4)	46.0 (16)
C7	2554 (5)	11421 (5)	5459 (4)	52.3 (18)
C8	3213 (5)	10802 (5)	5623 (4)	46.3 (16)
C9	3244 (4)	10177 (4)	5077 (3)	32.1 (12)
C10	3934 (4)	9504 (4)	5186 (3)	31.3 (12)
C11	4687 (4)	9515 (4)	5799 (4)	38.9 (14)
C12	5317 (4)	8879 (5)	5850 (4)	43.2 (15)
C13	5189 (4)	8230 (5)	5295 (4)	42.8 (15)
C14	4422 (4)	8250 (4)	4699 (3)	35.3 (13)
N15	3808 (3)	8868 (3)	4641 (3)	28.9 (10)
C16	1180 (5)	12066 (5)	4558 (6)	65 (2)
C17	5860 (5)	7512 (5)	5325 (5)	55.4 (19)
N18	1446 (3)	9077 (3)	2963 (3)	31.4 (10)
C19	1251 (4)	9502 (4)	2294 (3)	39.7 (14)
C20	425 (5)	9528 (5)	1782 (4)	50.1 (17)
C21	-218 (4)	9083 (5)	1969 (4)	54.7 (19)
C22	-37 (4)	8644 (5)	2650 (4)	47.4 (16)
C23	803 (4)	8646 (4)	3152 (3)	34.5 (13)
C24	1044 (4)	8252 (4)	3909 (3)	33.4 (12)
C25	467 (4)	7795 (5)	4195 (4)	44.8 (15)
C26	757 (5)	7474 (5)	4930 (4)	48.1 (17)
C27	1588 (4)	7620 (4)	5382 (4)	40.8 (14)
C28	2137 (4)	8058 (4)	5043 (3)	36.7 (13)
N29	1881 (3)	8361 (3)	4329 (3)	28.3 (10)
C30	252 (6)	10064 (7)	1047 (4)	69 (2)
C31	1905 (6)	7339 (5)	6191 (4)	54.8 (19)
C32	2786 (4)	7709 (4)	3262 (3)	29.8 (11)
O33	2749 (3)	6989 (3)	3761 (3)	45.9 (11)
C34	2803 (5)	6099 (4)	3489 (4)	45.9 (16)
C35	2037 (5)	5912 (5)	2757 (4)	50.3 (17)
C36	1235 (5)	6308 (5)	2701 (4)	52.1 (17)
C37	527 (5)	6122 (5)	2080 (5)	60 (2)
C38	588 (5)	5581 (5)	1533 (4)	50.3 (17)

C39	1338 (6)	5142 (6)	1548 (5)	69 (2)
C40	2084 (6)	5313 (5)	2200 (5)	62 (2)
C41	2666 (5)	5450 (5)	4096 (4)	49.0 (16)
C42	2632 (4)	4557 (5)	3982 (4)	44.4 (15)
C43	2505 (5)	3972 (5)	4520 (5)	54.2 (19)
C44	2396 (5)	4300 (6)	5182 (5)	64 (2)
C45	2398 (6)	5167 (6)	5295 (5)	69 (2)
C46	2551 (6)	5754 (6)	4758 (5)	63 (2)
C47	3697 (5)	5955 (5)	3402 (4)	51.1 (17)
C48	4394 (5)	5711 (5)	4042 (5)	54.7 (18)
C49	5219 (5)	5671 (6)	4017 (5)	61 (2)
C50	5384 (6)	5868 (6)	3324 (6)	69 (2)
C51	4732 (7)	6089 (7)	2714 (6)	80 (3)
C52	3885 (6)	6166 (6)	2733 (5)	63 (2)
P1	2173.1 (10)	2141.6 (12)	2341.3 (10)	40.0 (4)
F2	1269 (3)	1733 (4)	2375 (4)	61.2 (17)
F3	2674 (5)	1500 (6)	3024 (4)	70 (2)
F4	1623 (6)	2742 (7)	1645 (5)	84 (3)
F5	2074 (6)	2829 (6)	2960 (5)	91 (2)
F6	3041 (4)	2534 (6)	2296 (6)	101 (3)
F7	2203 (6)	1369 (7)	1763 (5)	103 (3)
F8	1777 (19)	3026 (12)	1907 (15)	50 (5)
F9	1476 (11)	1654 (12)	1840 (11)	80 (5)
F10	2724 (11)	1947 (13)	1806 (10)	50 (4)
F11	2913 (15)	2720 (17)	2917 (15)	77 (5)
F12	1631 (15)	2373 (15)	2846 (10)	64 (5)
F13	2535 (16)	1268 (17)	2759 (14)	56 (5)
Cl1	5112 (2)	6757 (3)	7891 (2)	118.1 (12)
Cl2	4243 (2)	6749 (2)	6260.9 (19)	108 (1)
C53	5210 (9)	6473 (11)	7052 (7)	112 (4)

Table of Anisotropic Displacement Parameters ($\text{\AA}^2 \times 10^3$) for x1505009. The Anisotropic displacement factor exponent takes the form: $-\pi^2 [h^2 a^{*2} U_{11} + 2hka^*b^* U_{12} + \dots]$.

Atom	U ₁₁	U ₂₂	U ₃₃	U ₂₃	U ₁₃	U ₁₂
Ru1	21.8 (2)	29.0 (2)	22.3 (2)	1.65 (14)	5.67 (16)	-0.65 (15)
C2	29 (3)	32 (3)	27 (3)	1 (2)	5 (2)	0 (2)
O3	47 (3)	54 (3)	39 (3)	6 (2)	21 (2)	-9 (2)
N4	31 (2)	32 (2)	31 (3)	1.1 (19)	12.0 (19)	-3.5 (19)
C5	32 (3)	36 (3)	43 (4)	4 (3)	14 (3)	0 (2)
C6	49 (4)	39 (3)	60 (4)	-3 (3)	31 (3)	5 (3)
C7	59 (4)	52 (4)	50 (4)	-19 (3)	25 (4)	1 (4)

C8	52 (4)	54 (4)	34 (4)	-12 (3)	15 (3)	-9 (3)
C9	35 (3)	34 (3)	28 (3)	1 (2)	11 (2)	-6 (2)
C10	31 (3)	34 (3)	28 (3)	3 (2)	7 (2)	-8 (2)
C11	34 (3)	45 (4)	33 (3)	1 (3)	4 (2)	-7 (3)
C12	30 (3)	52 (4)	40 (4)	4 (3)	0 (3)	-9 (3)
C13	28 (3)	45 (4)	51 (4)	8 (3)	5 (3)	3 (3)
C14	26 (3)	42 (3)	35 (3)	3 (2)	6 (2)	0 (2)
N15	27 (2)	30 (2)	30 (3)	3.6 (18)	8.8 (19)	-4.1 (18)
C16	59 (5)	50 (5)	91 (6)	-11 (4)	28 (4)	13 (4)
C17	35 (4)	63 (5)	61 (5)	4 (4)	4 (3)	12 (3)
N18	26 (2)	31 (2)	35 (3)	-2.7 (19)	5.9 (19)	1.7 (19)
C19	35 (3)	47 (4)	32 (3)	0 (3)	3 (2)	2 (3)
C20	50 (4)	48 (4)	40 (4)	-3 (3)	-4 (3)	5 (3)
C21	29 (3)	68 (5)	52 (4)	-4 (4)	-8 (3)	4 (3)
C22	29 (3)	49 (4)	57 (4)	-6 (3)	4 (3)	-2 (3)
C23	25 (3)	36 (3)	40 (3)	-6 (2)	6 (2)	-2 (2)
C24	27 (3)	33 (3)	40 (3)	-5 (2)	10 (2)	-2 (2)
C25	35 (3)	49 (4)	56 (4)	-7 (3)	22 (3)	-10 (3)
C26	47 (4)	47 (4)	62 (5)	-2 (3)	34 (3)	-12 (3)
C27	52 (4)	38 (3)	40 (4)	-1 (3)	24 (3)	-6 (3)
C28	39 (3)	40 (3)	32 (3)	-3 (2)	13 (2)	-9 (3)
N29	29 (2)	28 (2)	29 (2)	-4.5 (18)	11.2 (19)	-3.8 (18)
C30	59 (5)	87 (6)	43 (4)	12 (4)	-12 (4)	7 (4)
C31	76 (5)	52 (4)	46 (4)	5 (3)	33 (4)	-7 (4)
C32	34 (3)	30 (3)	25 (3)	-1 (2)	7 (2)	2 (2)
O33	53 (3)	41 (3)	45 (3)	6.8 (19)	17 (2)	1 (2)
C34	56 (4)	41 (4)	40 (4)	2 (3)	14 (3)	6 (3)
C35	56 (4)	40 (4)	56 (5)	3 (3)	19 (3)	3 (3)
C36	59 (4)	44 (4)	51 (4)	4 (3)	15 (3)	0 (3)
C37	50 (4)	46 (4)	74 (6)	7 (4)	6 (4)	-8 (3)
C38	48 (4)	39 (4)	52 (4)	-4 (3)	0 (3)	2 (3)
C39	80 (6)	50 (5)	71 (6)	-6 (4)	16 (5)	8 (4)
C40	66 (5)	52 (5)	60 (5)	1 (4)	8 (4)	10 (4)
C41	45 (4)	48 (4)	52 (4)	9 (3)	12 (3)	5 (3)
C42	36 (3)	44 (4)	51 (4)	4 (3)	10 (3)	6 (3)
C43	37 (4)	44 (4)	77 (6)	9 (3)	9 (3)	6 (3)
C44	56 (5)	68 (5)	72 (6)	33 (4)	23 (4)	8 (4)
C45	95 (7)	63 (5)	56 (5)	16 (4)	35 (5)	27 (5)
C46	83 (6)	59 (5)	54 (5)	19 (4)	30 (4)	13 (4)
C47	56 (4)	49 (4)	47 (4)	5 (3)	15 (3)	7 (3)
C48	54 (4)	52 (4)	57 (5)	8 (3)	17 (4)	8 (3)
C49	54 (5)	69 (5)	58 (5)	1 (4)	13 (4)	9 (4)

C50	59 (5)	80 (6)	75 (6)	7 (5)	32 (5)	15 (4)
C51	89 (7)	99 (8)	71 (6)	12 (5)	51 (6)	29 (6)
C52	62 (5)	80 (6)	50 (5)	18 (4)	21 (4)	15 (4)
P1	31.0 (8)	45.4 (9)	41.0 (9)	9.7 (7)	7.3 (6)	8.6 (7)
F2	45 (3)	70 (4)	72 (4)	9 (3)	21 (3)	0 (2)
F3	57 (4)	98 (6)	50 (4)	20 (3)	9 (3)	33 (4)
F4	49 (4)	133 (7)	72 (5)	55 (4)	21 (4)	24 (4)
F5	87 (5)	81 (5)	94 (5)	-25 (4)	15 (4)	4 (4)
F6	39 (3)	128 (6)	132 (7)	51 (5)	19 (3)	-2 (3)
F7	94 (5)	136 (6)	84 (5)	-35 (4)	34 (4)	21 (5)
F8	47 (9)	52 (7)	53 (9)	18 (6)	18 (7)	14 (6)
F9	65 (7)	84 (9)	80 (9)	1 (6)	6 (6)	-4 (6)
F10	61 (8)	47 (8)	44 (7)	24 (6)	17 (6)	24 (6)
F11	65 (8)	80 (9)	75 (9)	-13 (7)	6 (6)	-3 (6)
F12	63 (9)	70 (10)	64 (8)	30 (6)	26 (7)	24 (7)
F13	62 (10)	49 (7)	51 (10)	14 (6)	11 (7)	7 (6)
Cl1	75.8 (18)	160 (3)	115 (3)	18 (2)	23.7 (16)	-0.4 (19)
Cl2	84.1 (18)	113 (2)	113 (2)	41.1 (18)	9.5 (16)	-9.5 (16)
C53	117 (10)	139 (12)	83 (8)	-1 (8)	36 (7)	-27 (9)

Table 4 Bond Lengths for x1505009.

Atom	Atom	Length/Å	Atom	Atom	Length/Å
Ru1	C2	1.842 (6)	C32	O33	1.433 (7)
Ru1	N4	2.166 (5)	O33	C34	1.433 (8)
Ru1	N15	2.086 (5)	C34	C35	1.557 (10)
Ru1	N18	2.062 (5)	C34	C41	1.554 (10)
Ru1	N29	2.123 (4)	C34	C47	1.529 (11)
Ru1	C32	2.113 (5)	C35	C36	1.408 (11)
C2	O3	1.154 (7)	C35	C40	1.386 (11)
N4	C5	1.345 (8)	C36	C37	1.380 (11)
N4	C9	1.347 (7)	C37	C38	1.325 (11)
C5	C6	1.387 (9)	C38	C39	1.378 (11)
C6	C7	1.374 (11)	C39	C40	1.446 (12)
C6	C16	1.510 (10)	C41	C42	1.350 (10)
C7	C8	1.377 (11)	C41	C46	1.374 (11)
C8	C9	1.389 (9)	C42	C43	1.390 (10)
C9	C10	1.474 (8)	C43	C44	1.382 (12)
C10	C11	1.388 (8)	C44	C45	1.313 (13)
C10	N15	1.356 (7)	C45	C46	1.406 (11)
C11	C12	1.381 (10)	C47	C48	1.411 (10)
C12	C13	1.383 (10)	C47	C52	1.403 (11)
C13	C14	1.387 (8)	C48	C49	1.360 (11)
C13	C17	1.520 (9)	C49	C50	1.423 (12)
C14	N15	1.341 (7)	C50	C51	1.330 (14)
N18	C19	1.339 (8)	C51	C52	1.395 (13)
N18	C23	1.366 (8)	P1	F2	1.614 (6)
C19	C20	1.384 (9)	P1	F3	1.595 (7)
C20	C21	1.374 (11)	P1	F4	1.598 (8)
C20	C30	1.528 (10)	P1	F5	1.584 (8)
C21	C22	1.369 (11)	P1	F6	1.558 (7)
C22	C23	1.395 (8)	P1	F7	1.587 (8)
C23	C24	1.458 (9)	P1	F8	1.58 (2)
C24	C25	1.392 (9)	P1	F9	1.423 (16)
C24	N29	1.354 (7)	P1	F10	1.559 (17)
C25	C26	1.382 (10)	P1	F11	1.59 (2)
C26	C27	1.369 (10)	P1	F12	1.513 (18)
C27	C28	1.403 (8)	P1	F13	1.54 (2)
C27	C31	1.487 (10)	Cl1	C53	1.667 (13)
C28	N29	1.336 (8)	Cl2	C53	1.834 (14)

Table of Bond Angles for x1505009.

Atom	Atom	Atom	Angle/°	Atom	Atom	Atom	Angle/°
C2	Ru1	N4	99.5 (2)	O33	C32	Ru1	111.7 (4)
C2	Ru1	N15	92.5 (2)	C32	O33	C34	116.8 (5)
C2	Ru1	N18	94.7 (2)	O33	C34	C35	110.6 (5)
C2	Ru1	N29	171.8 (2)	O33	C34	C41	106.7 (6)
C2	Ru1	C32	86.7 (2)	O33	C34	C47	109.5 (6)
N15	Ru1	N4	77.53 (18)	C41	C34	C35	105.2 (6)
N15	Ru1	N29	94.99 (17)	C47	C34	C35	114.4 (6)
N15	Ru1	C32	95.5 (2)	C47	C34	C41	110.1 (6)
N18	Ru1	N4	97.67 (18)	C36	C35	C34	117.5 (7)
N18	Ru1	N15	171.92 (18)	C40	C35	C34	123.3 (7)
N18	Ru1	N29	78.04 (19)	C40	C35	C36	118.9 (7)
N18	Ru1	C32	88.6 (2)	C37	C36	C35	119.4 (8)
N29	Ru1	N4	85.43 (17)	C38	C37	C36	121.3 (8)
C32	Ru1	N4	170.76 (19)	C37	C38	C39	123.5 (7)
C32	Ru1	N29	89.25 (19)	C38	C39	C40	116.3 (8)
O3	C2	Ru1	176.6 (5)	C35	C40	C39	120.6 (8)
C5	N4	Ru1	126.7 (4)	C42	C41	C34	120.8 (7)
C5	N4	C9	119.0 (5)	C42	C41	C46	117.2 (7)
C9	N4	Ru1	113.8 (4)	C46	C41	C34	122.0 (7)
N4	C5	C6	123.1 (6)	C41	C42	C43	121.1 (7)
C5	C6	C16	120.0 (7)	C44	C43	C42	120.2 (7)
C7	C6	C5	117.4 (6)	C45	C44	C43	119.8 (8)
C7	C6	C16	122.6 (7)	C44	C45	C46	119.7 (8)
C6	C7	C8	120.3 (6)	C41	C46	C45	121.9 (8)
C7	C8	C9	119.6 (6)	C48	C47	C34	119.4 (7)
N4	C9	C8	120.6 (6)	C52	C47	C34	122.6 (7)
N4	C9	C10	115.5 (5)	C52	C47	C48	117.4 (7)
C8	C9	C10	123.9 (6)	C49	C48	C47	121.9 (8)
C11	C10	C9	123.1 (5)	C48	C49	C50	119.3 (8)
N15	C10	C9	116.4 (5)	C51	C50	C49	119.5 (8)
N15	C10	C11	120.5 (6)	C50	C51	C52	122.3 (9)
C12	C11	C10	119.8 (6)	C51	C52	C47	119.6 (8)
C11	C12	C13	119.7 (6)	F3	P1	F2	89.3 (4)
C12	C13	C14	117.9 (6)	F3	P1	F4	176.4 (5)
C12	C13	C17	121.9 (6)	F4	P1	F2	87.4 (4)
C14	C13	C17	120.2 (6)	F5	P1	F2	85.3 (4)
N15	C14	C13	122.9 (6)	F5	P1	F3	87.6 (4)
C10	N15	Ru1	115.9 (4)	F5	P1	F4	93.6 (5)
C14	N15	Ru1	124.8 (4)	F5	P1	F7	172.8 (5)
C14	N15	C10	119.2 (5)	F6	P1	F2	179.2 (5)

C19	N18	Ru1	125.7 (4)	F6	P1	F3	91.2 (5)
C19	N18	C23	118.7 (5)	F6	P1	F4	92.0 (5)
C23	N18	Ru1	115.5 (4)	F6	P1	F5	95.4 (5)
N18	C19	C20	123.3 (6)	F6	P1	F7	91.1 (5)
C19	C20	C30	119.8 (7)	F7	P1	F2	88.3 (4)
C21	C20	C19	117.8 (7)	F7	P1	F3	89.0 (5)
C21	C20	C30	122.3 (7)	F7	P1	F4	89.5 (5)
C22	C21	C20	120.1 (6)	F8	P1	F11	89.5 (13)
C21	C22	C23	119.9 (7)	F9	P1	F8	88.9 (9)
N18	C23	C22	120.1 (6)	F9	P1	F10	89.4 (8)
N18	C23	C24	116.1 (5)	F9	P1	F11	176.7 (12)
C22	C23	C24	123.7 (6)	F9	P1	F12	91.1 (9)
C25	C24	C23	123.6 (6)	F9	P1	F13	89.8 (9)
N29	C24	C23	115.2 (5)	F10	P1	F8	93.2 (13)
N29	C24	C25	121.2 (6)	F10	P1	F11	93.6 (13)
C26	C25	C24	118.8 (6)	F12	P1	F8	84.2 (13)
C27	C26	C25	121.1 (6)	F12	P1	F10	177.4 (10)
C26	C27	C28	116.6 (6)	F12	P1	F11	85.9 (13)
C26	C27	C31	122.5 (6)	F12	P1	F13	95.1 (14)
C28	C27	C31	120.9 (6)	F13	P1	F8	178.5 (14)
N29	C28	C27	123.7 (6)	F13	P1	F10	87.4 (13)
C24	N29	Ru1	114.5 (4)	F13	P1	F11	91.8 (13)
C28	N29	Ru1	127.1 (4)	Cl1	C53	Cl2	112.4 (8)
C28	N29	C24	118.4 (5)				

Table of Torsion Angles for x1505009.

A	B	C	D	Angle/°	A	B	C	D	Angle/°
Ru1	N4	C5	C6	169.4 (5)	C25	C26	C27	C28	-4.0 (10)
Ru1	N4	C9	C8	-168.6 (5)	C25	C26	C27	C31	175.7 (7)
Ru1	N4	C9	C10	10.4 (6)	C26	C27	C28	N29	2.7 (10)
Ru1	N18	C19	C20	177.6 (5)	C27	C28	N29	Ru1	-176.4 (5)
Ru1	N18	C23	C22	-177.1 (5)	C27	C28	N29	C24	0.9 (9)
Ru1	N18	C23	C24	6.5 (7)	N29	C24	C25	C26	1.9 (10)
Ru1	C32	O33	C34	178.5 (4)	C30	C20	C21	C22	-177.2 (8)
N4	C5	C6	C7	-1.2 (10)	C31	C27	C28	N29	-177.1 (6)
N4	C5	C6	C16	-178.7 (6)	C32	O33	C34	C35	-61.2 (7)
N4	C9	C10	C11	171.0 (5)	C32	O33	C34	C41	-175.1 (5)
N4	C9	C10	N15	-7.7 (7)	C32	O33	C34	C47	65.8 (7)
C5	N4	C9	C8	3.1 (8)	O33	C34	C35	C36	-34.5 (9)
C5	N4	C9	C10	-177.8 (5)	O33	C34	C35	C40	151.9 (7)
C5	C6	C7	C8	1.4 (11)	O33	C34	C41	C42	176.2 (6)
C6	C7	C8	C9	0.5 (11)	O33	C34	C41	C46	-2.1 (10)
C7	C8	C9	N4	-2.9 (10)	O33	C34	C47	C48	83.2 (8)
C7	C8	C9	C10	178.2 (6)	O33	C34	C47	C52	-88.2 (9)
C8	C9	C10	C11	-10.0 (9)	C34	C35	C36	C37	-176.6 (6)
C8	C9	C10	N15	171.3 (6)	C34	C35	C40	C39	177.4 (7)
C9	N4	C5	C6	-1.1 (9)	C34	C41	C42	C43	-179.7 (6)
C9	C10	C11	C12	-178.0 (6)	C34	C41	C46	C45	177.8 (8)
C9	C10	N15	Ru1	0.7 (6)	C34	C47	C48	C49	-172.5 (8)
C9	C10	N15	C14	178.4 (5)	C34	C47	C52	C51	174.6 (8)
C10	C11	C12	C13	-0.6 (10)	C35	C34	C41	C42	58.6 (8)
C11	C10	N15	Ru1	-178.0 (4)	C35	C34	C41	C46	-119.6 (8)
C11	C10	N15	C14	-0.3 (8)	C35	C34	C47	C48	-152.0 (7)
C11	C12	C13	C14	0.3 (10)	C35	C34	C47	C52	36.6 (10)
C11	C12	C13	C17	-179.8 (7)	C35	C36	C37	C38	-0.3 (12)
C12	C13	C14	N15	0.1 (9)	C36	C35	C40	C39	4.0 (12)
C13	C14	N15	Ru1	177.4 (5)	C36	C37	C38	C39	2.3 (13)
C13	C14	N15	C10	0.0 (8)	C37	C38	C39	C40	-1.0 (13)
N15	C10	C11	C12	0.6 (9)	C38	C39	C40	C35	-2.1 (13)
C16	C6	C7	C8	178.9 (7)	C40	C35	C36	C37	-2.7 (11)
C17	C13	C14	N15	-179.9 (6)	C41	C34	C35	C36	80.3 (7)
N18	C19	C20	C21	-1.0 (11)	C41	C34	C35	C40	-93.3 (8)
N18	C19	C20	C30	177.3 (7)	C41	C34	C47	C48	-33.8 (9)
N18	C23	C24	C25	179.5 (6)	C41	C34	C47	C52	154.8 (8)
N18	C23	C24	N29	-0.3 (8)	C41	C42	C43	C44	1.2 (11)
C19	N18	C23	C22	0.7 (9)	C42	C41	C46	C45	-0.5 (13)
C19	N18	C23	C24	-175.7 (5)	C42	C43	C44	C45	1.0 (12)

C19 C20 C21 C22	1.1 (11)	C43 C44 C45 C46	-2.9 (14)
C20 C21 C22 C23	-0.4 (11)	C44 C45 C46 C41	2.7 (15)
C21 C22 C23 N18	-0.6 (10)	C46 C41 C42 C43	-1.4 (11)
C21 C22 C23 C24	175.6 (6)	C47 C34 C35 C36	-158.7 (6)
C22 C23 C24 C25	3.2 (10)	C47 C34 C35 C40	27.7 (10)
C22 C23 C24 N29	-176.6 (6)	C47 C34 C41 C42	-65.1 (9)
C23 N18 C19 C20	0.1 (9)	C47 C34 C41 C46	116.7 (8)
C23 C24 C25 C26	-177.9 (6)	C47 C48 C49 C50	-0.9 (13)
C23 C24 N29 Ru1	-5.8 (6)	C48 C47 C52 C51	3.0 (13)
C23 C24 N29 C28	176.5 (5)	C48 C49 C50 C51	0.1 (14)
C24 C25 C26 C27	1.9 (10)	C49 C50 C51 C52	2.3 (16)
C25 C24 N29 Ru1	174.4 (5)	C50 C51 C52 C47	-3.9 (16)
C25 C24 N29 C28	-3.3 (8)	C52 C47 C48 C49	-0.7 (12)

Table of Hydrogen Atom Coordinates ($\text{\AA} \times 10^4$) and Isotropic Displacement Parameters ($\text{\AA}^2 \times 10^3$) for x1505009.

Atom	x	y	z	U(eq)
H5	1542	10737	3772	44
H7	2534	11853	5829	63
H8	3644	10803	6106	56
H11	4768	9960	6181	47
H12	5836	8887	6266	52
H14	4327	7807	4314	42
H16A	1151	12368	4081	98
H16B	1265	12511	4963	98
H16C	640	11741	4497	98
H17A	6433	7732	5619	83
H17B	5855	7368	4808	83
H17C	5723	6974	5567	83
H19	1701	9800	2166	48
H21	-789	9079	1626	66
H22	-483	8340	2780	57
H25	-115	7707	3890	54
H26	374	7146	5125	58
H28	2723	8144	5338	44
H30A	645	10577	1135	104
H30B	-347	10276	885	104
H30C	347	9681	651	104
H31A	2506	7137	6316	82
H31B	1546	6848	6274	82
H31C	1873	7846	6516	82
H32A	2317	7637	2775	36

H32B	3344	7685	3153	36
H36	1182	6701	3088	63
H37	-14	6387	2044	71
H38	89	5490	1108	60
H39	1362	4750	1152	83
H40	2612	5013	2248	75
H42	2696	4325	3525	53
H43	2494	3345	4434	65
H44	2319	3899	5553	77
H45	2297	5397	5738	83
H46	2577	6379	4856	76
H48	4285	5571	4504	66
H49	5679	5513	4457	74
H50	5957	5842	3298	83
H51	4846	6197	2250	96
H52	3439	6361	2296	76
H53A	5321	5822	7048	134
H53B	5714	6788	6981	134

Table of Atomic Occupancy for x1505009.

Atom	Occupancy	Atom	Occupancy	Atom	Occupancy
F2	0.776 (8)	F3	0.776 (8)	F4	0.776 (8)
F5	0.776 (8)	F6	0.776 (8)	F7	0.776 (8)
F8	0.224 (8)	F9	0.224 (8)	F10	0.224 (8)
F11	0.224 (8)	F12	0.224 (8)	F13	0.224 (8)

Crystal structure determination of [x1505009]

Crystal Data for $C_{46}H_{43}Cl_2F_6N_4O_2PRu$ ($M = 1000.78$ g/mol): monoclinic, space group $P2_1/c$ (no. 14), $a = 16.2910(10)$ Å, $b = 14.9484(10)$ Å, $c = 18.5327(12)$ Å, $\beta = 108.149(3)^\circ$, $V = 4288.6(5)$ Å³, $Z = 4$, $T = 100$ K, $\mu(\text{CuK}\alpha) = 5.066$ mm⁻¹, $D_{\text{calc}} = 1.550$ g/cm³, 64649 reflections measured ($5.708^\circ \leq 2\theta \leq 140.49^\circ$), 8013 unique ($R_{\text{int}} = 0.0785$, $R_{\text{sigma}} = 0.0444$) which were used in all calculations. The final R_1 was 0.0672 ($I > 2\sigma(I)$) and wR_2 was 0.1955 (all data).

Refinement model description

Number of restraints - 130, number of constraints - unknown.

Details:

1. Fixed Uiso
At 1.2 times of:
All C(H) groups, All C(H,H) groups
At 1.5 times of:

All C(H,H,H) groups

2. Restrained distances

F9-F8
2.09 with sigma of 0.01

F12-F9
2.09 with sigma of 0.01

F10-F9
2.09 with sigma of 0.01

F13-F9
2.09 with sigma of 0.01

3. Rigid body (RIGU) restrains

P1
with sigma for 1-2 distances of 0.004 and sigma for 1-3 distances of 0.004

P1
with sigma for 1-2 distances of 0.004 and sigma for 1-3 distances of 0.004

P1, F2, F3, F4, F5, F6, F7, F8, F9, F10, F11, F12, F13
with sigma for 1-2 distances of 0.004 and sigma for 1-3 distances of 0.004

4. Others

Sof(F8)=Sof(F9)=Sof(F10)=Sof(F11)=Sof(F12)=Sof(F13)=1-FVAR(1)
Sof(F2)=Sof(F3)=Sof(F4)=Sof(F5)=Sof(F6)=Sof(F7)=FVAR(1)

5.a Secondary CH2 refined with riding coordinates:
C32(H32A,H32B), C53(H53A,H53B)

5.b Aromatic/amide H refined with riding coordinates:
C5(H5), C7(H7), C8(H8), C11(H11), C12(H12), C14(H14), C19(H19), C21(H21),
C22(H22), C25(H25), C26(H26), C28(H28), C36(H36), C37(H37), C38(H38), C39(H39),
C40(H40), C42(H42), C43(H43), C44(H44), C45(H45), C46(H46), C48(H48),
C49(H49), C50(H50), C51(H51), C52(H52)

5.c Idealised Me refined as rotating group:
C16(H16A,H16B,H16C), C17(H17A,H17B,H17C), C30(H30A,H30B,H30C), C31(H31A,H31B,
H31C)

This report has been created with Olex2, compiled on 2015.01.26 svn.r3150 for OlexSys.

APPENDIX 3.1

CHAPTER 4 ADDITIONAL SPECTROSCOPIC DATA

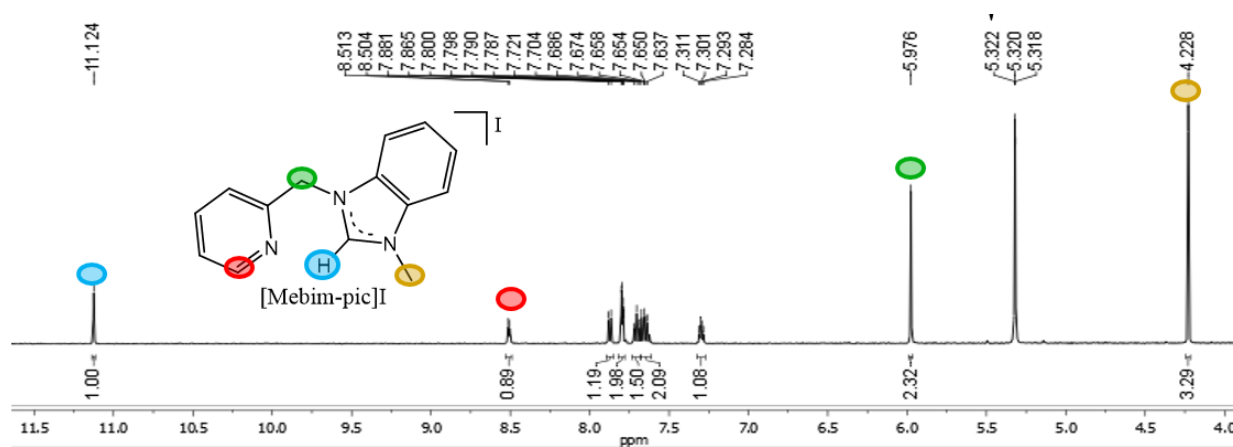


Figure A4.1: ¹H NMR of ligand precursor [Mebim-pic]I in d₆-DMSO.

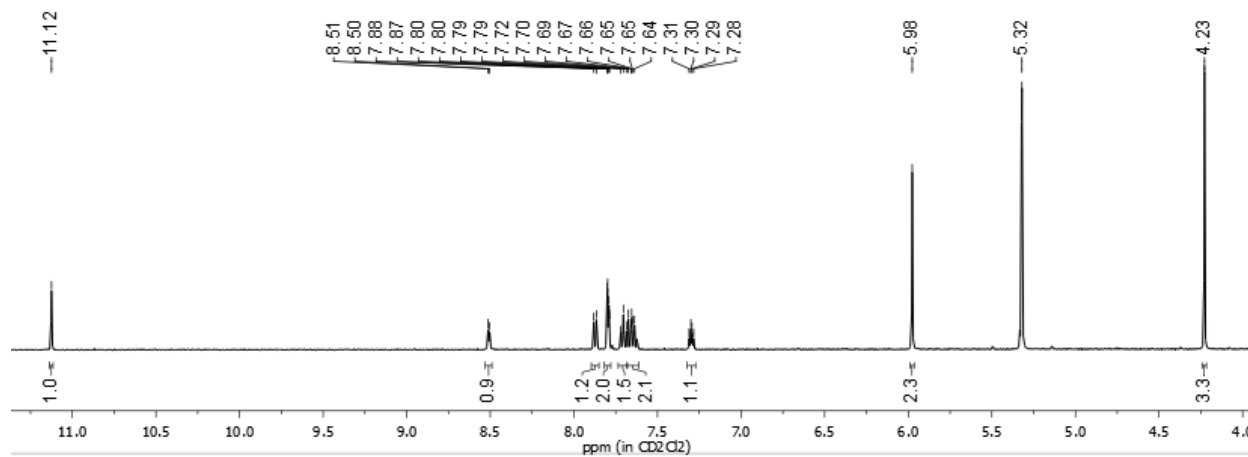


Figure A4.2: ¹H NMR of ligand precursor [Mebim-pic]I in CD₂Cl₂.

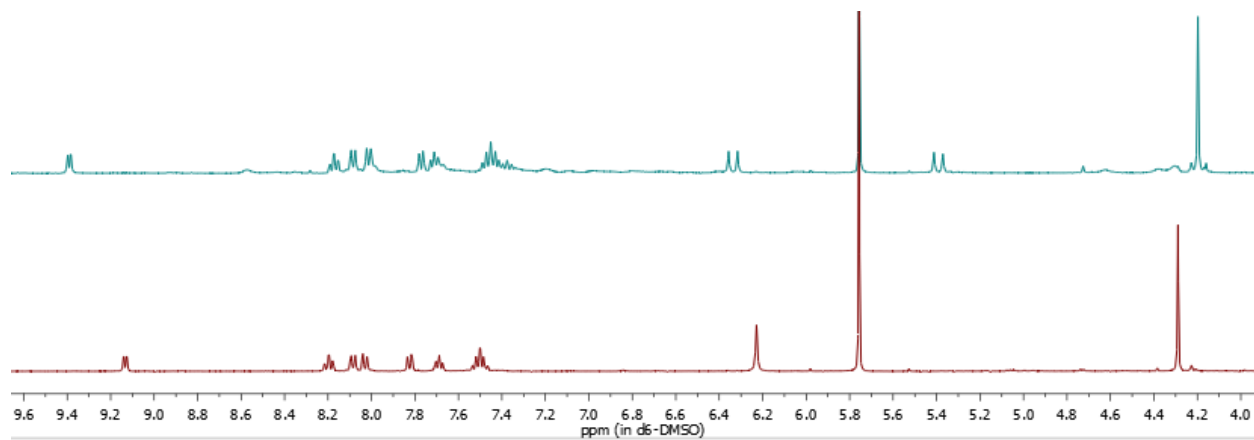


Figure A4.3: ^1H NMR of *cis*- (top in blue) and *trans*- (bottom in red) isomers of $\text{Ru}(\text{Mebim-pic})(\text{CO})_2\text{Cl}_2$ (**1a**) in d_6 -DMSO.

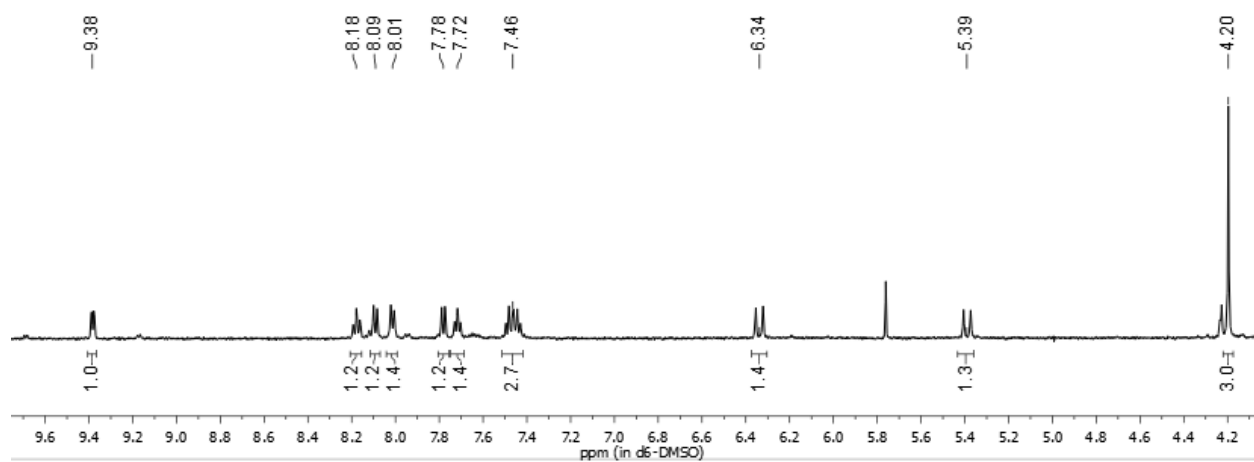


Figure A4.4: ^1H NMR of *cis*- $\text{Ru}(\text{Mebim-pic})(\text{CO})_2\text{Cl}_2$ (**1a**) in d_6 -DMSO.

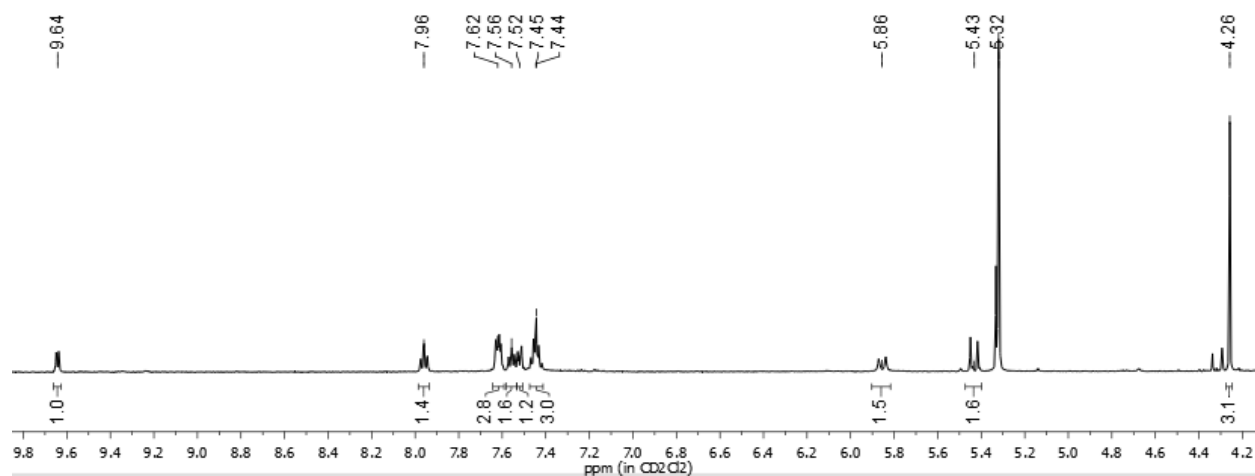


Figure A4.5: ¹H NMR of *cis*-Ru(Mebim-pic)(CO)₂Cl₂ (**1a**) in CD₂Cl₂.

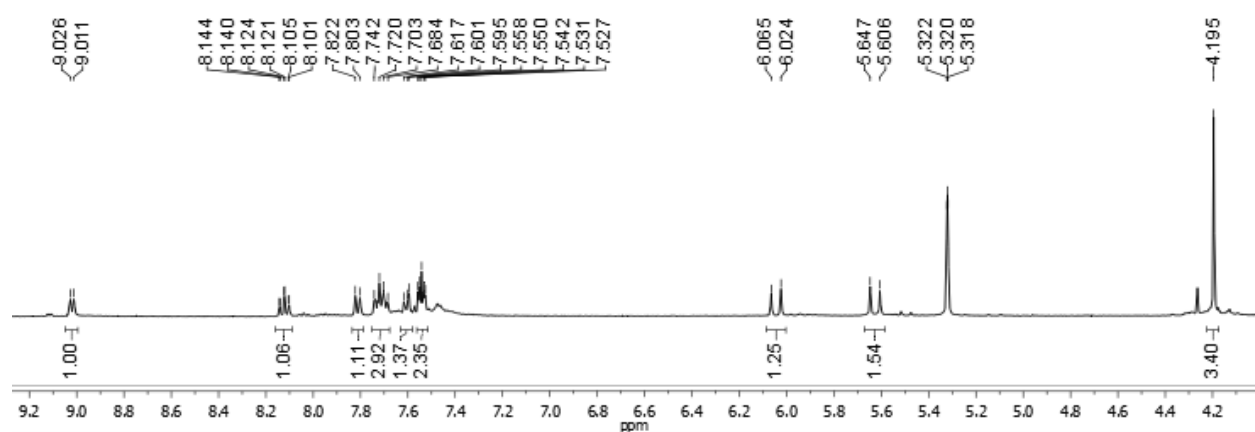


Figure A4.6: ¹H NMR of *cis*-Ru(Mebim-pic)(CO)₂(OTf)₂ (**2a**) in CD₂Cl₂.

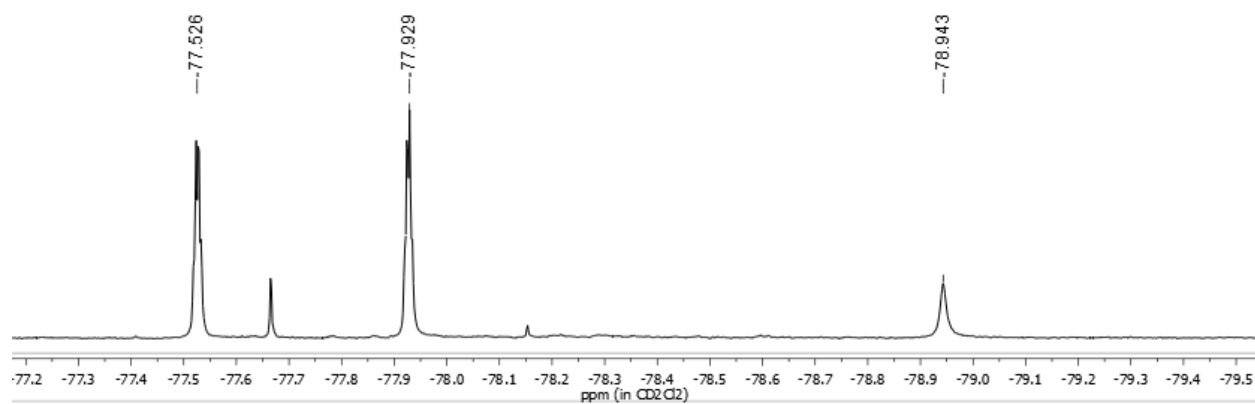


Figure A4.7: ¹⁹F NMR of *cis*-Ru(Mebim-pic)(CO)₂(OTf)₂ (**2a**) in CD₂Cl₂.

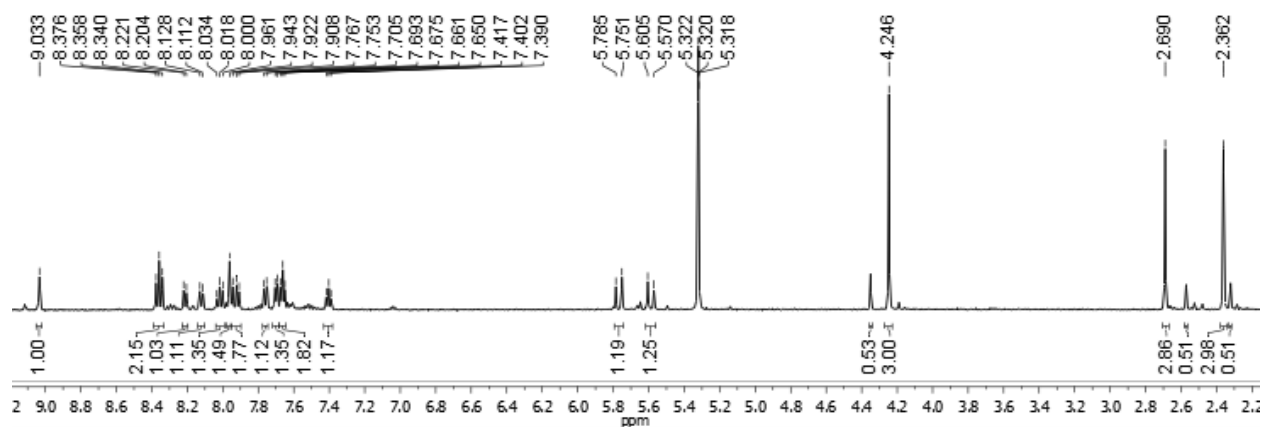


Figure A4.8: ¹H NMR of [Ru(Mebim-pic)(5,5'-Me₂bpy)(CO)₂][PF₆]₂ (**3a**) in CD₂Cl₂.

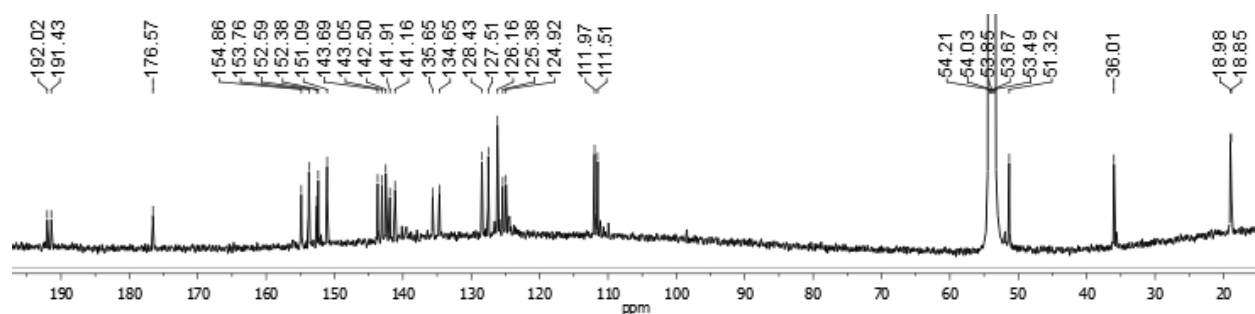


Figure A4.9: ¹³C{¹H} NMR of [Ru(Mebim-pic)(5,5'-Me₂bpy)(CO)₂][PF₆]₂ (**3a**) in CD₂Cl₂.

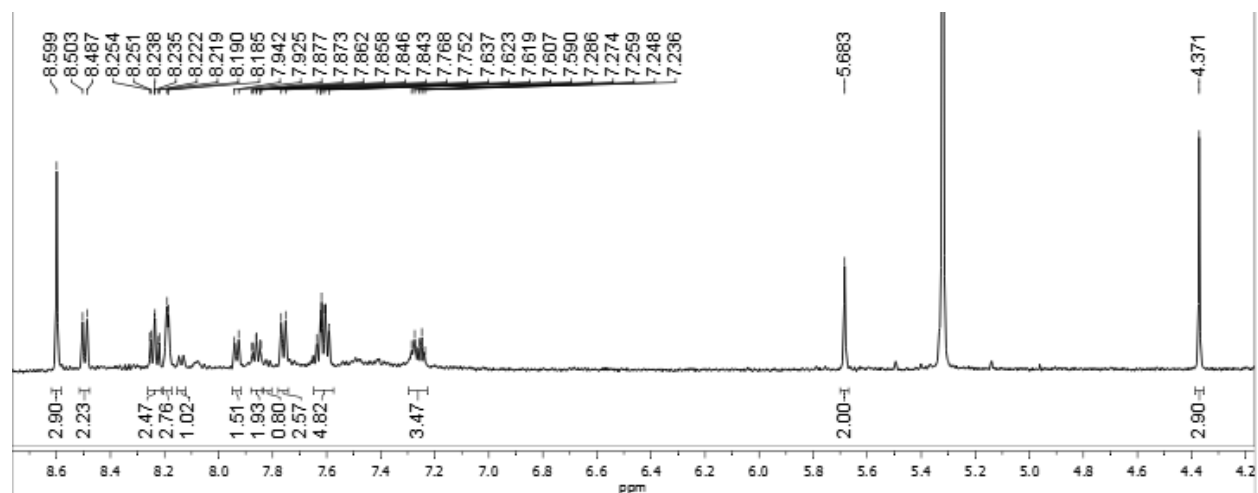


Figure A4.10: ¹H NMR of pyridine *trans* to CO isomer of **4a** [Ru(Mebim-pic)(tpy)(CO)][PF₆]₂ (**3a**) in CD₂Cl₂.

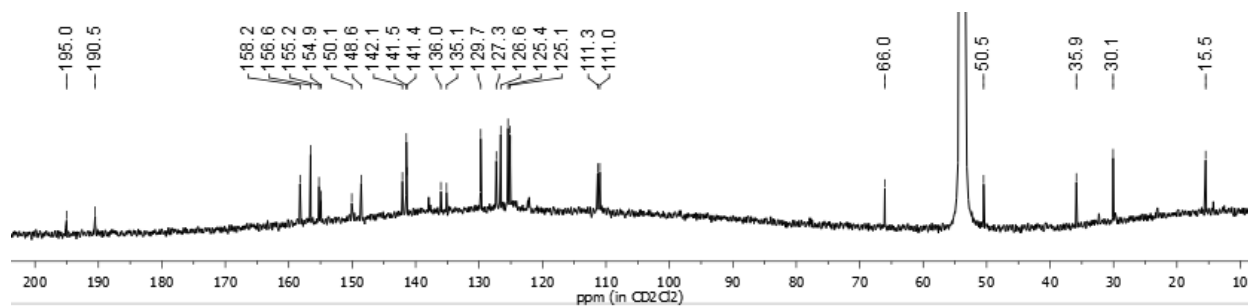


Figure A4.11: $^{13}\text{C}\{^1\text{H}\}$ NMR of pyridine *trans* to CO isomer of **4a** $[\text{Ru}(\text{Mebim-py})(\text{CO})][\text{PF}_6]_2$ (**3a**) in CD_2Cl_2 .

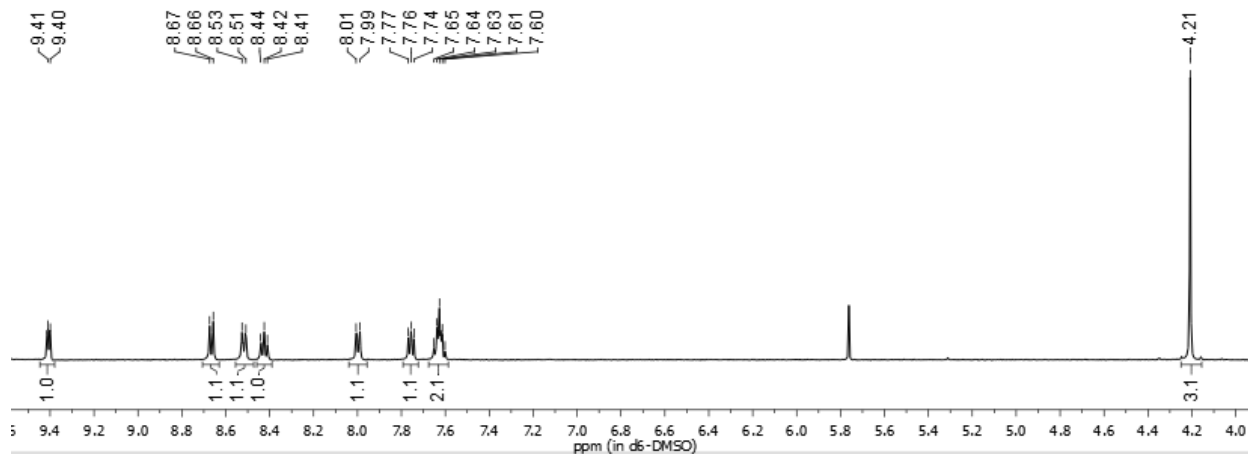


Figure A4.12: ^1H NMR of *cis*- $\text{Ru}(\text{Mebim-py})(\text{CO})_2\text{Cl}_2$ (**1a**) in $\text{d}_6\text{-DMSO}$.

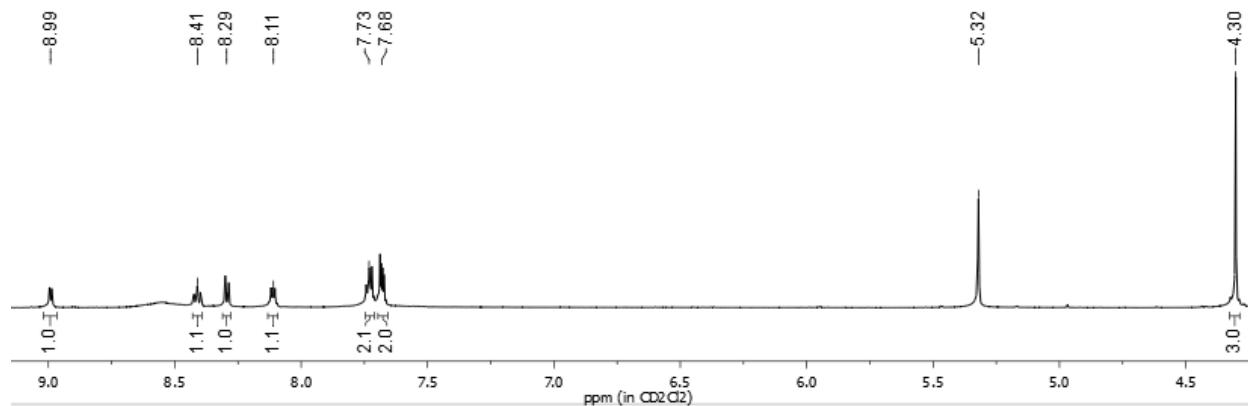


Figure A4.13: ^1H NMR of *cis*- $\text{Ru}(\text{Mebim-py})(\text{CO})_2(\text{OTf})_2$ (**2a**) in CD_2Cl_2 .

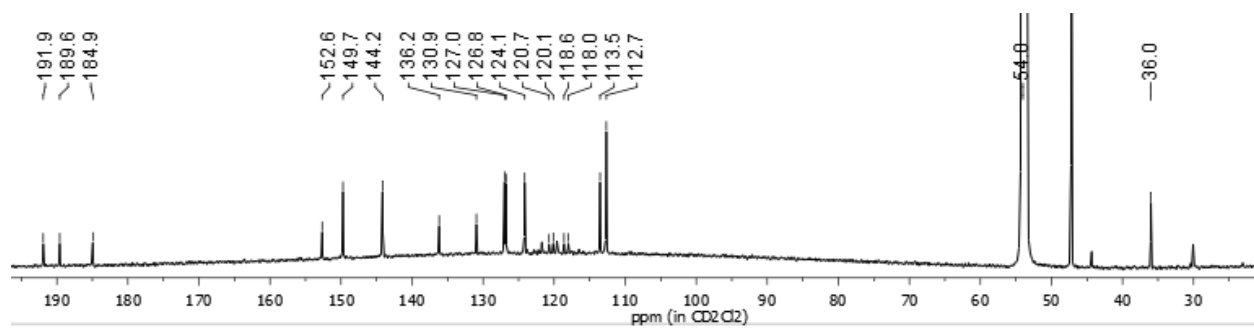


Figure A4.14: $^{13}\text{C}\{^1\text{H}\}$ NMR of *cis*-Ru(Mebim-py)(CO)₂(OTf)₂ (**2a**) in CD₂Cl₂.

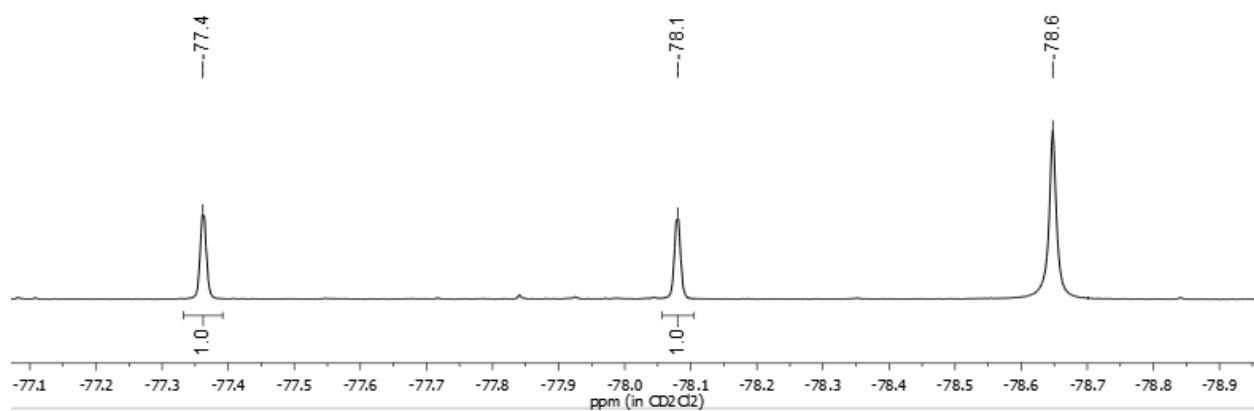


Figure A4.15: ^{19}F NMR of *cis*-Ru(Mebim-py)(CO)₂(OTf)₂ (**2a**) in CD₂Cl₂.

REFERENCES

- (1) (IEA), I. E. A. *IEA Headline Energy Data 2015 from Monthly Oil Data Service*; International Energy Agency, 2015.
- (2) Appel, A. M. *Chem. Ind.* **2014**, 78, 36–39.
- (3) Olivier, J. G. J.; Janssens-Maenhout, G.; Muntean, M.; Peters, J. H. A. W. *Trends in global CO₂ emissions - 2015 report from EDGAR*; 2014.
- (4) (IEA), I. E. A. *World Energy Outlook 2015*; 2015th ed.; 2015.
- (5) Kang, P.; Chen, Z.; Brookhart, M.; Meyer, T. J. *Top. Catal.* **2014**, 58, 30–45.
- (6) Kumar, B.; Llorente, M.; Froehlich, J.; Dang, T.; Sathrum, A.; Kubiak, C. P. *Annu. Rev. Phys. Chem.* **2012**, 63, 541–569.
- (7) Benson, E. E.; Kubiak, C. P.; Sathrum, A. J.; Smieja, J. M. *Chem. Soc. Rev.* **2009**, 38, 89–99.
- (8) Appel, A. M.; Bercaw, J. E.; Bocarsly, A. B.; Dobbek, H.; DuBois, D. L.; Dupuis, M.; Ferry, J. G.; Fujita, E.; Hille, R.; Kenis, P. J. A.; Kerfeld, C. A.; Morris, R. H.; Peden, C. H. F.; Portis, A. R.; Ragsdale, S. W.; Rauchfuss, T. B.; Reek, J. N. H.; Seefeldt, L. C.; Thauer, R. K.; Waldrop, G. L. *Chem. Rev.* **2013**, 113, 6621–6658.
- (9) Fujita, E. *Coord. Chem. Rev.* **1999**, 185-186, 373–384.
- (10) Bolton, J. R. *Science (80-.)*. **1978**, 202, 705–711.
- (11) Lu, X.; Leung, D. Y. C.; Wang, H.; Leung, M. K. H.; Xuan, J. *ChemElectroChem* **2014**, 1, 836–849.
- (12) Qiao, J.; Liu, Y.; Hong, F.; Zhang, J. *Chem. Soc. Rev.* **2014**, 43, 631–675.
- (13) Savéant, J.-M. *Chem. Rev.* **2008**, 108, 2348–2378.
- (14) Kuhl, K. P.; Hatsukade, T.; Cave, E. R.; Abram, D. N.; Kibsgaard, J.; Jaramillo, T. F. *J. Am. Chem. Soc.* **2014**, 136, 14107–14113.
- (15) Smieja, J. M.; Kubiak, C. P. *Inorg. Chem.* **2010**, 49, 9283–9289.
- (16) Kang, P.; Chen, Z.; Nayak, A.; Zhang, S.; Meyer, T. J. *Energy Environ. Sci.* **2014**, 7, 4007–4012.
- (17) Chen, Z.; Chen, C.; Weinberg, D. R.; Kang, P.; Concepcion, J. J.; Harrison, D. P.; Brookhart, M. S.; Meyer, T. J. *Chem. Commun. (Camb)*. **2011**, 47, 12607–12609.
- (18) Pitman, C. L.; Brereton, K. R.; Miller, A. J. M. *J. Am. Chem. Soc.* **2016**, 138, 2252–2260.

- (19) Johnson, B. A.; Maji, S.; Agarwala, H.; White, T. A.; Mijangos, E.; Ott, S. *Angew. Chem. Int. Ed. Engl.* **2016**, *55*, 1825–1829.
- (20) White, T. A.; Maji, S.; Ott, S. *Dalton Trans.* **2014**, *43*, 15028–15037.
- (21) Concepcion, J. J.; Jurss, J. W.; Norris, M. R.; Chen, Z.; Templeton, J. L.; Meyer, T. J. *Inorg. Chem.* **2010**, *49*, 1277–1279.
- (22) Gade, L. H. *Chem. Commun.* **2000**, 173–181.
- (23) Costentin, C.; Robert, M.; Savéant, J.-M. *Chem. Soc. Rev.* **2013**, *42*, 2423–2436.
- (24) Beley, M.; Collin, J.-P.; Ruppert, R.; Sauvage, J.-P. *J. Chem. Soc. Chem. Commun.* **1984**, 1315.
- (25) Collin, J.; Sauvage, J.-P. *Coord. Chem. Rev.* **1989**, *93*, 245–268.
- (26) Rakowski DuBois, M.; DuBois, D. L. *Acc. Chem. Res.* **2009**, *42*, 1974–1982.
- (27) Raebiger, J. W.; Turner, J. W.; Noll, B. C.; Curtis, C. J.; Miedaner, A.; Cox, B.; DuBois, D. L. *Organometallics* **2006**, *25*, 3345–3351.
- (28) Hawecker, J.; Lehn, J.-M.; Ziessel, R. *Helv. Chim. Acta* **1986**, *69*, 1990–2012.
- (29) Bourrez, M.; Molton, F.; Chardon-Noblat, S.; Deronzier, A. *Angew. Chem. Int. Ed. Engl.* **2011**, *50*, 9903–9906.
- (30) Grice, K. A.; Kubiak, C. P. *Chapter Five – Recent Studies of Rhenium and Manganese Bipyridine Carbonyl Catalysts for the Electrochemical Reduction of CO₂*; Advances in Inorganic Chemistry; Elsevier, 2014; Vol. 66.
- (31) Stanton, C. J.; Machan, C. W.; Vandezande, J. E.; Jin, T.; Majetich, G. F.; Schaefer, H. F.; Kubiak, C. P.; Li, G.; Agarwal, J. *Inorg. Chem.* **2016**, *55*, 3136–3144.
- (32) Riplinger, C.; Sampson, M. D.; Ritzmann, A. M.; Kubiak, C. P.; Carter, E. A. *J. Am. Chem. Soc.* **2014**, *136*, 16285–16298.
- (33) Johnson, F. P. A.; George, M. W.; Hartl, F.; Turner, J. J. *Organometallics* **1996**, *15*, 3374–3387.
- (34) Sullivan, B. P.; Bolinger, C. M.; Conrad, D.; Vining, W. J.; Meyer, T. J. *J. Chem. Soc. Chem. Commun.* **1985**, 1414.
- (35) Reutemann, W.; Kieczka, H. *Ullmann's Encycl. Ind. Chem.* **2000**.
- (36) Muckerman, J. T.; Achord, P.; Creutz, C.; Polyansky, D. E.; Fujita, E. *Proc. Natl. Acad. Sci. U. S. A.* **2012**, *109*, 15657–15662.
- (37) Connelly Robinson, S. J.; Zall, C. M.; Miller, D. L.; Linehan, J. C.; Appel, A. M. *Dalton*

Trans. **2016**.

- (38) Fong, H.; Peters, J. C. *Inorg. Chem.* **2015**, *54*, 5124–5135.
- (39) Taheri, A.; Berben, L. A. *Inorg. Chem.* **2016**, *55*, 378–385.
- (40) Taheri, A.; Berben, L. *Chem. Commun.* **2015**, *52*, 1768–1777.
- (41) Rail, M. D.; Berben, L. A. *J. Am. Chem. Soc.* **2011**, *133*, 18577–18579.
- (42) Kang, P.; Cheng, C.; Chen, Z.; Schauer, C. K.; Meyer, T. J.; Brookhart, M. S. *J. Am. Chem. Soc.* **2012**, *134*, 5500–5503.
- (43) Kang, P.; Meyer, T. J.; Brookhart, M. *Chem. Sci.* **2013**, *4*, 3497.
- (44) Slater, S.; Wagenknecht, J. H. *J. Am. Chem. Soc.* **1984**, *106*, 5367–5368.
- (45) Kobayashi, K.; Tanaka, K. *Phys. Chem. Chem. Phys.* **2014**, *16*, 2240–2250.
- (46) Kobayashi, K.; Kikuchi, T.; Kitagawa, S.; Tanaka, K. *Angew. Chem. Int. Ed. Engl.* **2014**, *53*, 11813–11817.
- (47) Nagao, H.; Mizukawa, T.; Tanaka, K. *Inorg. Chem.* **1994**, *33*, 3415–3420.
- (48) Schouten, K. J. P.; Qin, Z.; Pérez Gallent, E.; Koper, M. T. M. *J. Am. Chem. Soc.* **2012**, *134*, 9864–9867.
- (49) Kas, R.; Kortlever, R.; Milbrat, A.; Koper, M. T. M.; Mul, G.; Baltrusaitis, J. *Phys. Chem. Chem. Phys.* **2014**, *16*, 12194–12201.
- (50) Chen, C. S.; Handoko, A. D.; Wan, J. H.; Ma, L.; Ren, D.; Yeo, B. S. *Catal. Sci. Technol.* **2015**, *5*, 161–168.
- (51) Shen, J.; Kolb, M. J.; Göttle, A. J.; Koper, M. T. M. *J. Phys. Chem. C* **2016**, *acs.jpcc.5b10763*.
- (52) Kuhl, K. P.; Cave, E. R.; Abram, D. N.; Jaramillo, T. F. *Energy Environ. Sci.* **2012**, *5*, 7050.
- (53) Cox, P. A. *The Elements on Earth: Inorganic Chemistry in the Environment*; Oxford University Press, 1995.
- (54) Snyder, D. B.; Schauer, S. J.; Eyman, D. P.; Moler, J. L.; Weers, J. J. *J. Am. Chem. Soc.* **1993**, *115*, 6718–6729.
- (55) Reimer, K. J.; Shaver, A.; Quick, M. H.; Angelici, R. J. In *Inorganic Syntheses: Reagents for Transition Metal Complex and Organometallic Syntheses Volume 28*; Angelici, R. J., Ed.; John Wiley & Sons: New Jersey, 2007; pp. 154–159.

- (56) Dai, W.; Kim, S. B.; Pike, R. D.; Cahill, C. L.; Sweigart, D. A. *Organometallics* **2010**, *29*, 5173–5178.
- (57) Jackson, J. D.; Villa, S. J.; Bacon, D. S.; Pike, R. D.; Carpenter, G. B. *Organometallics* **1994**, *13*, 3972–3980.
- (58) Connelly, N. G.; Freeman, M. J.; Orpen, A. G.; Sheehan, A. R.; Sheridan, J. B.; Sweigart, D. A. *J. Chem. Soc. Dalt. Trans.* **1985**, 1019.
- (59) Neto, C. C.; Baer, C. D.; Chung, Y. K.; Sweigart, D. A. *J. Chem. Soc. Chem. Commun.* **1993**, 816.
- (60) Thompson, R. L.; Lee, S.; Rheingold, A. L.; Cooper, N. J. *Organometallics* **1991**, *10*, 1657–1659.
- (61) Brown, D. A.; Glass, W. K.; Kreddan, K. M.; Cunningham, D.; McArdle, P. A.; Higgins, T. *J. Organomet. Chem.* **1991**, *418*, 91–105.
- (62) Kuchynka, D. J.; Kochi, J. K. *Inorg. Chem.* **1988**, *27*, 2574–2581.
- (63) Sheldrick, G. M. *Acta Crystallogr. Sect. A, Found. Adv.* **2008**, *64*, 112–122.
- (64) Dolomanov, O. V.; Bourhis, L. J.; Gildea, R. J.; Howard, J. A. K.; Puschmann, H. *J. Appl. Crystallogr.* **2009**, *42*, 339–341.
- (65) Das Neves Gomes, C.; Jacquet, O.; Villiers, C.; Thuéry, P.; Ephritikhine, M.; Cantat, T. *Angew. Chem. Int. Ed. Engl.* **2012**, *51*, 187–190.
- (66) Bourhis, L. J.; Dolomanov, O. V.; Gildea, R. J.; Howard, J. A. K.; Puschmann, H. *Acta Crystallogr. Sect. A, Found. Adv.* **2015**, *71*, 59–75.
- (67) Sweet, J. R.; Graham, W. A. G. *J. Am. Chem. Soc.* **1982**, *104*, 2811–2815.
- (68) Sweet, J. R.; Graham, W. A. G. *J. Organomet. Chem.* **1979**, *173*, C9–C12.
- (69) Casey, C. P.; Andrews, M. A.; McAlister, D. R.; Rinz, J. E. *J. Am. Chem. Soc.* **1979**, *101*, 3371–3373.
- (70) Casey, C. P.; Andrews, M. A.; McAlister, D. R.; Rinz, J. E. *J. Am. Chem. Soc.* **1980**, *102*, 1927–1933.
- (71) Casey, C. P.; Andrews, M. A.; McAlister, D. R.; Jones, W. D.; Harsy, S. G. *J. Mol. Catal.* **1981**, *13*, 43–59.
- (72) Heinekey, D. M.; Radzewich, C. E. *Organometallics* **1998**, *17*, 51–58.
- (73) Wong, W.-K.; Tam, W.; Gladysz, J. A. *J. Am. Chem. Soc.* **1979**, *101*, 5440–5442.
- (74) Patton, A. T.; Strouse, C. E.; Knobler, C. B.; Gladysz, J. A. *J. Am. Chem. Soc.* **1983**, *105*,

5804–5811.

- (75) Merrifield, J. H.; Lin, G.-Y.; Kiel, W. A.; Gladysz, J. A. *J. Am. Chem. Soc.* **1983**, *105*, 5811–5819.
- (76) Kiel, W. A.; Lin, G.-Y.; Bodner, G. S.; Gladysz, J. A. *J. Am. Chem. Soc.* **1983**, *105*, 4958–4972.
- (77) Toyohara, K.; Tsuge, K.; Tanaka, K. *Organometallics* **1995**, *14*, 5099–5103.
- (78) Gibson, D. H.; Srinivas, B.; Niemann, B.; Sleadd, B. A.; Mashuta, M. S.; Vij, A.; Gallucci, J. C. *Organometallics* **2000**, *19*, 4179–4182.
- (79) Tanaka, K.; Ooyama, D. *Coord. Chem. Rev.* **2002**, *226*, 211–218.
- (80) Ooyama, D.; Tomon, T.; Tsuge, K.; Tanaka, K. *J. Organomet. Chem.* **2001**, *619*, 299–304.
- (81) Toyohara, K.; Nagao, H.; Mizukawa, T.; Tanaka, K. *Inorg. Chem.* **1995**, *34*, 5399–5400.
- (82) Chen, Z.; Concepcion, J. J.; Brennaman, M. K.; Kang, P.; Norris, M. R.; Hoertz, P. G.; Meyer, T. J. *Proc. Natl. Acad. Sci. U. S. A.* **2012**, *109*, 15606–15611.
- (83) Concepcion, J. J.; House, R. L.; Papanikolas, J. M.; Meyer, T. J. *Proc. Natl. Acad. Sci. U. S. A.* **2012**, *109*, 15560–15564.
- (84) Ishida, H.; Tanaka, K.; Tanaka, T. *Organometallics* **1987**, *6*, 181–186.
- (85) Norris, M. R.; Concepcion, J. J.; Glasson, C. R. K.; Fang, Z.; Lapides, A. M.; Ashford, D. L.; Templeton, J. L.; Meyer, T. J. *Inorg. Chem.* **2013**, *52*, 12492–12501.
- (86) Lee, L. A.; Wheeler, J. W. *J. Org. Chem.* **1972**, *37*, 497–498.
- (87) Curran, T. P.; Marques, K. A.; Silva, M. V. *Org. Biomol. Chem.* **2005**, *3*, 4134–4138.
- (88) Anderson, P. A.; Deacon, G. B.; Haarmann, K. H.; Keene, F. R.; Meyer, T. J.; Reitsma, D. A.; Skelton, B. W.; Strouse, G. F.; Thomas, N. C. *Inorg. Chem.* **1995**, *34*, 6145–6157.
- (89) Fulmer, G. R.; Miller, A. J. M.; Sherden, N. H.; Gottlieb, H. E.; Nudelman, A.; Stoltz, B. M.; Bercaw, J. E.; Goldberg, K. I. *Organometallics* **2010**, *29*, 2176–2179.
- (90) Kaski, J.; Lantto, P.; Vaara, J.; Jokisaari, J. *J. Am. Chem. Soc.* **1998**, *120*, 3993–4005.
- (91) Bodnar, T. W.; Cutler, A. R. *Organometallics* **1985**, *4*, 1558–1565.
- (92) Tam, W.; Lin, G. Y.; Wong, W. K.; Kiel, W. A.; Wong, V. K.; Gladysz, J. A. *J. Am. Chem. Soc.* **1982**, *104*, 141–152.
- (93) Saba, S.; Hernandez, R.; Choy, C. C.; Carta, K.; Bennett, Y.; Bondi, S.; Kolaj, S.; Bennett,

- C. J. Fluor. Chem.* **2013**, *153*, 168–171.
- (94) Kelly, J. M.; O’Connell, C. M.; Vos, J. G. *J. Chem. Soc. Dalt. Trans.* **1986**, 253.
- (95) Clear, J. M.; Kelly, J. M.; O’Connell, C. M.; Vos, J. G.; Cardin, C. J.; Costa, S. R.; Edwards, A. J. *J. Chem. Soc. Chem. Commun.* **1980**, 750.
- (96) Brookhart, M.; Grant, B.; Volpe, A. F. *Organometallics* **1992**, *11*, 3920–3922.
- (97) Kelly, J. M.; Vos, J. G. *J. Chem. Soc. Dalt. Trans.* **1986**, 1045.
- (98) Konno, H.; Kobayashi, A.; Sakamoto, K.; Fagalde, F.; Katz, N. E.; Saitoh, H.; Ishitani, O. *Inorganica Chim. Acta* **2000**, *299*, 155–163.
- (99) Santoro, F.; Althaus, M.; Bonaccorsi, C.; Gischig, S.; Mezzetti, A. *Organometallics* **2008**, *27*, 3866–3878.
- (100) Jahnke, M. C.; Pape, T.; Hahn, F. E. *Eur. J. Inorg. Chem.* **2009**, 1960–1969.
- (101) Jarusiewicz, J.; Yoo, K.; Jung, K. *Synlett* **2009**, *2009*, 482–486.
- (102) Guo, J.; He, P.; Yang, L.; Liu, X.; Lv, L.; Shi, Y.; Cao, C. *J. Chem. Res.* **2012**, *36*, 111–113.
- (103) Barczak, N. T.; Grote, R. E.; Jarvo, E. R. *Organometallics* **2007**, *26*, 4863–4865.
- (104) Jahnke, M. C.; Hahn, E. *Zeitschrift für Naturforsch. B* **2010**, *65*, 341–346.
- (105) Cheng, Y.; Lu, X.-Y.; Xu, H.-J.; Li, Y.-Z.; Chen, X.-T.; Xue, Z.-L. *Inorganica Chim. Acta* **2010**, *363*, 430–437.
- (106) St.C. Black, D.; Deacon, G. B.; Thomas, N. C. *Polyhedron* **1983**, *2*, 409–412.
- (107) Li, X.-W.; Wang, G.-F.; Chen, F.; Li, Y.-Z.; Chen, X.-T.; Xue, Z.-L. *Inorganica Chim. Acta* **2011**, *378*, 280–287.
- (108) Pavlishchuk, V. V.; Addison, A. W. *Inorganica Chim. Acta* **2000**, *298*, 97–102.
- (109) McGuinness, D. S.; Cavell, K. J. *Organometallics* **2000**, *19*, 741–748.
- (110) Wang, H. M. J.; Lin, I. J. B. *Organometallics* **1998**, *17*, 972–975.
- (111) Appel, A. M. *Nature* **2014**, *508*, 460–461.
- (112) Fujihira, M.; Hirata, Y.; Suga, K. *J. Electroanal. Chem. Interfacial Electrochem.* **1990**, *292*, 199–215.
- (113) Balazs, G. B.; Anson, F. C. *J. Electroanal. Chem.* **1993**, *361*, 149–157.

- (114) Balazs, G. B.; Anson, F. C. *J. Electroanal. Chem.* **1992**, 322, 325–345.
- (115) Lehn, J.-M.; Ziessel, R. *Proc. Natl. Acad. Sci.* **1982**, 79, 701–704.
- (116) Li, B.; Liu, T.; Popescu, C. V.; Bilko, A.; Darensbourg, M. Y. *Inorg. Chem.* **2009**, 48, 11283–11289.
- (117) Thomas, N. C.; Fischer, J. *J. Coord. Chem.* **1990**, 21, 119–128.
- (118) Ishida, H.; Tanaka, K.; Morimoto, M.; Tanaka, T. *Organometallics* **1986**, 5, 724–730.
- (119) Brookhart, M.; Studabaker, W. B. *Chem. Rev.* **1987**, 87, 411–432.
- (120) Brookhart, M.; Nelson, G. O. *J. Am. Chem. Soc.* **1977**, 99, 6099–6101.
- (121) Brookhart, M. S.; Kegley, S. E.; Husk, G. R. *Organometallics* **1984**, 3, 650–652.
- (122) Brookhart, M. S.; Tucker, J. R.; Husk, G. R. *J. Am. Chem. Soc.* **1981**, 103, 979–981.
- (123) Kegley, S. E.; Brookhart, M. S.; Husk, G. R. *Organometallics* **1982**, 1, 760–762.